INFN - Laboratori Nazionali di Frascati
Servizio Documentazione

LNF-90/005(R)
17 Gennaio 1990

ARES DESIGN STUDY

THE MACHINE

Editors

C. Pagani
S. Tazzari
G. Vignola
M. Bassetti
C. Biscari
R. Boni
M. Castellano
A. Cattoni
N. Cavallo
V. Chimenti
U. Gambardella
S. Guiducci
S. Kulinski
P. Michelato
L. Palumbo
M. Piccolo
C. Sanelli
L. Serafini
M. Serio
F. Tazzioli
L. Trasatti

Printed and Published by
Servizio Documentazione dei
Laboratori Nazionali di Frascati dell'INFN

INFN - Laboratori Nazionali di Frascati
Servizio Documentazione

LNF-90/005(R)
17 Gennaio 1990

ARES DESIGN STUDY
THE MACHINE

P.Amadei[1], A.Aragona[1], M.Barone[1], S.Bartalucci[1], M.Bassetti[1], M.E.Biagini[1], C.Biscari[1], R.Boni[1], M.Castellano[1], A.Cattoni[1], N.Cavallo[3], F.Cevenini[3,8], V.Chimenti[1], S.De Simone[1], D.Di Gioacchino[1], G.Di Pirro[1], S.Faini[1], G.Felici[1], M.Ferrario, L.Ferrucci, S.Gallo[1], U.Gambardella[1], A.Ghigo[1], S.Guiducci[1], S.Kulinski[1], M.R.Masullo[3], P.Michelato[2], G.Modestino[1], C.Pagani[2,7], L.Palumbo[1,5], R.Parodi[4], P.Patteri[1], A.Peretti[2], M.Piccolo[1], M.Preger[1], G.Raffone[1], C.Sanelli[1], L.Serafini[2], M.Serio[1], F.Sgamma[1], B.Spataro[1], L.Trasatti[1], S.Tazzari[1,6], F.Tazzioli[1], C.Vaccarezza[1], M.Vescovi[1], G.Vignola[1].

[1] INFN, Laboratori Nazionali di Frascati - CP13, 00040 - Frascati (Italy)

[2] INFN, Sezione di Milano, Via Celoria 16, 20133 - Milano (Italy)

[3] INFN, Sezione di Napoli, Mostra d'Oltremare, Pad.20, 80125 - Napoli (Italy)

[4] INFN, Sezione di Genova, Via Dodecaneso - Genova (Italy)

[5] Università di Roma "La Sapienza", Dip. di Energetica, Via A.Scarpa 14, 00161 - Roma (Italy)

[6] Università di Roma "Tor Vergata", Dip di Fisica - Via O. Raimondo - Roma (Italy)

[7] Università di Milano, Dip. di Fisica - Via Celoria 16, 20133 - Milano (Italy)

[8] Università di Napoli, Dip. di Sc. Fisiche - Mostra d'Oltremare, Pad.20, 80125 - Napoli (Italy)

ARES Design Study

The Machine

TABLE OF CONTENTS

ARES

THE MACHINE

1. - GENERAL DESCRIPTION

1.1. - DESIGN BASICS

The ARES accelerator complex consists of a 510 MeV once-recirculated SC Linac and of a two-ring colliding beam Φ-Factory .

The Linac serves as :

- an injector for the storage rings
- a FEL driver
- a test facility.

A schematic drawing of the layout is shown in Fig. 1.1.1

The Φ-Factory design luminosity is 10^{32} $cm^{-2}s^{-1}$ at 510 MeV. The storage rings are separated vertically and meet at a single interaction region; the opposite straight sections are dedicated to RF and injection. The rings are optimized at the Φ peak but can reach a top energy of ≥ .6 GeV. The injector energy allows the rings to be 'topped off' at the nominal energy, thereby improving the average integrated luminosity at the Φ.

The chosen parameters are conservative enough that, according to some of the existing models for the beam-beam limit, there is some hope to gradually achieve somewhat higher luminosities. The SC Linac also leaves open the possibility of testing the potential of a linear-against-circular collider.

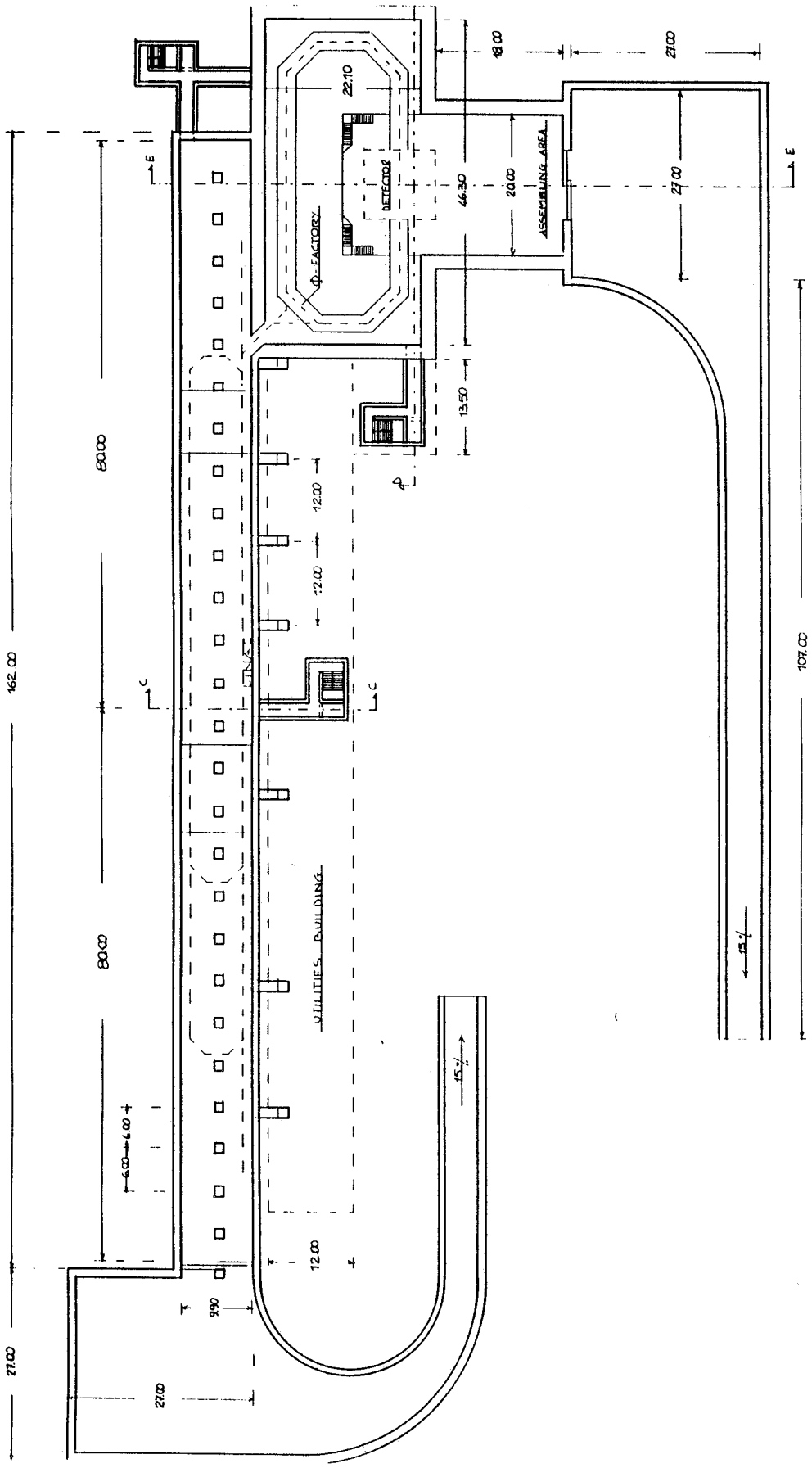

Fig. 1.1.1 - Schematic drawing of the ARES layout.

1.2. - SHORT HISTORY OF THE PROJECT

A definite interest for a superconducting linear accelerator arose in Frascati towards the end of 1985 when the long range future line of activity of the Laboratory started to be debated in preparation for the INFN 1989÷1993 five-year plan.

Physics interests in the Laboratory are very varied, ranging from the institutional topics of HEP and very high energy accelerators to intermediate energy Nuclear Physics and to Materials Science. In particular the local accelerator group has a long tradition of work on colliding beam rings and SR facilities and has, a few years ago, submitted proposals for a high duty cycle machine for Nuclear Physics and for a third generation, dedicated SR source, neither of which have been financed.

A SC Linac, a very versatile tool, presented a number features that were attractive for all of the above branches of Physics, namely :

- continuous beams with very high intensity and energy resolution
- production of FEL radiation in the short wavelength region
- possibility of testing the high charge, low emittance, high peak current, high repetition rate operation regime required by linear colliders.

A first Workshop[1] was held in Frascati in October 1986, during which physics applications and technical aspects of SC cavity design were discussed. The interest of the physics community was confirmed and shortly afterwards it was decided to launch an R&D program on SC cavities.

At the same time a feasibility study on a 5 to 10 GeV per beam collider based on SC linacs, with luminosity of $\approx 10^{33}$ $cm^{-2}s^{-1}$, capable of producing $\approx 10^7$ $B\underline{B}$ events per year and of supporting a 200 mA, CW beam with relative energy resolution of the order of 10^{-4}, was started along the lines suggested in references (5) and (6).

A Discussion Meeting on "Physics Possibilities of a high Luminosity e^+e^- Facility of up to ≈12 GeV" was held in Frascati in April 1987[2].

As a major part of the R&D program, LNF submitted the proposal for a small pilot facility, LIS-A, a SC linac in the 20 to 50 MeV range with state of the art beam quality and to be completed rapidly; it would serve the purpose of training the local personnel in the SC RF field

and it would also allow to study high power, high efficiency FELs in the infrared region, in collaboration with the neighbouring ENEA Laboratory.

LISA was approved at the end of 1987 and is today near to completion.

At about the same time INFN included in its five-year budget - approved by the Government in 1988 - provisions to carry out a vigorous R&D program on "*the technology of linear accelerators and SC RF cavities* " including "*a prototype low emittance, high pulse current injector,.. the development and construction of about 30, 10 MeV/m, high Q, SC cavities,.. the assembly of a string of cavities and of its ancillary equipment,.. the detailed design of a damping ring.. and of ..a positron source* ". The whole program was intended to develop the technologies and to test some of the most critical techniques proposed for the future linear colliders; it would be the basis for a subsequent decision to build a high quality accelerator for HEP.

The $B\bar{B}$ Factory feasibility study was completed during a third Workshop held in Courmayeur, in December 1987. A number of critical points in the design of a such high luminosity accelerators were evidenced and a number of important ideas and alternatives were put forward. However, in the course of the following discussions with INFN, it appeared that the dimensions of the project were not compatible with the size of the foreseeable commitment of resources.

A step-by step approach was therefore needed : from the accelerator side, a test facility of a more modest size but still capable of testing most of the critical technical solutions of larger installations seemed the best solution and, from the physics side, the great, albeit short-term, interest of a Φ-Factory, a much smaller project than a $B\bar{B}$ Factory, had actually been pointed out during the Courmayeur meeting[5]. Work therefore continued in this new direction.

Towards the end of 1988 the INFN Executive Committee formally decided to start the ARES Project with the charge of carrying out the R&D work laid down in the Plan and of producing a proposal for an accelerator complex that would include a Φ-Factory.

The present report covers the design work done during 1989 on the proposed ARES facility. Prototyping work on cavities was also financed and is in progress.

1.3. - GOALS

The goals of the project are - in compliance with the INFN five-year plan document - to develop the technology of linear accelerators, SC RF cavities and electron colliders, in order to build an accelerator complex consisting of high-field, high current, low emittance SC accelerator and of an annexed Φ-Factory.

- The first priority phase (phase 1) includes a Φ-Factory with a luminosity of at least 10^{32} $cm^{-2}s^{-1}$ - consisting of two separate high current storage rings - and a SC Linac configuration capable of producing electrons and positrons, at the desired rate and at the full Φ energy, for injection into the storage rings.

A R&D program, partly overlapping phase 1, would include the development of

- high performance RF cavities ($E_{acc} \approx 10$ MV/m @ $Q \approx 3\ 10^9$)
- high current low emittance beams and associated equipment (gun, steering, lenses, compressor, etc),
- special components and equipment for the two-ring collider.

- The subsequent phase would be devoted to the exploitation of the SC Linac potential as a FEL driver and as a test bench for the future high energy colliders.

A FEL program to produce high power laser beams in the region of wavelengths below 100 nm, not accessible to ordinary lasers [1] is briefly outlined in § 1.4.2.

Concerning future colliders, the focal points of interest for ARES are :

- the generation and acceleration of low emittance beams with high peak currents and the development of SC resonators such as to constitute a significant step towards collider-grade parameters,
- the investigation of the linear-against-circular principle to produce high luminosity e^+e^- collisions.

The Φ-Factory storage rings are in fact designed so that low emittance lattice configurations - necessary to obtain a high luminosity to beam power ratio in a linear-against-circular scheme - can rather easily be obtained; the rings are also located deep underground, to better handle the high beam powers involved.

An actual layout for the linac-against-ring test facility needs further detailed work and is not included in the present report.

Last, SC Linacs are a necessary step in the strive towards energies much higher than those obtainable today. Already now they are being considered as possible power sources for the future Linear Colliders and - as soon as the SC RF cavity technology will allow fields in the order of 40÷50 MV/m to be reached with high Q's - fully SC Linear Colliders will become the most cost-effective way of achieving very high energies[4]. SC resonators will also permit to reach the very high pulse currents and very low emittances and energy spreads required by high luminosity, multi-TeV Linear Colliders much more easily and with much lower energy consumption than afforded by 'warm' structures.

1.4 - THE PHYSICS : AN OUTLINE

A very short overview of the Physics programme is given here. A more detailed description of the physics goals and of the experimental apparata is given in a separate volume.

1.4.1 - Physics Program for a Φ-Factory

Many physics topics can be addressed by a Φ-Factory operating at a peak luminosity of 1-2 x 10^{32} cm^{-2} sec^{-1}. It is clear, however, that the first priority in the experimental program to be carried out at such a facility will be given to the measurements regarding CP violation phenomena. Examples of other interesting measurements that could be also carried out at such a high luminosity e^+ e^- collider are:

- Measurement of the e^+ e^- total cross section around 1 GeV.
- Measurement of the ν_μ mass.
- Measurement of the π and K form factor
- High statistic study of the η and/or η' resonances.

The physics measurements will prescribe - for each of the topics mentioned above - the characteristics of the experimental apparatus. However, because the design of the high luminosity storage rings is based on a single interaction point, the detector for such a facility has

to be optimized in such a way that it can meet most of the requirements of most of the experiments to be carried out.

CP violation is one of the most interesting phenomena in the entire field of particle physics. The existence of processes violating CP invariance is experimentally established in Kaon decays (6), but its origin is not completely clear. The explanation of CP violating processes is somehow built into the Standard Model with 3 generation of quarks, but the overall pattern of CP violation might be suggestive of Physics beyond the Standard Model; as a matter of fact at the moment of this writing it is not clear whether the superweak hypothesis (7) is ruled out by the latest experimental findings of Na-31 (8) and E-731 (9).

The measurement of CP violation in K^0 decays, as it can be obtained at an $e^+ e^-$ Factory operated at the Φ, will yield, provided the luminosity of the facility exceeds 10^{32} $cm^{-2}s^{-1}$, a measurement of ε'/ε not only with statistical accuracies better than the ones achieved so far with K^0_{long} beams but, most important, with systematic errors, which in the case of K^0_{long} beams are or are going to be in the near future the limiting factor to the precision of the various measurements, that will be substantially reduced thanks to the pair production of the K\s(0,long) K^0_{short} and to the overconstrained kinematical situation.

If the facility could be upgraded so that the luminosity would increase by an order of magnitude, ($\approx 1 \div 2 \times 10^{33}$ cm^{-2} sec^{-1}) then a completely new field of measurements, regarding CP violation in the K^0_{short} decays will open up, a field which is much more difficult to cover with the K^0_{short} beams technique.

As noted previously, even if the main goal for a Φ-Factory is the study of CP violation phenomena in the K system, other interesting pieces of experimental information will become available with the running of such a facility equipped with a suitable detector. To this regard we would like to stress that a 10^{32} cm^{-2} sec^{-1} machine will make available to experimenters data bases between 100 and 1000 times bigger than the ones collected up to now, with such obvious advantages that they need not be mentioned.

In conclusion from the point of view of fundamental interaction physics a Φ-Factory, is, in our opinion, a well balanced investment: the Physics return is quite high and the field covered is to a large extent unique.

1.4.2 - X-VUV FEL Experiments

In the context of the ARES project the production of high brightness e-beams at an energy of 300-600 MeV is foreseen, with typical peak currents in the range 200÷400 A and with anticipated normalized transverse emittance of $4 \div 8 \cdot 10^{-6}$ m rad (rms emittance).

The availability of these beams makes a wide set of FEl experiments in the VUV and soft X rays spectrum regions feasible; radiation wavelengths ranging from 150 nm down to 20 and, as an ultimate goal, 10 nm could be covered.

Because in this region of the e.m. spectrum - photon energies ranging from 7 eV to 100 eV - efficient mirrors are not available, coherent radiation must be generated by means of single pass high-gain FEL processes, of the SASE (self amplified from spontaneous emission) type.

As it will be shown later, the beams produced by the ARES SC LINAC are able, once injected into a properly tuned wiggler, to strongly radiate coherent radiation in the exponential gain regime, starting from noise. Detailed 3D numerical simulations[9] have indicated that a high power input signal is not needed if the beam emittance is low enough to ensure a good transverse phase-space overlapping between the electrons and the photon beams. Moreover, the FEL gain (in the high gain regime) exhibits a threshold behaviour, because Pellegrini's rule[10] - $\varepsilon_n \leq (\lambda \gamma)/(2 \pi)$ - makes it very sensitive to the beam emittance. A low emittance is therefore essential.

Recently A.M. Sessler and W.Barletta[11] proposed an interesting mechanism to improve the performance of high gain single pass FEL's. Filling the wiggler beam pipe with low pressure Helium and injecting a 'leading', high current (500 A) electron bunch an ionized plasma channel consisting of a positively charged column of Helium ions is produced. Injecting a 'trailing' high brightness bunch into the plasma channel one can fully or partially (depending on the Helium pressure) neutralize the beam space charge, giving rise to an intense pinch field (typically of the order of a few MGauss) which strongly focuses the beam. Since the FEL gain depends on the beam current density, the ion focussing can strongly enhance the FEL performance.

One-dimensional model predictions[12] for a few typical ARES beams are listed in Table 1.4.1, in terms of the main parameters characterizing the wiggler and the FEL outputs. The four types of beams presented have been selected to represent what could be achieved in successive upgrading steps of the SC LINAC performance. The first 300 MeV beam can be produced without any recirculation: its emittance and current values are conservative.

The next two intermediate beams require recirculation through the last LINAC section to raise the energy to 500-600 MeV. An emittance $\approx 5\ 10^{-6}$ m rad at a peak current of 400 A seems feasible on the basis of the preliminary calculations because of the low RF frequency (500

MHz) selected for the LINAC cavities, which strongly reduces the emittance and energy spread degradation induced by wake-fields.

The wiggler parameters listed in Table 1.4.1 are typical of hybrid undulators: the field levels are even slightly lower than the values predicted by the Halbach' scaling laws[13]. The fabrication of such 10 to 15 m long wigglers, is therefore well within the limits of the present state of the art.

Ion focussing has been incorporated in the last two cases, producing wavelengths down to 21 and 11 nm. The values listed for the parameter H give the corresponding reduction of the betatron wavelength in the wiggler. At H=.25 for example, the beam radius is pinched by a factor of two because of ion focussing. The output peak power of the coherent radiation generated in the wiggler is also listed in Table 1.4.1, together with the saturation length.

The results of some three dimensional numerical simulations, performed with the FRED-3D code[14] are reported (enclosed in parenthesis) for the sake of comparison. As an example, for the case at 50 nm, the output power computed by FRED-3D is 40 MW after 20 m of wiggler: the radiation field power is still continuously growing exponentially at a gain of 3.3 dB/m. The lower gain observed in the FRED-3D calculations, with respect to the one-dimensional model, is due to the fact that the beam emittance is just above the Pellegrini's threshold.

The radiation field power behaviour along the wiggler, as computed by FRED-3D for the 21 nm case, is reported in Fig. 1.4.1 (solid line). The typical exponential gain can be observed, with a saturation power level of 320 MW. In this case a slight ion-focussing effect (H=.38) has been applied to overcome the violation of Pellegrini's rule.The saturation power level is lower because of diffraction effects tending to remove the radiation from the electron beam.

The last case presented can be viewed as the ultimate goal for the FEL driver : a double recirculation in the last SC LINAC section could boost the beam energy up to 820 MeV. Pushing down the beam emittance to the lowest foreseeable value, the output power of the coherent radiation generated in the wiggler can reach 650 MW, with a radiation wavelength of 11 nm, i.e. a photon energy of 117 eV. The required wiggler length is $\approx$ 10 meters.

The preliminary studies, together with the performed simulations, indicate that bursts of VUV and soft X-ray coherent radiation will be available at the ARES SC LINAC facility: this opens great possibilities to perform both accelerator physics experiments in the mainstream of the TeV electron-positron colliders and a large class of experiments within the environment of solid state and applied physics.

Table 1.4.1 - Possible FEL Experiments

Beam energy	[MeV]	300	500	580	820
Peak current	[A]	200	400	400	400
Norm emitt.	[m rad]	$1 \cdot 10^{-5}$	$8 \cdot 10^{-6}$	$4 \cdot 10^{-6}$	$3 \cdot 10^{-6}$
Wiggler period	[cm]	3	3	2	2
Wiggler field	[T]	.75	.75	1.	1.
Ion focussing (H)		1	1	.38	.25
Rad. Wavelength	[nm]	140	50	21	11
Photon energy	[eV]	9	25	58	116
Satur. power	[MW]	140	400(40*)	550(320*)	650
Satur. length	[m]	12.2	15.(17.6*)	8.2(7.5*)	9.7

* FRED-3D calculations

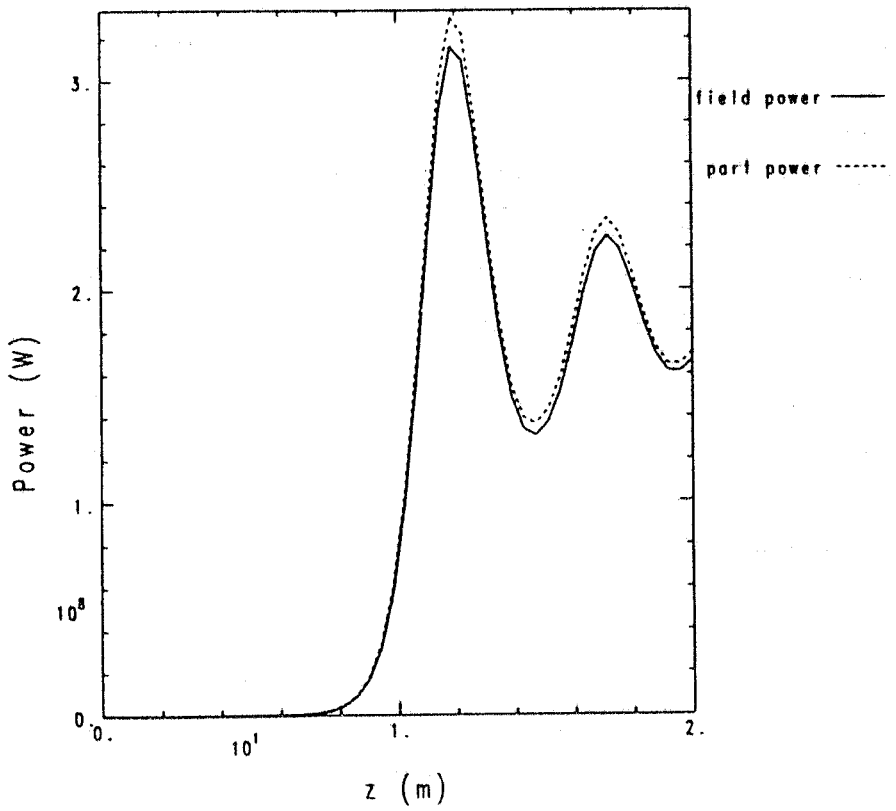

Fig. 1.4.1 - Computed radiation field power [W•10^8] along the wiggler [m•10], as generated by a 580 MeV, 400 A electron beam. The norm. emitt. is $4 \cdot 10^{-6}$ m rad, while the added ion focusing corresponds to: H = 0.38.

1.5 - LINAC

The SC Linac has to provide electron and positron beams at 510 MeV. The positron intensity must be such that a current of the order of 1 A can be injected in each of the Φ-Factory rings in a time of the order of a few minutes. In addition, the Linac must be capable of reaching a single-pass energy high enough to perform significant FEL experiments and beam quality tests, so that very low emittance beams can be accelerated without degradation.

While the ideal situation - both from the point of view of positron production and from that of beam quality - would be to install a number of SC cavities sufficient to reach the full 510 MeV energy in one pass, cost considerations favour a solution in which a number of cavities are used more than once by recirculating the beam through them, an option afforded by the SC structure that is capable of carrying up to several mA of average current.

Recirculation of course implies ring-like transport channels; these have a finite relative momentum acceptance estimated at around 4% at most [3].

On the other hand, positrons are generated within a finite momentum bite, that needs to be as large a possible to increase the yield; it is generally assumed to be of the order of 10 MeV. In our case the momentum spread requirements for Φ-Factory injection - ± 2.5 MeV - are more stringent (see § 2.3.) . Nevertheless, positrons must be accelerated to an energy larger than ≈ 300 MeV before they can be recirculated.

This fixes the minimum single-pass energy to be provided.

Two other problems have to be taken into account in determining the Linac configuration:

- the capture section following the positron converter has to be 'warm', because of radiation problems and also because the field in the capture section should be as high as possible to maximise the capture section acceptance and increase the conversion efficiency.

- from the converter onwards, and until an energy of ≈100 MeV or higher has been reached, the positron beam can not be put through any bending magnet because its energy dispersion, as already explained above, is too large.

The ensemble of these constraints leads to the configuration schematically shown in Fig. 1.5.1. Figure 1.5.2 shows, schematically, the physical arrangement of the transport and recirculation channels in the vertical plane. A short description of the rationale of the layout is given below.

Electrons are generated by the gun G, passed through a matching section that - depending on the type of gun - may include a chopper, a prebuncher, a warm section and other diagnostics and control elements (see § 2.3.2. - The Electron Preinjector), and accelerated by Linac Section L1 consisting of four SC cavities each providing a nominal voltage gain of 12 MV. The electron preinjector output energy is ≥ 4 MeV.

At the output of L1 the nominal beam energy is therefore ≈ 52 MeV or slightly higher, the exact value depending on the type of gun that is being used (see § 2.3.2.).

Each four-cell SC cavity in section L1 has its own cryostat and forms a cryomodule, the smallest unit of the cryogenic structure that can be individually tested. The distance between focusing elements is minimised in the low energy region where space-charge forces are important.

The distance between adjacent cryostats is kept to the minimum value of one RF wavelength (0.6 m); focusing, diagnostics, control and vacuum components are integrated within this length (see § 2.6.).

The axis through the gun and section L1 is below the main Linac axis and parallel to it. The vertical distance between the two is 1.0 m.

After Section L1 the electron beam enters an achromatic isochronous transport channel (TC12) including a pulsed dipole, is deflected unto the main Linac axis and enters Section L2, identical to section L1, that boosts its energy by a further 48 MeV (nominal). The overall nominal electron beam energy at the output of L2 is therefore ≥ ≈ 100 MeV.

The pulsed dipole is necessary because in the positron mode electron and positron bunches follow each other at a distance of only a few hundred ns and the positron bunch must enter section L2 undeflected.

Following Section L2 the electron beam is brought to the main Linac Section, L3, through an isochronous achromatic channel (TC23) that includes all splitter and combiner devices required to handle the primary and recirculated electron and positron beams.

Section L3 consists of 20 four-cell cavities, with one cryostat for each pair to increase the Linac filling factor. The cryomodule therefore contains of two cavities.

The overall nominal voltage provided by Section L3 is 240 MV. The electron beam nominal energy at the output of L3 is therefore ≥≈ 340 MeV.

In the electron mode, electrons are then brought back to the input of L3 through the isochronous achromatic transport channel indicated in Fig.1.1 as TC3 and passed once more through L3.

The electron beam final nominal energy at the output of the Linac is thus $\geq \approx$ 580 MeV affording a safety factor of $\approx$ 12 % with respect to the required energy of 510 MeV. In terms of accelerating voltage in the SC cavities this means that the actually required average accelerating voltage could be as low as 8.7 MV/m.

In the positron mode, the $\approx$300 MeV electron beam that has passed once through the Linac is brought back to the positron converter, PC, through the isochronous achromatic channel TC2 (see Fig. 1.5.2). The PC is described in more detail in the following.

The positrons produced in the converter target are collected in the 1.5 m long warm section LW4 (see Fig.1.5.2) that provides an accelerating field of $\approx$ 35 MV/m and an overall accelerating voltage of $\approx$ 40 MeV. They thus reach the input of L2 with about the same energy as that of electrons incoming from L1 and are further accelerated, through L2 . At this point they can be put through the splitter and recombiner magnets of the transport channel to L3.

The $\approx$ 300 MeV positron beam at the output of L3 is then recirculated once, via transport channel TC3, and finally reaches its final nominal energy of 510 MeV.

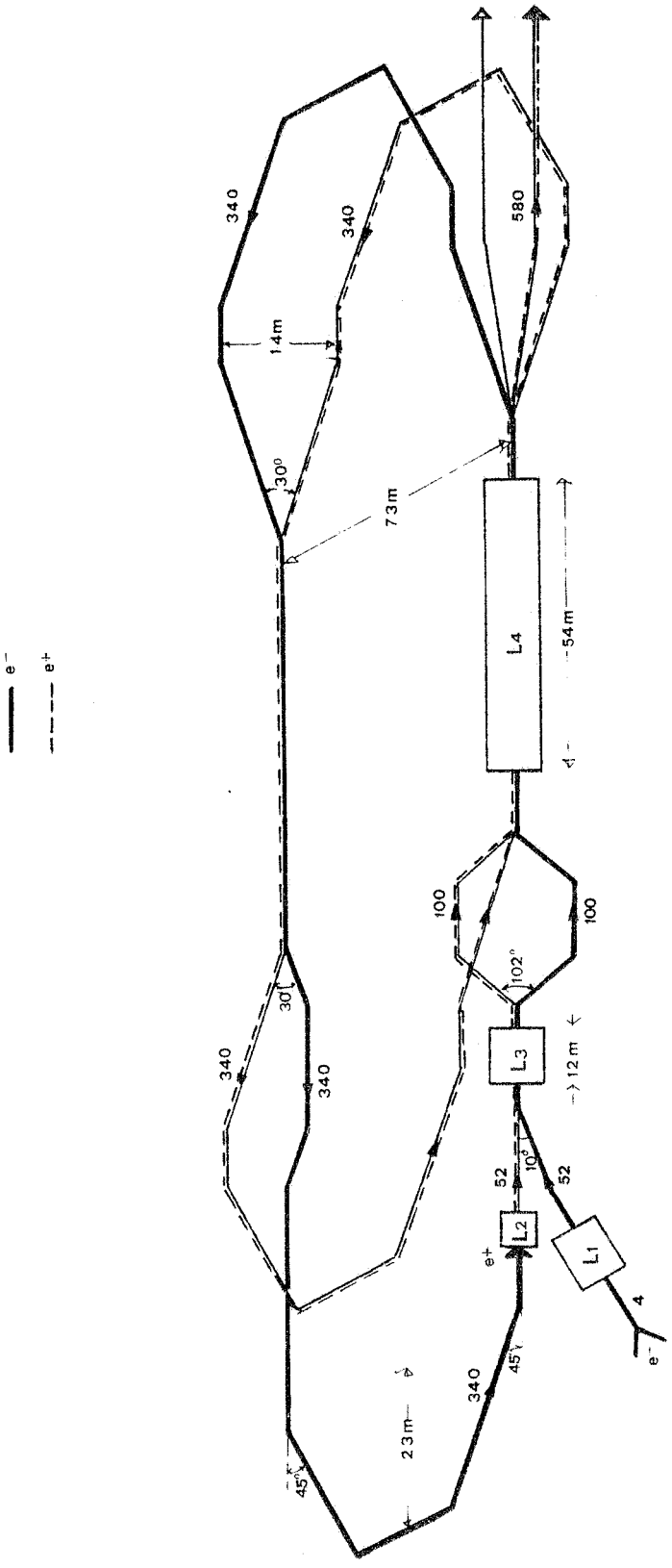

Fig. 1.5.1 - Schematic drawing of the recirculated Linac configuration.

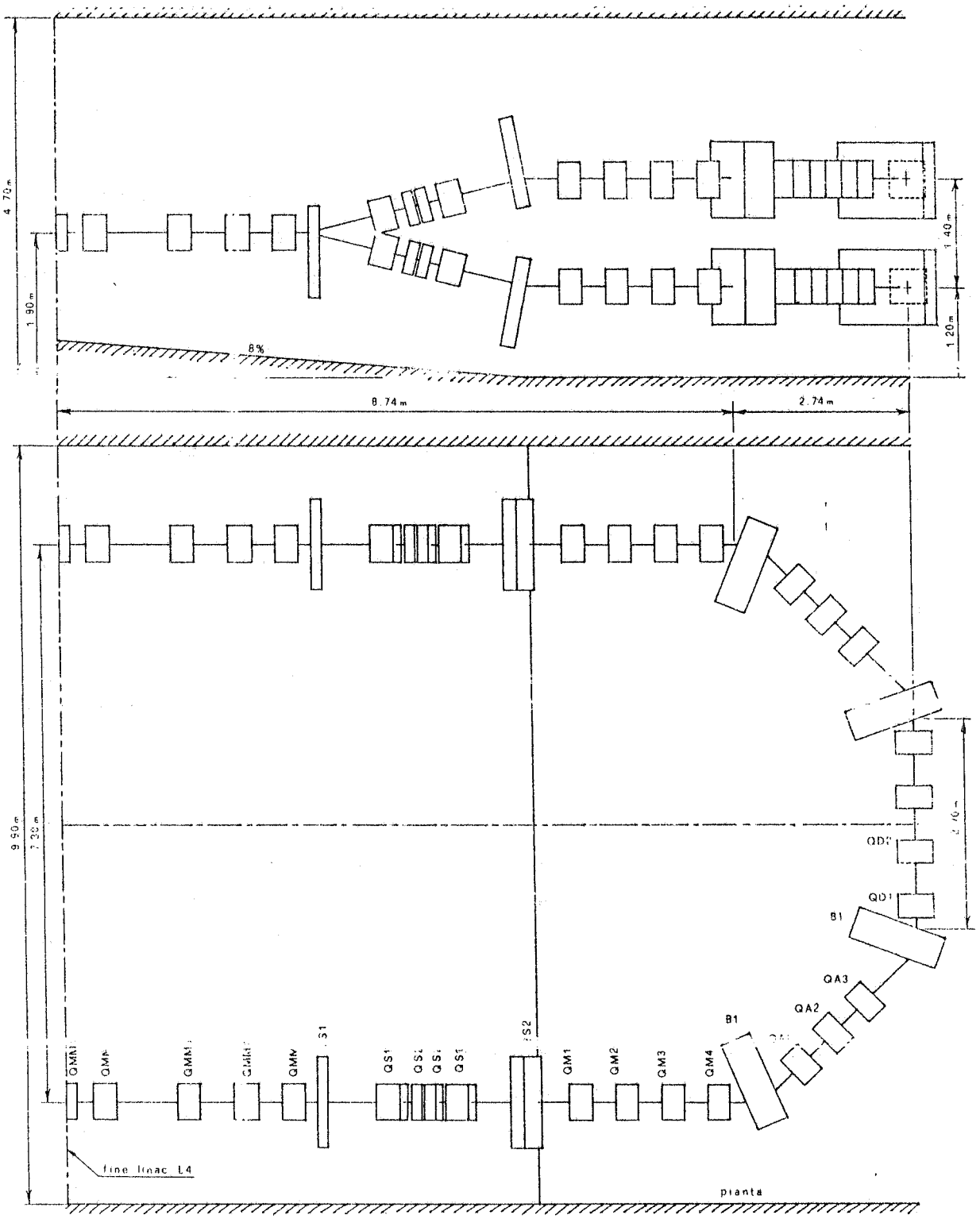

Fig. 1.5.2 - Schematic drawing showing the physical arrangement of the transport and recirculation channels of the Linac.

1.6. - Φ-FACTORY

The main goal of the ARES Φ-Factory is a luminosity $\geq 10^{32}$ $cm^{-2}sec^{-1}$ at 510 MeV .

This kind of luminosity has never been reached or even approached in a reliable way at such relatively low energies; the system parameters must therefore be carefully chosen and optimized based on the available experience an on existing models and scaling laws.

On the other hand a tight time schedule asks for a basically proven design, that relies on only a very limited amount of R&D and is flexible enough to allow the key machine parameters to be varied so as to optimize the luminosity and to explore alternative collision schemes such as the the linear-against-circular solution.

The proposed ARES design is therefore based on conventional technology, with electrons and positrons circulating in two separate storage rings, one above the other, and colliding head-on in a single interaction point. The two separate rings make it possible to increase the number of bunches and gain a substantial factor on luminosity through the high permissible collision frequency.

The rings are compact but the chosen bending field values do not require SC dipoles; a number of unexplored engineering problems related to the design of 'curved' SC dipoles, to the much stronger non linearities deriving from the very small bending radius and to synchrotron radiation in a superconducting environment are thus avoided.

The values of the betatron functions at the crossing point are low but not so low as to create problems with beam instabilities because of the very small longitudinal bunch length or with interferences of the interaction point quadrupoles with the experimental apparatus.

The beam emittance value is also a good compromise between the large values favoured by luminosity and the need to keep the machine physical aperture reasonable; the design of the lattice is moreover such that the emittance can be tuned over a wide range of values.

The coupling coefficient, κ, has been carefully optimized to reach the best compromise between lifetime and luminosity in the light of existing models and scaling laws

The maximum allowed linear tune shift in the beam-beam interaction, ξ^{max} , is the most important parameter and the primary limiting factor of luminosity. As of today no satisfactory theory exists that fully explains the mechanism of this limitation.

The value chosen in the ARES design takes into account all known scaling laws [15] and a recent model developed in Frascati [16].

All scaling laws predict that the maximum obtainable luminosity increases with increasing radiation damping, although with different power laws. The approach chosen for the ARES factory attempts at establishing a 'maximum likelihood' value and is believed to leave some

margin for development and improvements. Some basic features of the different models can and will be tested on ADONE, as discussed in more detail in Chapter 3.2.7.

The values of circulating current necessary to achieve the desired goal are high but not higher than obtained, as top performance, at some existing SR sources [17].

A summary of the Factory main parameters is given in Table 1.6.1.

Table 1.6.1 - Φ-Factory Main Parameters

Luminosity	[cm^{-2} sec^{-1}]	10^{32}
Emittance	[m rad]	10^{-6}
κ		.01
ξ_y		.04
ξ_x		.04
β_y	[cm]	4.5
Collision frequency	[MHz]	71.4
Bunch length	[cm]	3
N^{er} of particles per bunch		8.9 10^{10}

References

(1) Proc. Discussion Meeting on SC Linear Accelerators; Frascati, Oct. 1986
(2) Proc. Discussion Meeting on Physics possibilities of a high luminosity e^+e^- facility of up to 12 GeV; Frascati, Apr. 1987
(3) Courmayeur
(4) 40÷50 MV/m to be obtained with high Q's.
(5) G.Barbiellini and C.Santoni, " A detector for a Φ-factory", Courmayeur
(6) J. Christenson, J. Cronin, V. Fitch, R. Turlay. P.R.L. 138, 1964.
(7) L. Wolfenstein. P.R.L. 13, 562, 1964.
(8) Burkhardt et al. P.L. B209, 169, 1988.
(9) B. Winstein. Invited paper given at the 14th International Symposium on Lepton and Photon Interactions, Sanford, Aug. 1989.
(10) C. Pellegrini, NIM, 177, 227 (1980)
(11) W.A.Barletta and A.M.Sessler, Proc. INFN Int. School on e.m.radiation, Varenna, Italy, June 1988
(12) R.Bonifacio, C.Pellegrini and L.M.Narducci, Opt. Commun. 50, 373 (1984).
(13) K.Halbach, Proc. Undulator Mag. for SR and FEL, Trieste, Italy, June 1987.
(14) W.A.Barletta, Private communication.
(15) J.Seeman, Lecture Notes in Pysics, Vol 247, 1985 - Springer Verlag Ed.
(16) M.Bassetti, Int.Memo ARES-18
(17) 1985 NSLS Annual report - BNL 51947
1988 NSLS Annual report - BNL 52167

2. - LINAC

2.1. - OPTICS

2.1.1 - Introduction

As explained in § 1.5., the SC linear accelerator has three sections :

- Section L1 consisting of four SC cavities each providing a nominal accelerating voltage of 12 MV. The total nominal beam energy at its output is ≈ 50 MeV. Each four-cell SC cavity in section L1 has its own cryostat and constitutes a cryomodule.

- Section L2 is identical to L1 and accelerates - from ≈ 50 MeV to ≈ 100 MeV - both the positron beam coming from the capture section and the electron beam coming from L1.

- Section L3 consists of 20 four-cell cavities, with one cryostat to a pair of cavities to increase the Linac filling factor; the cryomodule is correspondingly longer. Its overall nominal output energy is ≈ 340 MeV. Electron and positron beams are passed through this section twice to reach their final nominal energy of ≈ 580 MeV.

2.1.2. - Linac focusing

Transverse focalization along the Linac is provided by a FODO sequence of 0.2 m long quadrupoles, one per cryogenic module.

The distance between quadrupoles is 3 m in L1 and L2; the focalization can be made weaker on L3, and the half FODO cell is therefore lengthened to 5.4 m to fit the longer cryomodule .

The first section, L1, needs a special treatment.

This because the effect of the RF field of an accelerating cavity on the beam transverse optical functions is negligible only insofar as the beam energy increase in the cavity is smaller than the input energy [1]; else, the FODO lattice focusing is highly perturbed and a strong mismatch occurs and proper corrective action has to be taken.

The condition is not verified along the first part of L1 since the beam is injected at 4 MeV and accelerated by the first cavity to 16 MeV. Both the input betatron functions and the quadrupole strengths must therefore be modified to compensate for the RF cavity effects.

The solution is to provide a FODO sequence that is not formed of identical cells, and is designed to guarantee that the optical functions at the end of the section match the following FODO cell eigenvalues. The betatron functions and the transverse beam sizes (for ε_n=1x10^{-6} m rad) along L1 are shown in Figure 2.1.1.

Note that the average beam sizes are almost constant along the section because the increase of the betatron functions in the second half of the section is counteracted by the adiabatic damping of the emittance due to acceleration.

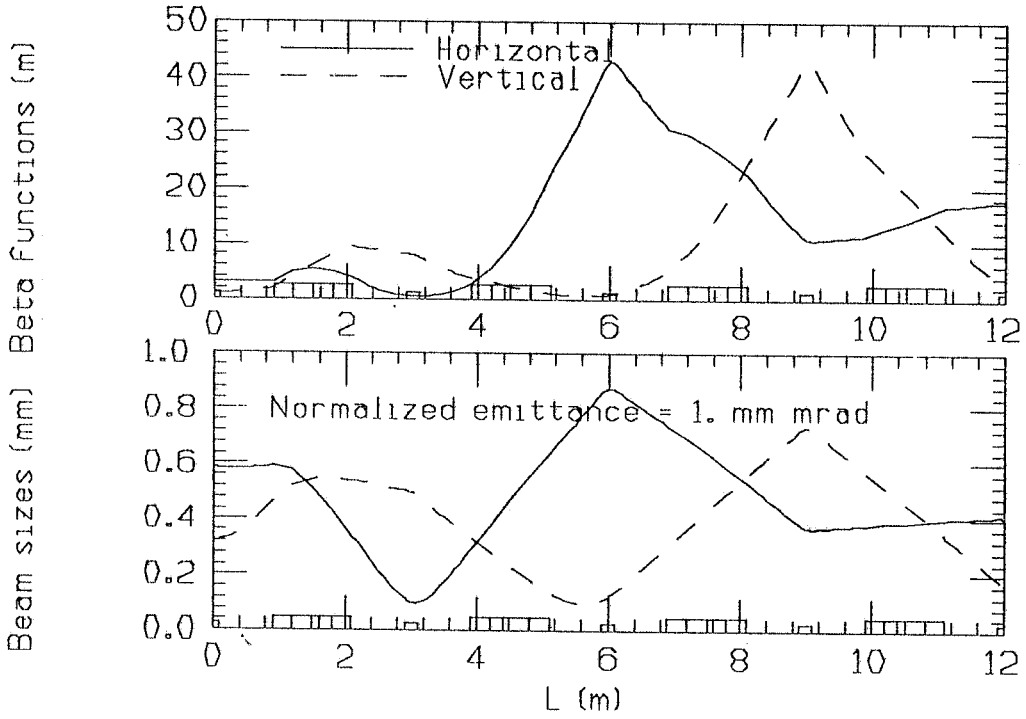

Fig.2.1.1 - Betatron functions and beam transverse sizes along linac L1 for a normalized emittance of 1x10^{-6} m rad. Initial energy = 4 MeV; final energy = 52 MeV.

In the second section, L2, the mismatch produced by RF fields in the transverse plane is negligible and the proposed conventional FODO structure with a 120° constant phase advance in both planes is adequate. The required quadrupole strengths (K^2 = 2.9 m^{-2}) correspond to a maximum gradient of 1 T/m in the last quadrupole.

The optical functions and the transverse beam sizes along L2 are shown in Fig.2.1.2.

Section L2 accelerates both positrons and electrons; the e^- transverse beam size is less than one mm for the foreseen normalized emittance value of about 10^{-5} m rad, while the maximum transverse positron beam size is of the order of 2.4 cm because the positron emittance is much larger, of the order of 5x10^{-3} m rad.

The maximum beam size occurs inside the quadrupoles; the largest beam size in the cavities is 1.8 cm, still providing good transmission efficiency.

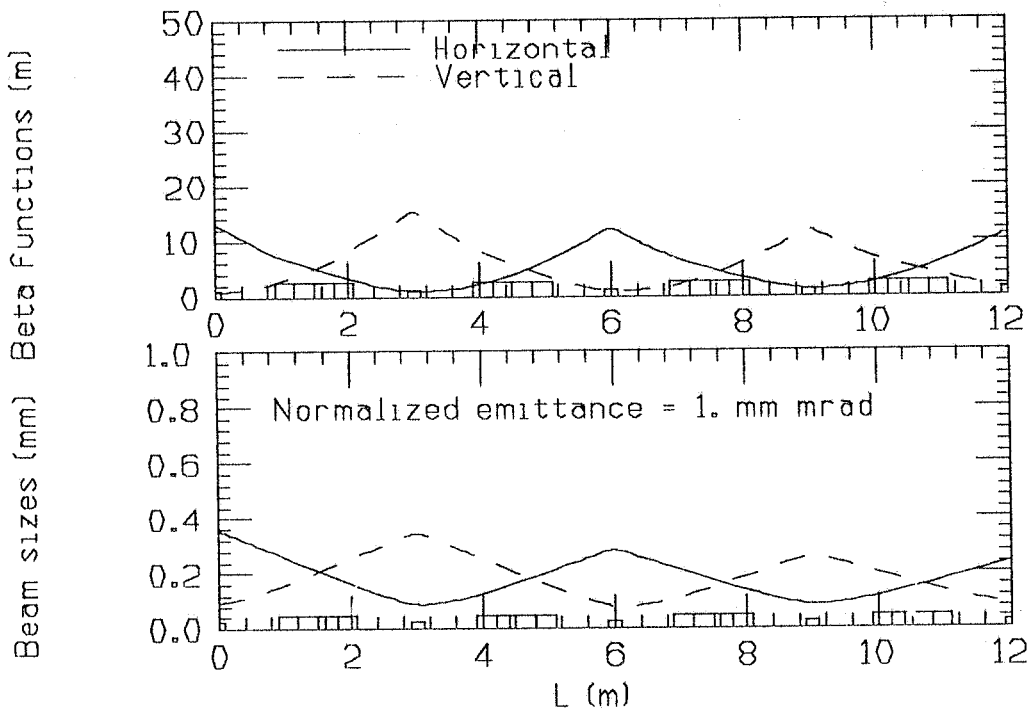

Fig.2.1.2 - Betatron functions and beam transverse sizes along linac L2 for a normalized emittance of $1x10^{-6}$ m rad. Initial energy = 52 MeV; final energy = 100 MeV.

Section L3 has double length cryomodules and both the e^+ and the e^- beams pass through it twice. In the first passage the beams are accelerated from ≈100 MeV to ≈340 MeV, in the second they are further accelerated to the final nominal energy of ≈ 580 MeV.

The focusing lattice must therefore cope not only with the varying beam energy in any one pass but also with the different input energy of the two passes.

The proposed lattice is still a standard 120° phase advance FODO; the cell is lengthened to 10.8 m to fit the cryomodule length. The quadrupole strength is reduced to 1.6 m^{-2}, corresponding to a maximum gradient of 2 T/m. The overall beam size is only slightly reduced with respect to that in L2, because even though the emittance has been adiabatically damped the greater length of the FODO cell makes the betatron functions larger.

On its second passage the beam sees a weaker focusing structure, but electron beam sizes are nevertheless kept smaller than 0.2 mm ($\varepsilon_n \approx 1x10^{-6}$) and positron beam sizes are smaller than 1.2 cm.

Figures 2.1.3 and 2.1.4 show the optical functions and the beam transverse dimensions on the first and second passage respectively. The two transverse planes are of course interchangeable.

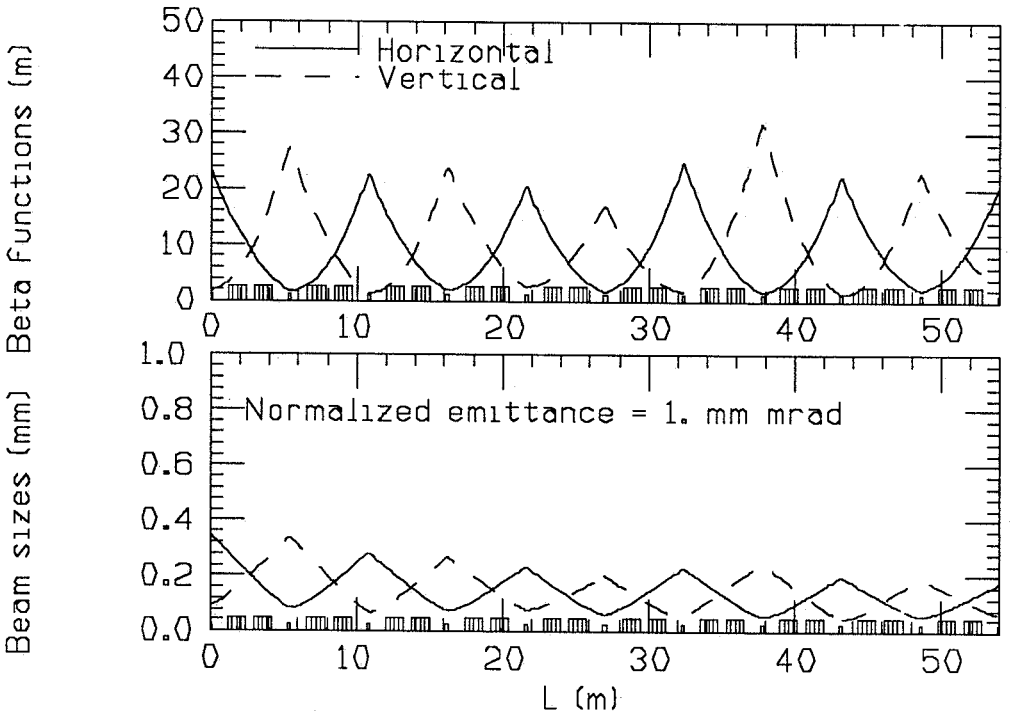

Fig.2.1.3 - Betatron functions and beam transverse sizes along linac L3 for a normalized emittance of 1×10^{-6} m rad in the first passage. Initial energy = 100 MeV; final energy = 340 MeV.

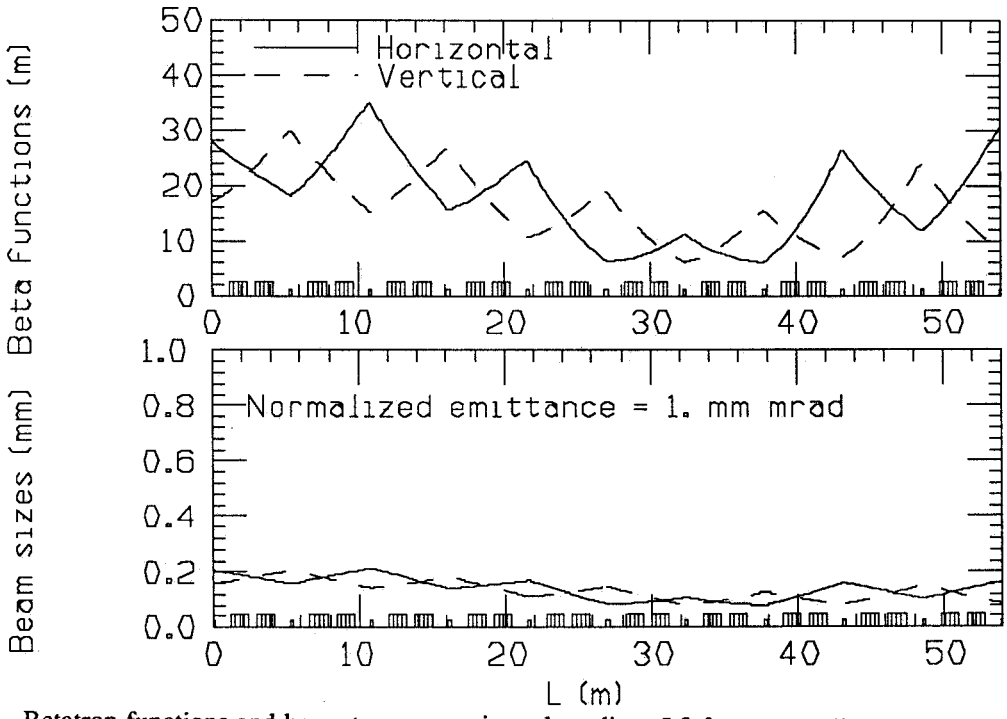

Fig.2.1.4 - Betatron functions and beam transverse sizes along linac L3 for a normalized emittance of 1×10^{-6} m rad in the second passage. Initial energy = 340 MeV; final energy = 580 MeV.

2.1.3 - Recirculation lattices

The general layout of the SC Linac and of the recirculation arcs has been described in paragraph 1.4.

The recirculation arcs lattice is described here in more detail. Note that the same lattice is used for both the transport line that recirculates the 340 MeV e^+ and e^- beams through Linac section L3 (TC3), and for the line which takes the electron beam from L3 to the positron converter (TC2).

L3 outputs four beams - e^- @340 MeV, e^+ @340 MeV, e^- @580 MeV, e^+ @580 MeV - that have to be routed through different transport channels. The routing is accomplished using a vertical splitter magnet .

The 340 MeV recirculation of electrons and positrons can be accomplished using the same channel to save on space and equipment.

The transport channels, TC2 and TC3 consist of arcs connected by a long straight section. The straight section portion connecting the arcs of TC3, can also be made common to TC2 and TC3 by properly retuning the quadrupoles when changing mode of operation.

This also allows the arc which reinjects the beams into L3 to be used (alternatively) for either electrons or positrons, because when positrons are reaccelerated, the 340 MeV electrons are only used for positron production and only one arc is needed. By proper retuning it can alternatively be used for electrons or positrons.

The layout of the whole structure is given in Fig.2.1.5 for the electron mode of operation and in Fig.2.1.6 for the mode of operation . Both beams are accelerated to 580 MeV.

It can be seen from the layout that double chicanes are needed at those three points where beams with different energies or charge must pass together; the use of kickers could have simplified the line design, but the rise times and kicker strengths required by our beam time structure fall outside the region covered by present fast kicker technology.

The chicanes are constrained to be in the vertical plane by the vertical splitting of the main arcs.

Recirculation line L3 must fulfil two basic requirements: achromaticity and isochronism. Both depend on the trajectories inside the bending magnets and are therefore driven by the arcs.

We recall that, for ultrarelativistic particles, an isochronous line is also achromatic and that the condition of isochronism is fulfilled if the integral over the arc of the dispersion function normalized to the curvature radius vanishes.

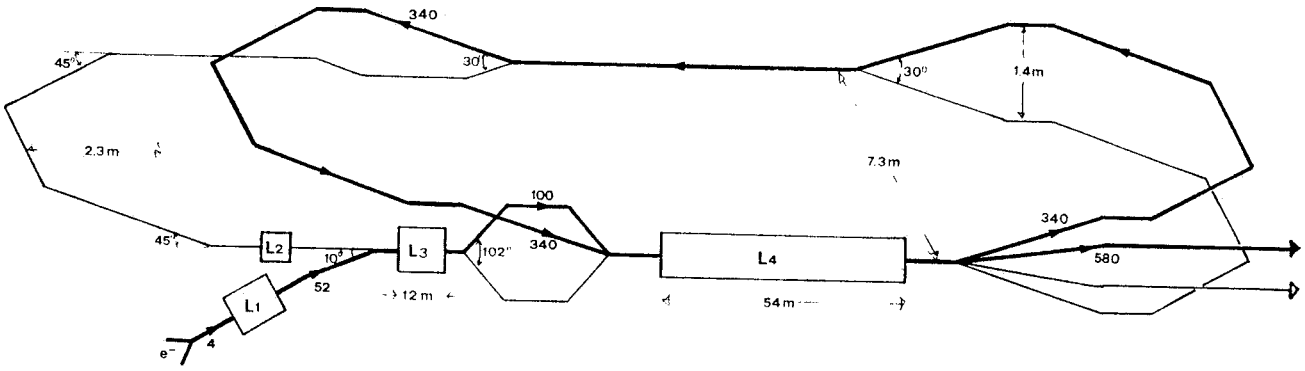

Fig.2.1.5 - Sketch of the Linacs and recirculating arcs layout in the configuration of electron acceleration. Numbers near the arrows are meant for the beam energies in MeV.

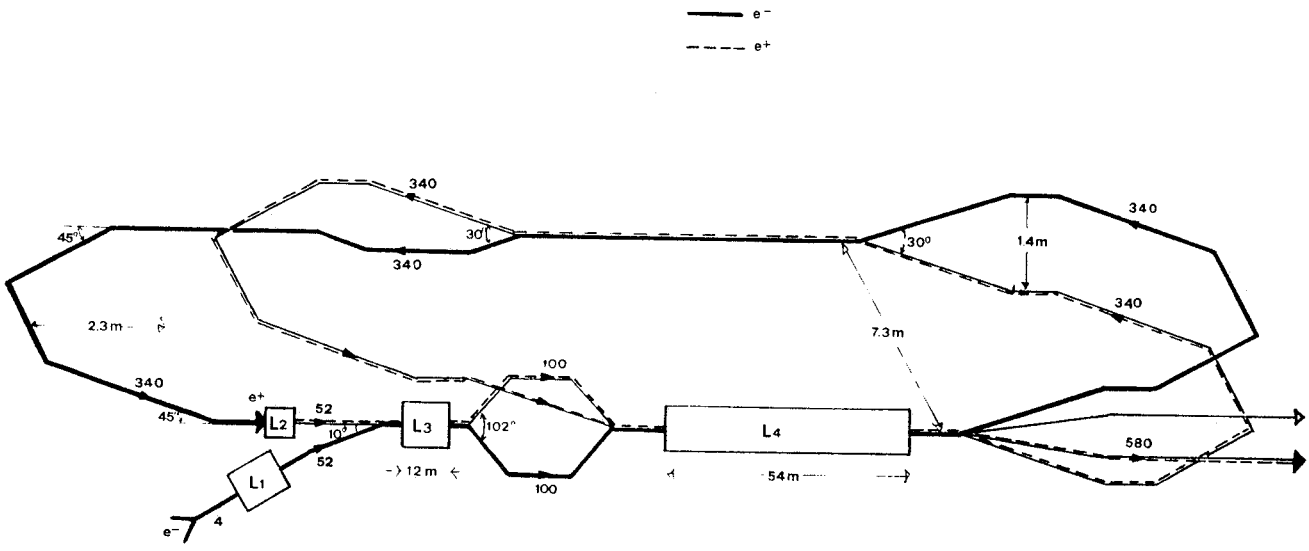

Fig.2.1.6 - Sketch of the Linacs and recirculating arcs layout in the configuration of positron acceleration. Numbers near the arrows are meant for the beam energies in MeV.

To meet the above specification a configuration with four dipoles, each bending the beam through 45° , has been chosen. Negative dispersion is produced at the two inner dipoles, so as to compensate both the positive dispersion introduced by the two outer dipoles and that produced by the splitter.

The splitter in turn consists of an achromatic, 15° bend chicane in the vertical plane.

The whole line is symmetric around the midpoint of the arc; the half arc consists of the following sequence : a matching section between L3 and the splitter, the splitter vertical chicane, a matching section between the splitter chicane and the arc, the 90° arc.

The overall arc length is 27.1 m.

The eigenvalues of the FODO lattice configuration along L3, described in § 2.1.2, provide the betatron function values at the output of L3; these are matched to those of the arc by the first matching section. The matching conditions to be fulfilled by the other matching sections - at the other end of the first arc and at both ends of the two other arcs - are of course different and the sections will consequently be tuned differently.

The optical functions have been forced to be symmetric with respect to the center of the arc. Their maximum values are less than 25 m, and the maxima occur in the nondispersive region, where there is no momentum spread contribution to the beam size. In the region where the horizontal dispersion function, D_x, is non-zero the maximum value of dispersion is D_x^{max} = 0.6 m and β_x is always less than 7 m. In the vertically dispersive region the maximum dispersion D_y^{max} = 0.2 m and β_y is less than 2 m.

The optical functions along one-half arc are plotted in fig.2.1.7.

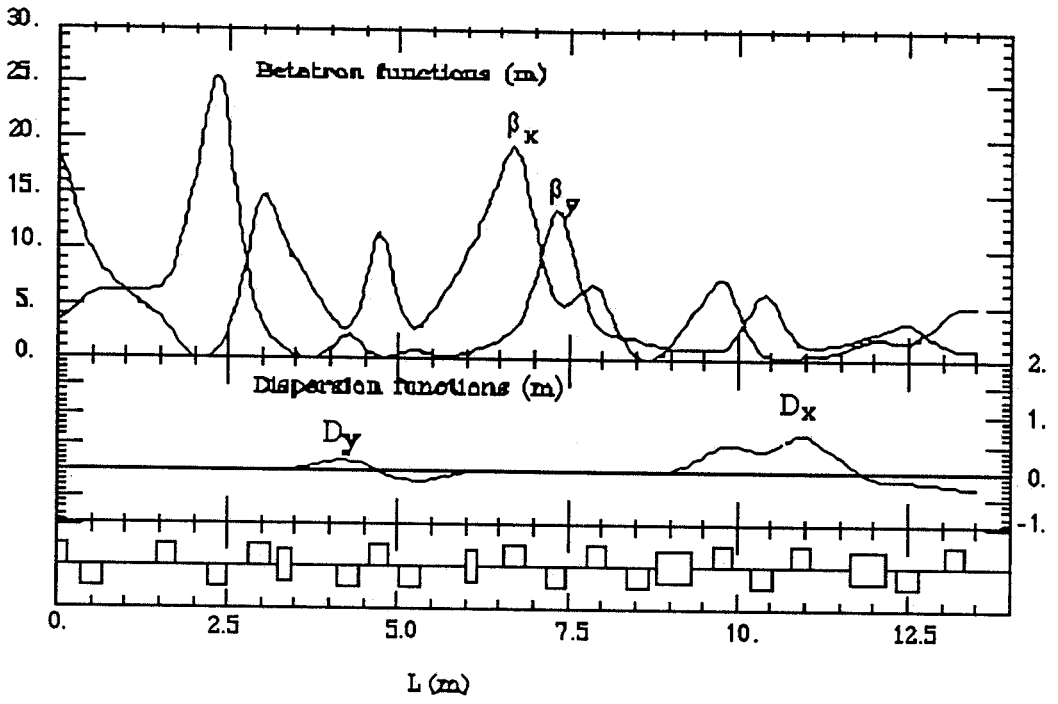

Fig.2.1.7 - Optical functions in half recirculating arc .

The quadrupoles are 0.30 m long. The highest quadrupole strength, K^2_{max}= 13 m^{-2}, is needed in the vertical chicane to satisfy the achromaticity condition; it corresponds to a field gradient G_{max} = 15 T/m.

The arc configuration, as described, applies to all four arcs of the proposed layout (see Figs. 1.5.1 and 1.5.2). The matching sections between the arcs and the vertical chicanes must still be defined, keeping in mind that if the chicanes are not isochronous the horizontal dispersion function inside the arcs must be adjusted for overall isochronism; this can be obtained easily because of the presence of the two symmetric quadrupole triplets between the 45° dipoles. Any other condition on the total transfer matrix can be fulfilled by properly retuning the quadrupoles of the long straight sections between the arcs.

2.2 - BEAM DYNAMICS

2.2.1 - Introduction

The dynamics of an "ensemble" of charges in a linear accelerator is affected by the so called "collective forces". These forces are generated by the electromagnetic fields created by the interaction of the beam with the surrounding walls. They act back on the beam itself perturbing the dynamics of particles guided by the externally applied fields. The physical process is characterized by energy loss of the beam and, depending on the current intensity, by instability phenomena in both the longitudinal and the transverse dimensions.

Collective effects are analyzed in the time domain by means of the "wake-potentials", defined as the integrated field per unit charge experienced by a unit test particle travelling in the fields induced by the bunches accelerated in the linac, in both the longitudinal and the transverse dimension.

Single bunch dynamics is dominated by the intensity - over the length of the bunch - of the short range wakefield mainly originated by the interaction of the bunch current with sharp discontinuities in the vacuum envelope.

The dynamics of many bunches in a linear accelerator is instead affected by long-range wakefields mainly due to persistent (high-Q) parasitic resonant modes excited by the bunch current in the r.f. cavities or in other cavity-like objects.

2.2.2 - Induced Wake-fields

The longitudinal wake-potential is defined as the energy lost by a unit charge that travels in the e.m. field created by a point charge Q a distance τ away, in front:

$$w_z(\tau) = -\frac{1}{Q}\int_d E_z\left(z, t = \frac{z}{c} - \tau\right) dz \qquad \text{[Volt / Coulomb]}$$

The above integral is relative to a point charge and defines the impulsive (Green function) wake-potential. The effective wake potential seen by a charge within a bunch depends on the bunch charge distribution $\rho(\tau)$ and can be calculated by means of the folding integral:

$$W_z(\tau) = \int_{-\infty}^{\tau} w_z(\tau - \tau')\, r(\tau')\, d\tau' \qquad \text{[Volt / Coulomb]}$$

If the trailing charge is also subject to transverse forces, a transverse wake potential is introduced and defined as the transverse momentum kick per unit charge experienced by the test particle :

$$\mathbf{M}(\tau) = Q\int_{d} \left[\mathbf{E}(z,t) + \mathbf{v}\times\mathbf{B}(z,t)\right]_{\perp} dz \;; \quad \text{with } t = \frac{z}{c} - \tau$$

$$w_{\perp}(\tau) = \frac{M(\tau)}{Q\, r_o}$$

By analogy with the longitudinal case we compute the effect on a real bunch, with a given space distribution, by applying the folding integral:

$$W_{\perp}(\tau) = \frac{M(\tau)}{q_1 q_2 r_o} = \int_{-\infty}^{\tau} w_{\perp}(\tau - \tau')\, \rho(\tau')\, d\tau'$$

The first step in the analysis of collective phenomena is to estimate the integrated longitudinal and transverse wakes. This can be done - more or less rigorously - by different methods.

For closed structures, both the longitudinal and the transverse impulsive wakes can be calculated as sums over the normal modes of the structure. This method is however in practice limited by the fact that r.f. cavities are not perfectly closed structures so that, above the iris cut-off frequency, some analytical correction is needed.

We estimated the impulsive wake potentials by applying general frequency-scaling laws to the SLAC and CEBAF wake-potentials. The approximated result has then been used to derive the bunch wakes and compare them with those calculated directly in the time domain by means of the TBCI computer code.

The code - severely limited by CPU time required for the huge number of mesh points - computes the wakefield induced by a gaussian bunch integrated over the bunch distribution that approaches the wake Green function for very short bunches . The scaled impulsive wakes are shown in Fig.2.2.1. The bunch wakes are compared to the TBCI results in Fig.2.2.2.

2.2.3 - Single bunch dynamics

a) Longitudinal wake field

The short range longitudinal forces cause particles to lose an amount of energy that depends on their position in the bunch; the bunch therefore experiences an average energy loss and has an energy spread correlated to position along the bunch itself.

Using the longitudinal bunch wake-potential we can calculate the overall energy loss ΔU and the structure loss factor $k(\sigma_l)$ (energy lost per unit charge square) as:

$$\Delta U = Q^2 \int_{-\infty}^{\infty} W_z(\tau)\, \rho(\tau)\, d\tau$$

$$k(\sigma_l) = \frac{\Delta U}{Q^2}$$

The rms energy spread induced by wakefields in a monoenergetic bunch is calculated to be:

$$\sigma_E^2 = \int_{-\infty}^{\infty} [E - \langle E \rangle]^2 f(E)\, dE = \int_{-\infty}^{\infty} \left[W_z(\tau)\right]^2 \rho(\tau) \frac{d\tau}{Q} = \frac{\Delta U}{Q}$$

The resulting energy loss and energy spread for the case of the ARES Linac are given in Table 2.2.1, where the design values are also reported for comparison.

It must be remembered that, if required, the energy spread, because it is correlated to position, can be partly compensated by accelerating the beam off-crest, so as to make use of the slope of the external rf voltage.

Proper control of the energy spread to position correlation can also be used to produce NBS damping of the transverse motion.

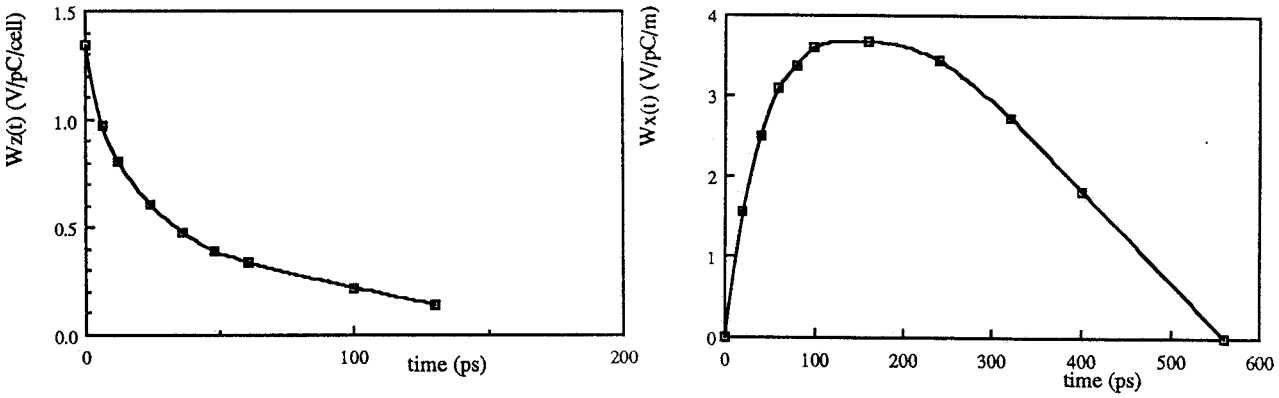

Fig.2.2.1 - Scaled impulsive wakes.

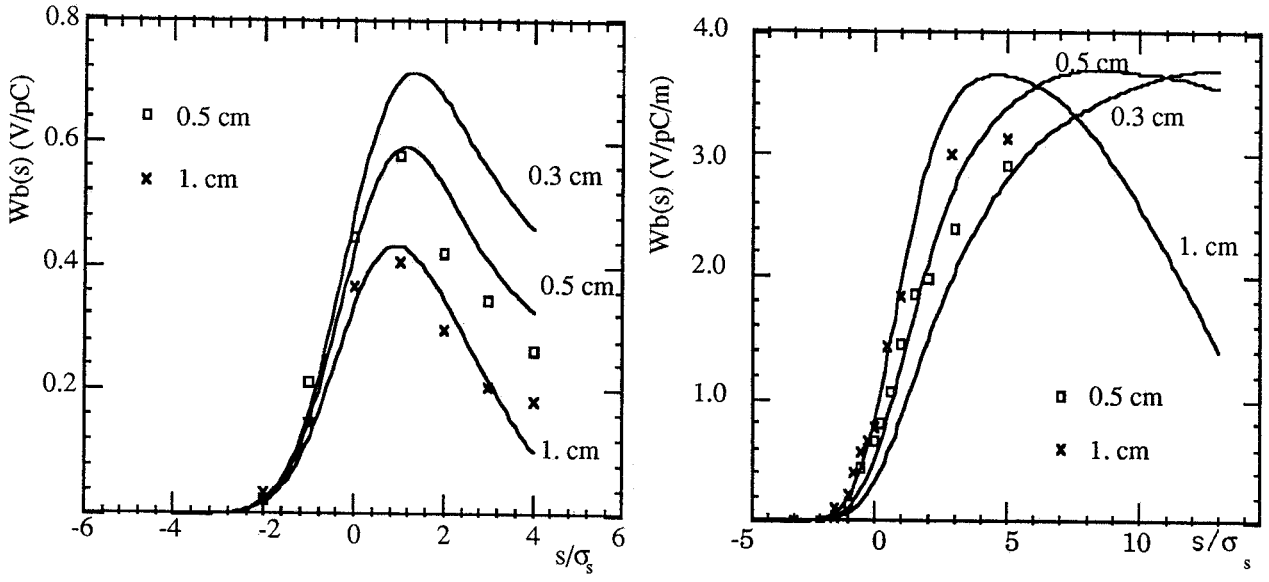

Fig.2.2.2 - The bunch wakes compared to the TBCI results.

b) Transverse wake field

In the smooth focusing approximation the equation of motion for a test particle at longitudinal position z within the bunch and at position s along the linac is:

$$\frac{d}{ds}\left[\gamma(s,z)\frac{d}{ds}x(s,z)\right] + k^2(s,z)\,\gamma(s,z)\,x(s,z) = \frac{e}{mc^2}\int_z^{\infty} dz'\,\rho(z')\,w_{\perp}(z'-z)\;x(s,z')$$

Assuming a linear dipole wake $w_{\perp}(z) = w_{\perp}' \cdot z$, this equation has been solved - by a perturbation method - for a rectangular charge distribution of length l. The result is :

$$x(s,z) = x_o\sqrt{\frac{E_o}{E(s)}}\;e^{iks}\sum_{n=0}^{\infty}\frac{1}{n!\,(2n)!}\left(\frac{\eta}{2i}\right)^n$$

where

$$\eta = \left(\frac{1}{2} - \frac{z}{l}\right)^2 \frac{e\,Q\,w_{\perp}'\,l}{K\,g}\ln\left(1 + \frac{g\,s}{E_o}\right) = a\,Q\,l\left(\frac{1}{2} - \frac{z}{l}\right)^2$$

being: g the energy gradient, K the integrated focalization and the front of the bunch at $z = l/2$

The term n=1 in the sum corresponds to the two-particle model; the model is applicable whenever the parameter η is less than ~ 48, which is the case for all three SC linac sections.

If one imagines the bunch divided into thin slices, the amplitude of the n=1 term gives the maximum displacement of the center of the slice found at a distance z from the bunch head, namely.

$$\frac{\Delta x\,(z)}{x_o} = \frac{1}{4}\sqrt{\frac{E_o}{E_f}}\, a\, Q\, l \left(\frac{1}{2} - \frac{z}{l}\right)^2$$

It is clear that the model predicts a dilution in the (x,x') phase space. The new rms value of the particle x distribution is:

$$\sigma_x = \sqrt{\sigma_{xo}^2 + \sigma_{xw}^2}$$

with

$$\left(\frac{\sigma_{xw}}{x_o}\right)^2 = \frac{(a\,Q\,l)^2}{180}\frac{E_o}{E_f}$$

The corresponding emittance degradation is given by:

$$\frac{\Delta\varepsilon}{\varepsilon} = \sqrt{1 + \left(\frac{\sigma_{xw}}{\sigma_{xo}}\right)^2} - 1 \approx \frac{1}{2}\left(\frac{\sigma_{xw}}{\sigma_{xo}}\right)^2$$

For the worst-case parameters discussed in Paragraph 2.3.2.1 - Q = 15 nC and l = 1cm - the computed emittance degradation is always less than 1% and is therefore negligible. The advantage of the low -frequency structure is here most evident.

Table 2.2.1 - ARES Linac energy loss and energy spread

Bunch Length, σ_l	[mm]	3	5	10
Energy loss per cell	[keV]	.44	.38 .41*	.29 .29*
Linac total energy loss	[keV]	85.	73. 79.*	56. 56.*
Energy spread per cell	[keV]	.22	.18	.13
Linac total energy spread	[keV]	42.	35.	25.

* TBCI calculations

2.3. - e^- AND e^+ GENERATION

2.3.1 - Introduction

The general requirements for the generation and acceleration of electrons and positrons to be injected in the ARES Φ-Factory rings have been discussed in References (2)÷ (4) .

The general layout of the linac is presented in Fig. 1.4.1. As shown in Fig. 1.4.1, the 48 MeV SC linac section L2, common to e^- and e^+, is fed by two separate preinjectors : the electron preinjector, consisting of the high energy (≥ 4 MeV) gun followed by a 48 MeV SC preaccelerator section, L1, and the positron preinjector consisting of the positron converter and the warm capture section L4.

The main requirements for injection into the Φ-Factory are collected in Table 2.3.1; they will be taken as the basis for our considerations.

Requirements concerning the application to FEL's, linear-against-circular collisions and collider-grade beams are mentioned in paragraph 2.3.2.1.

Table 2.3.1 - Φ-Factory Injection requirements

Beam energy	[MeV]	510
Overall injection efficiency		0.125
Positron filling time	[s]	300
Electron filling time	[s]	< 10
Linac pulse duration	[ns]	340
Linac repetition rate	[Hz]	10
Linac bunch repetition rate	[MHz]	71.4
N.er of bunches per Linac pulse		24
Total charge to be stored per ring	[nC]	340

Two layouts are being considered for the electron preinjector :

- a classical one - consisting of a thermionic gun followed by a subharmonic prebuncher and a normal-conducting buncher system with an output energy of 4 MeV - called 'standard preinjector' and

- a more advanced one - consisting of an RF SC gun followed by a bunch compression system - called 'RF Preinjector'.

The standard preinjector is almost identical to that of LISA [5,6], produces a beam of average quality, and can be implemented directly without any need for special R&D; it is described in detail in this paragraph.

The RF preinjector is a highly sophisticated system capable of producing state-of-the-art collider and FEL-grade beams in addition to those needed for injection into the Φ-Factory. Its implementation will require substantial R&D work. It is described here only briefly; a separate, detailed description is given in Paragraph 2.3.2.1.

A final decision on which system to implement for the injection into the Φ-Factory will have to be taken in due time during the development of the Project.

To evaluate the performance required of the preinjector in the injection mode has been evaluated - for positrons - as described in the following. The injection of electrons is much faster and need not be treated in detail.

The total positron charge to be stored in the Φ-Factory e^+ ring is:

$$\boxed{Q_t = q_b\, h \approx 340 \text{ nC}}$$

where q_b is the bunch charge and h the ring RF harmonic number (24); the average linac current required to fill the positron ring in a time T_{fp} is therefore :

$$I_{av} = q_1 f_r = Q_t / (\eta_i T_{fp})$$

where q_1 is the linac pulse charge, f_r the linac repetition rate and η_i the overall injection efficiency. We have assumed $\eta_i = 0.125$ and $T_{fp} = 300$ s, to obtain:

$$\boxed{I_{av} \approx 10 \text{ nA}}$$

Since the ring revolution period , T_0, is:

$$T_0 = h / f_{RF} = (24 / 71.4)\ 10^{-6} \text{ s} \approx 340 \text{ ns}$$

for a linac pulse of the same duration and a linac repetition rate $f_r = 10$ Hz, the required linac pulse charge, q_1, and average pulse current , I_{pl}, are :

$$q_1 \approx 1 \text{ nC} \qquad I_{pl} = q_1 / \tau_1 \approx 3 \text{ mA}.$$

To generate such a positron pulse current, we need from the electron gun cathode a pulse current, I_g, given by :

$$I_g = I_{pl} / (\eta_c \eta_-)$$

where η_c is the electron to positron conversion efficiency and η_- is the gun-to-converter transport efficiency.

The value of η_c depends on the accepted momentum bite. The requirement of a momentum standard deviation of $\pm$ 5 10^{-3} at E = 510 MeV for positron injection into the storage ring corresponds to

$$\eta_c \approx .015 \text{ GeV}^{-1}.$$

For a conversion energy of $\approx$ 300 MeV it follows that

$$\boxed{I_g \approx 2 \text{ A}}$$

Using the same parameters for the injection of electrons, an electron ring filling time,

$$T_{fe} = T_{fp} \eta_c$$

of only $\approx$ 1.5 seconds is obtained.

2.3.2. - The electron preinjector

2.3.2.1 - RF preinjector

As mentioned in the introduction, one of the most important design problems to solve for the design of TeV electron-positron colliders is the generation of intense, bright beams[6-11].

High current (some hundreds of Ampères) and low normalized emittance (some mm mrad) electron beams, accelerated to .5 ÷ 1 GeV, are also required for short wavelength (in the range from VUV to soft X rays) high gain, high power, single-pass FEL's [11-13].

The accelerated beam brightness can not be higher than that generated at the gun and transmitted through the main accelerator injection system; the performance of the Linac injector is therefore a primary concern.

As extensively reported in a dedicated paper [14], it is foreseen to develop, for ARES, a state-of-the-art injector that can also produce the more conventional beams needed for injection into the Φ-Factory rings.

Preliminary results on the expected performance are reviewed in the following, together with the rationale of the choices that have been made. We remark here that the proposed SC laser-driven RF gun operating at 500 MHz (the ARES SC Linac frequency) and featuring a 30 MV/m electric field value at the photocathode, looks very promising; in particular, the low operating frequency guarantees that harmful RF and wake-field induced effects are much less severe than in other similar projects [7,8,15].

The use of superconducting cavities is mandatory for CW or high repetition rate operation with high electric field on the cathode surface. The clean environment, typical of a SC cavity, is also instrumental in lengthening the cathode lifetime [16].

A schematic drawing of the SC injector is presented in Fig.2.3.1. It consists of two, separately powered and phased SC cavities, the first one being equipped with a laser driven photocathode. The peak current delivered by the SC RF gun within a normalized emittance - at the injector output - of a few mm•mrad is of the order of a few tens of Ampères; a magnetic compressor is therefore needed to raise it to the level of some hundreds of Ampères. The second cavity, independently phased and powered, is needed to linearize the longitudinal phase space so that the magnetic compression can be fully exploited.

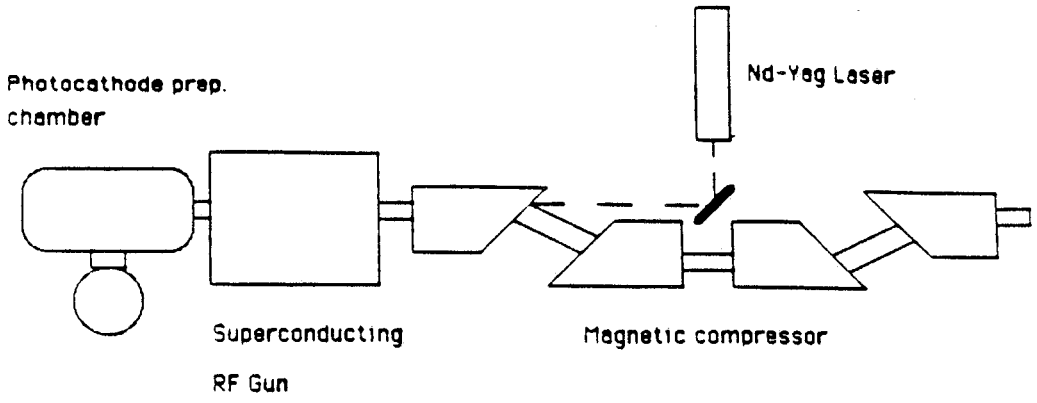

Fig. 2.3.1 - Schematic drawing of the superconducting RF preinjector. Magnetic compressor and photocathode preparation chamber are also sketched.

a) Basic Theory

The geometry of the gun cavities and the cathode and laser pulse characteristics are dictated by the need to preserve beam quality throughout the injection system.

The main phenomena tending to raise the electron bunch transverse temperature and therefore to blow-up the normalized transverse emittance, ε_n, are:

- RF linear effects
- RF non linear effects
- Wake field effects

A detailed discussion of these effects is given in Reference (14).

Here we just recall, for a better understanding of the main design problems, the results of a first order estimate [14,17] of the transverse normalized emittance deterioration suffered by a bunch emitted and accelerated in the RF gun, based on the following approximations :

- the electric RF field on the axis is a pure sinusoid;
- off axis RF fields are derived through a linear expansion;
- wake field effects are neglected; the bunch charge density distribution can be either gaussian or uniform.
- the emitted bunch is mono-energetic and beam envelope variations through the gun are neglected (only transverse and longitudinal momentum transfers are considered).

We also note that our definition of the normalized emittance is the following [18,19]:

$$\varepsilon_n = \sqrt{\langle x^2 \rangle \langle p_x^2 \rangle - \langle x\, p_x \rangle^2}$$

The results of the above approximations can be summarized in the following formula:

$$\Delta\varepsilon_{TOT}^2 = \Delta\varepsilon_{RF}^2 + \Delta\varepsilon_{SC}^2 + 2\, J_x\, \Delta\varepsilon_{RF}\, \Delta\varepsilon_{SC}$$

where $\Delta\varepsilon_{SC}$ is the emittance increase due to the space charge forces and $\Delta\varepsilon_{RF}$ is that due to RF linear effects, both computed at the injection phase ϕ_0 that minimizes the emittance blow-up. J_X is the transverse correlation factor[14]. $\Delta\varepsilon_{SC}$, $\Delta\varepsilon_{RF}$ and ϕ_0 are defined by the following equations:

$$\Delta\varepsilon_{SC}\,[\text{m rad}] = \frac{5.7 \cdot 10^{-6} \cdot Q_b[\text{nC}]}{\sin\phi_0 \cdot E_0[\text{MV/m}] \cdot (3\sigma_r[\text{m}] + 5\sigma_z[\text{m}])} \qquad E = E_0 \sin(\omega_{RF} t + \phi_0)$$

$$\Delta\varepsilon_{RF}\,[\text{m rad}] = .69 \cdot E_0[\text{MV/m}] \cdot \sigma_r^2 \cdot (k_{RF} \cdot \sigma_z)^2$$

$$(\frac{\pi}{2} - \phi_0)\sin\phi_0 = 5.1 \cdot 10^{11} \cdot \frac{E_0[\text{MV/m}]}{k_{RF}}$$

The normalized transverse emittance at the gun exit, ε_{no}, is given, in terms of the emittance at the cathode, ε_{nc}, and of the total emittance increase, by:

$$\boxed{\varepsilon_{no} = \sqrt{\varepsilon_{nc}^2 + \Delta\varepsilon_{TOT}^2}}$$

Under the approximation that all photo-electrons emerge from the cathode with the same energy (i.e. neglecting the straggling inside the cathode), assuming that this energy is given by the difference between the laser photon energy and the work function of the cathode material and considering a laser pulse with a double gaussian distribution in radius and time (with rms widths σ_r and σ_t), the normalized emittance at the cathode surface, ε_{nc}, is given by :

$$\varepsilon_{nc}[\text{m rad}] = \sqrt{\frac{W}{3m_0c^2}} \cdot \sigma_r[\text{m}]$$

where: $W = h\nu_{laser} - W_I$ [eV] and W_I is the e^- work function

To minimize ε_{nc} one can decrease the laser spot until the limit on the maximum cathode current density (typically 500 A/cm^2) is reached, giving a minimum laser spot radius of the order of 1 mm for some tens of Ampère of cathode current. All considered, typical values of ε_{nc} range from $\approx$.8 to $\approx$ 2 mm•mrad.

Once the RF frequency and the peak value electric field on the cathode have been fixed, the value of the output emittance is a function only of the bunch charge, σ_r and σ_z.

Figure 2.3.2 shows the iso-emittance lines as functions of the bunch spot radius and length for two different bunch charges, .5 nC and 10 nC. They are computed with the ARES parameters, namely an RF frequency of 500 MHz and a cathode peak field of 30 MV/m.

It can be easily seen that the emittance of short bunches is dominated by the space charge effect while that of long bunches is dominated by RF effects.

In defying the actual bunch shape the behaviour in the longitudinal phase space, not accounted for in the diagram, must also be considered. Too long bunches ($\geq$ few tenths of RF degrees) come out curved in longitudinal phase space and the magnetic compressor can not

operate efficiently. The emittance blow-up during bunch length compression has to be carefully evaluated to find the minimum compression energy at which it is still tolerable.

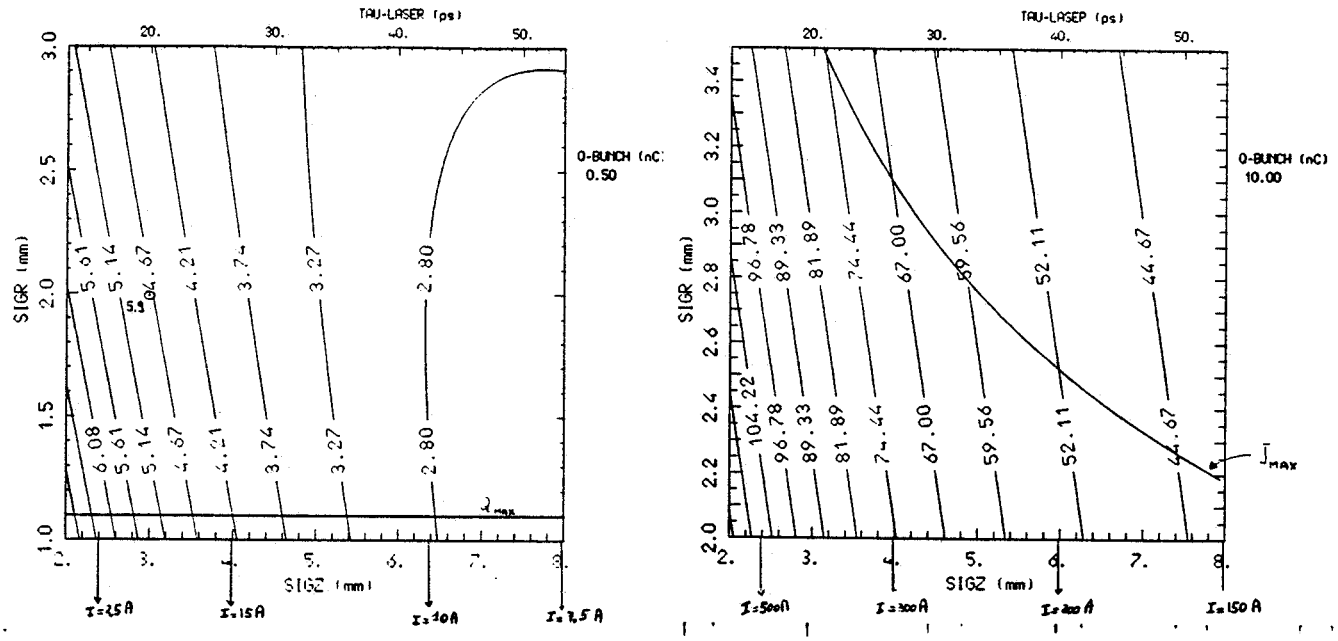

Fig. 2.3.2 - Iso-emittance plot respectively for a 500 pC and a 10 nC bunch emitted and accelerated by a RF-gun: the RF frequency is 500 MHz, the peak field on the cathode 30 MV/m and starting energy of the photo-electrons .2 eV, as typical for a semiconductor photocathode illuminated by a doubled Nd-YAG mode-locked laser. The plot shows the iso-emittance lines as functions of the bunch gaussian length (s_Z) and radial width (s_r) in mm. The upper scale mark the values needed for the laser pulse time-length (FWHM) in ps, while the arrows show the current values expected at the gun exit. The values of the normalized transverse emittance written on the lines are in mm mrad. The dots marked on the Plots show the value of the norm. transv. emittance computed by the PIC code ITACA.

b) Computational tools

The behaviour of the transverse normalized emittance is dominated by the interaction of the bunch with its self-field, and of the self-field with the environment (i.e. the cavity surface) [14]. That naturally claims for a numerical simulation procedure able to self-consistently describe both the self-field propagation inside the cavity and the electron beam dynamics in the presence of the RF field and of the self-field.

Numerical self-consistent procedures of the PIC (Particle In Cell) type have therefore been used to accurately estimate the behaviour of the emittance and of all other related beam dynamics quantities (energy spread, longitudinal emittance, etc.). Various codes, developed in the different laboratories have been available for quite some time, for instance MASK and PARMELA in Los Alamos [7,8] and Brookhaven[15] that take space-charge but not wake-field

effects into account, in a manner that is not self-consistent, TBCI-SF (a self consistent PIC code of the MAFIA family) in Wuppertal[16].

A new PIC code, named ITACA[20,21], recently developed by some of the authors at the Milan University has been used to design the ARES RF gun. ITACA has been extensively checked against other codes, agrees well with other analytical and experimental results, and has novel features and distinctive advantages.

ITACA is an axi-symmetrical code which solves, self-consistently, a sub-system of the Maxwell + Newton Lorentz equations for cylindrical symmetric fields and sources. The bunch current is assumed to have radial and axial components and the self-field is assumed to be a monopole field (TM_{0np}-like). A specially developed charge assignment algorithm minimizes unphysical fluctuations in the driving term, and the equations of motion fourth-order integration algorithm can compute all quantities related to particle dynamics - notably transverse and longitudinal emittances, energy spread, rms divergence, etc - very accurately.

An eigenvector finder, that can compute the TM_{0np} resonating modes of any axi-symmetrical structure, is included in the package to compute the accelerating RF field distribution inside the gun cavity.

The PARMELA-SUPERFISH code system, suitable for studying the bunch dynamics in the presence of the RF and the space-charge fields only, is operational both in Frascati and in Milan. It will be used to study the magnetic compressor.

c) Results of the numerical simulations

The gun SC RF cavity design must not only comply with the requirements by beam dynamics, but also those needed for reliable operation beam dynamics at the maximum accelerating field.

Re-entrant cavities, that are more difficult to clean, were therefore 'a priori' discarded. A number of other constraints follow :

- Because enough space must be left free on the cut-off tubes for the main coupler and the HOM coupler, radius and length of the cut-off tubes must exceed certain minimum values. The proposed values are: 85 mm for the radius and 150 mm for the length.
- Because the cells must be coupled in the π-mode the coupling coefficient (usually a few percent) also has a minimum value determining the iris thickness and aperture.

- Because we are interested in maximum peak field on the cathode, the iris profile must such as to minimize the ratio between the maximum electric field on the iris and the field on the cathode

The trade off between beam dynamics and RF superconductivity requirements is not straightforward. Our first attack to the problem has been to check the beam dynamics performance of a well tested cavity geometry. One and a half cells terminated by a cut-off tube are needed: the photocathode is placed in the center of the flat end wall of the first first half cell and the next cell, tuned to the same frequency, provides two further free parameters. The main coupler and the HOM coupler are attached to the cut-off tube.

The selected geometry is that of the ARES 500 MHz cavity, with only one and half cells. The peak field on the cathode is 30 MV/m, corresponding to an average accelerating field of about 13 MV/m, approximately 30% higher than the ARES cavity nominal field. The value should not prove excessive considering that one deals with a single dedicated structure with only one and a half cells.

The $TM_{010-\pi}$ accelerating mode is computed using the RELCAV part of the ITACA package. The energy stored in the cavity is about 86 J, with an R/Q of about 210 Ohm.

The beam dynamics simulations have been carried out for three different values of the bunch charge (100 pC, .5 nC and 1 nC) each with a different pulse length, typical of the ARES foreseen modes of operation. The results are summarized in Table 2.3.2. Note that the different values of the optimum injection phase, due to the different time lengths of the laser pulse, cause slight variations of the gun output energy.

A complete analysis of the data is given elsewhere[14]; it however worth pointing out once more that , because the head of the bunch enters the second cell too early, when the RF field sign has not yet reversed, and gets a slight deceleration, the longitudinal phase space at the cavity output is slightly curved, especially towards the bunch head (see Fig. 2.3.3). The effect is more pronounced for longer bunches and limits strongly the performance of the magnetic compressor.

The latter, usually consisting of four dipoles, rotates the bunch in longitudinal phase space so as to decrease the bunch-length. The rotation, based on path length differences for particles of different momenta, exploits the strong correlation between energy and phase, clearly visible in Fig. 2.3.3. The path length difference versus momentum is represented in TRANSPORT notation by the R56 matrix element.

Table 2.3.2 - SC Gun Parameters

Bunch charge	[nC]	.1	.5	1.
RF injection phase	[Deg]	56	60	48
Laser spot (s_r)	[mm]	2	2	2
Laser length ($2s_t$)	[psec]	40	20	47
Output energy	[MeV]	6.8	7.3	6.7
Energy spread (rms)	[KeV]	± 68	± 28	± 30
Bunch radius (rms)	[mm]	6.3	6.3	5.3
Bunch length (rms)	[mm]	12.1	5.9	14.2
Bunch divergence (rms)	[mrad]	6.0	5.9	6.2
Bunch transv. norm. emitt.	[m rad]	$1.4 \cdot 10^{-6}$	$5 \cdot 10^{-6}$	$4.2 \cdot 10^{-6}$
Bunch long. norm. emitt.	[m rad]	$\approx 10^{-5}$	$2.6 \cdot 10^{-5}$	$2.7 \cdot 10^{-5}$
Peak curr. (no compression)	[A]	4.8	20.2	16.3
Peak current (with comp.)	[A]	5.2	> 200	25

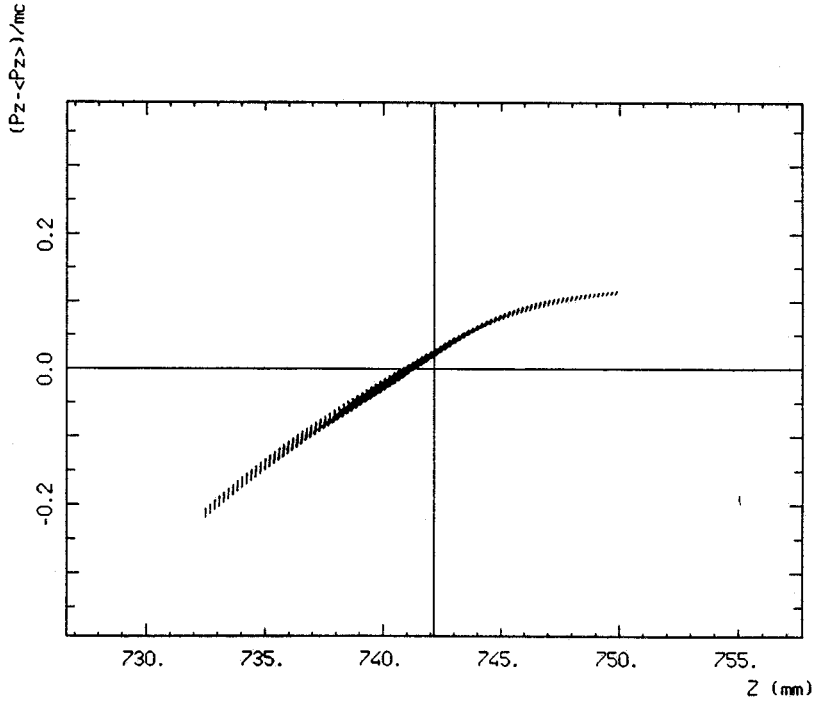

Fig. 2.3.3 - Longitudinal (z[mm], Δp_Z) phase space at the exit of the gun for the case of the .5 nC bunch. The momentum deviation is in unit of m_0c. The peak current in the bunch is 20 A.

The case corresponding to R56 = -.73 cm/percent and .5 nC, one obtains at the compressor output the longitudinal phase ellipse shown in Fig. 2.3.4. The output current is about 200 A, with a rms bunch length of .8 mm. As evident from the figure, the more the correlation in phase space is linear the higher is the output current.

The behaviour of the bunch energy and energy spread are presented in Fig. 2.3.5 for the case of the .5 nC bunch. The other two cases (100 pC and 1 nC) are quite similar. The rms divergence and radius at the exit of the gun are fully compatible with the expected acceptance of the magnetic compressor.

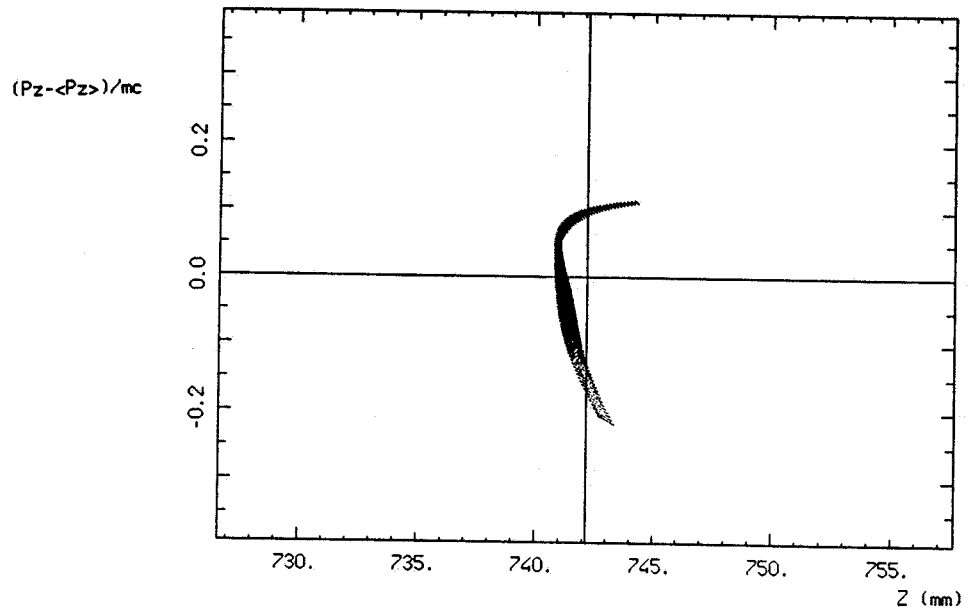

Fig. 2.3.4 - Longitudinal (z[mm], Dp_Z) phase space after the magnetic compressor for the case of the .5 nC bunch. The magnetic compression is achieved applying in the transport matrix, representing the magnetic compressor, R56 = -.73 cm/percent. The peak current is 200 A.

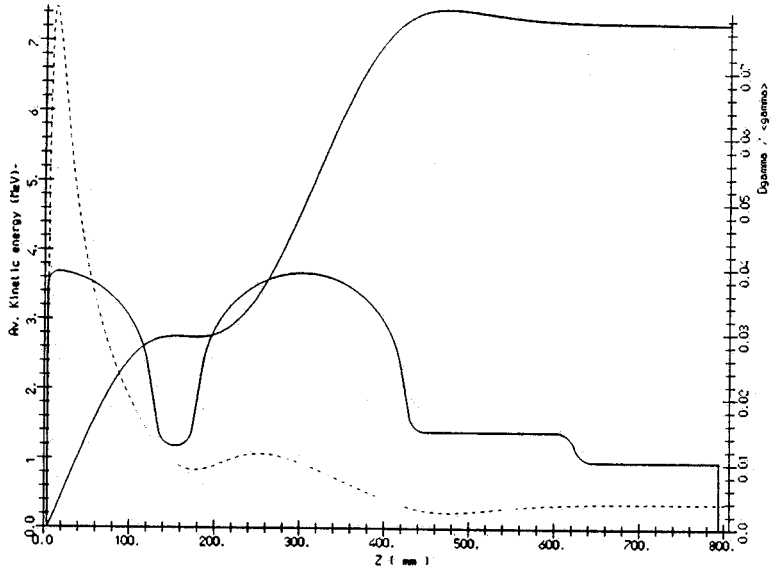

Fig. 2.3.5 - Bunch energy (left scale, solid line) and relative rms energy spread (right scale, dashed line) behaviours during the acceleration of a .5 nC bunch in a SC RF gun with a modified geometry. The final energy is 5. MeV and the final energy spread (rms) is ± 40 keV (.8 % of the final energy). On the diagram, the boundary profile of the gun cavity is also plotted.

For a fixed gun cavity geometry, higher injection phases give better longitudinal phase space distributions: since higher injection phases also reduce the transverse emittance blow up by space-charge forces, one is interested to push up the injection phase as much as possible. One solution that has been considered as a possible alternative is the addition of a third harmonic cell to flat-top the RF field. A preliminary study shows that the price paid is a severe degradation of the transverse phase space because of the effect of the smaller iris of the 1500 MHz cell.

A more promising idea, is to add a single, fully decoupled first-harmonic cell, as shown in Fig. 2.3.6. The extra free parameter - the injection phase into the extra cell - can be used to decouple the actions on longitudinal phase space from those on transverse phase space, to further optimize both [14]. Work on the decoupled cell geometry is in progress.

The data given in Table 2.3.3 are a sample of what can be obtained - after only a preliminary optimization and for two typical bunch charges - including the first harmonic de-coupled cell. They are sufficient for significant experiments to be performed on both collider-grade beams and X-UV FEL's. The normalized transverse emittance could be in principle lowered by increasing the peak field on the cathode.

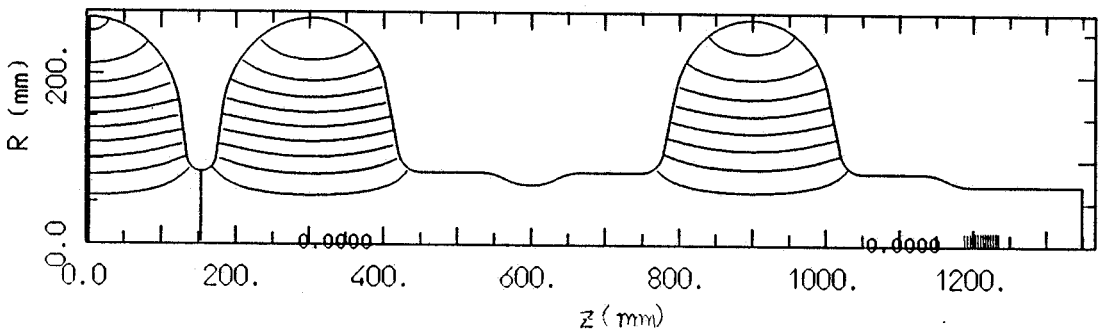

Fig. 2.3.6 - Boundary profile of the SC RF-gun attached to a single full-decoupled cell. See text for details.

Table 2.3.3 - RF Preinjector Expected Performances

Bunch charge	[nC]	.5	10
Output energy	[MeV]	10	10
Energy spread $\Delta\gamma/\gamma$	[%]	$\pm$ .5	$\pm$ 3
Bunch transv. norm. emittance	[m rad]	$< 5 \cdot 10^{-6}$	$< 4 \cdot 10^{-5}$
Peak current; no compression	[A]	20	200
Peak current; with compression	[A]	400	1000

d) Photocathodes

Laser-driven photoemissive electron sources has the capability of emitting the high density, properly shaped, electron bunches required by the RF gun operation, to achieve the minimal emittance grow.

The specifications for the electron bunch from the cathode are listed in Table 2.3.4

A high quality electron emitter is needed in order to meet them. Standard thermionic dispenser cathodes have too low a current density and produce continuous beams (at least at the ps level) that have then to be at low energy, where space charge effects dominate and blow the emittance up. Moreover the transverse component of the thermal motion of the emitted electrons gives a lower limit to the beam emittance that can not be overcome [7] .

The adoption of a photocathode is therefore mandatory.

Table 2.3.4 - Electron bunch specifications

Bunch charge	[nC]	.5 ÷ 20
Pulse duration ($2\sigma_t$)	[ps]	10 ÷ 40
Spot radius (σ_r)	[mm]	1.5 ÷ 3.5
Current density	[A/cm2]	150 ÷ 700

The characteristics of the electron beams produced with various photocathodes in different laboratories, together with the photocathode material work function and quantum efficiency[9] are presented in Table 2.3.5.

We recall that the dependence of the current, I, delivered by a photocathode on the incident laser power, P, is given by :

$$I\,[A] = P\,[W] \cdot \eta / h\nu\,[eV]$$

where $h\nu$ is the photon energy and η the photocathode quantum efficiency[3]. As discussed above, the photon energy must be slightly higher than the work function of the photocathode material.

Photocathodes can be broadly classified into two categories: semiconductor photoemitters and metal photoemitters :

- Alkali semiconductor photoemitters (Cs_3Sb, Na_2KCsSb, etc.) are characterized by their high quantum efficiency and low work function. Current densities up to 600 A/cm^2 have been observed from a Cs_3Sb photocathode, with laser pulse lenghts of 60 ps [22]. Their drawback is extreme sensitivity to vacuum conditions [23].

- Metal photoemitters like Yttrium[24] and LaB_6[25] have relatively high quantum efficiency but still 2÷3 order of magnitude lower than semiconductor ones. They have some interesting properties : very long lifetime also in a relatively poor vacuum (P ≈ 10^{-6} mbar), very fast risetime (≈ ps) and easier preparation compared to alkali photoemitters.

Our specifications are best met by using cesiated semiconductor photoemitters - particularly Cs_3Sb - and we expect it can be placed inside the SC RF gun cavity [26].

The development of the preparation technology of cesiated photoemitters is in progress [16]. Particularly the photocathode preparation chamber developed at the Wuppertal University is shown in Fig. 2.3.7.

It should be added that other high quantum efficiency alkali photoemitters, like Na_2KSb, could also be used and that the laser system described in the next paragraph provides sufficient photon energy (3.5 eV) and enough pulse power (≈.2 mJ) to also operate metallic photoemitters
A final decision on the type of cathode can therefore be taken later in the project.

Table 2.3.5 - Photocathode Characteristics

Material	Work Function [eV]	Quantum Eff.	Current Dens. [A/cm^2]	Pulse Duration [ps]
Cs_3Sb (K)	1.6÷3	$1÷3 \cdot 10^{-2}$	600	60
GaAs (Cs)	1.6÷2	$4÷10 \cdot 10^{-2}$	180	70
LaB_6	2.6	10^{-4}	200	$1 \cdot 10^4$
Yttrium	3.1	$2 \cdot 10^{-4}$	500	2
Magnesium	3.6	10^{-4}	20	$3 \cdot 10^6$
Copper	4.5	$6 \cdot 10^{-5}$	70	$1 \cdot 10^4$
Gold	4.7	$5 \cdot 10^{-6}$	500	10

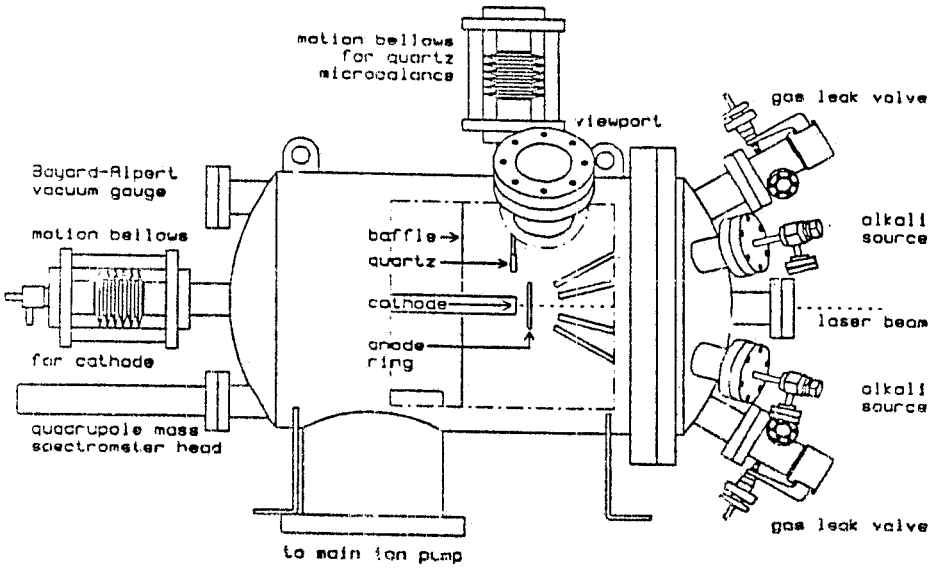

Fig. 2.3.7 - Photocathode preparation chamber developed at the Wuppertal University.

e) Laser system

For injection into the Φ-Factory a train of electron bunches with ~ 70 MHz repetition rate and a macropulse duration of 350 nsec at 10÷100 Hz has to be produced. In principle, the electron bunch charge and brightness must be as large as possible.

FEL operation asks for electron bunches having high peak current and brightness at the maximum possible repetition rate.

The laser system proposed to meet all these requirement is a combination of a short pulse solid state laser and a dye lasers[27,28].

The main oscillator is a mode-locked CW Nd:YLF laser. It generates a continuous train of 35 picosecond long ($2\sigma_t$), low energy pulses at 71.4 MHz repetition rate. The output beam is locked to the 500 MHz RF master oscillator to keep the electron pulses in phase with the accelerating field; it is fed to different amplifier systems, depending on the machine mode of operation.

As shown in Fig. 2.3.8, line A, used for injection into the Φ-Factory, starts with a Pockel cell, that selects the right number of pulses (24). The two following Nd:YAG amplifier stages raise the pulse energy to the value required for extracting the desired electron bunch charge. A second and a third harmonic generator crystals then lower the infrared wavelength to visible and finally to near ultraviolet. The visible and the near ultraviolet pulses will be used alternatively, depending on the electron photoemission threshold of the photocathode.

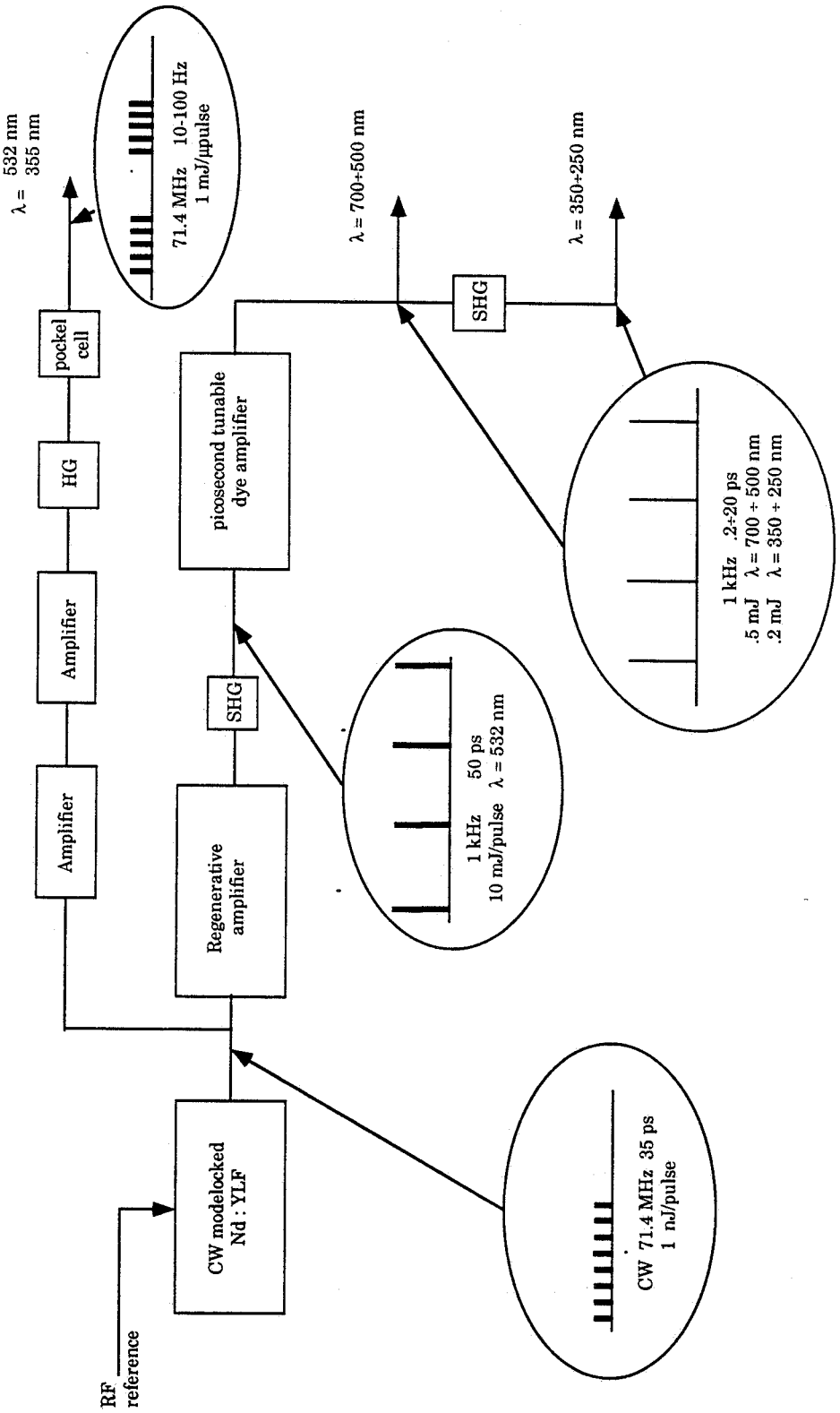

Fig. 2.3.8 - Laser System main performances.

Line B, proposed for FEL operation, contains a regenerative amplifier consisting of two Pockel cells and a large amplifier stage enclosed in an optical resonator. A single pulse is amplified in a multipass mode and delivered at 1 KHz repetition rate. After amplification, it is passed through a doubling crystal and then splitted in two :

- the first half is used to pump an ultrafast dye laser formed by two dye jets enclosed in an optical resonator, one being the active medium and the other the saturable absorber for pulse compression.
- the second half is used to synchronously pump three dye amplifier stages, through which the pulses coming from the ultrafast oscillator pass to be amplified.

The main characteristics of the system as presented are summarized in Table 2.3.6.

All laser components described and shown in Fig.2.3.8 are commercial and state-of-the-art. It should also be remarked that the field is in rapid evolution and that better performances, in particular higher repetition rates, are to be expected in the near future .

Table 2.3.6 - Laser System Characteristics

Tunability on a large wave length spectrum	700 ÷ 250 nm
Variable micropulse length	0.2 ÷ 20 ps
Continuous high energy pulse rep. rate	1 kHz
High pulse energy	0.2 ÷ 0.5 mJ

f) Diagnostics

A short list of the diagnostic tools that are an integral part of the RF Gun system is given below .

- A wall-current monitor, at the output of the last SC cavity, measures the beam current.
- The beam transverse emittance is measured by the pepper-pot method or using transition radiation.
- A streak-camera looking at the Cerenkov radiation from a quartz plate gives the bunch time profile.
- A magnetic spectrometer analyzes the beam momentum spread; an intercepting fluorescent screen, located at the position where the dispersion is largest, is looked-at by a TV camera.
- A Faraday-cup is used to measure the bunch charge.

2.3.2.2 Standard electron preinjector

a) The Gun

The maximum electron peak current to be produced by the gun, is that needed for the production of positrons. For electron operation the required currents are much lower and the same system can therefore be used. The parameter specifications are listed in Table 2.3.1.

It is seen that the gun has to deliver a pulse current, I_g :

$$I_g = 2 \text{ A.}$$

The value is well within the current capability of a LISA-type gun (6), with larger cathode diameter. The main parameters of this gun are listed in Table 2.3.7 for the desired value of current.

The geometry of the gun, the electron trajectories and the equipotential lines are shown in Fig. 2.3.9.

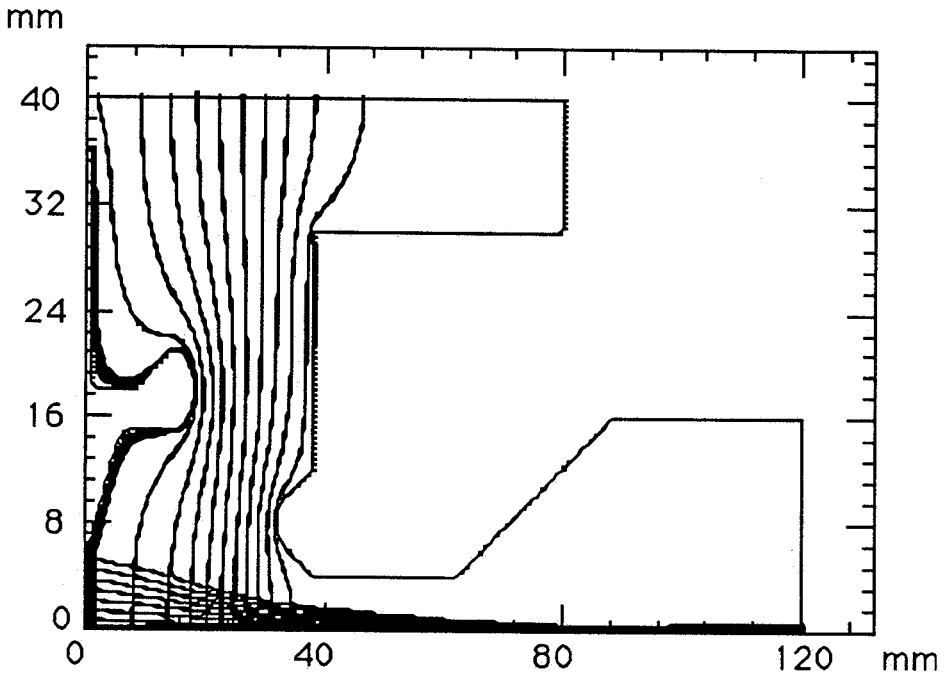

Fig. 2.3.9 - The standard preinjector thermionic gun: Va = 100 kV, Vg = 445 V, I = 2.2 A, Perveance = 0.067 μ-perv., Norm. Emittance = 5.3 [mm mrad].

Table 2.3.7 - Main parameters of a LISA-type gun

Spherical radius of the cathode, R_k	[mm]	40
Cathode diameter (height), D_k	[mm]	11.2
Anode potential, U_a	[kV]	100
Current (@ grid pot.= 450 V), I_g	[A]	2.2
Invariant Emittance , ε_n	[m rad]	$5.3 \cdot 10^{-6}$
Macrobunch length, τ	[ns]	350

b) The buncher system

Also the standard bunching system is similar to that of LISA. Its main components are :

- sub-harmonic (SH) buncher cavity at the storage ring bunch frequency of 71.4 MHz,
- harmonic (H) prebuncher @ 3 GHz,
- high energy (4 MeV) SW capture section @ 3 GHz,
- Linac section L1.
- magnetic focusing lenses and solenoids.

The main task of the system is to transform the ≈ 340 ns long pulse of electrons leaving the gun into a train of short bunches that can be accepted by both the 3000 MHz and the 500 MHz accelerating structures.

Since the proposed bunch frequency for the Φ-Factory storage rings is

$$f_B = 500 / 7 \text{ MHz} = 71.43 \text{ MHz}$$

we have chosen this as the frequency of the first subharmonic prebuncher which will also serve as a kind of chopper.

In fact preliminary calculations have shown that such a prebuncher followed by a 3000 MHz, 4 MeV, buncher will accelerate at least 30% of the gun current with a relative energy spread of approximately ± 5% and a phase spread smaller than 60° at 3 GHz.

The SH-prebuncher consists of a TM_{010}-like resonator that produces a longitudinal RF electric field at a frequency of 71.4 MHz. The RF voltage required to produce the desired amount of bunching is estimated to be 20 kV peak. The cavity is an aluminium quarter-wave coaxial resonator.

With R/Q ≈ 200 Ω and $Q_0 \approx 5000$, the power on the cavity walls at the required RF voltage is ≈500 W. Practically no net power is taken up by the beam.

The RF source is a solid state amplifier driven by a low level signal, prescaled from the 500 MHz main reference source of the superconducting linac. The usual amplitude and phase controls of the cavity drive are foreseen, in addition to the cavity tuning system needed to keep the resonant frequency constant independent of temperature.

The 3 GHz harmonic H-prebuncher system provides additional bunching before acceleration in the capture section. A reentrant copper pill-box cavity operating in the fundamental TM_{010} mode is used. At 3 GHz the cavity main parameters are the following:

$$Z_{eff} \approx 1.5\ M\Omega \qquad Q_o \approx 10{,}000.$$

For a gap RF voltage of 10÷15 kV peak, the power dissipated in the cavity is less then 200 W, a value easily obtainable either by derivation from the capture section feed line or from a dedicated solid state amplifier. The control system is the same as that for the SH buncher except for the cavity tuning system that will probably not be necessary because of the large resonator bandwidth.

c) Capture Section

The Capture Section has a field of ≈ 12 MeV/m, is approximately 50 cm long and accelerates the electron beam to an energy of ≈ 4 MeV; it consists of a graded-β standing wave (SW) biperiodic structure of the same type as that used for LISA.

The average effective shunt impedance, Z_{eff}, is ≈ 70 MW/m.

To produce the desired energy gain the RF power required is given by the sum of the power dissipated in the cavity, P_D

$$P_D = (V_{acc})^2 / (Z_{eff} \cdot l) \approx 0.5\ MW$$

and the beam power, P_B, for an average beam current, $\langle I_b \rangle$, of 600 mA in the 350 ns long macrobunch.

$$P_B = V_{acc} \cdot \langle I_b \rangle = 2.4\ MW$$

The overall RF power over the 1 μs long RF pulse is thus :

$$P \approx 3\ MW.$$

The coupling factor between the RF source and the section is :

$$\beta = 1 + P_B / P_D \approx 6$$

corresponding to the no-beam standing wave ratio (SWR) in the waveguide.

The average power needed is only 30 W due to the very low duty factor. In the S-band frequency range klystrons for this output power are in large supply. The klystron is connected to the capture section through a waveguide and is protected against reflections by a RF isolator.

Standard RF feedbacks loops on amplitude and phase have to be provided to keep the beam parameters in accordance with the design values.

2.3.3 - Positron production

a) Introduction

Electrons from the capture section are fed to the first SC Linac section, L1. Section L1 consists of 4 standard four-cell superconducting cavities, each in its own cryostat, giving a nominal overall voltage of 48 MV. The electrons enter L1 with a nominal energy of 4 MeV and exit from L1 with a nominal energy of 52 MeV. The relative energy spread has decreased to $\pm 5 \times 10^{-3}$ and the phase spread is less than $\pm 5°$ @ 500 MHz.

This allows the beam to be injected unto the main SC linac axis using a pulsed inflector. The beam is further accelerated to 100 MeV in section L2 and then injected into the main section, L3, and the recirculation system.

To generate the positrons, electrons that have reached the nominal energy of 340 MeV after one passage through the main linac are bent back to the e^-e^+ converter.

Because the transport channel from the output of the linac to the converter is isochronous and achromatic, the above phase spread of the electrons will be conserved and the phase of the produced positrons, at the entrance of the 3 GHz positron capture section, will be contained within 60° .

The main components of the positron production line are:

- converter
- magnetic focusing
- high gradient capture and acceleration section

b) Converter and magnetic focusing

The average power of the 300 MeV electron beam striking the converter is :

$$P_C = E\, I_g\, \eta_- \tau\, f_r \approx 0.7 \text{ kW}$$

where $\tau = 340$ ns is the pulse duration, $f_r = 10$ Hz is the repetition frequency, E is the primary electron energy, η- the electron bunching and transport efficiency, and I_g the electron gun pulse current.

For high energy electrons the energy loss is almost entirely due to bremsstrahlung - for heavy elements such as W, Au or Pb this is already true for energies higher than about 20 $m_o c^2$ [29] - and the power dissipated in the converter is only a fraction of P_c. The average energy loss per cm is given by

$$(-dE/dx)_{rad} = N\,E\,F_{rad}$$

where N is the number of atoms per cm^3, E is the energy of the incident electrons and F_{rad} is a bremsstrahlung cross section.

Again, for energies $E >> E_o = 137\ m_o c^2\ Z^{-1/3}$ - where Z is the atomic number of the target material (for gold, $E_o \approx 32\ m_o c^2$) -, F_{rad} is practically independent on the energy of the incident electrons[29]. According to Amman[30], for E > 100 MeV the ratio of the power deposited to the primary beam energy is practically constant and the deposited power,P_d, is approximately 16% of the incident power. For our case:

$$P_d \approx .16\ P_c = 0.11\ kW$$

This is much below the power rating of the ADONE converter (about 3 kW). Considering the good performance of the latter, we therefore propose to adopt a similar solution for ARES.

The energy of the incident electrons is higher for ARES than for ADONE (300 MeV instead of about 100 MeV) and the thickness of the converter target has accordingly been increased from ≈ 1 to ≈ 1.5 radiation lengths.

For good positron production efficiency the diameter of the electron beam spot on the converter should be of the order of 1 mm. This is obtained by means of a special focusing system consisting of a quadrupole triplet. Care must also be taken to ensure that the spot diameter does not decrease below $\approx$ 1 mm, because excessive power density would cause excessive thermal stresses and eventually damage the target.

To optimize the positron capture efficiency, the converter should be closely followed by a high magnetic field ($\approx 5 \div 6$ Tesla) region and then by a short capture section with a very high accelerating electric field and immersed in a solenoidal magnetic field.

The very intense magnetic field next to the converter is generated by a pulsed tapered solenoid with the help of a 'flux concentrator' similar to those employed at SLAC and DESY. The magnetic field value in the flux concentrator must be matched to that of the the capture

section solenoid; the chosen values are shown in Table 2.3.8. A drawing of the converter - flux concentrator - capture section configuration is shown in Fig. 2.3.10.

The high gradient (> 30 MV/m) required for the capture section makes it difficult to use the 500 MHz SC linac operating frequency because there are no klystrons on the market that can deliver the necessary few tens of MW at this frequency . The frequency of 3000 MHz, very close to the European standard (2998 MHz) at which 30 MW klystrons are available, is therefore chosen.

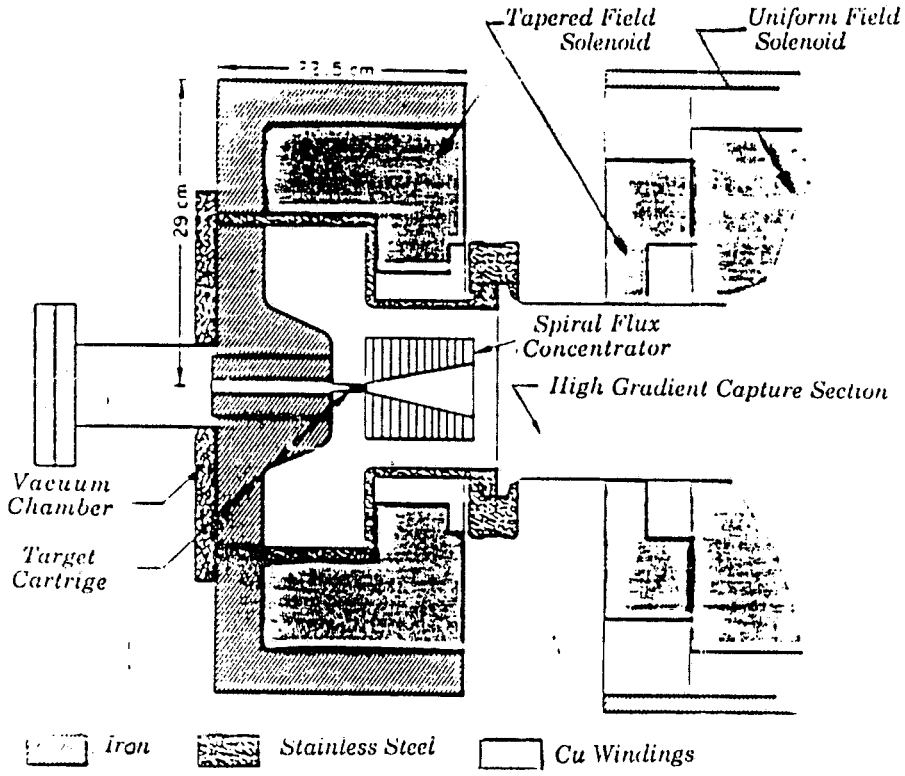

Fig. 2.3.10 - Converter: Flux Concentrator and solenoids for matching to the High Gradient Capture Section

Table 2.3.8 - Concentrator and Solenoid parameters

Flux concentrator field	[T]	5.8
Tapered solenoid field	[T]	1.2
Uniform solenoid field	[T]	0.5

Note that in our case the SLED-type pulse compression technique can not be used because the combination of long pulse duration (400 ns) and low positron peak current (a few mA) would lead to an unacceptable high energy dispersion (>20%) [4].

c) High gradient capture section

The main specifications for the capture section are the following:

- High field gradient : E ≥ 30 MV/m
- Short length : L ≤ 2 m
- No SLED; single Klystron drive : P_{RFmax} = 35 MW
- Maximum cavity input power : P_{RF} ≈ 30 MW.

Different types of accelerating structures can be chosen to fulfil the above requirements : a preliminary discussion on the choice of the accelerating structure is given in [4] where the choice has been restricted to travelling wave (TW) constant gradient (CG) and standing wave (SW) structures. By choosing for the length the value L = 1.5 m and for the power P_{RF} = 30 MW, one obtains for the accelerating field E , and the overall nominal voltage V_{acc} the values shown in the following Table 2.3.9.

Taking into account that the mean positron energy accepted for acceleration will be about 10 MeV, both structure types can accelerate the positrons to an average energy ≥ 50 MeV, comparable to that of the electron beam produced by the electron source at the location where both beams merge. The standing wave structure, capable of higher fields and therefore affording a larger safety factor, is nevertheless preferred.

Table 2.3.8 - Accelerating structure parameters

RF Structure	E [MV/m]	V_{acc} [MV]
CG Travelling wave	27	40
$\pi/2$ biperiodic SW	37	56

The nominal energy at the output of the capture section is taken to be identical to that of the electron beam at the output of L1 and is namely 52 MeV. The section is driven by 1 msec long RF pulses at a repetition rate of 10 Hz.

The effective impedance of the structure being 70 MΩ/m, for an energy gain of 40 MeV and a structure length of 1.5 m the dissipated power is:

$$P_D \approx 15.2 \text{ MW}$$

and the beam power for an average beam current $<I_b>$ of 3 mA is:

$$P_B \approx 0.1 \text{ MW}$$

The overall RF power is thus :

$$P = 15.3 \text{ MW}.$$

High peak power klystrons generators in this power range are nowadays available; for instance the LIL klystron outputs up to 30 MW peak. This would leave enough power available for driving also the electron capture section by means of a 10-12 dB directional coupler.

Computer control of the parameters of the control electronics and of the power feeders is foreseen.

A schematic layout of the RF system for the standard electron preinjector together with the positron preacceleration - 50 MeV - section, is presented in Fig. 2.3.11.

The energy spread at the end of the capture section is of the order of 10% which makes it difficult to transport the beam achromatically along a curved trajectory. This is the reason why the positron source is specified to be on-axis with respect to accelerating Section L2.

d) Remarks on the positron recirculation

The recirculation of the positron beam has to be considered when designing the electron and positron sources because the maximum energy spread which can be tolerated in the positron recirculation arcs is at most 4% [31] and this imposes some constraints on the phase and energy dispersion in the electron and positron accelerating lines.

The main requirement will be on the bunch length of the electrons striking the converter since it defines the phase width (or the duration) of the produced positron micropulses. The problem has been analysed in Reference (3) : according to the results obtained there, the phase spread of the positrons accepted for the acceleration in the S-Band linac must be $\leq \pm 30°$ around

the optimum phase in the 3000 MHz system, corresponding to ±5° of the 500 MHz SC linac frequency.

Such a phase width must be guarantied by the electron injection system.

As mentioned above, the proposed electron preinjector does indeed fulfil this requirement.

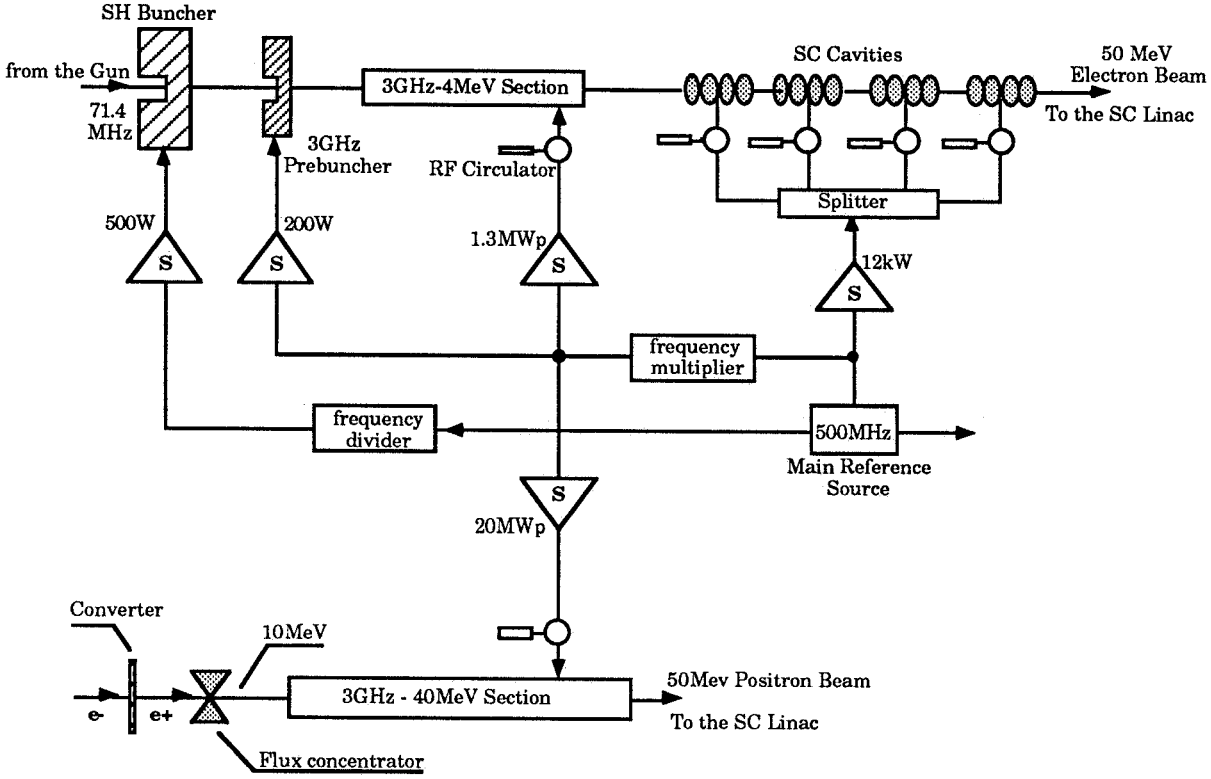

Fig. 2.3.11 - Schematic layout of the RF system for the standard electron preinjector together with the positron preacceleration - 50 MeV - section.

2.3.4. - Transport channels and pulsed inflector

a) Pulsed inflector

The proper functioning of the layout scheme (Fig. 1.4.1) requires the last dipole magnet (inflector) in the 52 Mev electron beam transport channel to be pulsed. The pulse duration must be longer than the beam pulse width (340 ns) and less than the time it takes a particle to go through the main linac and come back, through the converter, to the inflector itself. The pulse repetition frequency is dictated by the injection requirements.

A pulse flat top of 340 ns and a rise and fall times of the order of 50 ns satisfy the above specified requirements. These values do not seem incompatible[10] with the desired repetition frequency of ≈ 10 Hz. Should much higher repetition frequencies be required for other applications, a second dedicated transport line with a fixed field inflector can be provided in parallel.

The kick that the inflector must impart to the beam is given by:

$$B\,l \approx P\,\Theta / 0.3$$

where B is the magnetic field in Tesla, Θ is the deflection angle in radians, l is the magnet length in meters and P is the momentum in GeV/c.

For the required value of the deflection angle, $\Theta = 0.175$ rad , this gives a kick of 0.03 T m; the peak field in the 0.6 m long magnet therefore has to be B= 500 Gauss.

Construction-wise, the magnet will need a delay line structure with ferrite core similar to that developed for the ELETTRA SR source [32]. Since to achieve the desired fast rise time the magnet is subdivided in 15 cm long sections driven in parallel, the yoke can be easily curved to match the electron trajectory.

b) L1-L2 Transport line

The transport line of the 52 MeV beam between L1 and L2 is bent in the vertical plane. It consists of 10 quadrupoles and a chicane consisting of two opposite-bending 10° dipoles, the second being the pulsed inflector. Ten degrees is the maximum bend allowed by the inflector strength.

The input characteristics of the beam are determined by the Linac optics; the transport channel is achromatic and matches to the input of the recirculation loop. Its input and output functions, which are almost identical, are presented in Table 2.3.10.

The transfer line is 12 m long and is mounted below the positron preinjector, parallel to the main linac axis.The additional floor space needed is 18 m.

A schematic layout of the line and the behaviour of the optical functions are shown in Fig.1.3.12.

Table 2.3.10 - Input and output functions

Radial emittance		[m rad]	$5 \cdot 10^{-8}$
Vertical emittance		[m rad]	$5 \cdot 10^{-8}$
Optical functions:	β_x	[m]	13
	β_y	[m]	1

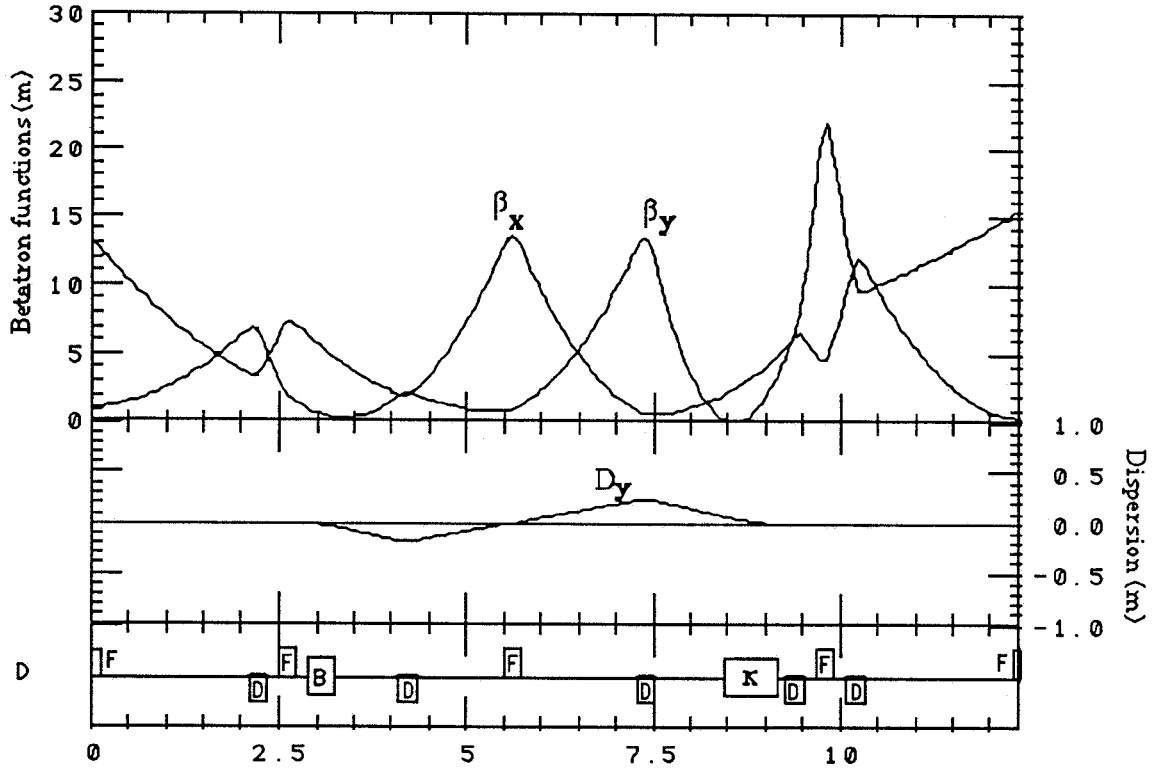

Fig. 2.3.12 - 52 MeV e^- beam transport line, vertical-bend solution: Optical functions .

2.4 - ACCELERATION SYSTEM

2.4.1 - Superconducting cavities

Superconducting cavities performances, compared to those of normal conducting cavities, outweigh the disadvantage of their very low operating temperature. In fact, their quality factor Q_0 being $4 \div 5$ orders of magnitude higher than that of standard copper cavities, they can be operated CW - at low temperature - while the large amount of stored energy makes for a much reduced beam energy spread.

For the construction of high acceleration field cavities for ultrarelativistic particles, the use of bulk Niobium is favoured because of its relatively high critical temperature, $T_c = 9.2$ K, and its good mechanical properties compared to those of other superconducting metals.

At 500 MHz, theoretical upper limits can be derived for the corresponding accelerating field and Q values from the Nb upper critical field ($H_{c2} = 1600$ Gauss) and from its surface resistance, R_S, at 4.2 K calculated from the BCS theory of superconductivity ; one obtains : $E_a \approx 40$ MV/m and $Q_0 \approx 4 \times 10^9$ (33).

With present technology, fields in the range of $E_a \geq 10$ MV/m (at 4.2 K and 500 MHz) and low-field Q values $\approx 3.4 \times 10^9$ are routinely obtained in vertical tests of four-cell cavities. Degradation of Q_0 vs E_a and of the maximum E_a when cavities are horizontal, are topics under investigation. The field emission of Nb surface in SC cavities, a factor limiting the obtainable Q at high surface electric fields, is related to the surface cleaning: it has been ascertained that very clean Nb surfaces can support fields larger than 100 MV/m without electron emission.

To raise Q_0, SC cavities can be operated at lower temperatures; this does not however usually improve E_a in the same way because E_a is limited by the presence of non superconducting defects. These defects also produce the so called "residual" surface resistance, R_{res}. The value of R_{res}, that can not be computed from theory because it depends on the actual surface physical and chemical conditions, of course sets the lowest useful temperature of operation, below which no further benefit on Q_0 is obtained.

The presence of surface defects is considered unavoidable and the main effort over the past 10 years, has been devoted to reducing their size and number and to handle the local heating they generate. In fact better cryostabilization by using high thermal conductivity Nb, is the best techinque known to raise E_a.

The same idea underlies the technique of sputtering thin Nb films on copper cavities [34]. In addition one saves the cost of the ultrapure bulk Nb, which can reach 20÷25 % of the overall cost of a fully equipped horizontal cavity. Finally, one hopes to be able to sputter different superconductive materials with higher critical temperatures and/or lower RF losses.

For ARES, the standard bulk Nb technology has been adopted as a first approach, with some mechanical improvement. developments in the field of copper coated cavities are also in progress [35]. Experimental studies on the superconducting properties of Niobium alloys and compounds (NbN, NbTi, NbZr) realized in form of thin films are also in progress. Some results on NbN films are reported in TAB 2.4.1.

TABLE 2.4.1 - NbN superconducting thin films

	Ar [mbar]	N_2 [mbar]	N_2 flow [sccm]	Deposit. rate [Å/s]	Sputter power [W]	Measured thickness [Å]	T_c [K]
NbN 1	$1\ 10^{-2}$	$2.0\ 10^{-3}$	-	-	609	-	0
NbN 2	$1\ 10^{-2}$	$2.0\ 10^{-3}$	-	-	900	-	4.1
NbN 3	$5\ 10^{-3}$	$3.4\ 10^{-4}$	-	10.5	598	2300	11.66
NbN 4 (*)	$5\ 10^{-3}$	$3.0\ 10^{-4}$	-	10.5	575	3500	14.5
NbN 5	$5\ 10^{-3}$	$3.4\ 10^{-4}$	24	10.5	585	-	0
NbN 6	$5\ 10^{-3}$	$1.2\ 10^{-4}$	10	10.5	432	2500	10.5
NbN 7 (*)	$5\ 10^{-3}$	$1.2\ 10^{-4}$	10	10.5	407	1200	11.25
NbN 8	$5\ 10^{-3}$	$2.0\ 10^{-4}$	15	10.5	484	-	11.33
NbN 9 (*)	$5\ 10^{-3}$	$2.0\ 10^{-4}$	15	10.5	484	900	11.6
NbN10(*)	$5\ 10^{-3}$	$2.6\ 10^{-4}$	20	10.5	545	1200	12.3

*Deposited on sapphire substrate

In the following we discuss the design of the ARES superconducting cavity and the rationale behind the choice of its main parameters. A summary of the R&D program that has been started in collaboration with Italian industry is also presented, together with the expected milestones to reach the specified performance. Finally, fall-back solutions, that would anyway guarantee the

minimum performance needed for injection into the Φ-Factory, within the proposed time schedule, are sketched.

a) Frequency

To guarantee the high quality of beam specified in paragraph 2.3.2.1, we are forced to select a SC Linac frequency on the low side of the .35 GHz ÷ 3 GHz range currently used for the acceleration of ultrarelativistic beams. In fact one can show [36] that to ensure the kind of single bunch performance required for linear colliders and FEL's, the frequency should lie below 1500 MHz.

If we further restrict the choice to most commonly used frequency values, we are left with only two frequencies : 350 MHz, developed and used at CERN, and 500 MHz, developed and used at DESY, KEK and on LISA in our own Laboratory.

From a purely technical point of view, the advantages of 500 MHz over 350 MHz are mainly three:

- 500 MHz is a sub-harmonic of other widely used frequencies: 1, 1.5 and 3 GHz ;
- standard power sources are easily found on the market ;
- the cavities and their ancillary equipment, being smaller, are easier to handle.

The last argument is of course important but the two others are more fundamental since they are linked to the positron capability required from our Linac and, we believe, to the development potential of the accelerator.

In fact, from the latter point of view, one of the goals of ARES is to produce a very low emittance beam, with high peak current and high repetition rate, so that the installation may become a test bench for future TeV colliders.

As shown by several authors [37] a fully superconducting linear accelerators may become advantageous for SC TeV Colliders if accelerating fields exceeding 30 MV/m can be achieved since the cost would then become competitive - for long (10÷20 cells) structures in the frequency range upwards of ≈ 3 GHz - with that of warm structures. The rate of increase of the useful field in SC cavities over the past 10 years, together with the number and quality of R&D programs in progress all over the world, make it reasonable to envisage that the goal will be reached in the not too distant future. In a 3 GHz Collider, however, the high peak current, high bunch charge, low emittance first part of the accelerator (below ≈ 1GeV) would presumably have to operate at much lower frequency. ARES could therefore be considered as a prototype of the injector for a TeV collider and, as such, it should be operated on a subharmonic of one of the higher standard frequencies.

A number of other minor advantages and disadvantages can be found for each of the two frequencies. Some the arguments that are usually given and that, in our opinion, balance out are:

- the 350 MHz cavity has a lower RF power loss per meter of active length. In fact the BCS part of the surface resistance, at a given temperature, scales like ω^2.
- for a constant number of cells, 350 MHz requires less cavities and less associated equipment. For a given E_{acc}, the numbers scale like ω.
- the 500 MHz cavity has a smaller surface (it scales like ω^{-2}) and therefore, presumably, a smaller number of field emitters and defects that limit the maximum field holding capability and produce the negative slope in the measured Q versus E_{acc} curves.
- the 500 MHz cavity smaller overall dimension, scaling like ω^{-3}, give greater freedom to implement and test cleaning techniques.

It is our conclusion that with 500 MHz cavities the chance obtaining the high specified design value of E_{acc} is greater.

Moreover, on an overall project basis, it has to be taken into account that the slight capital cost increase for cavities is almost exactly balanced by the lower cost of the RF power sources, which - at 500 MHz and for the ARES power level - are standard and available from stock.

b) Cavity Geometry

Once the operation frequency has been fixed, the base cavity geometry has to be optimized to best meet the overall design specifications, and all the ancillary equipment has to be designed. In practice, as far as geometry is concerned, the only important parameter is the number of cells because, since 1979, all SC accelerating structures for ultrarelativistic particles are either spherical or elliptical. As a consequence, apart from the frequency scaling factor, they differ just on minor details (usually dictated by the fabrication procedure) that affect the overall cavity parameters only marginally .

The origin of this uniform design were the experimental results first obtained in Genova[38], and later confirmed by other Laboratories [39,40], showing that multipacting - at that time the foremost field limitation - was suppressed by giving the cavity a proper (spherical or elliptical) shape.

For ARES we choose four cells per cavity, a reasonable compromise between filling factor (which increases with the number of cells) and maximum field holding capability (which decreases with the number of cells).

As mentioned above, the technology used for cavity fabrication has some influence on the nominal cavity dimensions. Moreover the achievable mechanical tolerance and reproducibility, also dependent on the fabrication technique, are essential for the quality of the SC cavity.

To gain some insight on the problem of tolerances let us make some general consideration.

In this type of cavity the resonant mode used for acceleration is the $TM_{010-\pi}$, in which the accelerating field in two adjacent cells has the same amplitude but opposite sign.

A $TM_{010-\pi}$-like mode exists for any multicell cavity, but to have this mode at the nominal frequency, with almost the same field amplitude inside each cell (field flatness of few per cent), each cell - with its real boundary conditions determined by the adjacent cells and the cut-off tubes - must resonate at exactly the same, desired frequency. The sensitivity is of few kHz per percent of field flatness.

From a purely mechanical point of view this means that the shape of each cell should be identical to the ideal one to the order of a few hundredths of a millimetre; in practice however the resonant frequency is an integral property of the cell volume. The way the resonant frequency depends on the cell geometry can be better understood by looking at Fig. 2.4.1 that shows the sensitivity curves (for the $TM_{010-\pi}$ mode) for a 500 MHz half cell, scaled from the LEP design. The sensitivity is expressed as the frequency variation, in KHz, for a change of one cm^2 in the area of the cell axial cross section [41].

It can be seen that :

- standard mechanical tolerances are at least one order of magnitude too large: the sensitivity on the value of the equatorial diameter is of the order of 1MHz per millimetre when a frequency accuracy of less than $\approx$ 20 kHz is desired.
- using the degree of freedom afforded by the axial position of the actual profile, a volume compensation is possible, with respect to the $TM_{010-\pi}$ accelerating mode, which gives a good equivalence, between the real translated geometry and the theoretical one.

A technique to manufacture cells that are identical from the electromagnetic point of view, in spite of mechanical tolerances, has therefore been implemented in collaboration with an industrial firm. It consists essentially in measuring the profile of each half cell and then cutting it so that an equivalent shift of the cell profile in the axial direction - and a consequent electromagnetic compensation, according to the concept of volume equivalence mentioned above - are produced.

This technique has been successfully tested on a number of Cu and Nb half cells, produced by spinning under the supervision of ANSALDO CO. As a further improvement, it has been decided, for the ARES cavities, to change the fabrication technology, from spinning to deep-drawing. The reason is mainly that deep-drawing is intrinsically more reproducible, so that the need for costly compensation procedures is drastically reduced. Moreover, because cell obtained by deep drawing and electron beam welding, once tuned to the proper frequency, are

mechanically almost identical to each other, the actual field distribution of higher order modes (HOM) is much better known and HOM couplers can be rendered much more efficient.

A comparison of the results obtained at KEK[42] , where deep-drawing is used, with those of DESY[43] and CERN[44] , where half-cells are spinned, confirms that the choice is correct.

A schematic drawing of the ARES cavity is presented in Fig. 2.4.2. The major modifications with respect to the CERN scaled cavity are the shape of the cut-off tubes, the position and dimension of the coupling ports and, finally, the cell diameter. Because each modification has a rationale dictated by experience or suggested by the specific ARES parameters, we will briefly discuss these choices in the following.

- All nominal dimensions have been rounded-off; the tuning of the cavity to the proper frequency and the field flatness are achieved by adjusting the central cell diameter, and the equatorial radius of curvature of the end half-cells. Both parameters are specified to within 0.1 mm, to be consistent with mechanical tolerances.

- Since deep-drawing nicely and consistently reproduces the nominal shape, dimensions are specified in such a way that the proper frequency at room temperature is reached after a total of 0.1 mm have been uniformly removed from the surface by electropolishing. The experimental [45] coefficient used to convert the room temperature frequency value to 4.3 K is 1.00138. A SUPERFISH[41] computation over one half cavity, with 32,000 mesh points, gives a theoretical field flatness of 0.4 %.
- The cut-off tube diameter has been slightly reduced and the chicane profile has been appreciably modified to reach a reasonable compromise between HOM out-coupling and wake field effects on the low energy beam.
- The dimension and position of the HOM and main coupler tubes has been modified to reduce the coupler induced field perturbation at the cost of a reduction in maximum coupling strength. The choice is consistent with the ARES beam parameters.

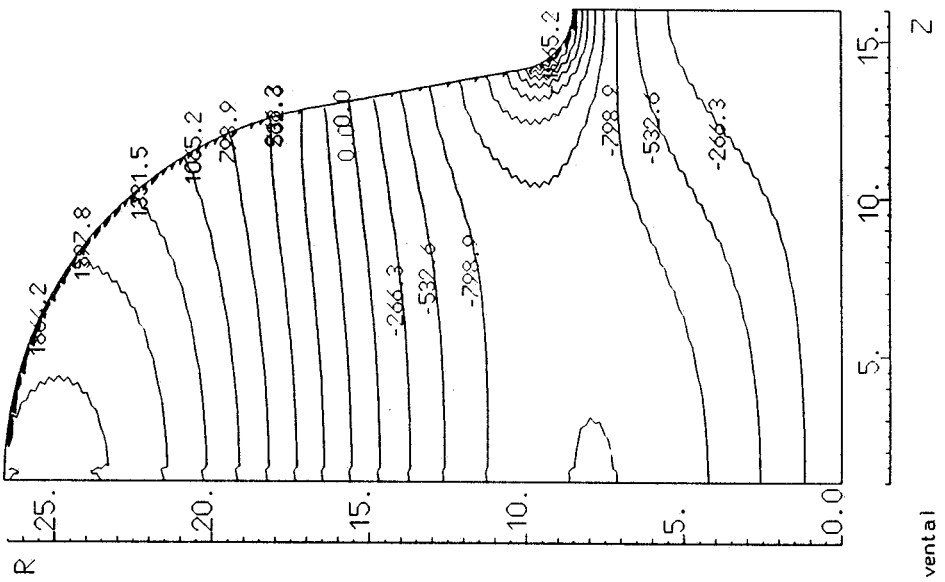

Fig. 2.4.1 - Sensitivity curves (for the TM_{010}-π mode) for a 500 MHz half cell, scaled from the LEP design. The sensitivity is expressed as the frequency variation, in kHz, for a change of one cm^2 in the area of the cell axial cross section

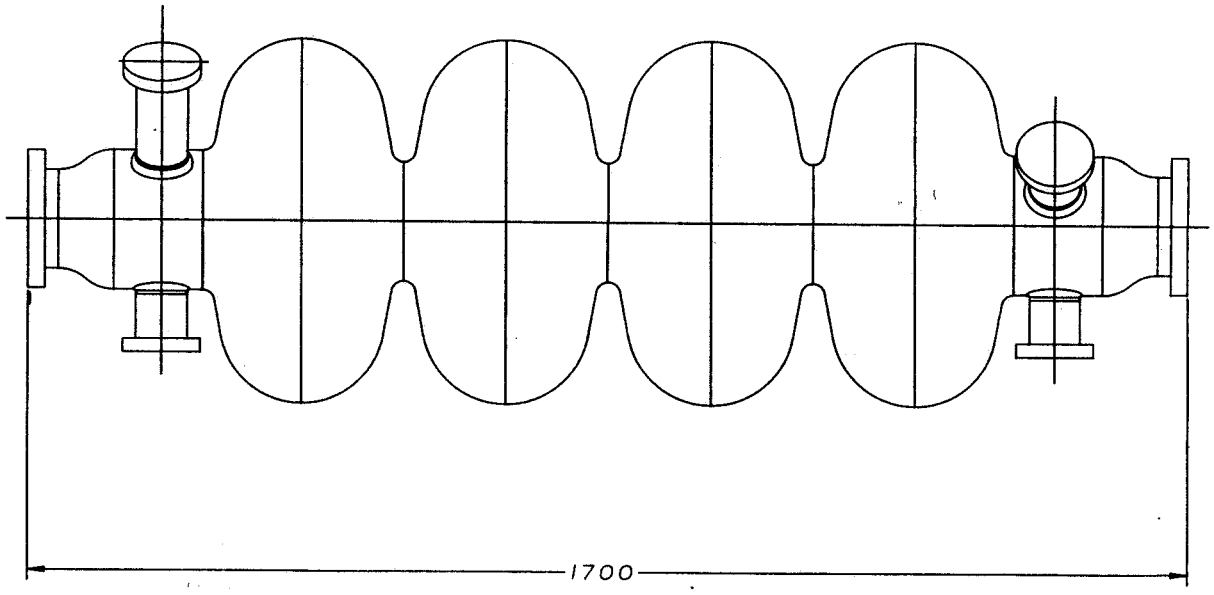

Fig. 2.4.2 - Schematic drawing of the ARES cavity

c) HOM and Main Couplers

Each SC cavity is coupled to its RF driver via a coaxial line. A special device - the coupler - transforms the electromagnetic field configuration existing in the coaxial line into the configuration most suitable for exciting the fundamental (TM_{010}-π-like) accelerating mode in the resonator.

Usually the transition from the atmospheric pressure coaxial line to the cavity vacuum is through a cylindrical ceramic window. A straight cooled antenna couples to the electric field of the SC cavity in the region of the drift tube; the depth of its penetration inside the tube determines the coupling coefficient β and hence Q_{ext}.

The SC cavity drift tube also carries higher order modes (HOM) couplers. Their function is to damp the HOM's by extracting the energy deposited by the bunched beam in the corresponding modes of oscillation of the e.m. field in the cavity. This is necessary because the interaction of the bunch with high order mode electromagnetic fields left in the cavity by preceding bunches can lead to instability or emittance blowup.

The HOM couplers are essentially high pass filters which do not couple to the fundamental mode but only to the higher frequency spurious fields. Connected to an external load they lower the HOM quality factor Q and field intensity. Each ARES cavity is equipped with two HOM couplers; the extracted RF power is dissipated in resistive loads located outside the cryostat.

The development of the couplers for the ARES cavities is in progress, taking into account the beam parameters. Particularly, due to the wide range of average beam current which are expected to be used, a main coupler with a variable coupling coefficient is foreseen.

A list of the monopole modes computed for the ARES cavity is presented in Table 2.4.1, together with their expected values of the R/Q parameter. The expected values of the average current density, $\langle j_s \rangle$, and of the average radial electric field, $\langle E_r \rangle$, at the coupler position are also given, for a proper design of the HOM couplers.

The frequency of the modes listed in table 2.4.1 are computed with the code OSCAR2D, while the electric field and the current density are obtained from the output of an implemented version of the code SUPERFISH, able to accept up to 32,000 mesh points[41]. For a better resolution of the computed electric field on the cavity surface, a new routine has also been implemented.

Figure 2.4.3 shows the field pattern of few of the TM_{0np} modes of the ARES cavity, as computed with the code OSCAR2D.

Table 2.4.1 - ARES Cavity TM_{0np} Modes

Mode family	Frequency [MHz]	R/Q [Ω]	$\langle j_s \rangle$ [A/cm^2]	$\langle E_r \rangle$ [MV/m]
TM_{010}	491.9	0.0	0.2	0.1
	495.0	0.0	0.4	0.2
	498.0	0.0	0.5	0.2
	499.4	470.0	0.4	0.2
TM_{011}	884.8	0.1	0.5	0.1
	893.7	8.1	1.0	0.2
	903.1	50.5	1.4	0.3
	906.7	109.0	1.2	0.3
TM_{020}	1038.8	0.1	1.2	0.2
	1046.5	1.5	1.4	0.3
	1056.6	0.2	1.3	0.3
	1066.1	0.2	0.9	0.2
TM_{021}	1318.2	1.1	2.7	0.4
	1341.5	0.8	5.6	0.8
	1367.0	0.4	8.4	1.2
	1392.5	2.4	8.2	1.2
TM_{012}	1410.6	1.3	5.0	0.7
	1417.6	13.2	1.7	0.3
	1425.4	4.7	1.9	0.3
	1425.6	22.4	1.8	0.3

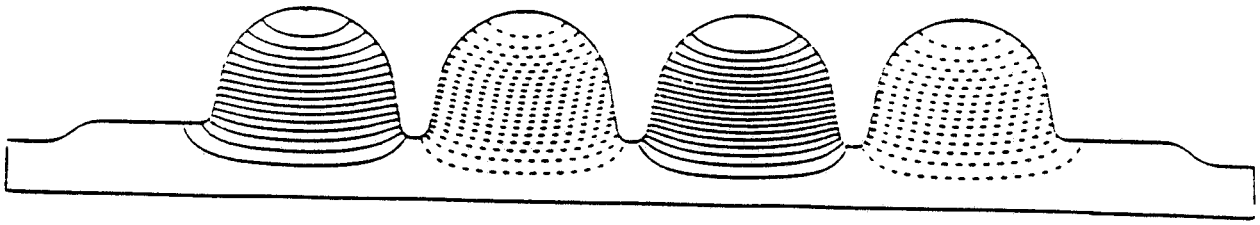

$TM_{010-\pi}$ f = 499.4 MHz

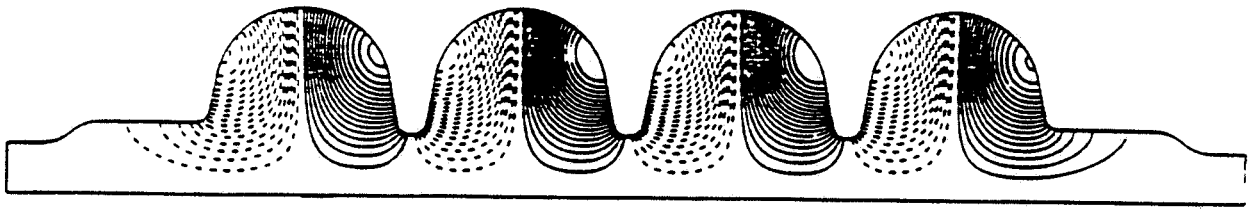

TM_{011} f = 907 MHz

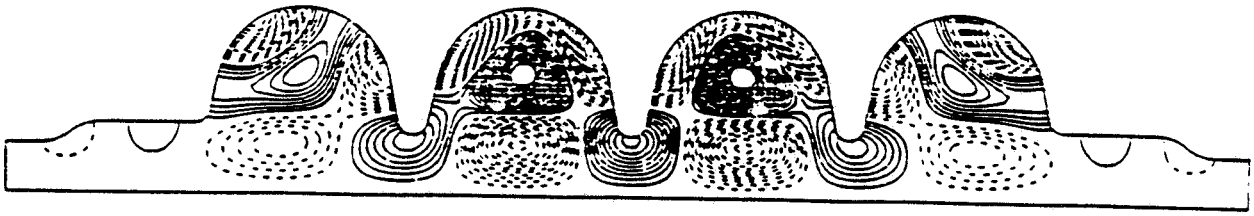

TM_{032} f = 1790 MHz

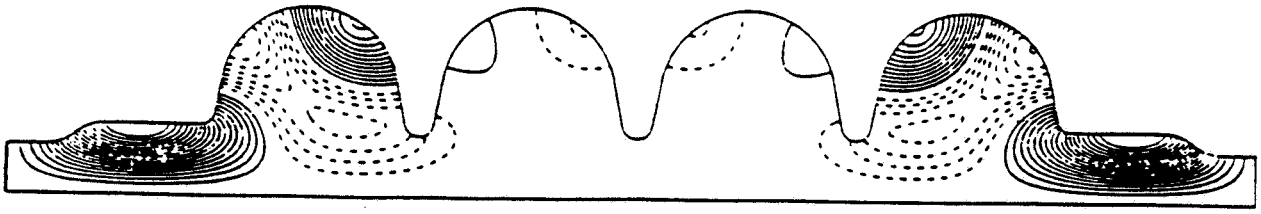

"Tube mode" f = 1250 MHz

Fig. 2.4.3 - Field pattern of few of the TM_{0np} modes of the ARES cavity, as computed with the code OSCAR2D.

2.4.2. - Radiofrequency

a) General Design Criteria

The Superconducting LINAC consists of a total of twenty-eight 4-cell cavity resonators. Section L1 of the electron injector has four cavities, section L2 has again four cavities and the main linac section - L3 - has twenty cavities.

For a design maximum average current (i_b) of 0.2 mA, the maximum beam power per cavity (P_b) is:

$$P_b = V_A \langle i_b \rangle = 12MV \times 0.2mA = 2.4kW$$

and P_d, the power dissipated on the walls of the superconducting cavity at the nominal gradient of 10 MV/m, is given by :

$$P_d = \frac{V_A^2}{\left(\frac{R}{Q}\right) Q_0} = \frac{(12MV)^2}{470\Omega \times 3\ 10^9} = 102W$$

The total required average RF power per SC cavity is thus 2.5 kW for an accelerating gradient of 10 MV/m and a cavity low field quality factor,Q_0, of $3 \cdot 10^9$.

Because of the maximum beam power is rather low, the external Q (Q_{ext}), given by the cavity coupling to the RF source, is rather high, even if the best coupling is chosen at P_b .

In fact we have :

$$Q_{ext} = \frac{Q_0}{\beta} \approx 1.2 \cdot 10^8$$

where β is he coupling coefficient β given by :

$$\beta = \frac{P_b + P_d}{P_d} \approx 25$$

The bandwidth of the system,B_L , given by :

$$B_L = \frac{F_0}{Q_{ext}} \approx 4\ Hz$$

is consequently very narrow.

Such a narrow bandwidth could create some problem in connection with the required accelerating field phase stability. In fact, the helium flow in the cryostat can induce mechanical vibrations in the accelerating structure (microphonic noise) that may be difficult to counteract with a mechanical tuning system. It is however at present believed that the problem can be solved using fast piezo-electric or magnetostricitve tuning devices. Furthermore, the topic will be further investigated experimentally on LISA before a final decision on the RF system is taken.

The presently envisaged and costed layout of the RF system relies on the fact that the phase stability problem will be solved and is based on the use of seven amplifier chains, each feeding four SC cavities via a coaxial distribution system, as shown in Fig 2.4.3 .

Because of the narrow bandwidth of the cavity-source system, an individual RF isolator (or circulator) is foreseen for each cavity. This provides the necessary isolation and avoids unwanted interactions between cavities. The installation of the isolators next to the resonators allows the system to operate under matched conditions. Small size, inexpensive, non-pressurised coaxial lines (i.e. the standard 3-1/8") can thus be used, so that part of the extra cost of circulators is actually recovered.

To adjust the phase of the accelerating field in each cavity within a group of four, a set of three coaxial phase shifters per group is provided. The phase adjustment between groups of four cavities is made at the low-power chain level.

A more complicated and costly solution than the one described, consisting of an independent power generator per cavity, that allows the phase of each cavity to be individually controlled at the low power electronics level, will be adopted should the microphonic noise prove to be a problem.

b) Power Sources

The availability on the market of a large number of standard RF power generators for broadcasting applications - especially in the UHF band that contains the operating frequency of our SC cavities - makes the choice of the RF sources very easy. In particular, tetrodes cover the range of up to 1 GHz with powers up to 20 kW-cw.

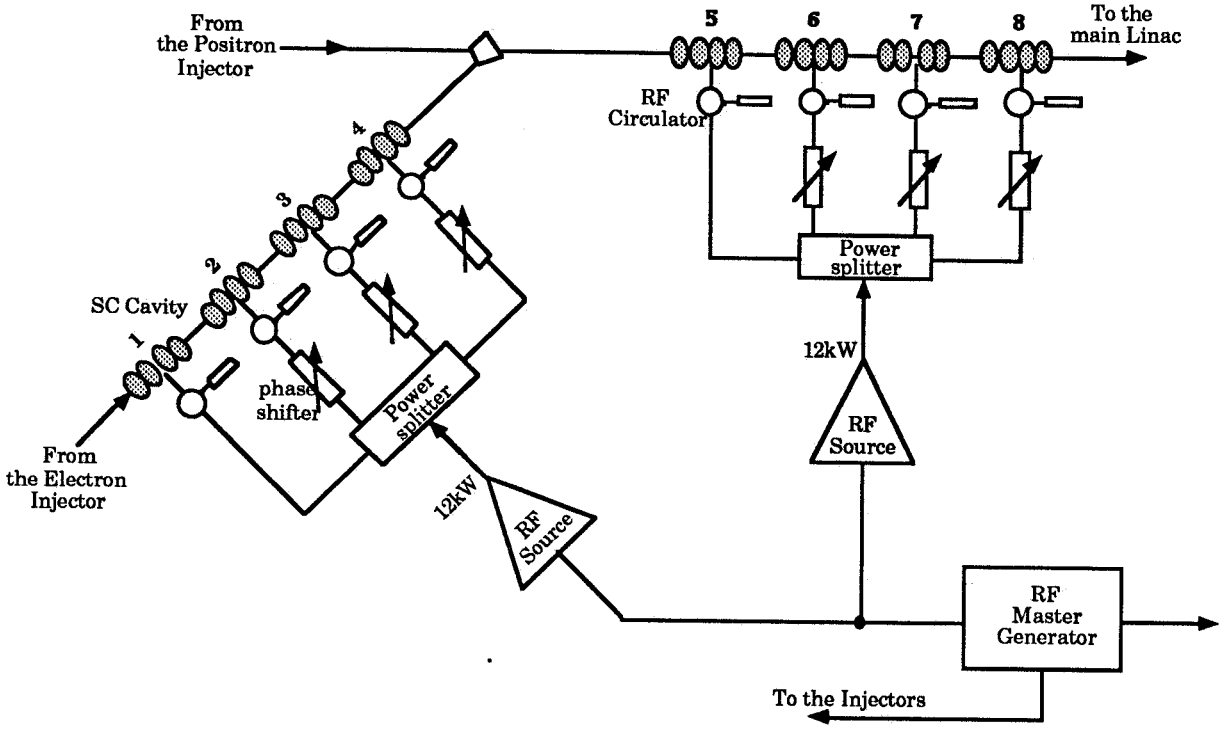

Fig. 2.4.3 - RF feeding system for two groups (L1 and L2) of four SC cavities. A similar layout is foreseen for the main Linac.

With a maximum beam power rating of 2.4 kW per cavity, including the allowance for cavity and coaxial line losses, a 12 kW tetrode amplifier has been selected as the best candidate for powering one group of four SC cavities.

The amplification chains include a predriver stage, consisting of a 30÷40 W transistor amplifier, and two power stages, respectively rated 1 kW and 12 kW. The power is fed to the cavities via coaxial lines.

Alternate solutions such as klystron generators will also be considered; output powers of up to 20 kW for small size tubes are easily obtained.

Should it become necessary to power each cavity individually, 3 kW tetrode generators, easily found on the market, would be our preferred choice.

c) The control system

To control both the beam energy and the beam size as particles travel through the accelerator, some of characteristic parameters of the SC cavities must be carefully controlled and continuously adjusted by means of dedicated circuitry and feedback loops.

The main parameters that have to be kept under control are: the amplitude of the cavity accelerating field, the phase of the cavity voltage with respect to that of the main RF driver and the cavity resonant frequency. These parameters, that all affect the beam energy spread, are not altogether independent from each other.

In the present design the specification for a beam energy spread of $\leq 10^{-3}$ requires the amplitude variation of the accelerating field in each cavity to be kept below 10^{-4}.

This specifies the performance of the automatic gain control (AGC) system and of the RF chains phase and tuning control feedback loops. The design of the feedbacks also has to take into account the fact that the bandwidth of the coupled superconducting cavities is very narrow ($\approx$ 4 Hz for ARES cavities). Obviously the phase control is effectve if an adequate power margin is available and phase fluctuations remain inside the cavity bandwidth.

Fig. 2.4.4 shows a block diagram of the proposed RF control system for ARES.

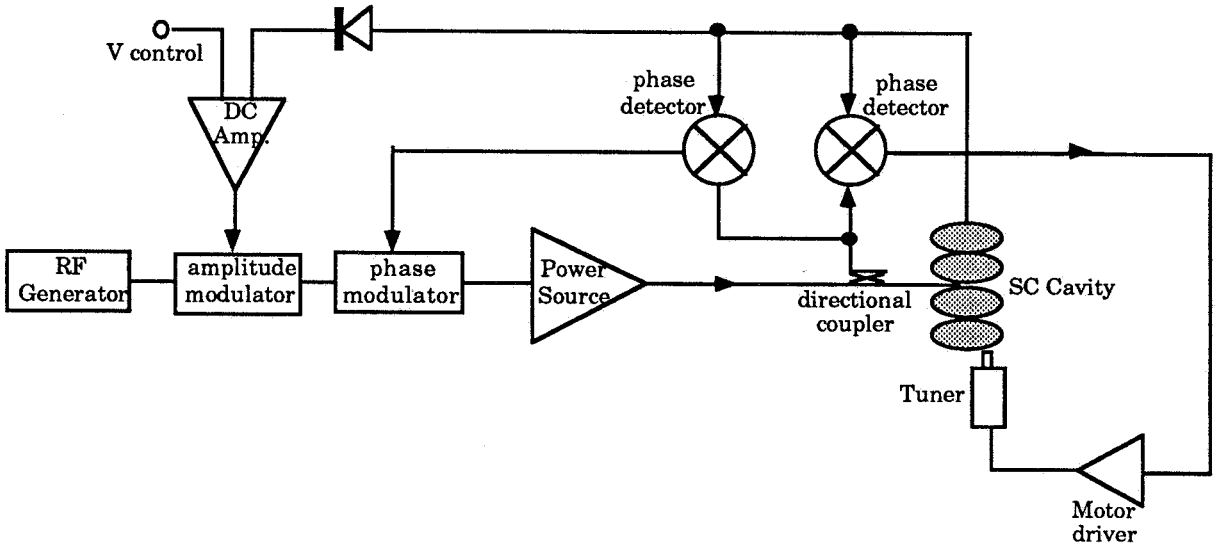

Fig. 2.4.4 - Schematic layout of the RF controls in case of individual driving.

2.4.3 - Cryogenics

a) Introduction

The cryogenic system is divided into four main sub-systems, each with its own function, namely :

- Cold Box (CB),
- Distribution System (transfer lines and connection U-tubes)
- Compressors and ancillary equipment (oil removal and the gas management systems)
- Cryostats.

The operating temperature of the cavities has to be as close as possible to the lowest LHe temperature attainable at normal pressure, that is between 4.24 K and 4.30 K when the unavoidable pressure drop along the lines and the heat exchangers is considered. This temperature is low enough to keep the surface resistance of superconducting Nb low at 500 MHz while avoiding the need for sub-atmospheric operation.

Table 2.4.2 - Steady state operation parameters

Transfer line:	overall length	[m]	200
	Mass to cool	[kg]	150
Nº single cavity cryostats			8
	Mass to cool	[kg]	3200
No. double cavity cryostat			10
	Mass to cool	[kg]	8000
Total RF dissipation @ 4.3 K, E_a =10 MV/m, $Q_0 = 3 \times 10^9$		[W]	2856
Static heat load @ 4.3 K on cryostats and distribution system		[W]	350
Heat load on radiation shields		[W]	3000
	Mass to cool	[kg]	3100
TOTAL POWER:	@ 4.3 K	[W]	3206
	radiation shields	[W]	3000

Moreover, to better control the cold flow he 4.3 K feeding line is operated in the He supercritical region, i.e. at 2.8 atm. Single phase Helium flow through the feeding lines is thus obtained and the cryogenic fluid is free to expand, producing a two phase stream, only just next to the cryostat. The main heat loads and the total power to be extracted at low temperature in the steady state operation regime are listed in Table 2.4.2.

b) Cold Box

The CB specification has to include, in addition to the input design power, an appropriate allowance for all those extra low-temperature losses that must be manageable without needing to shut down the superconducting linac refrigeration.

The power specification for the CB is set at

$$4'000 \text{ W @ } 4.3 \text{ K} \quad \text{plus} \quad 6'000 \text{ W @ } 60 \text{ K},$$

providing a low temperature heat load capability of 800 W above the nominal requirement. The safety factor is thus ≈ 1.25. The main features of the Cold Box are summarized in Table 2.4.3.

Since the coolant is the same He used to cool the cavities, care must be taken - to prevent plugging of the needle valves - to avoid all contamination of the Helium gas.

The upper pressure limit specification pressure will depend somewhat on the manufacturer, but should remain in the range of 12÷15 atm.

The thermodynamic efficiency, expressed as a percent of the efficiency of an ideal Carnot cycle operating between the same temperatures, implies an overall cryogenic plant plug-power requirement of 1.3 MW at room temperature

Table 2.4.3 - Cold Box main features

Operating temperature	[K]	4.3
Power @ 4.3 °K	[W]	4000
Additional power @ 60 °K	[W]	6000
Flow rate @ 4.3 °K	[g/s]	201
Room temp. pressure	[Atm a]	12
Pressure @ 4.3 °K	[Atm a]	2.8
Return pressure	[Atm a]	1.082
Carnot efficiency	[%]	21.4

Figure 2.4.5 shows a diagram of the gas flow path, while Figure 2.4.6 shows the corresponding temperature-entropy (T-S) thermodynamic cycle diagram.

The incoming stream, at 300 K and 12 atm, is cooled at constant pressure by means of counter flow heat exchangers in which the cold return gas produced by the two isoentropic expansion stages is heated-up to room temperature. The isoentropic expansions on the T-S diagram are intentionally drawn as "not ideal" to emphasise that the actual transformations are not completely reversible. A final stage of isoenthalpic expansion, obtained by means of a Joule-Thomson (J-T) valve, provide the necessary counter flow cooling at 4.3 K for the 2.8 atm (supercritical) Helium stream.

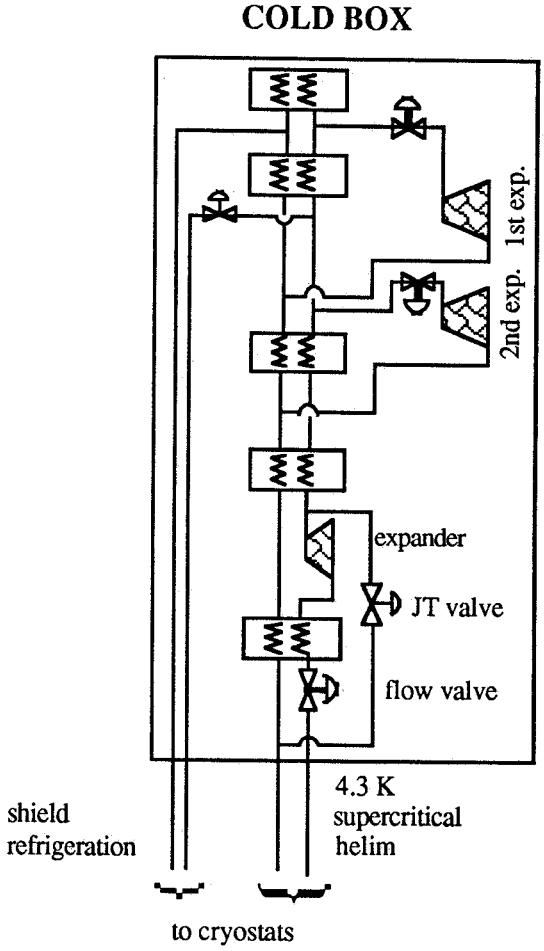

Fig. 2.4.5 - Block diagram of a refrigerating machine

The final J-T expansion of the supercritical flow, which actually takes place just next to the cryostat, far from the CB, is also shown on T-S diagram. In fact the supercritical condition is

maintained in the transfer line throughout, so that the single phase Helium flow can be better controlled.

The CB also provides the necessary intermediate temperature radiation-shield cooling, in the range 40 K÷ 80 K, for the whole cryogenic system. Closed-cycle intermediate temperature refrigeration is obtained using the same process He gas. This makes the plant operation simpler and cheaper and avoids the need for different cryogenic fluids; it will however not be possible to keep the cavities at LN_2 temperature for a long time unless the CB is in service.

To ensure maximum flexibility and reliability, all functions and parameters of the CB, such as pressures, temperatures, turbine speed, valve throttling, etc., are remotely controlled and monitored. An independent computer automatically controls the flow valves, the LHe level inside the cryostats, the shield temperatures and the alarm and safety procedures; the automatic control may be manually overridden whenever non-standard values of temperatures and pressures are required or during recovery from an emergency.

The CB control system provides the main control system with the refrigerator status data and takes care of all interlocks and links to other linac components (vacuum, RF, injector, etc.).

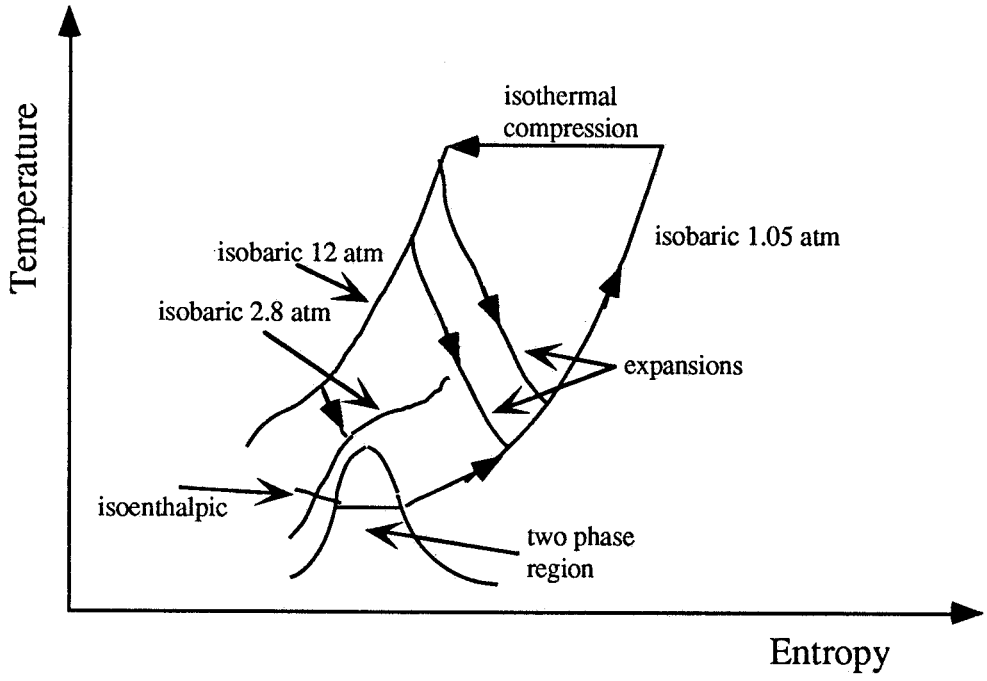

Fig. 2.4.6 - Thermodynamic cycle on the T-S diagram

Many technical details of the CB that do not affect the basic performance of the system, such as the upper pressure limit, the use of serial instead of parallel turbine expanders, the use of a

"wet" expander instead of a J-T expansion valve, etc., will need to be finalized in collaboration with the manufacturer.

c) Distribution system

The distribution system function is to transport and distribute the 4.3 K and at 60 K cold streams to the cryostats with losses that must be negligible in comparison with the main heat loads.

As shown in Fig.2.4.7 all cryostats are connected to the CB via the main transfer line, and are fed in parallel. The distribution scheme is very simple and the task of regulating the cold flow as required by each cavity is left to the final J-T expansion valves.

In fact, the cavities will dissipate different amounts of energy depending on their quality factor Q_0, which, in addition, may vary during operation. A feedback on the liquid level inside the cryostats, acting independently on each final J-T valve, is therefore provided so as to keep the cavities always fully immersed in the LHe bath. The feedback is software-implemented in the CB controller.

The distribution system design also facilitates the maintenance of the cavities : individual cryomodules can be disconnected while the refrigerator stays in operation to keep the rest of the cryogenic complex cool. The technical solution uses fast connections (U-tubes) between the main transfer line and the cryostats, similar to those foreseen for CEBAF.

There are four U-tubes for each cryostat : two (input and return) on the 4.3 K line and two on the 60 K line. Each fast connection is equipped with valve and purging port so that it can be mounted and dismounted without introducing contaminants that could freeze and plug the refrigerator.

Table 2.4.4 - Transfer line main parameters

Piping scheme		4 product streams; cold shield; superinsulataion
Pressure of incoming 4.3 °K He	[Atm a]	2.8
Pressure of return 4.3 °K He gas	[Atm a]	1.082
Max. pressure drop on 4.3 °K return pipe	[Atm a]	0.002
Total heat loss @ 4.3 °K	[W]	20
No. of cryostat connections		18
Type of connection		U-tube for each stream
U-tube heat loss @ 4.3 K	[W]	180
Flow control		2.8 atm, 4.3 °K pipe : J-T valve 60 K pipe : needle valve

A cross sectional view of the main transfer line is shown in the inset of Figure 2.4.7 . It is of the four-product-stream type with shield and superinsulation. The expected dynamic heat loss is less than 0.1 W/m @ 4.3 K. The main parameters are listed in Table 2.4.4.

As previously pointed out the pressure drop along the 4.3 K return line has to be kept as low as 210^{-3} atm in order to keep the LHe bath temperature inside the cryostat close to 4.3 K.

The pressure drop on the 4.3 K, 2.8 atm feed line is not as critical as that on the return line; it is only necessary to keep the end pressure higher than 2.245 atm, the critical pressure of He. It is also worth noting that no cooling occurs during the isoenthalpic expansion of He from 2.8 to 1.082 atm at 4.3 K.

As it can be seen from the data of Table 2.4.4 the largest heat load in the distribution system, 180 W @ 4.3 K, comes from the U-tube connections. The distribution system thermal losses add up to $\approx$ 5 % of the overall 4.3 K heat load.

d) Compressors and ancillary equipment

An efficient compression system is vital to keep the cryogenic plant working. Figure 2.4.8 shows the block diagram of the CB together with the compressors, purifiers, and medium pressure storage tanks.

Two make the system more reliable two compressors are mounted in parallel so that one can be switched on if the other fails. This because, while in the event of a fault on the CB the compressor can keep the cavities cold for a long time, a compressor fault will cause the LHe evaporation to stop and the cavities to warm up very fast.

Unless the compressor is equipped with an oil removal system and downstream adsorbing filters, during compression the pure Helium will become contaminated with the compressor lubricant oil. As first approach we foresee only one heavy-duty purifier that can work continuously for one year; the filters can be replaced and/or purged while the purifier is in service.

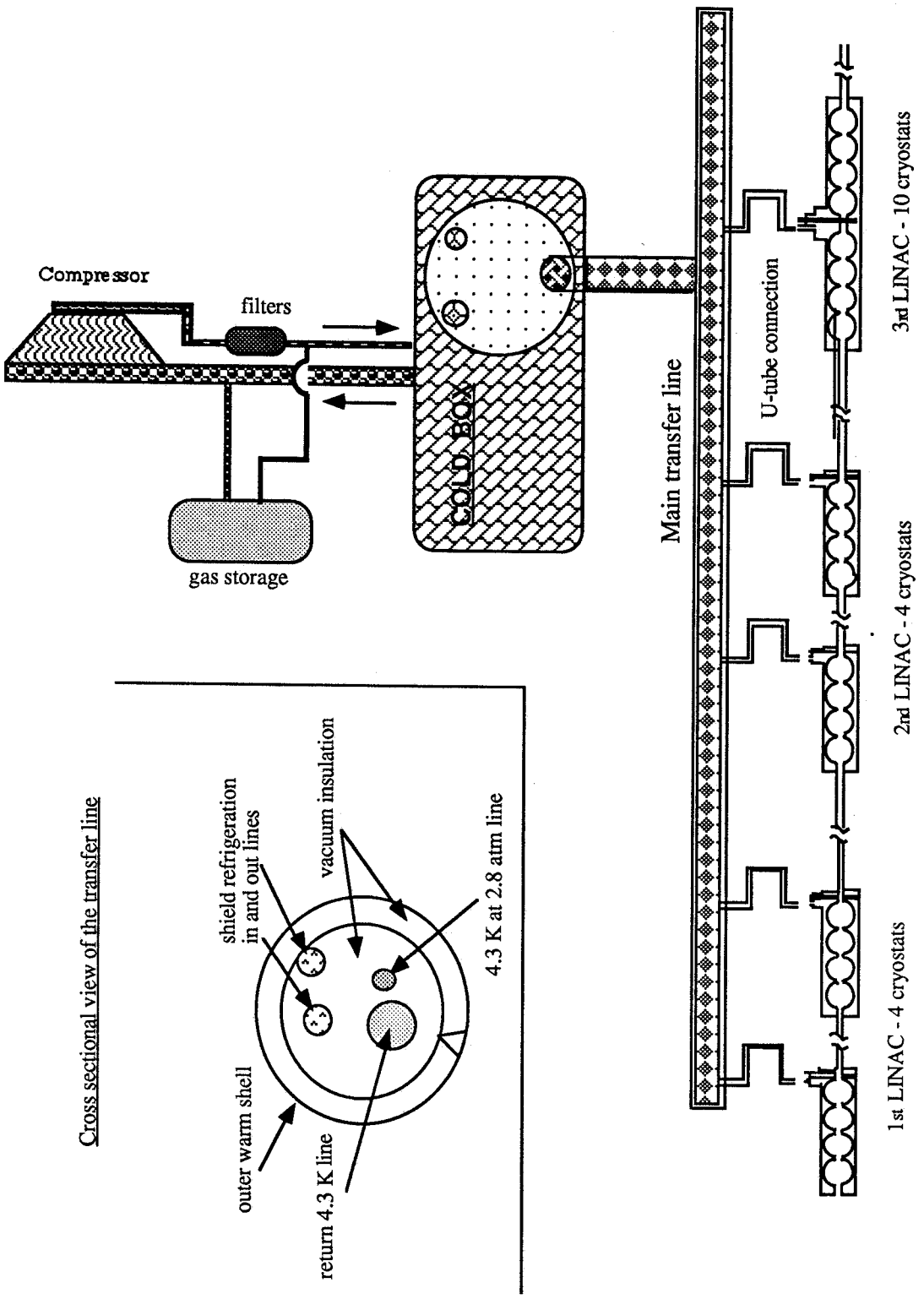

Fig. 2.4.7 - Schematic layout of the cryogenic system. A cross sectional view of the main transfer line is shown in the inset.

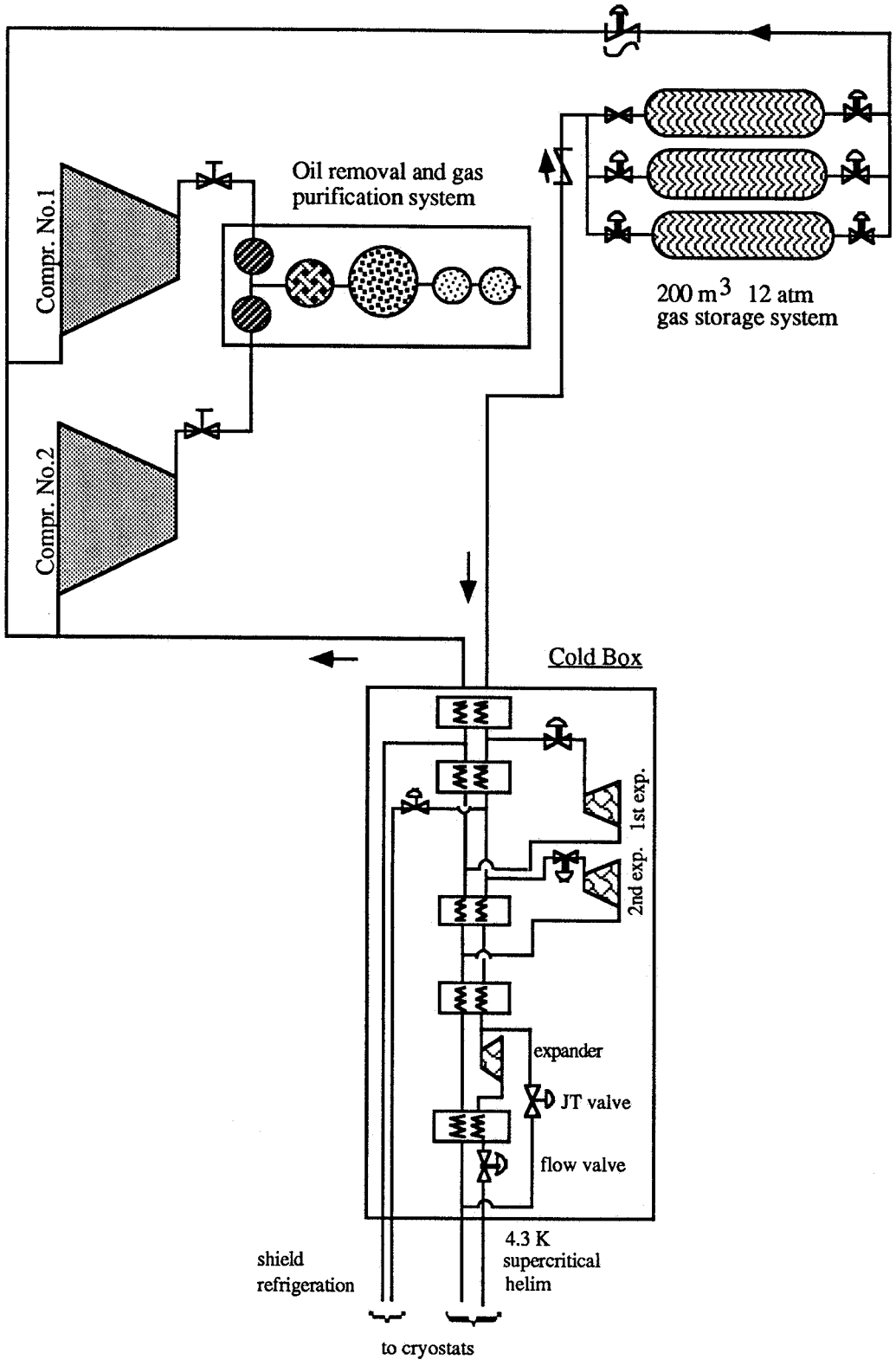

Fig. 2.4.8 - Block diagram of the cold box, together with the compressors, purifiers, and medium pressure storage tanks.

The system operates as follows: when the system is warm the pure Helium gas is stored in the pure gas storage tank and all the piping, cryostats, compressors and the CB, are filled with pure Helium gas.

The total gas inventory is about 2142 m^3 S.T.P., or 186 m^3 at room temperature and 12 atm.

For easier handling and purification the storage tank consists of three separate vessels of 70 m^3 each. After the compressors and the CB have been started the He starts to condense in the CB, the transfer lines and the cryostats, so that the return pressure lowers; this actuates a constant pressure make up valve that takes gas from the vessels and fills the return line at constant pressure. Once the steady state is reached, i.e. the cryostats are full of LHe, the CB starts operating in a closed cycle and the vessels can be closed.

When the cryostats have to be warmed up, the Helium can be recovered either by means of the CB compressors, in the form of pure He, and stored in the storage vessels or using a standard recovery system (gas bag and high pressure compressor, not included in the drawing). The latter system however leaves the He exposed to contaminants.

d) Cryostats

From an engineering point of view, the cryostat must provide a proper environment for the SC cavities. Thermal insulation, shielding from magnetic fields, removal of the RF heat at constant temperature ($\approx$ 4.3 K), tuning, auxiliary equipment, clean conditions, UHV techniques, easy handling and mounting are the main features that have to be kept in mind in designing and manufacturing the cryostat.

At this stage no development has been attempted since SC cryostats have reached a satisfactory standard level of performance; the preliminary design and manufacture specifications are therefore based on existing designs, notably those for the CERN cavities [46].

The main components making up our cryostat are:

- outer vacuum vessel,
- GHe cooled radiation shield,
- magnetic shield,
- LHe vessel,
- thermal-magnetostrictive tuners (three).

Internal electrical cabling, waveguides, feedthrough tubes, support rods, niobium beam-pipe extensions, probes, etc., are also considered parts of the cryostat.

Two prototypes are under construction at ANSALDO CO.

Vacuum vessel

A stainless-steel (AISI 316 LN) bar to which two rings of the same material are welded is the main support structure; aluminium-alloy staves are then bolted to the s.s. rings circumference. Two covering plates and a stainless-steel outer shell give the vacuum vessel the final required stiffness.

After assembly the vessel is He-leak pressure tested .

GHe cooled radiation shield

The GHe cooled radiation shield is made of high conductivity, phosphorous free ETP or OF copper plates. The shield surface temperatures is kept approximatively constant by the GHe evaporated from the LHe bath; the cold gas flows inside copper pipes brazed on the copper sheets. The radiation shield is sorrounded by a multilayer, aluminized mylar (NRC-2) "superinsulation" blanket to decrease the radiant heat load on the shield; the blanket also provides a low thermal conductivity layer on the path of residual gas molecules.

Magnetic shield

Any magnetic flux in the vicinity of the cavity is "captured" within the niobium during cool-down and produces a degradation of the SC cavity performance.

Beside avoiding the use of magnetic materials in the construction of the cryostat, the cavity has therefore to be shielded, during cool-down, from external magnetic fields; a μ-metal shield is therefore usually incorporated in the cryostat.

Other precautions must nevertheless be observed during the cool-down sequence of operations; for example the tuner may be switched on only when the cavity is already cold because magnetic fields may appear during tuner activation.

LHe tank

The LHe tank is a low magnetic permeability stainless-steel (AISI 316 LN) container built from two half-shells; its shape follows approximatively the shape of the cavity in order to minimize the LHe volume.

The half-shells are formed by pressing and then welded together. The complete shell is finally TIG-welded to the cavity end-flanges.

The final weld is performed after mechanically tuning the cavity, an operation consisting in a plastic deformation of each individual cell. The deformation should produce the desired RF field flatness and at the same time preserve the elastic behaviour of the four-cell cavity necessary for

the operation of the tuner. To facilitate tuning, the following mechanical arrangements are implemented:

- a single-corrugation bellow is inserted at both ends to decrease the tank longitudinal stiffness so that the tank is less rigid than the cavity along the direction of the tuner forces.
- the central cavity iris is fixed to the tank by a collar. Transverse oscillations of the cavity are thus reduced both because of the symmetry of the structure and because of the transverse stiffness of the large diameter tank.
- the resonance frequencies of longitudinal mechanical oscillations are made as high as possible by connecting the cavity to the tuners by means of very stiff arms .

Thermal magneto-strictive tuners

Beam current changes, vibrations induced by vacuum pumps, LHe bath pressure changes induced by the liquid level control valves, drifts in the support temperatures reflecting on their length, may all lead to undesirable resonant frequency variations that have to be controlled by the tuner mechanism.

The cavity is "tuned" by changing its total length since individual cells are mechanically similar and their own frequency changes proportional to the overall length. Three equally spaced tuning bars are attached to both ends of the cavity by means stiff arms in order to obtain a circumferential symmetry. Because of the symmetry, the structure ends should remain parallel to each other and normal to the structure axis; any transverse mechanical resonance frequency should be higher than the relevant excitation frequencies.

Mechanical resonances of the cavity must also be taken into account to optimize the tuner response.

The selected thermal-magnetostrictive tuning system also complies with all the following general requirements:

- high precision in the presence of large forces;
- absence of rotating equipment that may scuff;
- tolerance of compression, tension and torque (which may appear during cavity cooldown, evacuation and thermal transients);
- mechanical stability;
- possibility to handle fast and slow responses separately.

The tuner bars consist of insulated, rectangular excitation coils wound around both ends of a copper tube. The copper tube is inserted in a coaxial nickel tube that provides the fast magneto-strictive elongation and kept in place by three low thermal conductivity spacers; the spacers also provide good thermal insulation so as to reduce the heat flux related to the Joule effect in the

coils. Nickel is chosen because, even though it needs high exciting fields, it is less brittle than other magnetostrictive materials.

The tuner slow action is thermal and is obtained by inserting a heater inside the Ni tube, next to its midpoint. Cold GHe flowing through a labyrinth path (as in a counter flow exchanger) removes the generated heat. Radiation shields around the tuner are also provided to further improve its thermal insulation.

Note that the GHe mass flow rate must be carefully determined as a function of the current in the heater; improper heat exchange coefficients may lead to undesirable temperature gradients along the whole tuner.

A schematic drawing of the cavity inside the cryostat is presented in Fig.2.4.9, while Fig. 2.4.10 shows the magnetostrictive tuning system.

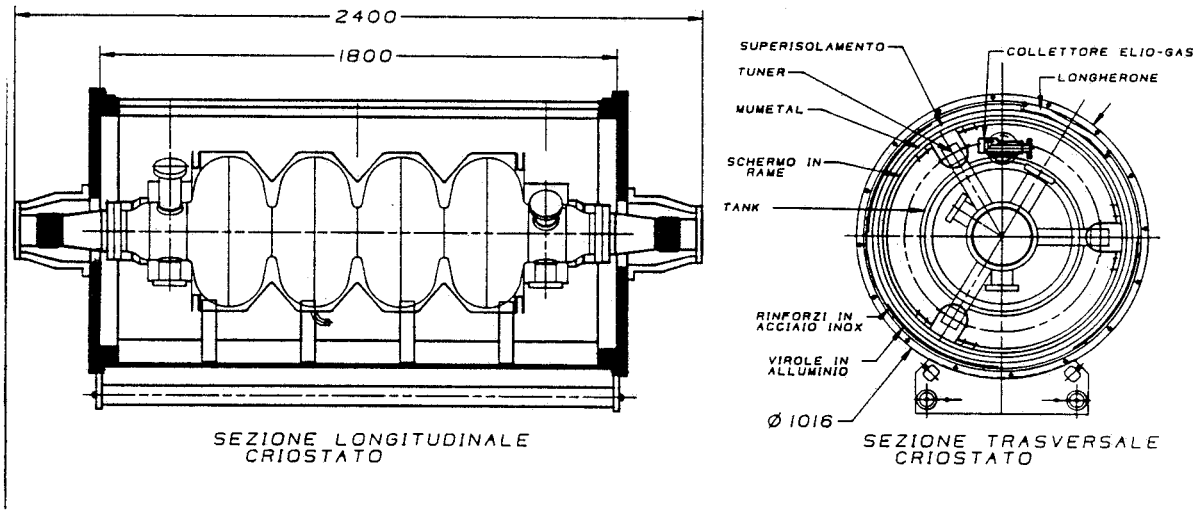

Fig. 2.4.9 - Schematic drawing of the ARES cavity inside the cryostat.

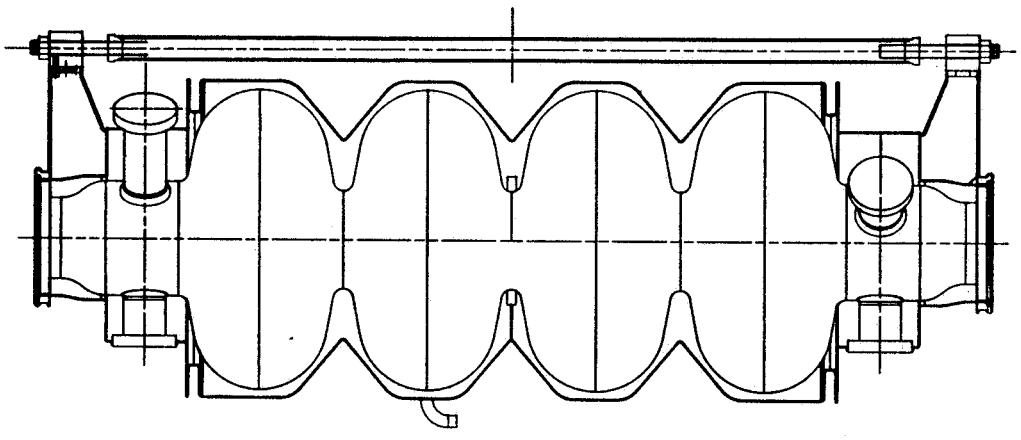

Fig. 2.4.10 - Schematic drawing of the magnetostrictive tuning system.

2.5 - VACUUM SYSTEM

2.5.1 - Introduction

In superconducting accelerator systems very high vacuum is mainly required to protect the superconducting RF cavities from the condensation of molecules of the residual gases on the low temperature superconducting surface: the condensation of few hundreds of monolayers on the superconducting niobium surface would seriously degrade the RF cavity performance, in particular lowering its Q value.

In fact, for a SC linear accelerator this is the dominant phenomenon that sets the most severe requirements on the vacuum system ; interaction with the residual gas is a comparatively minor effect because the beam covers only a few hundreds of meters within the accelerator.

The pressure in the beam pipe and the SC cavities must be in in the 10^{-8} mbar range before cavity cooldown can be started in order to guarantee operation of the RF cavity for at least 2 years at a Q value not lower than 90 % of its initial value.

Very clean vacuum condition (no oil, no dust and no hydrocarbons) are imperative but no titanium sublimation pump can be used because titanium can easily form unwanted alloys with niobium.

It should also be recalled that SC cavity cryostats have to be evacuated to provide the necessary thermal insulation between room temperature and the liquid helium container.

From the point of view of vacuum the ARES linac complex consists of 3 superconducting Sections - that total 18 cryomodules - and about 200 meters of beam lines.

2.5.2 - The cryomodule

The cryomodule is the smallest unit of the superconducting accelerator structure that can be individually tested. Each cryomodule consists of either 4 or 8 RF cells, assembled in a single cryostat.

A gate valve is mounted at each end of a cryomodule to make it easier to test it and to prevent any contamination of the cavities after the initial testing by keeping them under good vacuum conditions at all subsequent times.

Moreover, thanks to the valves, each cryomodule can be separated from the accelerating structure, for instance to replace a defective cryomodule, without breaking the vacuum in the adjacent modules .

The all-metal, bakeable gate valves have a 100 mm inside diameter.

No elastomer sealing is acceptable because the outgassing rate would be too high. Moreover, all-metal gate valves can be supplied with RF contacts that perform a direct electrical connection between the two valve flanges, thereby shielding the inner valve mechanism from the beam.

A bake-out jacket is permanently assembled around the valve; it allows to perform a moderate temperature (200 ∞C) bake-out.

A total of 36 all-metal valves are needed for the three superconducting linac sections.

The pumping of the cryostat vacuum chamber is ensured, on each cryomodule, by a 50 l/s turbomolecular pump, connected to a valved port. After leak testing, if the chamber is He-tight, the valve can be closed and the pump can be switched off after the cryomodule has been cooled down. Should a leak be detected, the turbomolecular pump can be kept in continuous operation to keep the pressure in the insulation chamber below 10^{-4} mbar until the leak has been repaired.

2.5.3 - The cryomodule pumping system

As explained above, each cryomodule is terminated at each end by a valve.

In normal operation the valves are opened only when the pressure in the beam pipe has become lower then 10^{-9} mbar, to reduce the amount of condensable gases entering the cryomodule.

A room temperature stainless steel beam pipe connects two adjacent cryomodules; the UHV pumping system is connected to the pipe through a bellow.

The UHV pump is 230 l/s Starcell ion pump that maintains the pressure in the beam pipe at less than 10^{-7} mbar when the RF cavity is at room temperature.

Two other bellows are mounted at the pipe ends - on the beam line - to compensate for manufacturing tolerances and to simplify the beam pipe alignment easier. A proper shielding sleeve with sliding contacts must be provided inside all bellows to keep the vacuum chamber impedance seen by the beam low [46,47].

The beam pipe connecting two cryomodules contains all beam monitors. A focusing quadrupole also fits around it.

Figure 2.5.1 shows the layout of a cryomodule connection assembly.

The total niobium surface exposed to vacuum is about 4 m^2; the overall surface of the stainless steel parts is instead less than 1 m^2. In order to reduce the outgassing a moderate in-situ bake-out (≈ 150 °C) of the beam pipe is foreseen. Thin kapton heaters are mounted on the chamber and fit in the space between the beam pipe and the quadrupole pole faces.

A total of 15 ion pumps are used along the SC linac sections.

Rough pumping of the system and pumping during bake-out operations will be ensured by a mobile station that can be connected to the beam pipe, close to the ion pump, by means of an all metal corner valve. After bake-out, at the start of normal operation of the ion pump the roughing

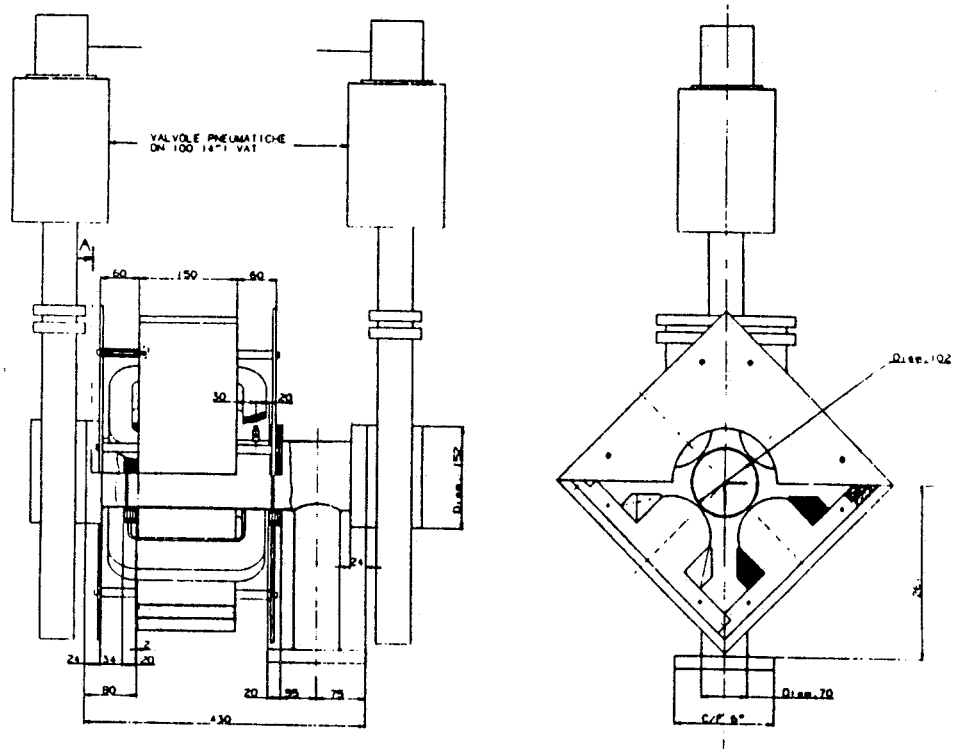

Fig. 2.5.1 - Layout of the connection assembly between two cryomodules of the sections L1 and L2.

system is detached from the beam tube.

In all, three roughing stations are foreseen for all Linac vacuum systems.

The solution is obviously cheaper than providing a fixed roughing pump station at each of the 22 forevacuum ports.

The roughing system must be absolutely free from hydrocarbons to avoid contamination. It consists of a magnetic-bearings turbomolecular pump with dry forevacuum pump or - alternatively - of a refrigerator-cooled cryopump backed by a dry pump.

An ionization gauge is mounted close to the beam tube and connected to the control system, to provide information on the total pressure in the beam line.

Table 2.5.1 - SC Linac Vacuum Components

	Ion pumps	Gate valves	RGA	Ion gauge	Forevacuum ports
Section L1	3	8	3	3	3
Section L2	3	8	3	3	3
Section L3	9	20	9	9	9
Total	15	36	15	15	15

A residual gas analyzer (RGA) is also mounted close to each high vacuum pumping port, between pairs of cryomodules, and provides on-line information on the composition of the residual gas in the beam pipe.

A total of 19 RGAs, controlled through a multiplexed system, are mounted on the SC linac. The information on the residual gas composition is used to diagnose the presence of a leak or of a pump malfunctioning before a permanent degradation of the RF cavity performances can occur.

Table 2.5.1 shows the inventory of the SC linac vacuum components.

2.5.4 - Recirculation beam lines vacuum system

From the point of view of vacuum the recirculation beam line consists mainly of ≈160 m of a 100 mm inner diameter stainless steel tube, vacuum pumps, valves, gauges and forevacuum ports.

Vacuum requirements in the recirculation line, as previously explained, are less stringent than on the SC linac because the line contains no superconducting exposed surface.

To pump-down the recirculation lines, only 25 ion pumps - identical to the ones used in SC linac, ≈10 m away from each other - are therefore sufficient. The estimated mean pressure will be in the 10^{-8} mbar range.

Usual UHV surface cleaning treatments are used in order to reduce stainless steel outgassing [48]. Medium temperature in-situ bake-out (≈ 300 °C) is foreseen.

Forepumping is normally done by connecting one of the mobile pumping stations to one of the 7 valved ports. The presence of 6 all-metal gate valves on the beam line makes it easier to service the vacuum system and to deal with abnormal situations.

22 ionization gauges and 7 RGA's are used for vacuum monitoring and diagnostics.

Table 2.5.2 summarizes the main vacuum components of the whole Linac system.

Table 2.5.2 - Vacuum Component Overall Inventory

	Ion pumps	Gate valves	RGA	Ion gauge	Forevacuum ports
Beam lines	25	6	5	22	7
SC Linacs	15	36	15	15	15
Total	40	42	20	37	22

2.6 - MAGNETS AND POWER SUPPLIES

2.6.1 - Linac Quadrupoles

The quadrupoles in between the s.c. cavities are fully symmetric quadrupoles with an aperture radius of 55 mm. The pole shape is, at this design stage assumed to be circular. The required quadrupolar constants and field gradients depend on the maximum energy of the particles along the Linac; they are given below for two energies.

Emax [GeV]	Length [m]	K^2 [m^{-2}]	Gradient [T/m]
0.1	0.2	2.9	1.0
0.3	0.2	1.6	1.6

The quadrupoles have been optimized for the maximum gradient of 1.6 T/m by means of the 3-D code Magnus. The gradient has been determined by analyzing the field harmonic content over a cylindrical region of radius R_N around the quadrupole axis, inside the aperture. The gradient function along the radius can be expressed in cylindrical coordinates as :

$$G(x) = \Sigma_{n=1,\infty} (n\, r^{n-1}) / (R_N)^n \bullet b_n$$

where n is the harmonic number (n=1, quadrupole; n = 5, dodecapole and so on) of the field component, b_n the corresponding expansion coefficient and r the radial cylindrical coordinate.

The coefficients b_n found by Magnus with R_N = 50 mm are the following:

n	1	5	9	13	17	21
b_n	760	-10.5	2.6	8.3	-10.1	-8.2

Better accuracy will be obtained by proper shaping of the pole tips in the course of the more detailed work still in progress.

Figure 2.6.1 shows the gradient along the radius in the median plane of the quadrupole. Magnus predicts a gradient variation of -0.1 % for x > 17 mm and of -1 % for x > 32 mm.

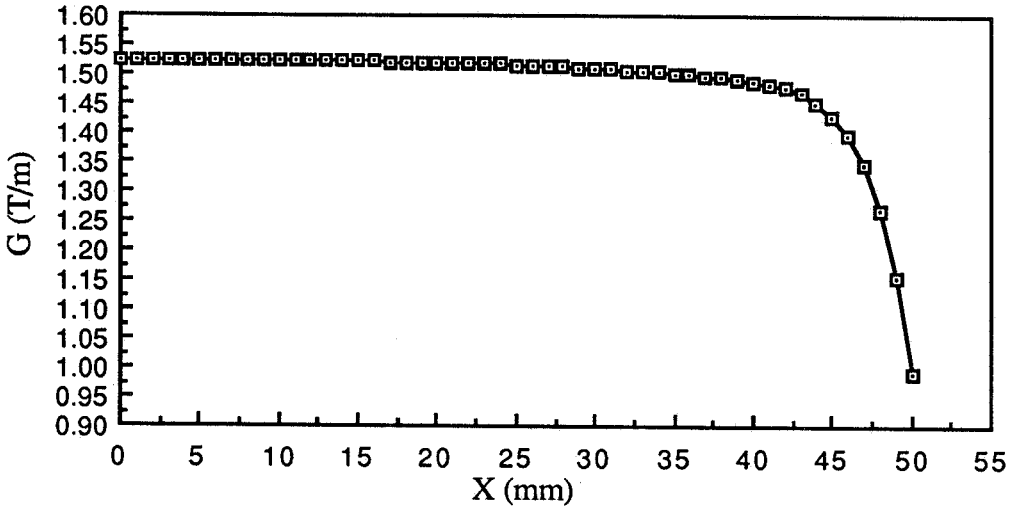

Fig. 2.6.1 - Quadrupole gradient as a function of radial distance from axis.

The magnetic length of the half quadrupole defined as :

$$L_{mag} = \int [\, G(s)/Go \,] \cdot ds \,.$$

has been calculated by integrating over an axis parallel to the quadrupole axis, through a point 5 mm away from the quadrupole center.

Figure 2.6.2 shows the normalized value of G(s) with respect to the value on the central plane.

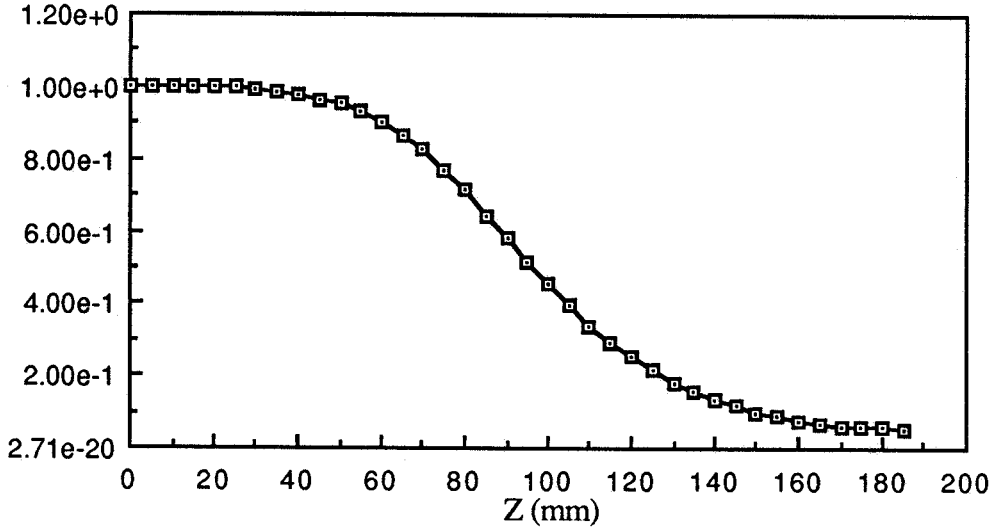

Fig. 2.6.2 - Normalized value of G(s) with respect to the value on the central plane.

The value for ($L_{mag}/2$) obtained by integrating the curve of Fig. 2.6.2 (half length) is 103.6 mm, this means that the mechanical length of the quadrupole must be 142.8 mm instead of the nominal 150 mm to obtain the desired magnetic length of 200 mm.

The same cross-section has been adopted for the two kinds of quadrupole. Corrector windings are provided for dipolar correction of the beam orbit. The quadrupole will be shielded so that the fringe fields can not get to the SC cavities.

The mechanical lay-out of the quadrupole is shown in Fig. 2.6.3.

Table 2.6.1 lists the basic parameters.

Table 2.6.1 - Quadrupole basic parameters

Gradient(maximum)	[T/m]	1.6
Inscribed radius	[mm]	55
Pole field	[T]	0.09
Pole shape		circular
Ampere-turns per pole		2000
Current	[A]	40.8
Current density	[A/mm2]	3.14
Turns per pole		49
Copper conductor		4.5*4.5 Ø 3
Magnetic length	[m]	0.2
Magnet resistance	[mΩ]	200
Power	[W]	341
Voltage	[V]	8.2
Iron weight	[Kg]	73
Copper weight	[Kg]	15,5

The main characteristics of power supplies needed to individually power each quadrupole are the following:

Voltage	[V]	12.5
Current	[A]	50
Stability		$\leq 1 * 10^{-4}$
Ripple (rms)		$\leq 1 * 10^{-4}$
Resolution		$\approx 5 * 10^{-5}$

The reserve voltage necessary to account for voltage drops on connections is included.

Further optimization of the system should include arrangements where magnets can be powered in series so as to simplify the power supplies and the corresponding control circuitry.

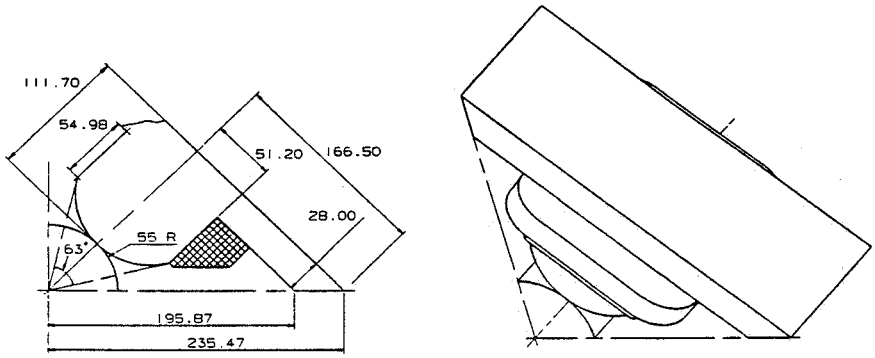

Fig. 2.6.3 - Mechanical layout of the Linac Quadrupole.

2.6.2 - Recirculation arc dipole magnets

With a nominal field of 1.13 T (@ 0.34 GeV) and a maximum field of 1.3 T, the dipoles can be regarded as conventional magnets.

The magnetic circuit has been designed so as not to exceed 1.8 T anywhere in the iron when the gap field is 1.3 T.

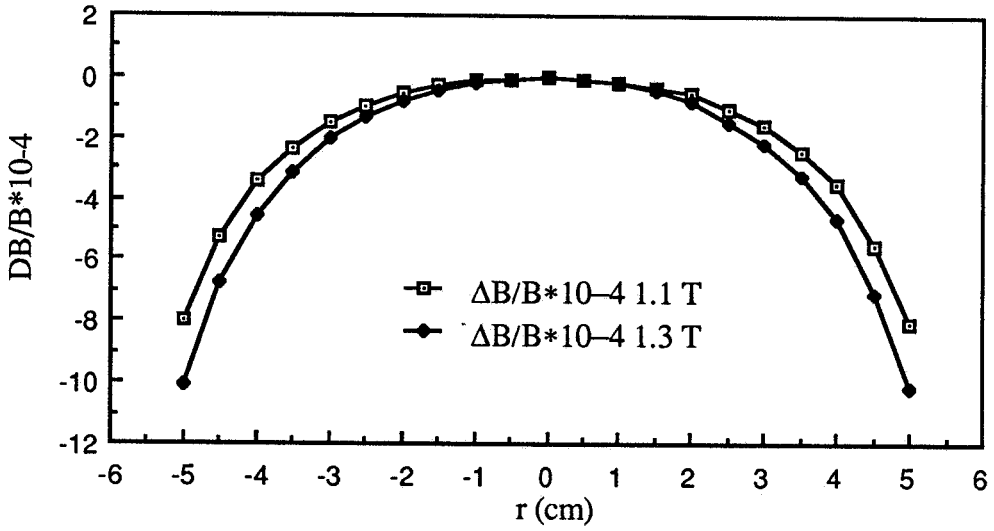

Fig. 2.6.4 - Field profile of the recirculation arc dipoles.

The field profile has been studied by means of POISSON. At the moment the final shimming has not been taken into account. The field quality is already satisfactory at both the nominal and the maximum energy, as can be seen from Fig.2.6.4. and from the following Table 2.6.2.

The laminated magnet yoke is curved to follows the beam radius of curvature and has parallel end faces. A possible technical assembly is shown in Fig. 2.6.5.

Table 2.6.2 - Dipole field quality

	@ x=20 mm	@ x=30 mm
(DB/B) * 10^{-4} @ 1.13 T	-0.57	-1.50
(DB/B) * 10^{-4} @ 1.3 T	0.80	-2.06

The design current density is very close to the one that minimizes the sum of capital and running costs. It is 3.4 A/mm^2 at the nominal field and reaches 3.85 A/mm^2 at 1.3 T.

With the chosen steel dimensions, at maximum field value the iron absorbs about 8.5 % of the applied Ampere-turns.

The dipole main parameters are listed in Table 2.6.3.

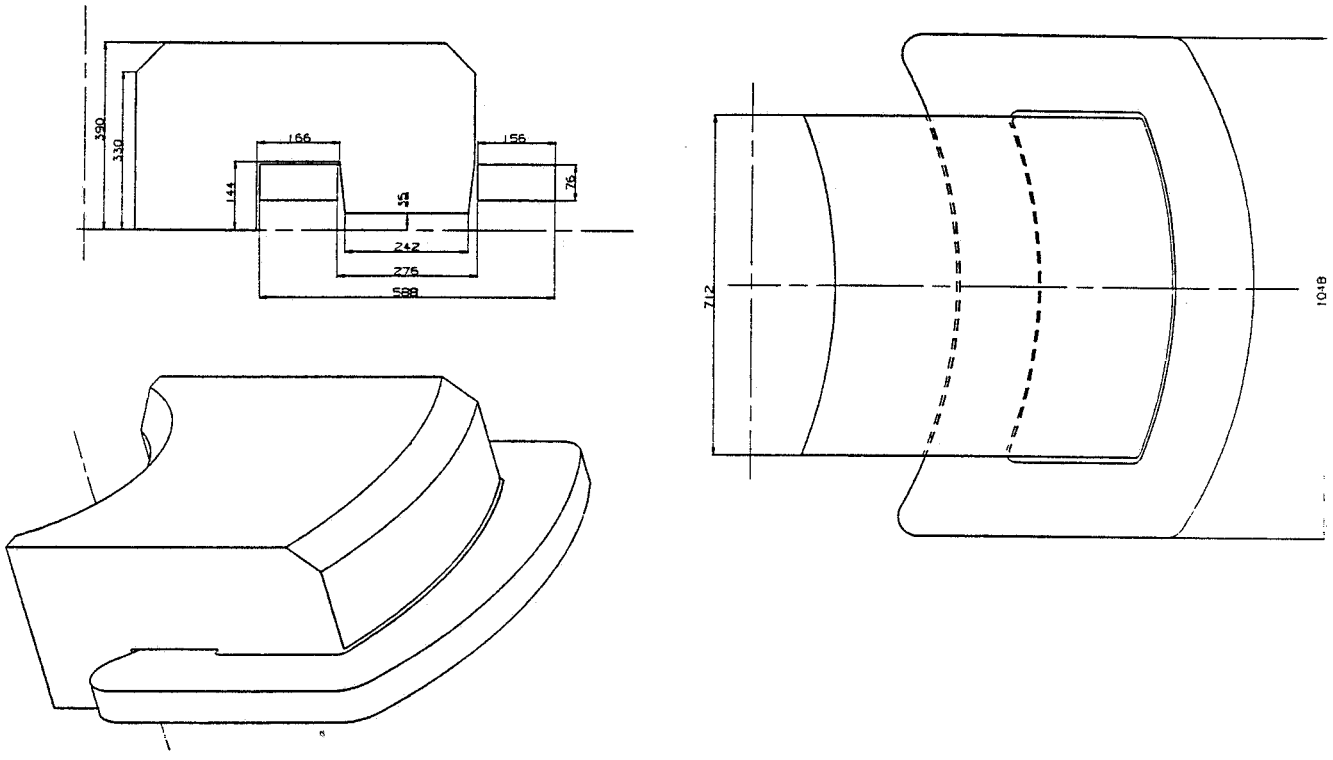

Fig. 2.6.5 - Possible mechanical layout of the Recirculation Arc Dipoles.

Table 2.6.3 - Recirc. Arc Dipole parameter list

Energy	[GeV]	0.34
Bending radius	[m]	1.0
Magnetic length	[m]	0.785
Nominal field	[T]	1.133
Pole/gap ratio		3.8
Return leg/gap ratio		0.92
Gap	[mm]	70
Pole width	[mm]	266/244
Amp.-turns per coil		34,000
Current	[A]	354
Current density	[A/mm2]	3.4
Turns per pole		96
Conductor : Copper		12*12 Ø7
Coil resistance (@ 60° C)	[Ω]	0.051
Coil inductance	0.115	H
Power per dipole	[kW]	12.8
Voltage per dipole	[V]	36
Iron weight	[kg]	2586
Copper weight	[kg]	506
Total weight	[kg]	3092

No attention has been at the moment paid to the longitudinal effective field profile. Work with the three dimensional code Magnus is in progress to determine the mechanical length that will give the required magnetic length.

As concerns power supplies for the dipoles, each recirculation arc (180°) contains four 45° dipoles that can be series connected. The resulting circuit has the following electrical characteristics :

- Circuit resistance (@ 60° C) : 0.204 Ω
- Static circuit inductance : 0.92 H.

and the output voltage and current required of a classical twelve-phase bridge converter, with a 10% allowance for voltage drops on connecting cables, are :

- d.c. Voltage : 160 V
- d.c. Current : 360 A

The main transformer power is ≈ 62 kVA, with a secondary voltage of 115 V and a line current of 170 A.

The current ripple at full current is about $6 * 10^{-5}$. Additional filtering is however foreseen to guarantee a current ripple of less than $1 * 10^{-4}$ down to current levels of ≈ 10% of the maximum value.

The power supply resolution is better than $1 * 10^{-4}$. A long term stability of the same order or better can easily be reached by means of a high stability ($1 * 10^{-6}$) commercial transducer .

2.6.3 - Recirculation arc quadrupoles

The recirculation arc lattice contains 34 quadrupoles, whose characteristics are listed in Reference (49) and summarised in Table 2.6.3..

The magnetic length, 0.3 m, is the same for all quadrupoles. The values of k^2 (and of the gradient G) are very different, ranging from a minimum of 1.08 m^{-2} (G= 1.22 T/m) to a maximum of 13.32 m^{-2} (15.1 T/m).

The quadrupole has been optimized for the average value of k^2, i.e. 6.68 m^{-2} ; the currents are then scaled so as to reach the other gradient values with the same geometry. A single type of quadrupole is thus foreseen at this first-order optimization stage and, consequently, no attempt to simplify the powering scheme has made; these points will have to be reconsidered in the course of further study.

The electromagnetic design has been made using the bi-dimensional code Poisson; two possible solutions, both with hyperbolic pole profiles have been studied. The first fits around a rectangular vacuum chamber with a cross-section of 11(horizontal) * 7 (vertical) cm^2, the second fits around an elliptical vacuum chamber inscribed in the above rectangle. In both cases the pole profile is hyperbolic.

Because of the eight-fold symmetry of the magnet only one-half pole, has been studied.

The magnetic field can be expressed in complex form as :

$$(B_X - i\,B_Y) = i * \sum n *(A_n + i\,B_n)/R * (z/R)^{(n-1)}$$

where B_X and B_Y are the horizontal and vertical components of the field respectively, n is the harmonic number (2 for quadrupole, 6 for 12-pole and so on), A_n and B_n are the coefficients of the expansion, R is a normalization radius and z is the complex variable. The normalization radius is 60 mm for the rectangular vacuum chamber case and 40 mm for the other case.

The field along the x axis can be obtained by simply replacing z by x and taking the first derivative to obtain the field gradient.

In our approximation B_n is identically zero for all n's and A_n takes on the values shown in Table 2.6.4 for the optimized quadrupole at the average gradient. At maximum gradient the scaling factors are 2.3 for the rectangular chamber and 2.37 for the elliptical vacuum chamber. At the lowest gradient the scaling factors become (1/ 5.40) and (1/ 5.43) respectively.

The gradient uniformity for the two quadrupole apertures is shown in Fig. 2.6.6.

Table 2.6.4 - Quadrupole gradient uniformity

n	Rectangular V.Ch $n(A_n)/R$	Elliptical V.Ch. $n(A_n)/R$
2	3955.3	2661.2
6	-136.09	-78.40
10	-88.39	-3.188
14	-19.956	-20.765
18	31.174	8.020

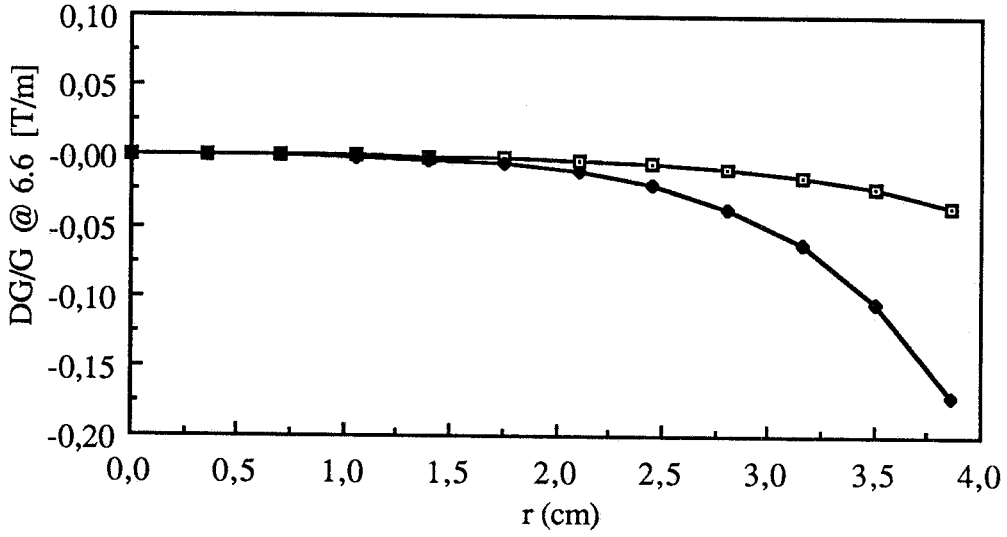

Fig. 2.6.6 - Gradient uniformity of the two quadrupoles

The predicted gradient variation is : -0.1 % @ r=16.3 mm and @ r=11.2 mm respectively and -1% @ r=27.3 mm and r = 20.4 mm respectively.

The maximum value of the field in the iron is always lower than 1.8 T at the highest gradient, well away from saturation.

Correction windings are included in the main coils. They can produce about 10 % of the total Ampere-turns and can be used to generate dipolar fields in both planes.

Table 2.6.5 lists the main parameters of the two kind of the quadrupoles.

Figure 2.6.7 shows the mechanical lay-out of one of the two optimized quadrupoles.

Table 2.6.5 - Main parameters of the two quadrupoles

		Rectangular v.c.	Elliptical v.c.
Gradient (nominal)	[T/m]	6.6	6.6
Inscribed radius	[mm]	62	44
Pole field	[T]	0.435	0.29
Pole shape		Hyperbolic	Hyperbolic
Ampere-turns per pole		10250	5160
Current	[A]	157.5	151.8
Maximum current		454	368
Nominal current density	[A/mm2]	3.55	3.42
Max. current density	[A/mm2]	10.23	8.29
Min. current density	[A/mm2]	0.66	0.63
Turns per pole		65	34
Copper conductor		8*8 Ø 5	8*8 Ø 5
Magnetic length	[m]	0.3	0.3
Magnet resistance	[mΩ]	132	60.
Nominal voltage	[V]	20.8	9.
Maximum voltage	[V]	60	22.
Nominal power	[W]	3300	139
Maximum power	[W]	27240	8170
Iron weight	[Kg]	193	94
Copper weight	[Kg]	116	53

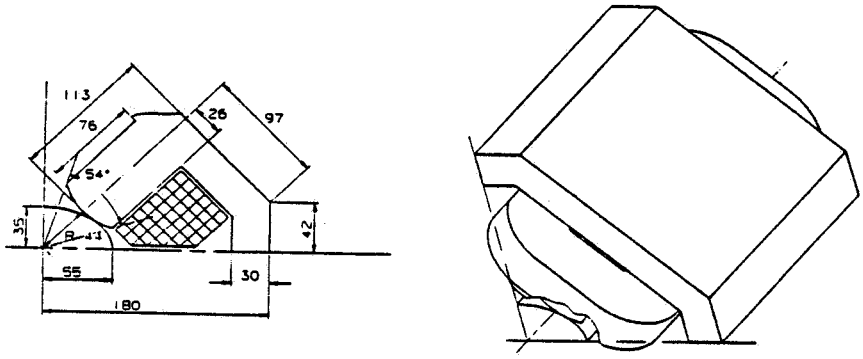

Fig. 2.6.7 - Mechanical layout of one of the two optimized quadrupoles.

References

(1) S.Bartalucci, L.Palumbo, M.Bassetti - Int.Report- LNF-89/051(R)
(2) S. Tazzari - "ARES: Prime Considerazioni Sull' Iniezione" - MEMO ARES 9, Frascati Sept. 1989.
(3) C. Pagani, S. Tazzari - "ARES: Configurazione del Linac SC" - MEMO ARES 12, Frascati October 1989.
(4) S. Kulinski - "Some Remarks on Positron Creation and Acceleration in the Injection System of ARES Φ-Factory" - MEMO ARES 19, Frascati Nov. 1989.
(5) C. Biscari et al. "An Injector for LISA" - Rep. LNF-88/08(R) Frascati 1988.
(6) S. Kulinski, M.Vescovi - "A Gun For LISA" - Rep LNF 87/98(R) Frascati Nov. 1987.
(7) J.S.Fraser, R.L.Sheffield, High-brightness injectors for RF-driven Free-electron lasers, Los Alamos 1987, IEEE Jour. Quan. Electr. Vol. QE-23 No. 9 Sept. 1987 p. 1489/1496.
(8) R.L.Sheffield, High-brightness electron injectors, Proc. of the ICFA workshop on low emittance e-e+ beams, Brookhaven National Laboratory, March 20-25,1987, p. 141-152.
(9) P.E.Oettinger, A selections of high-brightness laser driven cathodes for electron accelerators and FEL's, Proc. of the ICFA workshop on low emittance e-e+ beams, Brookhaven National Laboratory, March 20-25,1987, p. 153-163.
(10) W.A.Barletta, A.M.Sessler, Radiation from fine, intense, self focussed beams at high energy, Proc. of INFN Int. School of Electromagnetic Radiation and Particle Beam Acceleration, Varenna, Italy, June 20-25, 1988, p. 211-220.
(11) G.Vignola, et al., A new method for pumping an optical klystron, Proc. of International Workshop on Coherent and Collective Properties in the Interaction of Relativistic Electrons and Electromagnetic Radiation, Villa Olmo (Co), Italy, September 13-16, 1984, p. 43-46.
(12) J.C.Goldstein, Electron beam requirement for soft X-ray/XUV free electron laser, Proc. of the ICFA workshop on low emittance e-e+ beams, Brookhaven National Laboratory, March 20-25,1987, p. 180-196.
(13) J.M.Peterson, et al., Summary of the working group on design of an a FEL/storage ring for L<1000 A, Proc. of Int. Workshop on Coherent and Collective Properties in the Interaction of Relativistic Electrons and Electromagnetic Radiation, Villa Olmo (Co), Italy, September 13-16, 1984, p. 43-46.
(14) Serafini et al.: INFN Report, 1/90 and LNF Int. Memos ARES 2, 14.
(15) K.T.McDonald, Design of the laser driven Radio-Frequency electron gun for the Brookhaven accelerator test facility, Princeton University, January 17, 1988.
(16) H. Chaloupka, H. Heinrichs, H. Piel, et al, A Proposed Superconducting Photoemission Source of High Brightness, Proc. 1st EPAC, Rome, June 7-11, 1988.
(17) K.J.KIM, Rf and space charge effects in laser-driven electrons guns, Berkeley 1988, Nucl.Instr. and Meth. A275 (1989) 201-218.
(18) P.M.Lapostolle, Possible emittance increase through filamentation due to the space charge in continuous beams, IEEE Trans. Nucl. Sci. vol. NS-18, no. 3, p. 1101-1104, 1971.
(19) J.D.Lawson, The physics of charged-particles beams, Oxford University Press 1977.
(20) Serafini et al., Proc. first EPAC, Rome, Italy, June 1988.
(21) Serafini et al., Proc. of INFN Int. School of Electromagnetic Radiation and Particle Beam Acceleration, Varenna, Italy, June 20-25, 1988, p. 211-220.
(22) T.Weiland, CERN/ISR-TH/80-07, 1980
(23) J. S. Fraser et al., Proc. 1987 Part. Accel. Conf., Washington. DC, March 16-19, 1987.
(24) C. H. Lee et al, Practical Laser Activated Photo-emissive Electron Source, Rev. Sci. Instrum, 56, (4), 1985.
(25) K.Batchelor et al., Development of high brightness electron gun for the ATF at BNL, Proc. 1st EPAC, Rome, June 7-11, 1988.
(26) M. Boussoukaya et al, Pulsed Photocurrents from Lanthanum Hexaboride Cathodes in the ns Regime, Nucl. Instr. and Methods, a 264, 1988.

(27) H.E.Koechner, Solid State Laser Engineering, Springer-Verlag, New York, 1976.
(28) S.L.Shapiro, Ultrashort Light Pulses: Picosecond Techniques and Applications, Springer-Verlag, New York, 1977.
(29) W. Heitler - "The Quantum Theory of Radiation". Oxford 1966.
(30) F. Amman - "Positron Accelerators in Linear Accelerators". Edited by P. Lapostolle , A.L. Septier. North Holland 1970.
(31) U. Amaldi et al. Proc. Courmayer Workshop Dec. 1987 page 78.
(32) G. Stange - "Considerations for the Kicker Magnets Design for the Sincrotrone Trieste" - Trieste July 1989.
(33) H. Piel, Wuppertal University note WUB 87-13, (1987).
(34) C. Benvenuti, N. Cirelli, M. Hauer, W. Weingarten, Proc. 2nd Workshop on RF Superconductivity, H. Lengeler Ed., Geneva, July 23-27, 1984
(35) D. Di Gioacchino, U. Gambardella, P. Gislon, G. Paterno', C. Vaccarezza, INFN note LNF 89/064 (R), (1989)
(36) Proc. Discussion Meeting on SC Linear Accelerators, Frascati, October 1986.
(37) R.Sundelin, "Fully Superconducting Linear Colliders", Proc. Capri Workshop on Linear Colliders, Capri, 13-17 June 1988.
(38) V.Lagomarsino, G.Manuzio, R.Parodi, R.Vaccarone, IEEE Trans. MAG-15, 25 (1979).
(39) C.M.Lyneis, H.A.Schwettman, J.P.Turneaure, Appl. Phys. Lett. 31, 541 (1977).
(40) U.Klein and D.Proch, Proc. of the Conf. on Future Possibilities for Electron Acc., Charlottesville (Virginia), 1979.
(41) L.Serafini, S.Gustafsson, C.Pagani, Proc. 11th Int. Conf. on Cyclotrons and Their Appl., Tokyo, October 1986, Ionics Pub., Tokyo, 370 (1987).
(42) T.Tajima, T.Furuya, T.Suzuki and Y.Iino, "Pre-tuning of TRISTAN Superconducting RF Cavities", Proc. 4th Workshop on RF Soperconduc., KEK, Japan, August 1989.
(43) B.Dwersteg et al. "Superconducting Cavities for HERA", Proc. 3st Workshop on RF Soperconductivity, ANL, Argonne, Illinois, September 1987.
(44) Ph.Bernard et al., "Superconducting RF Cavities for LEP", Proc. 1st European Particle Acc. Conf., Rome, Italy, June 1988.
(45) D.Boussard et al., CERN/EF/RF 88-3, 12 October 1988.
(46) Ph.Bernard et al.,Test of a 352 MHz Superconducting Cavity in the CERN SPS, Proc. European Particle Accelerator Conference, Rome, June 1988, p. 988. World Scientific, Singapore.
(47) "The Vacuum Bellows and the Optimization of their Shielding", LEP Note 568, Sept.1986.
(48) A.G. Mathewson, "The effect of cleaning and other treatments on the vacuum properties of technological materials used in ultra-high vacuum." Proc. 10th Italian Nat. Conf.on Vacuum Science and Technology, Stresa, Italy, Oct. 1987, Il Vuoto.
(49) LNF Internal note Ares-22

3. - THE Φ-FACTORY

3.1. - INTRODUCTION

The main goals of the ARES Φ-Factory are:

- Achievement of 10^{32} $cm^{-2}sec^{-1}$ luminosity at 510 MeV.
- Construction and commissioning in 5-6 years .
- Possibility to investigate the linear-against -circular collision scheme.

The nature of a Φ-Factory in itself dictates a minimum target luminosity of 10^{32} $cm^{-2}sec^{-1}$, and at least a non negligible probability that an improvement factor of the order of 3 can be gradually achieved.

A luminosity of 10^{32} $cm^{-2}sec^{-1}$ has never been reached or even approached in a reliable way on existing machines in the Φ energy range; the system parameters must therefore be carefully researched, chosen and optimized and new solutions must be identified.

On the other hand, the luminosity optimization process itself is uncertain because there is no theory that fully explains the performance limitations of existing storage rings.

Our philosophy has been to make educated guesses on the basis of the available data, models and scaling laws.

Moreover, when one considers the tight time schedule, one concludes that the design should not require more than a limited amount of R&D, and must be flexible enough to allow the key machine parameters to be easily changed to fine-tune the luminosity and to exploit alternative collision schemes.

In agreement with the general criteria described above the design presented here

- is based on conventional technology, and
- has two distinctive features:
  - electrons and positrons circulate in two vertically separated storage rings and collide head-on in a single interaction point ;
  - the ring magnetic lattice is a 4 period modified Chasman-Green type with a 1.9 Tesla conventional wiggler magnet inside the achromat. This last choice allows ample emittance tunability and at the same time gives strong radiation damping, one of the fundamental properties that lead to high luminosity.

In case even more damping should prove to be necessary, it can be produced by inserting additional wiggler magnets.

3.2. - DESIGN CRITERIA

3.2.1 - Basic formulae

The single bunch luminosity for an electron-positron storage ring collider is given by the well known formula :

$$L = \frac{f\, N^2}{4\, \pi\, \sigma_x\, \sigma_y} \qquad (3.1)$$

where f is the revolution or collision frequency, N is the number of electrons and positrons (assumed to be the same) and σ_x and σ_y are the horizontal and vertical r.m.s. beam sizes at the interaction point, IP.

During a collision the two bunches focus each other causing a tune shift ΔQ. An appropriate indicator of the focusing force, in a linear approximation, is the tune shift parameter ξ given by

$$\xi_{x,y} = \frac{r_e\, N\, \beta_{x,y}}{2\, \pi\, \gamma\, \sigma_{x,y}\, (\sigma_x + \sigma_y)} \qquad (3.2)$$

where γ is the electron energy in units of its rest mass, r_e the classical electron radius, $\beta_{x,y}$ the value of the horizontal (vertical) betatron function at the IP. For all practical cases :

$$\xi \sim \Delta Q. \qquad (3.3)$$

For a given beam current, ξ is usually different in the horizontal and vertical planes ($\xi_x << \xi_y$). However, in order to achieve the maximum luminosity, it is convenient to have

$$\xi = \xi_x = \xi_y \qquad (3.4)$$

This condition can be satisfied by choosing

$$\kappa = \frac{\varepsilon_y}{\varepsilon_x} = \frac{\beta_y}{\beta_x} = \frac{\sigma_y}{\sigma_x} \qquad (3.5)$$

where κ is the coupling coefficient [1] that can take on any value between 0 and 1. By putting equations (3.2), (3.4), (3.5) together, luminosity and ξ can be rewritten as:

$$L = \pi \left(\frac{\gamma}{r_e}\right)^2 \frac{\xi^2\, f\, \varepsilon\, (1 + \kappa)}{\beta_y} \qquad (3.6)$$

or equivalently

$$L = \pi \left(\frac{\gamma}{r_e}\right)^2 \frac{\xi^2\, f\, \varepsilon\, (1 + \kappa)}{\kappa \beta_x} \qquad (3.7)$$

and

$$\xi = \frac{r_e}{2\pi\gamma} \frac{N}{\varepsilon} \qquad (3.8)$$

Eqs. (3.6) and (3.7) show the interrelation between the luminosity, κ, β_y and β_x . To gain in luminosity, for example, it is not sufficient to assume a small β_y, but it is also necessary to reduce either β_x or the coupling coefficient according to (3.5).

Equations (3.6) and (3.7) also remark, from the quadratic dependence of luminosity on ξ, the leading parameter role of the linear tune shift in collider design.

ξ is generally assumed to depend quadratically on the number of crossings per turn, n_i, namely :

$$\xi \propto \frac{1}{\sqrt{n_i}} \qquad (3.9)$$

n_i is usually equal to twice the number of bunches in one beam.

If one tries to increase the luminosity by increasing n_i , and therefore the collision frequency f, ξ decreases according to eq. (3.9) and defeats the purpose (insofar as 3.9 is exact), as can be seen from eq. (3.6) or (3.7) . This is the reason why electrostatic separating plates are used to reduce n_i while mantaining the same frequency of crossings (see for example CESR[2] where n_i is reduced from 14 to 2 by an electrostatic separation system producing a pretzel like orbit deformation) .

The maximum attainable ξ value can not be computed from theory. Experimentally, however, the maximum value for ξ (in the case of two interactions per turn), averaged over most of the existing electron colliders, is remarkably constant at :

$$< \xi^{max} > = \ .038 \pm .013 \qquad (3.10)$$

As shown by eq. (3.8), equation (3.10) sets an empirical limit on the ratio between the number of particles N and the beam emittance ε, i.e. a limit on the transverse beam density. Therefore, as ε and N can not be indefinitely increased because of aperture and instability limits, eq. (3.10) sets a limit on the luminosity.

3.2.2 - Collision frequency

From the luminosity point of view one would like the collision frequency to be as high as possible or, equivalently, the storage ring footprint to be as compact as possible.

Ultra-compact rings on the other hand require the use of superconductive dipoles, a feature we do not deem desirable for the machine under design for reasons we try to explain in the following.

Straight superconducting magnets are used in large high energy proton accelerators, whether existing (Tevatron, HERA, etc) or planned (HLC, SSC, RHIC), with very large bending radius.

For a Φ-Factory however the bending radius would be extremely small ($\rho << 1$ m) and one would have to face the engineering problems connected with the design of such 'curved' dipoles, the strong non linearities coming from the small bending radius and the large synchrotron radiation power in a superconducting environment.

While therefore it is true that small superconducting machines are being developed for industrial applications and have also been proposed [3,4] for Φ-factories, the adoption of such a technology is in our opinion more appropriate for an R&D program than for a time-pressed project.

Moreover, we maintain that the gain in collision frequency is not substantial because the ring size will eventually be dominated by the need for space to accomodate the low-β insertion and the experimental apparatus.

In conclusion the most efficient way of increasing the collision frequency is multibunch operation.

In multibunch operation one has of course, according to eq.(3.9), to avoid parasitic collisions that lower the tolerable tune shift parameter ξ . One has the choice of either design complicated separation schemes or store the beams in two (horizontally or vertically) separated rings and collide them head-on in a single interaction point.

We propose to build two vertically separated rings because, for several practical reasons, the gain in collision frequency is greater for the two-ring scheme; the gain factor is $\sqrt{2}$ on $\sqrt{n_i}$ and, consequently, on ξ . We choose the vertical solution because less expensive than the horizontal one from the conventional constructions point of view.

Experience with DORIS[5] has shown that the crossing angle should be as close to zero as possible, and that any residual error crossing angle has to be canceled by accurately monitoring and correcting the orbits.

On the 'minus' side it should also be mentioned that multibunch operation is prone to multibunch instabilities, that have to be carefully suppressed, and it is at risk of ion trapping unless proper, nontrivial countermeasures are taken.

If L_b is the spatial separation between two consecutive bunches and we assume to fill uniformely all the ring circumference, the collision frequency becomes

$$f = \frac{c}{L_b}$$

Our design choice is :

$$\boxed{f = \frac{500}{7} = 71.4 \text{ MHz}, \quad \text{giving} \quad L_b = 4.2 \text{ m}.}$$

The first unwanted crossing would occur at a distance $L_b/2$ from the IP, and the electrostatic separation system must therefore provide a vertical beam separation [6] $\Delta Y > 2\,\sigma_x$ at a distance of 2.1 m from the IP. This distance is not very large but, in our opinion, due to the relatively low energy, a suitable separation scheme can be designed.

3.2.3 - Vertical β-function at the IP

The luminosity increases linearly with the inverse of β_y at the IP. To take full advantage of this dependence, one has to be ready to pay a price in terms of RF system voltage, ring impedance and, because also the r.m.s longitudinal bunch length must be small, of single bunch instabilities. In fact, an empirical rule states that

$$\sigma_z \leq \sim \frac{\beta_y}{1.5}$$

in order to avoid geometrical luminosity reductions.

In addition, the Liouville theorem prescribes that to a very small β_y at the IP there must correspond a large beam divergence; the latter has to be corrected locally, as close as possible to the IP, or the necessary machine acceptance will become too large.

In practice, one is forced to put a very strong quadrupole close to the interaction point that will necessarily limit the solid angle available for the experiment.

This kind of limitation, common to all the low-β schemes, is particularly severe in the case of a Φ-Factory; it imposes a coordinated design of the low-β insertion and the experimental apparatus.

The beam divergence correcting quadrupole also has the effect of raising the machine chromaticity that has to be corrected by the addition of strong sextupoles; the dynamic aperture is consequently reduced.

In conclusion, the value of β_y can not be arbitrarily small; a reasonable choice for the design value turns out to be :

$$\beta_y = 4.5 \text{ cm} \qquad \text{with} \qquad \sigma_z = 3.0 \text{ cm}.$$

The low-β insertion will be designed with a wide range of tunability around this value. Lower values of β_y, such as those claimed by other designs, could therefore be attempted once the machine behaviour has been fully understood, providing an upgrade potential for luminosity.

3.2.4 - Coupling coefficient

The coupling coefficient design value has been chosen to be :

$$\kappa = .01$$

this choice, apparently in contrast with the main goal of maximizing the luminosity (see Eq. 3.6), will be justified in § 3.2.7. We add here a few practical considerations.

From eq. (3.5) we deduce that, with $\kappa = .01$:

$$\beta_x = 100 \cdot \beta_y = 4.5 \text{ m}$$

To achieve such very low value of the coupling coefficient is however not easy; the orbit has to be measured and corrected very precisely, and the vertical dispersion function has to be carefully minimized, especially because of the vertical beam separation scheme. The Touschek effect, limiting the useful lifetime, also becomes of paramount importance. In our case we compute a Touschek lifetime ~ 4 hrs.

The problems are nevertheless solvable; many storage rings in operation have obtained κ values less than 1%. In particular, the Brookhaven 750 MeV VUV ring has reached $\kappa = 0.0017$, after careful machine alignment and after spending one day to correct the residual closed orbit to the desired precision (7).

Alternative solutions, with lower emittance or smaller β_y (small σ_z), would no doubt require stronger coupling to reach an acceptable lifetime.

A potential advantage of the low coupling is the reduction of ion trapping at least when the design dynamic vacuum of ~ 10^{-9} torr is assumed.

3.2.5 - Design emittance

The emittance ε affects the luminosity linearly but cannot be made arbitrarily large; the limit is given by the machine physical and dynamic apertures necessary for a reasonable beam lifetime. Very large emittance also implies that the number of particles, N, necessary to achieve a large ξ is very large (see 3.8).

All considered, a reasonable choice for ε is :

$$\varepsilon = 10^{-6} \text{ m·rad}$$

but, as for the case of β_y , the storage ring is designed to allow a wide range of tunability and consequently has some potential for improvement. The upper emittance limit is essentially determined by aperture requirements, while the lower one is in the 10^{-9} m·rad range.

3.2.6 - The linear tune shift parameter ξ

The linear tune shift ξ, appearing squared in the luminosity formula, plays the most important role and, because of (3.10), is the fundamental, not yet fully understood limiting factor (see also § 3.2.7).

A sensible choice is to estimate the luminosity value on the basis of the experimental average ξ^{max} given by (3.10), namely :

$$\xi^{max} \approx .04$$

By this choice we also implicitly fix the number of particles per bunch, N : by substituting the values of ε and ξ into (3.8) we obtain:

$$N = 8.9\ 10^{10} \text{ particles/bunch}$$

and the resulting average current in each beam is :

$$\langle i \rangle = e f N = 1.02 \text{ A}$$

This is an unusually high current value that will require a careful design of the RF and the vacuum systems. Let us however point out that similar current values have been reached at storage rings now in operation : as an example, a current in excess of 1.3 Amp has been accumulated in the BNL VUV ring [7] that runs routinely with stored currents of .8÷.9 Amp.

3.2.7 - Luminosity scaling laws

As often mentioned above, there is no exhaustive explanation of the luminosity limit.

Among existing phenomenological models we have singled out the work by J.Seeman [8] and by M.Bassetti [9], because the former is in reasonable agreement with the ξ^{max} experimental data from several machines, while the latter introduces something new in the direction of a better understanding the luminosity limits. In the following we briefly summarize their results.

Let us first recall the definition of the synchrotron integrals I_2 an I_3 [10]:

$$\int_{Dip} \frac{ds}{\rho^2} \quad ; \quad \int_{Dip} \frac{ds}{|\rho^3|} \qquad (3.11)$$

For an isomagnetic machine with a bending radius ρ, the integrals over one turn are given by:

$$I_2 = \frac{2\pi}{\rho} \quad ; \quad I_3 = \frac{2\pi}{\rho^2} \qquad (3.12)$$

U_o[10] and σ_R[9], the radiation energy loss per turn and the r.m.s. quantum fluctuation per turn respectively, can be expressed through (3.11) as follows:

$$U_{o\,(KeV)} \sim 14.1\, E^4_{(GeV)}\; I_{2\,(m^{-1})} \qquad (3.13)$$

$$\sigma_{R\,(KeV)} \sim 6.5\;\; E^{3.5}_{(GeV)}\; \sqrt{I_{3\,(m^{-2})}} \qquad (3.14)$$

J.Seeman has reviewed, in a very exhaustive paper [8], the data on beam-beam interaction obtained at most of the existing e+e- storage rings; he shows that by empirically fitting the dependence of the linear tune-shift ξ on the various relevant parameters he can explain them all rather well. His best fit shows that the maximum vertical linear tune shift (at the maximum luminosity) divided by the beam energy, increases with the square root of $1/(n_i\rho)$, where n_i is the number of crossings per turn and ρ is the bending radius. This can be expressed as:

$$\left(\frac{\xi_y}{\gamma}\right)^{max} \sim 1.4\;10^{-5}\sqrt{\frac{I_{2\,(m^{-1})}}{n_i}} = \text{const}\,\sqrt{\frac{1}{\rho\, n_i}} \qquad (3.15)$$

By substituting eq. (3.15) into (3.6) we have a first luminosity scaling law:

$$L^{max} \propto \gamma^6\, I_2 \qquad \text{(Seeman's law)}$$

The open question is if one is allowed to extrapolate the experimental fit (3.15) to the case of a very small bending radius (large U_0); the Novosibirsk Φ-Factory design by Barkov et al.[3] featuring a very small bending radius (ρ = 28cm with 6 Tesla s.c. dipoles), claims a ξ^{max} of $\approx$ .07 in both planes, not far from the value one would calculate from (3.15).

Using the conservative value ξ^{max} = .04 discussed under § 3.2.6 and considering that we have only one crossing point, we obtain from (3.6) and (3.15) the minimum acceptable value of I_2:

$$I_2^{\,min} \sim 11\ m^{-1} \qquad \text{(Seeman's criterion)}$$

or, equivalently through (3.13), the minimum acceptable value of the radiated energy:

$$U_0^{\,min} \sim 10.5\ \text{KeV}.$$

In a recent study [9] M. Bassetti suggests that a <u>further luminosity limitation</u> comes from the perturbation of the radiative damping mechanism by the beam-beam interaction. In fact the maximum energy, ΔE_{bb} , lost or gained by a particle working against the electric field of the opposite beam must - according to his model - be lower than the average quantum fluctuation, σ_R ,of the synchrotron radiation between two interactions, in order for the machine to behave properly. According to his formalism ΔE_{bb} is given by:

$$\Delta E_{bb\ (KeV)} \sim 3.58\ 10^3\ r_e\ F\left(\frac{\sigma_y}{\sigma_x}\right)\frac{N}{\beta_y} \qquad (3.16)$$

where F is a form factor shown in Fig. 3.1 that depends strongly on the ratio $\kappa = \frac{\sigma_y}{\sigma_x}$.

By analising the behaviour of existing storage rings, it is found that at maximum luminosity many storage rings have :

$$\sigma_R \geq 9\ \Delta E_{bb} \qquad (3.17)$$

The coefficient has been derived empirically and will require further studies with numerical simulations and experimental check. Eq. (3.17) implies a limitation on the maximum N, independently from the transverse beam density. By using (3.17), according to Bassetti, we can write a luminosity scaling law :

$$L^{max} \propto \gamma^5 \sqrt{I_3} \qquad \text{(Bassetti's law)}$$

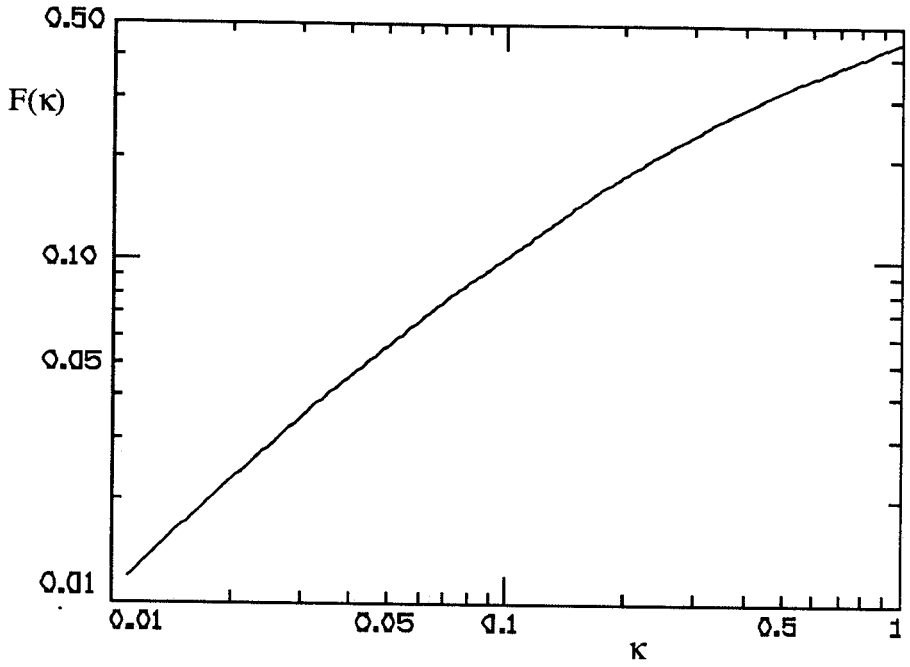

Fig. 3.1 - The form factor F as a function of the ratio $\kappa = \sigma_y/\sigma_x$.

To follow prescription (3.17) while keeping the required value of I_3 manageable, one is forced to choose (see Fig. 3.1) the very small value for the coupling coefficient, $\kappa = .01$, already mentioned in § 3.2.4 . With this value, I_3^{min} computed from eqs. (3.6) and (3.17) is equal to :

$$I_3^{min} = 12.1 \ m^{-2} \qquad \text{(Bassetti's criterion)}$$

(With $\kappa = .10$ the corresponding value for I_3^{min} would have been $\sim 900 \ m^{-2}$!).

Let us point out that, by incorporating the Seeman's and Bassetti's criteria in our design, we are making a conservative luminosity estimate. We also proposed to verify the range of validity of the two models on ADONE [11] before the Φ-Factory parameters are frozen.

3.2.8 - Conclusions

The parameters so far discussed are summarized in Table 3.1. We also summarize, as a conclusion, our basic design philosophy.

TABLE 3.1 - Design Parameters

Luminosity	(cm^{-2} sec^{-1})	10^{32}	Bunch separation	(m)	4.2
Emittance	(m-rad)	10^{-6}	N^{er} of particles/bunch		8.9 10^{10}
κ		.01	Bunch peak current	(Amp)	57
ξ_y		.04	Total average curr.	(Amp)	1.02
ξ_x		.04	I_2^{min}	(m^{-1})	11
β_y	(m)	.045	I_3^{min}	(m^{-2})	12
β_x	(m)	4.5	σ_R	(KeV)	2.0
Bunch length σ_z	(m)	.03	ΔE_{bb}	(KeV)	.22
Collision frequency	(MHz)	71.4	U_o	(KeV)	10.5

For the ARES Φ-Factory we envisage a two stage project : the PHASE I Factory will be entirely based on very conventional technology, and is supposed to reach the specified design luminosity. The design however affords enough flexibility so that any further modification that may prove necessary or desirable to upgrade the machine performance can be incorporated during PHASE II, dedicated to the upgrade of luminosity and to the implementation of alternative collision schemes.

This scheme minimizes the technical risks and we believe that, after a commissioning period of 4÷ 5 months, the design current can be reached in both rings. At the end of the first year of operation, the luminosity target of 10^{32} $cm^{-2}sec^{-1}$ should have been reached by fine-tuning all other machine parameters (ε, κ, β_y etc.).

3.3. - BEAM OPTICS

3.3.1 - Low-β insertion

The low-β insertion and the vertical separation system are the most crucial parts of the Φ-Factory design, because of the constraints imposed by the experimental apparatus and by the relatively short bunch-to-bunch longitudinal distance L_b.

The experimental apparatus, not yet completely defined, has of course to cover the largest possible solid angle; a solenoidal field of $\approx .5 \div 1.$ kG over a length of approximately 5 meters on each side of the IP is also required. The beam trajectory will be actively shielded from solenoidal field, with the exception of $\pm$ 0.5 m around the IP, where the vacuum chamber wall must be very thin and no active or passive shield can be used.

The details of of the residual field compensation and of the resulting shielding arrangement are still under study and only a general feasibility study is therefore presented.

The most serious constraint posed by the experimental apparatus on the design of the low-β insertion is the requirement of a large unencumbered solid angle around the IP. A tentative agreement has been reached with the users on a low-β insertion confined to a cone of half-aperture angle $\theta = 8.5^o$, over a length of $\pm$ 5 m from the IP. The distance of the first quadrupole from the IP is $\geq$ 45 cm and the quadrupole maximum outer diameter $Ø_Q$ is given by:

$$Ø_Q = 2 \cdot \tan(8.5^o) \cdot 45 \text{ cm} = 13.45 \text{ cm}$$

It is important, because of the low κ value chosen, to suppress the vertical dispersion function D_y locally . Moreover the beam separation system has to satisfy the condition:

$$\Delta Y > 2\,\sigma_x$$

at the first unwanted collision point ($L_b/2$) as well as at the second one (L_b).

The relevant lattice design parameters are as follows:

$\beta_y = 4.5$ cm $\beta_x = 4.5$ m $\kappa = .01$ $\varepsilon = 10^{-6}$ m·rad $L_b = 4.2$ m

Starting from the IP, there is a first lattice region, inside the detector, where two electrostatic separators, VS1 and VS2, begin to gradually separate the beams. The separators are schematized as vertical magnets with a bending radius given by

$$\rho_E \text{ (m)} \sim \frac{.511\ \gamma}{E \text{ (MV/m)}}$$

where $E = V / d$ is the electric field value , V the voltage and d the distance between the plates. We assume :

$$\rho_E = 200 \text{ m}, \qquad V = 100 \text{ KV}, \qquad d = 4 \text{ cm}$$

to obtain :

$$E \approx 2.5 \text{ MVolt / m}$$

The β-functions in the region from the IP to the second unwanted crossing are shown in Fig. 3.2; the resulting half-separation Y and the horizontal beam size σ_x are plotted in Fig.3.3

By inspecting Fig. 3.3 we can see that the criterion $\Delta Y > 2\,\sigma_x$ is satisfied.

Let us point out that the first quadrupole, QF1, is rather weak and focussing in the horizontal plane. This provides better control over the β functions along the rest of the insertion.

The mechanical design of the first two quadrupoles, QF1 and QD1, whose maximum allowable outer diameters are

$$\text{Ø}_{QF1} = 13.45 \text{ cm} \qquad \text{Ø}_{QD1} = 20.92 \text{ cm}$$

is still under study; at the moment the most likely solution for QF1 foresees the use of permanent magnets.

In the second region, near the edge of the detector, we increase the vertical separation with two thin septum magnets VB1 and VB2 . Two additional vertical magnets VB3 and VB4, of opposite sign, take the beam horizontally to the following dispersion suppressor region. The dispersion suppressor consist of three 120° FODO cells with missing magnets.

The β-functions in the region in between the IP and VB4 are plotted in Fig. 3.4 ; the vertical dispersion D_y is shown in Fig. 3.5 .

Fig.3.6 shows the vertical half separation, Y, along the low-β insertion.

Finally the low-β insertion is connected to the main arcs by a matching section consisting of four quadrupoles.

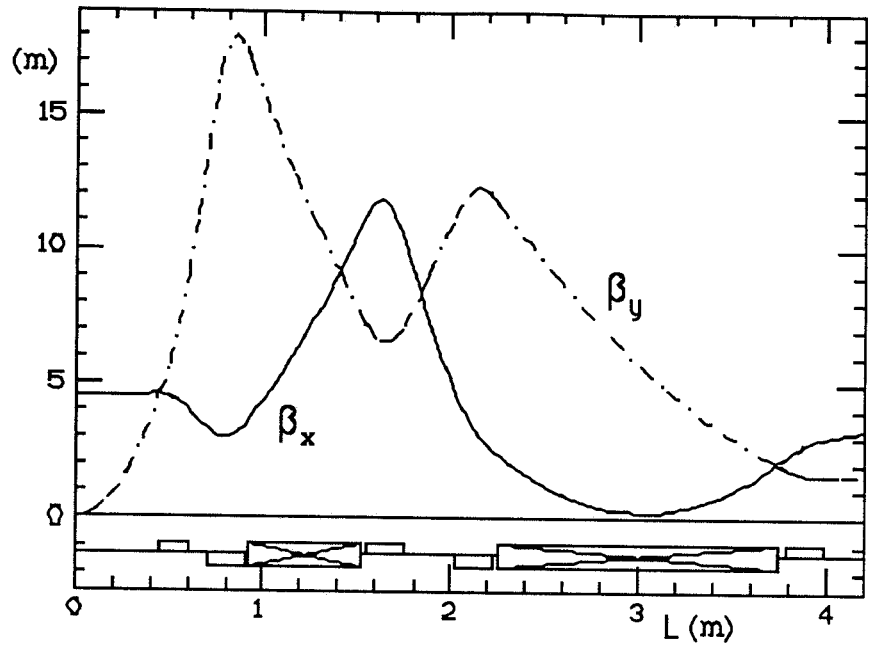

Fig. 3.2 - β-functions from the IP to the 2nd parasitic crossing point.

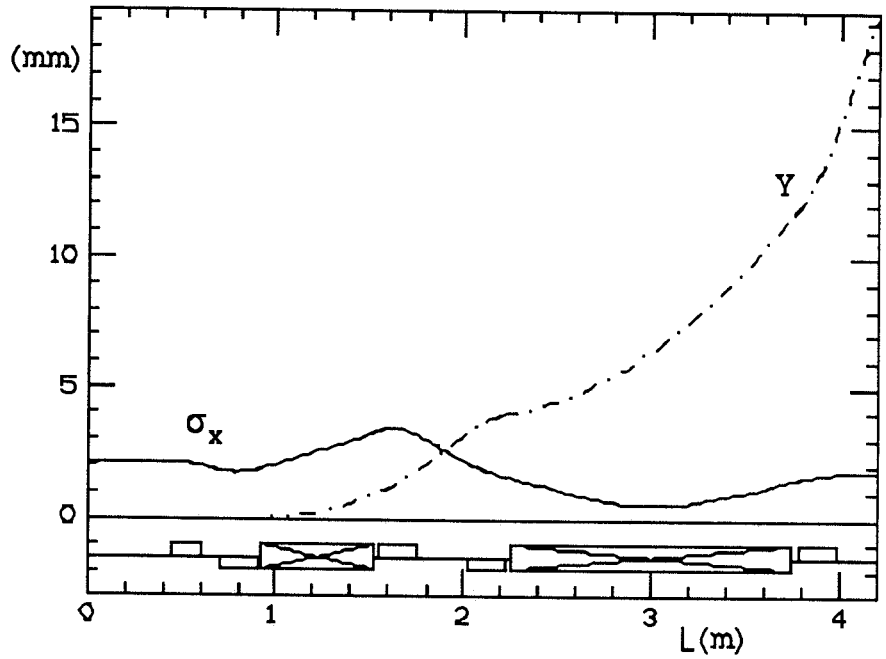

Fig. 3.3 - Half-separation Y and horizontal beam size σ_x from the IP to the 2nd parasitic crossing.

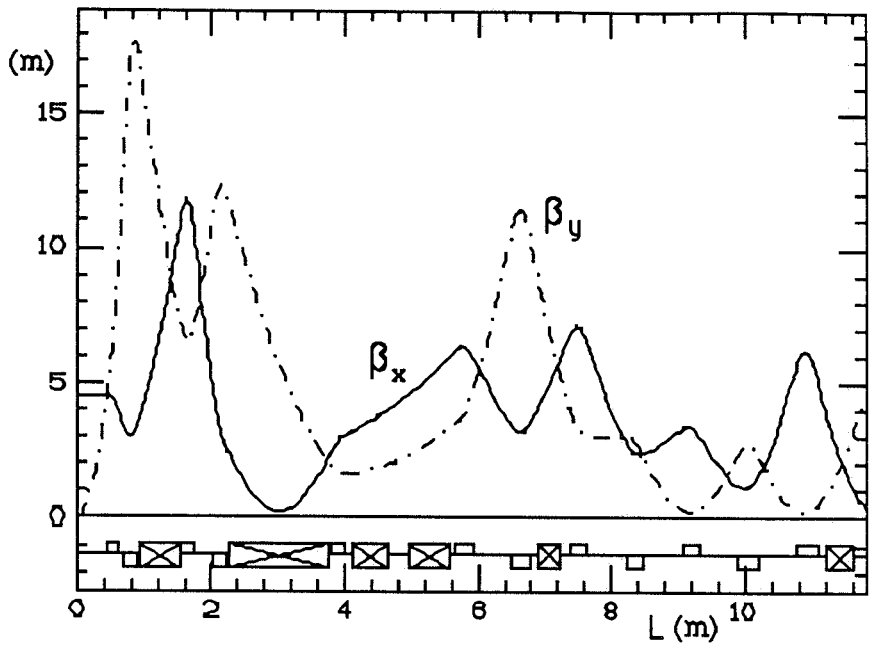

Fig. 3.4 - β-functions in between the IP and the last vertical magnet, VB4.

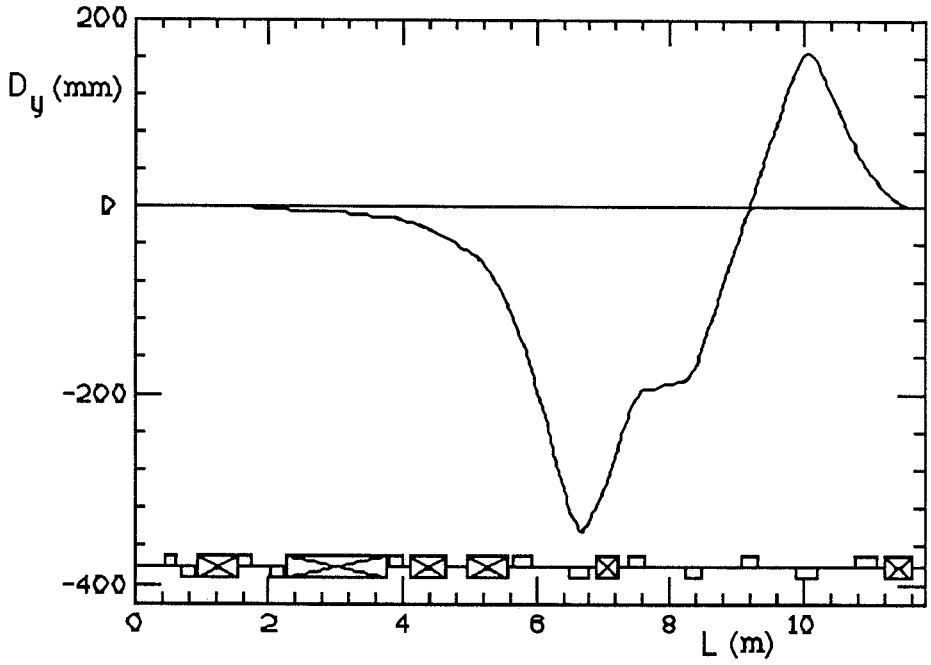

Fig. 3.5 - Vertical dispersion function along the low-β insertion.

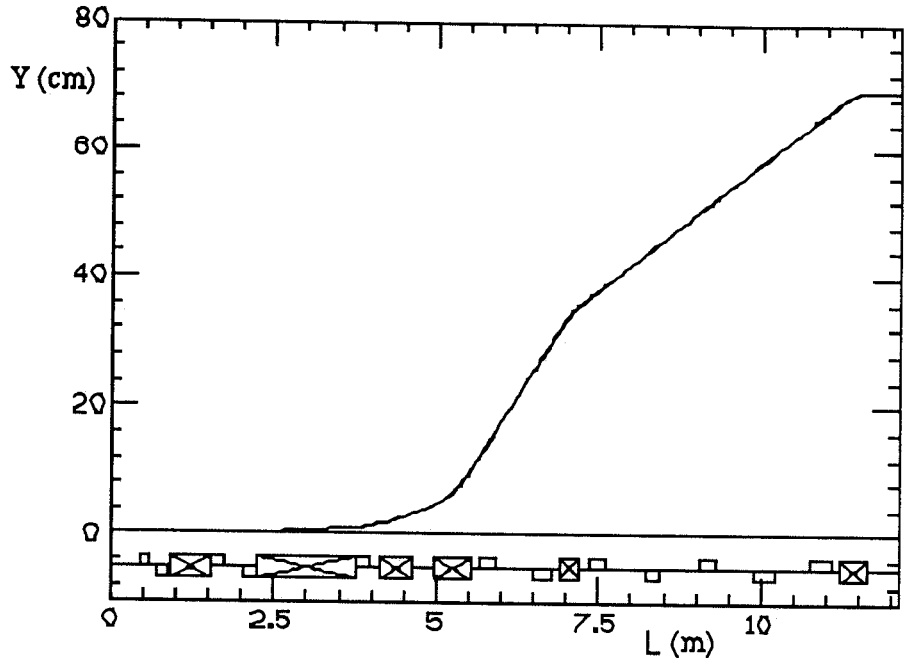

Fig. 3.6 - Half-separation Y along the low-β insertion.

From Fig.3.6 it can be seen that the total vertical separation H between the two storage ring orbits, outside the low-β insertion, cannot be less than

$$H = 1.391 \text{ m}$$

The total length of the insertion is ~ 30 m and it can not be reduced without compromising the lattice flexibility and increasing its chromaticity.

Let us point out that the design leaves room for a raising the collision frequency, and consequently in the luminosity, by $\approx 20\%$ because :

- VS1 and VS2 can probably be operated at higher electric field
- the separation criterion, $\Delta Y > 2\,\sigma_x$ is probably too conservative.

3.3.2 - Storage rings

The storage ring lattice is a four-period modified Chasman-Green[12] type. This kind of lattice is commonly used for low emittance, high periodicity machines and its main limitation then comes from the chromaticity correction wich, because of the small value of the dispersion function, requires strong sextupoles and consequently produces rather small dynamic apertures. In our case this is however not a serious problem because the periodicity is only 4, the lattice is detuned and the dispersion is therefore comparatively high.

To increase the radiated energy per turn, a 1.5 m long, 1.9 T normal-conducting wiggler is incorporated into each achromat. Because the wiggler is in a high dispersion region a rather large emittance of 10^{-6} m-rad is obtained. To emittance value can be adjusted by tuning the dispersion function in the wiggler region by through a D-type Q-pole that is also part of the achromat.

The optical functions , for a four-fold symmetric ring, are shown in Fig. 3.7.

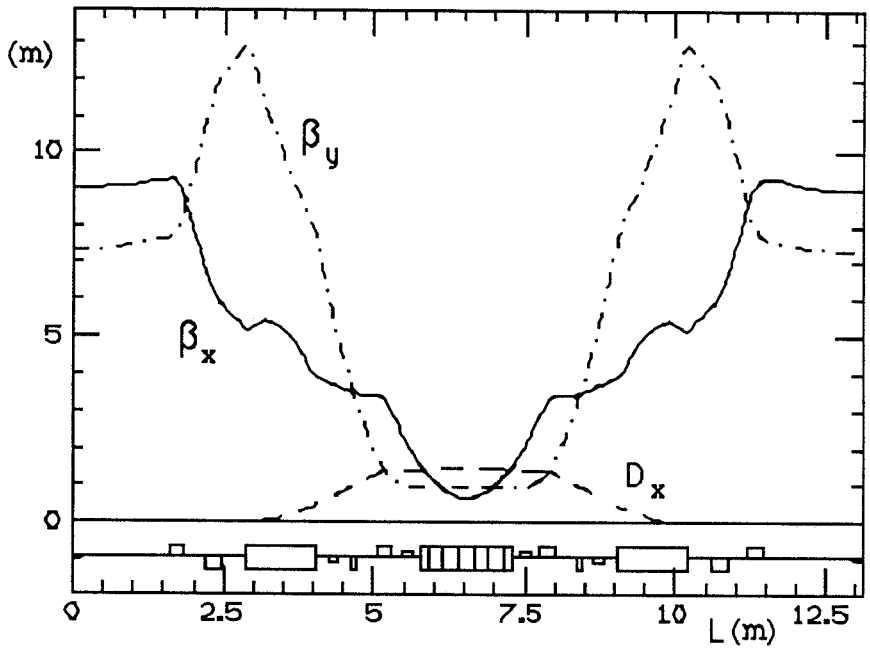

Fig. 3.7 - Main arc optical functions.

Normal conducting wigglers are used to avoid the strong field non linearities created by short bending radius superconducting devices. According to our experience it is instead rather easytask to achieve a very good field quality in a normal wiggler, by making the poles wide enough and by shimming.

In Fig. 3.8 we plot the optical functions over one half the ring, including the low-β insertion; the half-ring layout is shown in Fig. 3.9.

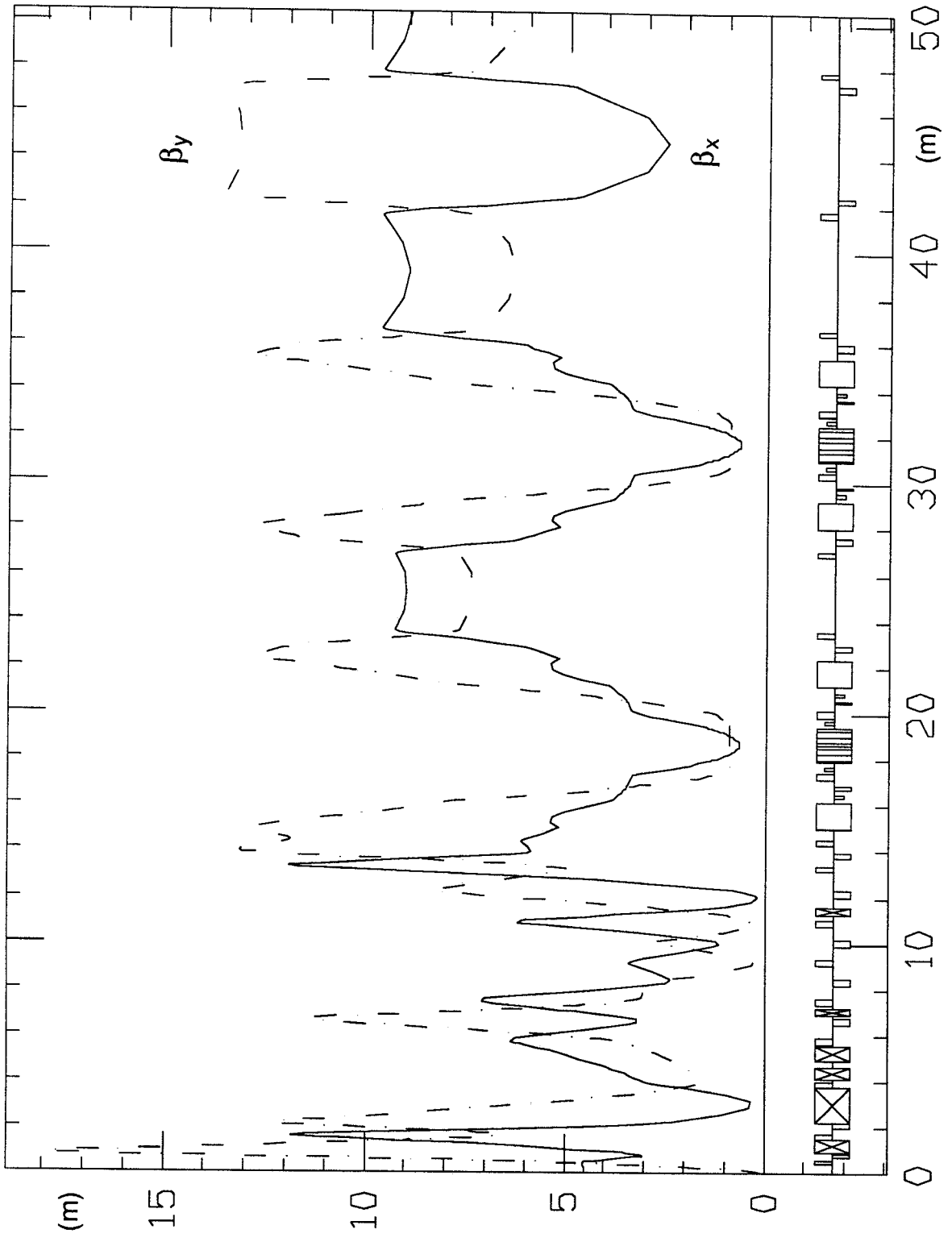

Fig. 3.8 - Optical functions for half ring.

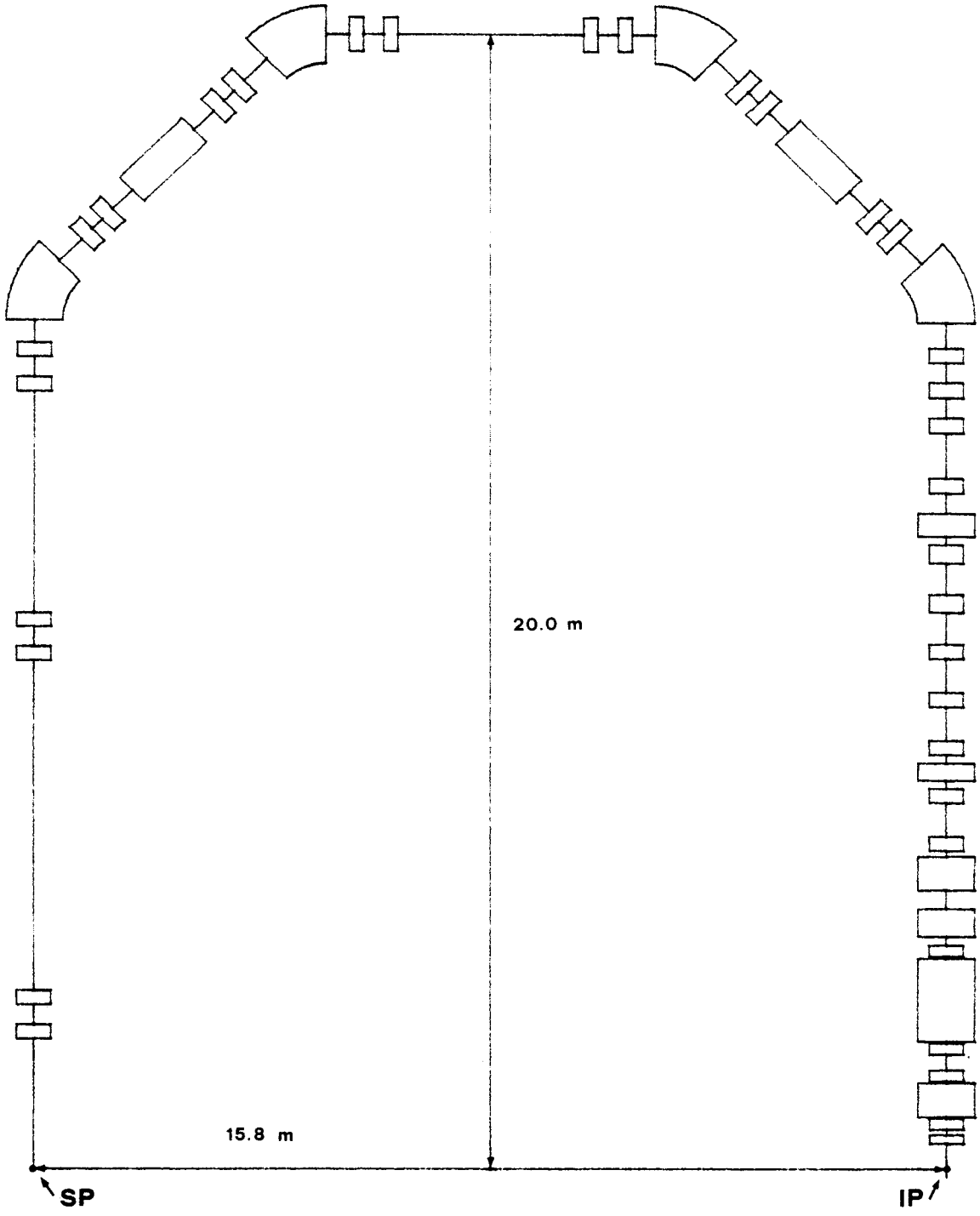

Fig. 3.9 - Layout of one half of the storage ring.

A complete parameter list is given in Table 3.2 , while Tab. 3.3 reproduces the output of the LEDA[13] code, used to design most of the storage ring .

TABLE 3.2 - Parameter List

Energy (MeV)	510.		
Circumference (m)	100.73	Luminosity (cm^{-2} sec^{-1})	10^{32}
Dipole bending radius (m)	1.464		
Wiggler bending radius(m)	0.9	N^{er} of particles/bunch	$8.9\ 10^{10}$
Wiggler length (m)	1.5	N^{er} of bunches	24
Wiggler period (m)	0.5	Collision frequency (MHz)	71.4
Rings separation (m)	1.391	κ	.01
		ξ_y	.04
Horizontal β-tune	5.8	ξ_x	.04
Vertical β-tune	5.85	β_y at I.P. (cm)	4.5
Momentum compaction	.0086	β_x at I.P. (m)	4.5
Energy loss/turn (KeV) :		σ_y at I.P. (μm)	21.1
H. bend. magnets	4.08	σ_x at I.P. (mm)	2.11
V. bend. magnets	0.12	I_2 (m^{-1})	11.7
Wigglers	7.06	I_3 (m^{-2})	11.2
Total	11.26	σ_R (KeV)	2.06
Damping times (msec) :		ΔE_{bb}(KeV)	.20
τ_s	15.2		
τ_x	30.4	RF freq. (MHz)	357.14
τ_y	30.4	Harmonic number	120
Rel. r.m.s. en. spread	$4.25\ 10^{-4}$	RF voltage (MV) at Z/n = 2 Ω	273.
Natural emittances (m-rad) :		at Z/n = 1 Ω	131.
Horizontal	10^{-6}	Parasitic losses (keV Ω)	4.0
Vertical	$1.82\ 10^{-11}$	Bunch length σ_z (cm)	3.0
		Bunch peak current (Amp)	57.
Natural chromaticities :		Total average curr. (Amp)	1.02
Horizontal	-10.3	Synch. Rad. Power/beam (kW)	11.5
Vertical	-16.4		

TABLE 3.3 - LEDA output

```
ENERGY (MEV)                  510.0
B*RO (TESLA*METERS)            1.70
TOTAL BENDING ANGLE (H-V)  0.741971882D+03   0.356509987D+02
NUMBER OF PERIODS              1
PERIOD LENGTH (m)          0.100730266D+03
TOTAL LENGTH (m)           0.100730266D+03

ACHIEVED CONVERGENCE =  0.117552217D-07

HALF-PERIOD LATTICE : REFLECTED SYMMETRY
```

	NAME	LENGTH (m)	K2(m-2)	RADIUS (m)
1	O	0.450000000D+00	0.000000000D+00	0.000000000D+00
2	QF1	0.150000000D+00	0.600000000D+01	0.000000000D+00
3	O	0.100000000D+00	0.000000000D+00	0.000000000D+00
4	QD1	0.200000000D+00	0.113828586D+02	0.000000000D+00
5	O	0.250000000D-01	0.000000000D+00	0.000000000D+00
6	VS1	0.600000000D+00	0.000000000D+00	-0.200000000D+03
7	O	0.250000000D-01	0.000000000D+00	0.000000000D+00
8	QF2	0.200000000D+00	0.911302561D+01	0.000000000D+00
9	O	0.275000000D+00	0.000000000D+00	0.000000000D+00
10	QD2	0.200000000D+00	0.550094163D+01	0.000000000D+00
11	O	0.300000000D-01	0.000000000D+00	0.000000000D+00
12	VS2	0.150000000D+01	0.000000000D+00	-0.200000000D+03
13	O	0.300000000D-01	0.000000000D+00	0.000000000D+00
14	QF3	0.200000000D+00	0.443788888D+01	0.000000000D+00
15	O	0.150000000D+00	0.000000000D+00	0.000000000D+00
16	VB1	0.500000000D+00	0.000000000D+00	-0.250000000D+02
17	O	0.325000000D+00	0.000000000D+00	0.000000000D+00
18	VB2	0.600000000D+00	0.000000000D+00	-0.500000000D+01
19	O	0.100000000D+00	0.000000000D+00	0.000000000D+00
20	QF4	0.250000000D+00	0.251166800D+01	0.000000000D+00
21	O	0.600000000D+00	0.000000000D+00	0.000000000D+00
22	QD3	0.250000000D+00	0.466394100D+01	0.000000000D+00
23	O	0.150000000D+00	0.000000000D+00	0.000000000D+00
24	VB3	0.300000000D+00	0.000000000D+00	0.370695567D+01
25	O	0.150000000D+00	0.000000000D+00	0.000000000D+00
26	QF5	0.250000000D+00	0.420034400D+01	0.000000000D+00
27	O	0.600000000D+00	0.000000000D+00	0.000000000D+00
28	QD4	0.250000000D+00	0.452639900D+01	0.000000000D+00
29	O	0.600000000D+00	0.000000000D+00	0.000000000D+00
30	QF6	0.250000000D+00	0.384354930D+01	0.000000000D+00
31	O	0.565000000D+00	0.000000000D+00	0.000000000D+00
32	QD5	0.320000000D+00	0.729970000D+01	0.000000000D+00
33	O	0.555000000D+00	0.000000000D+00	0.000000000D+00
34	QF7	0.320000000D+00	0.561495665D+01	0.000000000D+00
35	O	0.150000000D+00	0.000000000D+00	0.000000000D+00
36	VB4	0.410000000D+00	0.000000000D+00	0.514527802D+01
37	O	0.400000000D+00	0.000000000D+00	0.000000000D+00
38	QD6	0.270000000D+00	0.378930439D+01	0.000000000D+00
39	O	0.850000000D+00	0.000000000D+00	0.000000000D+00
40	QF8	0.270000000D+00	0.542510247D+01	0.000000000D+00
41	O	0.300000000D+00	0.000000000D+00	0.000000000D+00
42	QD7	0.270000000D+00	0.334056224D+01	0.000000000D+00
43	O	0.300000000D+00	0.000000000D+00	0.000000000D+00
44	QF9	0.250000000D+00	0.896585488D+00	0.000000000D+00
45	O	0.450000000D+00	0.000000000D+00	0.000000000D+00
46	HB	0.115000000D+01	0.000000000D+00	0.146422540D+01
47	O	0.250000000D+00	0.000000000D+00	0.000000000D+00
48	SD	0.150000000D+00	0.118700000D+02	0.000000000D+00
49	O	0.200000000D+00	0.000000000D+00	0.000000000D+00
50	QD8	0.100000000D+00	0.383721329D+00	0.000000000D+00

TABLE 3.3 - LEDA output - (continue)

	NAME	LENGTH (m)	K2(m-2)	RADIUS (m)
51	O	0.3500000000D+00	0.0000000000D+00	0.0000000000D+00
52	QF10	0.2500000000D+00	0.249525412D+01	0.0000000000D+00
53	O	0.1625000000D+00	0.0000000000D+00	0.0000000000D+00
54	SF	0.1500000000D+00	0.1346000000D+02	0.0000000000D+00
55	O	0.1625000000D+00	0.0000000000D+00	0.0000000000D+00
56	WIG	0.1500000000D+01	0.0000000000D+00	0.9000000000D+00
57	O	0.1625000000D+00	0.0000000000D+00	0.0000000000D+00
58	SF	0.1500000000D+00	0.1346000000D+02	0.0000000000D+00
59	O	0.1625000000D+00	0.0000000000D+00	0.0000000000D+00
60	QF10	0.2500000000D+00	0.249525412D+01	0.0000000000D+00
61	O	0.3500000000D+00	0.0000000000D+00	0.0000000000D+00
62	QD8	0.1000000000D+00	0.383721329D+00	0.0000000000D+00
63	O	0.2000000000D+00	0.0000000000D+00	0.0000000000D+00
64	SD	0.1500000000D+00	0.1187000000D+02	0.0000000000D+00
65	O	0.2500000000D+00	0.0000000000D+00	0.0000000000D+00
66	HB	0.1150000000D+01	0.0000000000D+00	0.1464225400D+01
67	O	0.4000000000D+00	0.0000000000D+00	0.0000000000D+00
68	QD9	0.2500000000D+00	0.932084352D+00	0.0000000000D+00
69	O	0.3500000000D+00	0.0000000000D+00	0.0000000000D+00
70	QF11	0.2500000000D+00	0.1401641060D+01	0.0000000000D+00
71	O	0.3225132940D+01	0.0000000000D+00	0.0000000000D+00
72	QF11	0.2500000000D+00	0.1401641060D+01	0.0000000000D+00
73	O	0.3500000000D+00	0.0000000000D+00	0.0000000000D+00
74	QD9	0.2500000000D+00	0.932084352D+00	0.0000000000D+00
75	O	0.4000000000D+00	0.0000000000D+00	0.0000000000D+00
76	HB	0.1150000000D+01	0.0000000000D+00	0.1464225400D+01
77	O	0.2500000000D+00	0.0000000000D+00	0.0000000000D+00
78	SD	0.1500000000D+00	0.1187000000D+02	0.0000000000D+00
79	O	0.2000000000D+00	0.0000000000D+00	0.0000000000D+00
80	QD8	0.1000000000D+00	0.383721329D+00	0.0000000000D+00
81	O	0.3500000000D+00	0.0000000000D+00	0.0000000000D+00
82	QF10	0.2500000000D+00	0.249525412D+01	0.0000000000D+00
83	O	0.1625000000D+00	0.0000000000D+00	0.0000000000D+00
84	SF	0.1500000000D+00	0.1346000000D+02	0.0000000000D+00
85	O	0.1625000000D+00	0.0000000000D+00	0.0000000000D+00
86	WIG	0.1500000000D+01	0.0000000000D+00	0.9000000000D+00
87	O	0.1625000000D+00	0.0000000000D+00	0.0000000000D+00
88	SF	0.1500000000D+00	0.1346000000D+02	0.0000000000D+00
89	O	0.1625000000D+00	0.0000000000D+00	0.0000000000D+00
90	QF10	0.2500000000D+00	0.249525412D+01	0.0000000000D+00
91	O	0.3500000000D+00	0.0000000000D+00	0.0000000000D+00
92	QD8	0.1000000000D+00	0.383721329D+00	0.0000000000D+00
93	O	0.2000000000D+00	0.0000000000D+00	0.0000000000D+00
94	SD	0.1500000000D+00	0.1187000000D+02	0.0000000000D+00
95	O	0.2500000000D+00	0.0000000000D+00	0.0000000000D+00
96	HB	0.1150000000D+01	0.0000000000D+00	0.1464225400D+01
97	O	0.4000000000D+00	0.0000000000D+00	0.0000000000D+00
98	QD10	0.2500000000D+00	0.1092365090D+01	0.0000000000D+00
99	O	0.3500000000D+00	0.0000000000D+00	0.0000000000D+00
100	QF12	0.2500000000D+00	0.1542579710D+01	0.0000000000D+00
101	O	0.4878138620D+01	0.0000000000D+00	0.0000000000D+00
102	QF13	0.2500000000D+00	0.2122339080D+01	0.0000000000D+00
103	O	0.3500000000D+00	0.0000000000D+00	0.0000000000D+00
104	QD11	0.2500000000D+00	0.1870786050D+01	0.0000000000D+00
105	O	0.4650982080D+01	0.0000000000D+00	0.0000000000D+00
106	QD11	0.2500000000D+00	0.1870786050D+01	0.0000000000D+00
107	O	0.3500000000D+00	0.0000000000D+00	0.0000000000D+00
108	QF13	0.2500000000D+00	0.2122339080D+01	0.0000000000D+00
109	O	0.2470879300D+01	0.0000000000D+00	0.0000000000D+00

TABLE 3.3 - LEDA output - (continue)

```
 PARAMETERS :
 ----------

  QX - QZ                          5.800        5.850
 tunes/period                      5.800        5.850
ETA0  (H/V) - BX0   - BZ0      -.6444E-08  0.6484E-10   4.500      0.4500E-01
ETAMAX (H/V) - BXMAX - BZMAX    1.455       0.1642       11.95      17.94
ETAMIN (H/V) - BXMIN - BZMIN   -.1243E-07  -.3432       0.1734     0.4500E-01
<ETA> (H/V) - <BX>  - <BZ>     0.2526      -.1236E-01    5.195      6.871

 SYNCHROTRON RADIATION INTEGRALS (R.H.HELM et al.) :

  I1(H-V) (meters)          0.870459662D+00  -0.279060893D-01
  I2(H-V) (1/meters)        0.116985402D+02   0.124342210D+00
  I3(H-V) (1/meters**2)     0.111611031D+02   0.274631442D-01
  I4(H-V) (1/meters)        0.000000000D+00  -0.269400316D-02
  I5(H-V) (1/meters)        0.289805931D+02   0.563461960D-03

 MOM. COMPACTION             0.8641E-02
 U0 (H-V-Tot) (KeV)           11.14       0.1184       11.26
 D (H-V)                     0.0000E+00   -.2279E-03
 JS,JX,JZ                     2.000       1.000        1.000
 DAMPINGS(ms)                 15.22       30.43        30.43
 REL. R.M.S. ENERGY-SPREAD   0.4254E-03
 EMITTANCE(H-V) (m-rad)      0.9876E-06  0.1822E-10

 CHROMATICITIES (M.BASSETTI LEP NOTE 504) :

 TOTAL CROM.      -10.34        -16.44
 COR.TOT.CROM.  0.0000E+00   0.0000E+00
 SEXT (T/M^2)  :    SD =  142.9
                    SF =  182.0
```

TABLE 3.3 - LEDA output - (continue)

```
BEAM PAR & dN/dt FOR T=293K - P=1nTorr - Z(biatomic)=8 :
--------------------------------------------------------

REV. FREQUENCY (MHZ)        0.297619048D+01
HARMONIC NUMBER             0.120000000D+03
RF.F.REQUENCY (MHZ)         0.357142857D+03

ENERGY (MEV)                510.0
MOM. COMPACTION             0.8641E-02
U0 (H-V-Tot) (KeV)          11.26
VRF(KV)                     131.0
F SYNC.(KHZ)                19.34
RF ACCEPTANCE               0.1170E-01

NAT.BUNCH LENGTH(m)         0.9069E-02
AN. BUNCH LENGTH(m)         0.3036E-01
REL. R.M.S. ENERGY-SPREAD   0.1424E-02

AV.CURRENT/BUNCH(mA)        42.43
# ELECTRONS/BUNCH           0.889917603D+11
PEAK CURRENT/BUNCH(A)       56.16
HW Th(Z/n=1)/BUNCH(A)       5.012

EMITTANCE(H-V) (m-rad)      0.9876E-06
EMITTANCE COUPL.            0.1000E-01
HOR. APERTURE (m)           0.4000E-01
VER. APERTURE (m)           0.3000E-01

QUANTUM LIFE (hrs)-SANDS    0.2898E+08
LIFETIME GB (min)           2104.
LIFETIME SC (min)           1300.
LIFETIME GBe (min)          0.1295E+05
LIFETIME SCe (min)          0.2144E+05
TOUSCHEK (min)              154.5
LIFETIME TOT.(min)          127.5
```

Let us conclude with a comment about the emittance: the very low emittance required for linac-storage ring collisions can be obtained by switching off the wigglers inside the achromat (which brings the emittance down to $\approx 10^{-8}$ m-rad) and switching on the wigglers foreseen for PHASE II to finally reach an emittance $\approx 10^{-9}$ m-rad.

3.3.3 - Dynamic aperture

The fully periodic Chasman-Green lattice would have a large dynamic aperture even with only two families of chromaticity correcting sextupoles. When the low-β insertion is included, the dynamic aperture shrinks because of the larger chromaticity and the lower symmetry.

A preliminary on-momentum dynamic aperture at the IP, as evaluated with PATRICIA[14] and with only two sextupole families, is shown in Fig. 3.10.

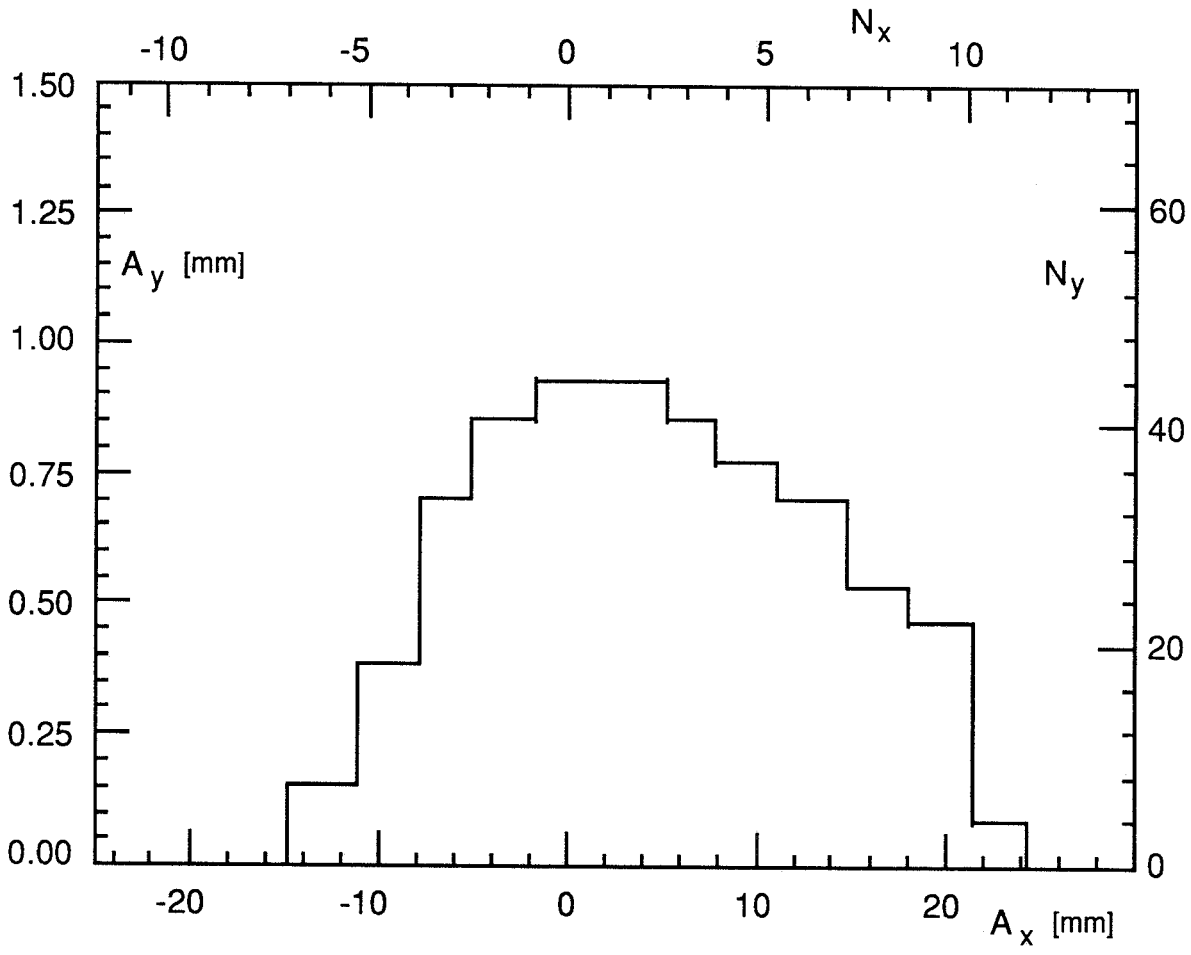

Fig. 3.10 - On energy dynamic aperture at the IP: A_X and A_Y are the horizontal and vertical maximum stable amplitudes, while N_X and N_Y are the same in units of numbers of σ's, for κ=.01.

A more elaborate chromaticity correction scheme and further optimisation of the working point in the tune diagram will allow to achieve a dynamic aperture that matches the lifetime and injection requirements.

3.3.4 - Injection aperture

For injection it is foreseen to implement a conventional full energy scheme based on a thin septum and a fast closed orbit bump produced by four kicker magnets. In order to evaluate the necessary ring aperture, the horizontal and vertical r.m.s. beam size are shown in Fig. 3.11 for the following conservative characteristic parameters of the injected beam :

$$\varepsilon = 2.\,10^{-5} \text{ m rad}$$
$$\kappa = 1.$$
$$\frac{\Delta p}{p} = 1.\,\%$$

The required error closed orbit allowance on the aperture can be of a few millimiters only.

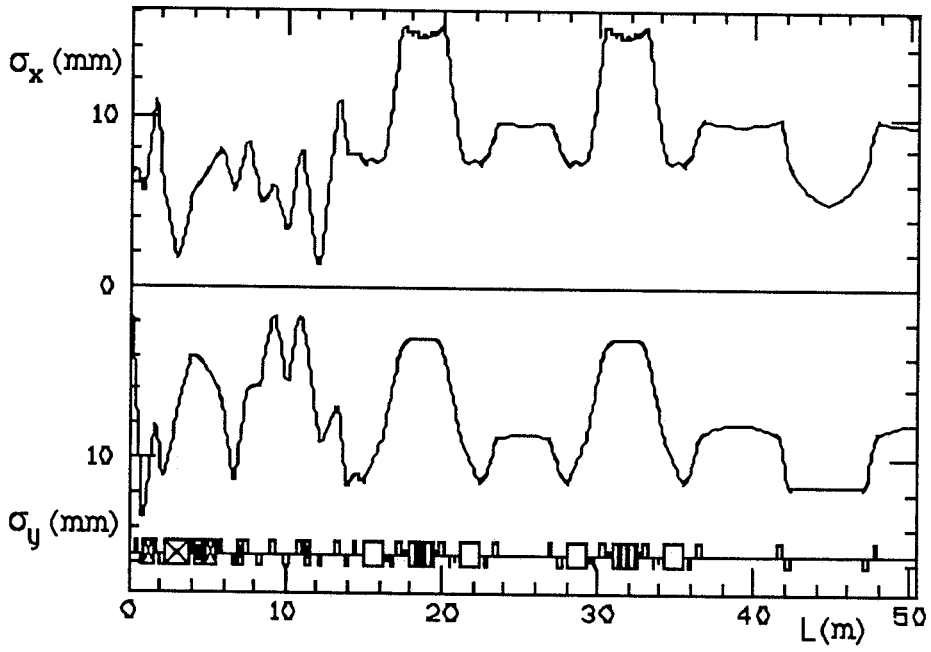

Fig. 3.11 - Horizontal and vertical r.m.s. beam sizes

3.4. - BEAM STABILITY AND LIFETIMES.

High currents in both the single and the multibunch modes of operation, short bunch lengths, long lifetimes and the stablest possible beam conditions are all to be achieved at the same time, thereby putting severe constraints on the design of the overall system.

The above parameters are very much interconnected: single-Tousheck lifetime can be relevant at the energy of 510 MeV and is determined by the bunch density and the momentum acceptance. In turn the bunch density depends on the lattice and RF parameters, and can be affected by intrabeam scattering and by μ-wave instabilities whose current thresholds are related to the vacuum chamber geometry and the RF cavity properties.

A self consistent computation has therefore been carried out to find an optimum. The main phenomena considered in the analysis are : single bunch instabilities including turbulent bunch-lengthening, lifetime limiting effects (such as Tousheck scattering, gas scattering, and beam-beam single bremsstrahlung), coupled bunch instabilities and intrabeam scattering.

3.4.1 - Single bunch dynamics

Instabilities are caused by the electromagnetic fields excited by the interaction of the bunch with the surrounding structure. The effects of these fields on the bunch dynamics are estimated using the concept of "machine impedance".

The single bunch dynamics is affected by those bunch excited fields whose strength is relevant over a distance of the order of the bunch length. The fields are mainly produced in correspondence with vacuum chamber discontinuities (including the cavity irises) and are described in the frequency domain by the so called broadband (BB) impedance. They cause the particles to lose energy depending on their position and therefore induce additional momentum spread and bunch-lengthening.

The threshold peak current of this "turbulent" bunch-lengthening is given by:

$$\hat{I}_l = \frac{2\pi\, \alpha_c\, (E/e)\, \sigma_p^2}{Z/n} \qquad (3.18)$$

With the σ_p and α_c values given in Tab. 3.2, one obtains

$$\hat{I}_l \approx 5\ \text{Amp}\cdot\Omega$$

The 57 A design peak current exceeds the μ-wave threshold for any reasonable choice of RF parameters and BB impedances. In order to keep the bunch length at the design value the values of the RF parameters h (harmonic number) and $\hat{V}$ (Peak voltage) must satisfy the equation:

$$h\hat{V} = \frac{ecN R^2}{\sqrt{2\pi}\,\sigma^3} \frac{\left(\frac{Z}{n}\right)_{BB}}{\cos(\phi_s)} \qquad (3.19)$$

where

$$\cos(\phi_s) = \sqrt{1 - \left(\frac{U}{e\hat{V}}\right)^2} \qquad (3.20)$$

with $U = U_0 + U_z$, U_0 being the radiation loss and U_z the energy dissipated in the resistive impedance.

Note that U_z depends on the bunch-length (σ_z^{-3}), and therefore for short bunches it may contribute significanlty to the overall losses:

$$U_z\,(\text{keV}) \approx 4\left(\frac{Z}{n}\right)_{BB}(\Omega) \qquad (3.21)$$

Equation 3.19 has been solved for h, as a function of $\hat{V}$ and Z/n. Since the impedance can be only roughly estimated several BB impedance values, chosen in the range

$$\left(\frac{Z}{n}\right)_{BB} = 1 \div 10\ \Omega$$

(a reasonable range covering the measured impedances of almost all existing machines) have been considered.

Fig. 3.12 shows the curves (dashed lines) relating the peak voltage, $\hat{V}$, necessary to obtain the nominal bunch-length of 3 cm, to the harmonic number h. It is apparent that by choosing the RF frequency to be ≈ 350 MHz, the bunch-length can be controlled using reasonable peak voltage values independent of the exact machine impedance value.

On the contrary, the effect of the short-range wakefields on the transverse dynamics is destructive, and most often determines the maximun storable current. By assuming a beam pipe radius b = 3 cm , equal to the bunch-length, and using the relation between the longitudinal and the transverse BB impedance:

$$|Z_\perp| = \frac{2R}{b^2} \cdot \left(\frac{Z}{n}\right)_{BB}$$

one finds that the current stays below the transverse threshold, provided that h and $\hat{V}$ fulfill the condition:

$$h\hat{V}\cos(\phi_s) < 4\,\alpha_c \frac{E}{e} \cdot \left(\frac{R}{<\beta>}\right)^2 \qquad (3.22)$$

where $<\beta>$ is the largest between the horizontal and the vertical β function average. Figure 3.12 shows the limit curve (solid line) below which the eq. 3.22 is satisfied.

Note that, because of the rather weak dependance on impedance through $\cos(\phi_s)$, the four curves corresponding to the four considered impedance values are practically superimposed on each other. The limit is exceeded at the design current if the impedance exceeds $Z/n \approx 5\Omega$. The maximum allowed design impedance is thus defined.

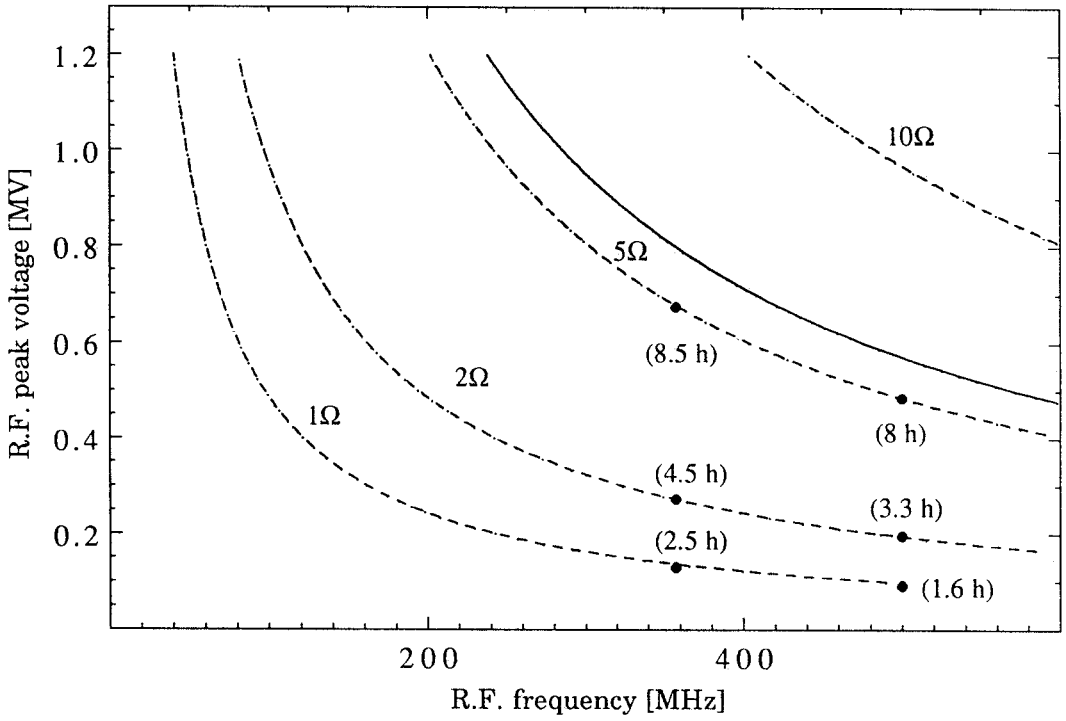

Fig. 3.12 - Peak voltage versus R.F. frequency for different machine impedances (dashed lines). The solid line is the limiting curve for transverse instabilities. The dots are the calculated Toschek life-times for the two different R.F. frequencies: 357 and 500 MHz.

3.4.2 - Beam Lifetime

The single Touschek scattering effect induces a momentum deviation depending on the bunch density and r.m.s. angular divergence $\sigma_{x'}$. The Touschek lifetime τ_T averaged along the machine, has been calculated assuming that the machine acceptance is limited longitudinally by the RF bucket heigth and transversely by the physical aperture. The results of the calculation are shown as dots on the iso-impedance curves in Fig. 3.12 , for the chosen RF parameter values . It is found that, since the bunch volume stays constant along the curves, lifetimes are limited by the physical aperture in the upper-left region while, moving down and to the right, they decrease because the RF momentum acceptance is reduced. Remembering the constraints on the RF parameters deriving from single bunch dynamics, we conclude that an RF frequency around 350 MHz, giving a lifetime of several hours, is the most suitable for our purposes.

At 350 MHz the Touschek lifetime, τ_T, is practically limited only by the RF acceptance, ε_{RF} and by varying the peak voltage in the range $0.1 \div 0.7$ MV, ε_{RF} can be changed from 1.2% to 2.8%.

The lifetimes relative to all other mentioned processes are calculated on the basis of this choice.

Radiation in the bending magnets and in the wigglers leads to the loss of those particles with energy deviations larger than the machine energy acceptance. The effect however, even including the momentum spread increase induced by microwave instabilities give a practically infinite quantum life time τ_q provided too high values of the frequency are avoided. As an example, should one choose 500 instead of 350 MHz, for $(Z/n)_{BB} = 1\ \Omega$ one would need only 93 KV peak voltage to keep the bunch length at 3 cm but the R.F. momentum acceptance would be reduced to 0.8% and the quantum lifetime would dramatically drop to 80 minutes.

By choosing a 350 MHz system, the range of R.F. momentum acceptances ($\approx 1.2\% \div \approx 2.8\%$) is such that other phenomena causing energy deviations of the particles in the bunch do not affect the overall beam lifetime. Single bremsstrahlung in beam-beam collisions gives a lifetime of 20 hours at least, inelastic scattering on the residual gas a lifetime of 35 hours in the worst case and, elastic scattering on residual gas -causing particles to be lost on the beam pipe - gives a lifetime of 22 hours at the design pressure of $\approx 10^{-9}$ torr.

In conclusion we expect an overall beam lifetime in the range $3 \div 6$ hours limited by Tousheck scattering. Topping-off injection is nevertheless desirable in order to keep the average luminosity high.

3.4.3 - Multibunch instabilities

The impedance of parasitic high order modes (HOM) are characterized by a resonant frequency ω_r, a shunt impedance R_s and a quality factor Q_s:

$$Z_{//}(\omega) = \frac{R_s}{1 + jQ_s\left(\frac{\omega_r}{\omega} - \frac{\omega}{\omega_r}\right)}$$

They are responsible for the multibunch instabilities. Many of such narrow band impedances are originated in the RF cavities or in cavity-like vacuum chamber components coupled to the beams.

The motion of M equidistant bunches is similar to that of M rigid coupled oscillators. The frequency spectrum of the oscillations is given by a set of sidebands at frequencies:

$$f_p = f_0\,(Mp + n + m\nu_s),\ [m = 1,2,...;\ n = 0 \div M-1;\ -\infty < p < +\infty]$$

The amplitude of these sidebands is not constant but depends on the bunch length σ and shape and on the frequency f_p. According to Sacherer's theory [15] a single sideband of the umperturbed distribution will undergo a complex frequency shift $\Delta\omega_m$ because of the coupling. The real part of $\Delta\omega_m$ gives a real frequency shift while its imaginary part causes the oscillation amplitude to grow with a rise time:

$$\tau_m \sim \frac{1}{\Im[\Delta\omega_m]}$$

A simple approximation of the growth rate can be derived [16] under the following assumptions holding in our machine: $M(\sigma/R) \ll 1$ and a single sideband f_p coupled to the resonator, i.e. $f_r/f_0 \ll Q_s$. In the particular case of full coupling we get:

$$\Im[\Delta\omega_m] \sim \frac{m}{m+1}\,\frac{2^{m-1}}{(2m-1)!!}\,\frac{I\,R_s\,\omega_s}{\omega_{RF}V_{RF}\cos\phi_s}\,\frac{\omega_r^{2m-1}}{\bar{\omega}^{2m-2}}\,\exp\left[-\left(\frac{\omega_r}{\bar{\omega}}\right)^2\right] \qquad \text{with } \bar{\omega} = \frac{c}{\sigma}$$

where I is the total current, and the double factorial applies only to odd terms.

By assuming that this instability is damped by radiation we get the current thresholds for the dipole and quadrupole modes:

$$I_{th}^{m=1} = 2\sigma_p \frac{U_o}{R_s} \frac{\exp\left(\frac{\omega_r}{\bar{\omega}}\right)^2}{\left(\frac{\bar{\omega}}{\omega_r}\right)} \qquad I_{th}^{m=2} = \frac{9\sigma_p}{4} \frac{U_o}{R_s} \frac{\exp\left(\frac{\omega_r}{\bar{\omega}}\right)^2}{\left(\frac{\bar{\omega}}{\omega_r}\right)^3}$$

Calculations of these thresholds have been done considering as an example the LEP 350 MHz RF cavity whose HOM are listed in Table 3.4 togheter with the corresponding thresholds.

TABLE 3.4 - LEP 350 MHz Cavity Full Coupling Threshold

Parasitic Resonance			Full Coupling Thresholds [mA]		$\frac{\Delta\omega_r}{\omega_r} 10^3$
f_r [MHz]	R_s [MΩ]	Q_r	m=1	m=2	
506	1.3	40600	.02	.24	2.8
920	0.75	40700	.03	.10	2.2
1163	0.33	50400	.06	.13	1.3
1204	0.36	70400	.05	.10	1.0
1745	0.37	66500	.07	.07	0.9
1990	0.20	66700	.16	.12	0.6

It is apparent that coupled bunch coherent instabilities could be harmful under hardly predictable particular conditions; cures to fight them must therefore be envisaged. On the other side for a relatively short machine we expect the instability to be caused by only few offending HOM. We discuss here three main cures and we make an estimate of the required performances:

a) damping of the HOM thereby reducing shunt impedance R_s (HOM damping);
b) shifting of the frequency of the harmful HOM's ;
c) implementing an active feedback system.

In the worst case, corresponding to full coupling, the threshold current is inversely proportional to the shunt impedance of the HOM which therefore should be reduced by a factor quite high and consequently not easily pursuable.

By shifting the HOM frequency there is a strong increase of the current threshold by a factor:

$$\left(2Q_r \frac{\Delta\omega_r}{\omega_r}\right)^2$$

In order to store the design current, a frequency shift of ~ 0.3 % could be required, as shown in the last column of Table 3.4.

Finally the use of a feedback system introduces a damping given by:

$$\frac{1}{\tau_D^{FB}} = \frac{1}{2} \frac{f_o}{E_o} \frac{eV_{FB}}{\Delta p/p}$$

where $\frac{\Delta p}{p}$ is the relative bunch energy deviation.

The feedback signal, in order to damp all possible coupled modes, has to act separately on each bunch. Accordingly the system bandwidth should be at least twice the bunch frequency, therefore the use of broad band longitudinal strip-line kickers is required. The feedback system gain turns out to be very high and most likely limited by the maximum allowed voltage (200÷500 V) on the longitudinal strip-line kickers.

In conclusion, we have given a rather pessimistic estimate of multibunch instabilities, in the worst possible scenario. It is clear however that the problem must be carefully studied foreseeing the combined use of HOM frequencies detuning and of feedback systems, including the one recently developed by Kohaupt [17].

3.5. - GENERAL CONSIDERATIONS ON BEAM DIAGNOSTIC AND INSTRUMENTATION

The beam instrumentation to be implemented in the Φ-Factory storage rings is discussed in the following, with reference to the peculiar features wich influence the design and choice.

The storage rings characteristics, which reflect in particular requirements of the beam instrumentation and of the general hardware, are the following:

- High current (~ 1 A). The longitudinal and transverse parasitic impedance of the vacuum chamber should be the lowest possible to increase the thresholds of collective instabilities.

- Many bunches. The rather large number of circulating bunches calls for a careful design of the RF cavities, where coupled bunch instabilities are most likely to be excited by high order resonating modes. The more seriously offending modes may be identified and damped in the cavities by suitable antennas, but nevertheless a coupled-bunch feedback system must be provided.

- Small bunch dimensions (σ_y <~ 0.02 mm at the IP). Careful closed-loop control of the stability of the IP vs. drifts of the longitudinal and vertical bunch position in the separate rings is required.

- Small coupling factor (κ ~ .01). To achieve such low value of the coupling factor, a careful control of the closed orbit distorsion at quadrupoles and sextupoles locations is required in order to reduce the strength of the driving term of vertical dispersion. Vertical dispersion is also introduced, and must be suppressed, by the vertical bending of the separator in the Interaction Region and by rotated quadrupoles and vertically misaligned sextupoles. Careful surveying and high absolute accuracy of the beam position monitors is required.

3.6 - RF SYSTEM

With an operating frequency of 357.14 MHz the maximum required RF voltage is ≈ 0.8 MV (see § 3.4).

The energy loss/turn is 11.26 keV and the RF power to the beam is 11.26 kW for a stored current of ≈ 1 A (see Tab. 3.2). The power loss to parasitic HOM's is estimated to be ≈ 4 keV per Ohm of broadband impedance. An 8 kW additional power loss must therefore be taken into account for an overall chamber impedance of 2 Ω. In conclusion, the total required RF power is ≈ 20 kW per beam.

The proposed RF system consists of two normal-conducting single-cell copper cavities in each ring. Each cavity is rated at 400 kV. The main system parameters are summarized in the following Table 3.5 :

Table 3.5 - RF System Parameters

RF Frequency	f_0 =	357.14	MHz
Cavity Q factor	Q_0 =	40.000	
Effective cavity shunt-impedance	ZT^2 =	6	MΩ
RF peak voltage per cavity	V_p =	400	kV
Dissipated power per cavity	P_D =	27	kW
Beam power per cavity	P_B =	10	kW
Cavity to source coupling factor	β =	1.4	
Bandwidth of the System	B_L =	21	kHz
Maximum generator power	P_A =	50	kW
Number of RF chains per ring		2	

Each resonator can be powered by a single 50 kW source; reliable tetrode amplifiers are available on the market in this range of frequency and power.

Standard feedback systems are foreseen to control amplitude, phase and frequency of the resonant cavities.

The cavities will be equipped with HOM couplers to damp the parasitic modes excited by the bunched beam. Some R&D will be necessary to specify and test the performance of the dampers.

3.7 - VACUUM SYSTEM

Ultra high vacuum (UHV) is necessary in an electron storage ring in order to achieve good beam lifetime and to avoid ion trapping.

Good vacuum conditions have to be maintained in the presence of the heavy gas load produced by the radiation induced photo-desorption. Hard radiated photons ($h\nu > 10$ eV) extract photoelectrons from the inside wall of the vacuum chamber; these in turn extract atoms or molecules absorbed on the surface. The process is characterized by the "photodesorption efficiency" parameter, D, wich gives the average number of desorbed molecules per incident photon. Typical values of D are in the range of $10^{-1} \div 10^{-7}$ molecules/photon. The lowest D values are reached with appropriate treatments of the vacuum chamber and after long periods of conditioning with the stored beam ($\approx$ 100 A·h).

From the design parameter values listed in Tab 3.2 we estimate a total gas load, Q, of

$$Q = 8.7\ 10^{-6} \text{ mbar l/s} \quad \text{for} \quad D = 10^{-6} \text{ molecules/photon}$$

The total pumping speed, S, necessary to achieve the design value of 10^{-9} mbar is therefore :

$$S = Q/p = 8700 \text{ l/s.}$$

With 10 identical ion pumps per sector we obtain a required nominal pumping speed of 220 l/s per pump; a rough figure of 400 l/s per pump actual pumping speed is estimated to account for the pumping speed degradation at 10^{-9} mbar and for vacuum chamber conductances. The preferred vacumm chamber material is stainless steel; usual UHV technology precautions such as accurate cleaning procedures, high temperature bake-out, etc., will also have to be taken.

In summary, the main vacuum system components for the two rings are:

- 2 stainless steel vacuum chambers
- bakeout systems
- 80 sputter ion pumps, 400 l/s each.
- 8 cryopumps, 1500 l/s each.
- 8 oil-free roughing pumps.
- 16 U.H.V. gauges.
- 1 mass spectrometer (8 heads).
- interfaces to the central control system.

3.8 - THE DETECTOR SOLENOID

The main specifications for the Detector solenoid are :

- Axial length	≈ 10	m
- Radius	≈ 5	m
- Axial magnetic field	1	kGauss max
- Field on axis	≈ 0	

The main conclusions from of a preliminary feasibilty study of the solenoid are presented here. The details can be found in Reference (18).

The detector and the detector solenoid have to clear the region inside a conical surface, coaxial with the beam, having a half-aperture angle of 8.5° and the vertex on the IP. The beam has to be shielded from the solenoidal field; however, no shield can be foreseen in the ± 22 cm region surrounding the IP because the experiment tolerates only a very thin layer of material in that region.

The solenoid main coil dimensions are:

- average radius	437.5	cm
- thickness	25	cm
- total length	9	m

and the iron yoke ones are :

- maximum external radius	5	m
- thickness	25	cm
- thickness of the terminating iron plates	25	cm
- terminating iron plate hole radius	75	cm

The main solenoid linear current density, determined using POISSON, is ≈ 88900 A/m. An active shielding system using current sheets has also been investigated; a typical layout, including the current sheet profile and the field lines as computed by POISSON, is shown in Figure 3.13.

Finally, the magnetic field on axis is plotted for different shield configurations in Figure 3.14. From these preliminary calculations we do not anticipate any problem in locally compensating the residual solenoidal field even though the correction scheme has not yet been worked out in full detail.

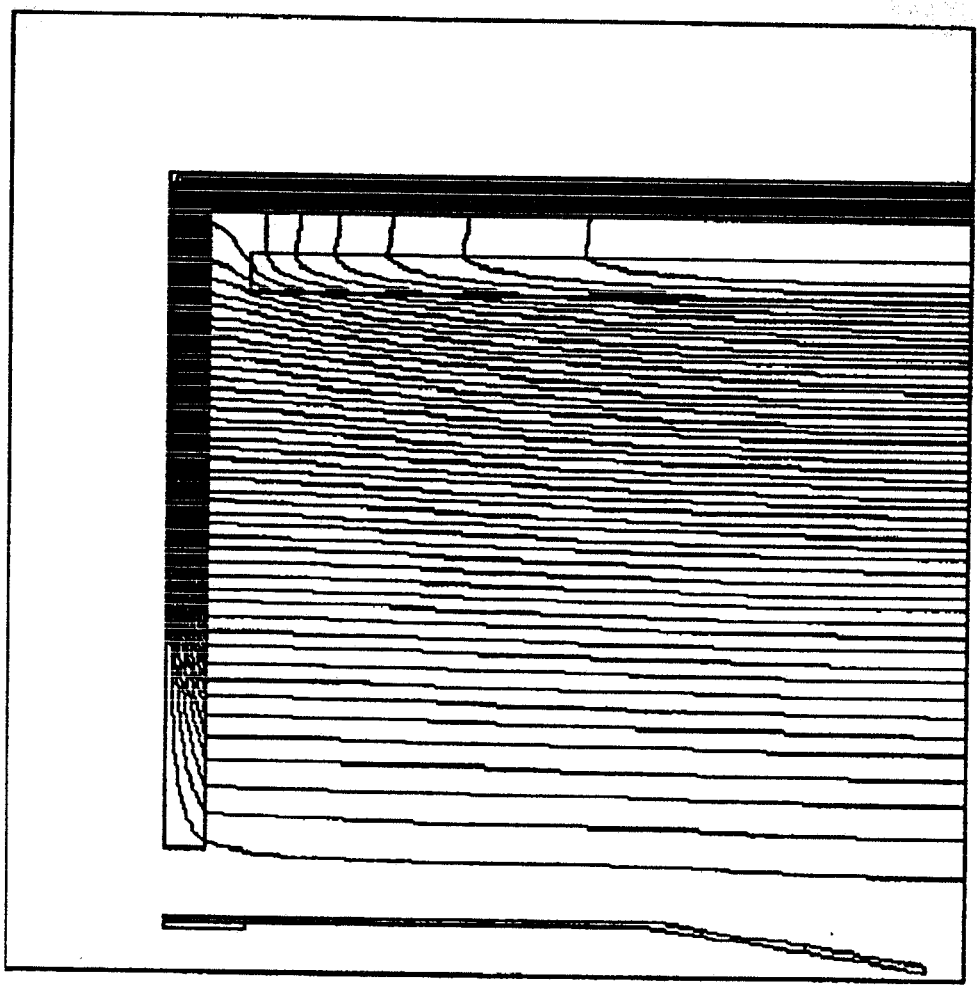

Fig. 3.13 - Magnetic field lines for the shielded solenoid configuration.

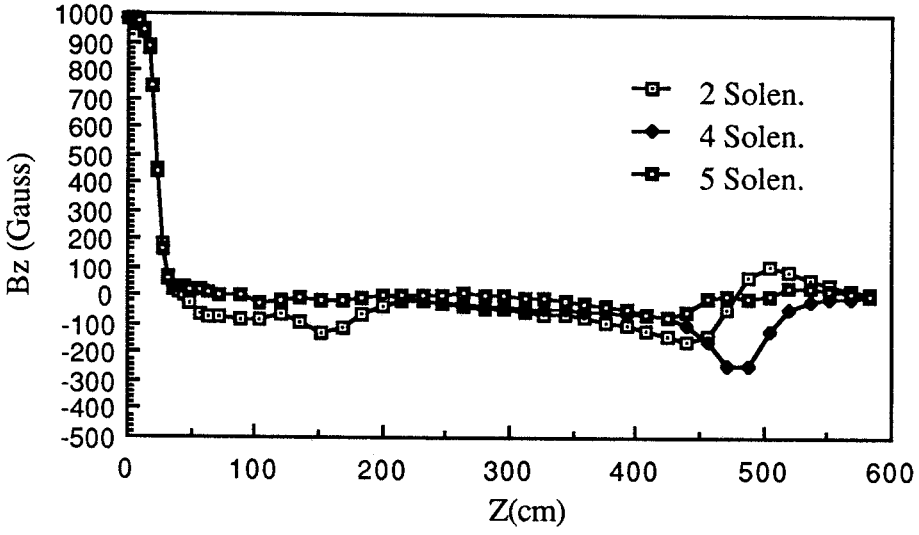

Fig. 3.14 - Magnetic field along the axis with different shield configurations.

References

(1) M.Sands, The physics of electron storage rings. An introduction, SLAC-121,(1970)
(2) R.Littauer et al., XII Intern. Conference on High Energy Accelerators, FNAL (1983)
(3) Barkov et al., The F-Factory project in Novosibirsk, Proc. of 1989 ICFA Meeting on Beam Dynamics, Novosibirsk
(4) W.A.Barletta and C.Pellegrini, A full energy positron source for the UCLA F-Factory CAA 0048,UCLA 10/89
(5) H.Neseman, Proc. UCLA Workshop "Linear Collider, BB Factory, Conceptual design, Jan.1987, Edited by D.H.Stork, World Scientific - Singapore.
(6) S.Myers and J.Jowett, Proceeding of the Tau-Charm Factory Workshop, SLAC-343 (1989)
(7) 1985 NSLS Annual report - BNL 51947
1988 NSLS Annual report - BNL 52167
G.Vignola, private communication
(8) J.Seeman, Lectures Notes in Physics, Vol. 247 (1985) - Springer Verlag Ed.
(9) M.Bassetti, Int. Memo ARES 18 (1989)
(10) R.H.Helm, M.J.Lee, P.L.Morton, M.Sands, IEEE Trans. Nucl. Sci., NS 20 (1973)
(11) M.Bassetti, S.Guiducci, M. Preger, G. Vignola, Int.Memo ARES 26 (1989)
(12) R.Chasman, G.K.Green and M.Rowe, IEEE Trans. Nucl. Sci., NS 22 (1975)
(13) J.B.Murphy and G.Vignola, LEDA : A computer code for linear lattices (Unpublished)
(14) H.Wiedeman, PEP Note 220 (1976)
(15) F.Sacherer, IEEE Trans. Nucl. Sci., NS 24 (1977)
(16) S.Bartalucci and L.Palumbo, Int. Memo T-120 (1985)
(17) R.D. Kohaupt, DESY 86-121 (1986)
(18) C.Sanelli, Int. Memo ARES 32 (1990)

4. - BEAM INSTRUMENTATION AND CONTROL SYSTEM

4.1. - BASIC REQUIREMENTS

The Beam Instrumentation and Control system should allow the Ares performance and hardware to be monitored and controlled from a single Main Control Room. All monitoring and control components and systems , such as Diagnostics elements, DC and pulsed Magnets, RF, Beam and Machine timing, Cryogenics, Vacuum, etc., must be under full computer control. To be more specific, the Beam Instrumenrtation and Control system should fulfill the following basic requirements :

- to present meaningful yet concise information or alarms about the operational status of the hardware and the performance of components;
- to automatically reset to a wanted condition a given sub-component, component or a combination thereof in a consistent and safe way;
- to decode complex commands (e.g. set-up of a particular Linac beam) into a sequence of separate, synchronized, interdependent actions. A machine timing system is thus necessary to synchronize the various states of the accelerators. A fast analogic beam timing system is also necessary to tag the various beams (electrons, positrons, electrons for positron conversion, FEL);
- to let the machine physicist interact with the Instrumentation & Control system in a transparent way in terms of accelerator physics quantities;
- to simulate, in real time, the effect of commands on performance;
- to simulate the beam behaviour according to analytical or empirical models of the various components in order to avoid or reduce to a minimum, already in the commissioning stage, the trial and error time-consuming practice;
- to be extremely reliable and capable of fast response times.

The requirements listed above are rather crucial especially in view of the experimental nature of the machine that will require maximum operating flexibility. In particular the last one is essential for a safe handling of high power beams in a superconducting environment.

Moreover, as extensive use of modeling is to be implemented since the very beginning, the full integration of the diagnostic system into the computer control system is a major design constraint.

The ultimate goal of the diagnostic and control system is the capability for the operator to set the requested value of a given beam characteristics (e.g. emittance, current intensity, time

structure) and let the computer system act so that the measured beam characteristic matches within reasonable limits the requested value.

Tuning and maintaining the optimal conditions of a beam may eventually require the implementation of real-time feedback loops acting on different systems, on a time scale that can range from minutes down to seconds, sometimes on a pulse-to-pulse basis (e.g. correction of a kicker magnet firing time); these loops could be computer-mediated. The need for within-the-pulse feedback is at this stage excluded.

The features of the Ares Linac most relevant for establishing the number and type of beam diagnostics and control components and instruments are:

- high power beams may permanently damage the accelerator and/or create inacceptable radiation levels if mis-steered. We recall that the SC RF cavities can be quenched by few Joules of incident energy, to be compared with a beam power in the order of tens of kWatts.
- very low emittance beams;
- the intention of using the accelerator as a test-bench for collider and FEL grade beams. This calls for extensive and redundant general-purpose beam instrumentation. Moreover, the implementation of special instrumentation and of sections devoted to some particular beam measurement may be occasionally required.

A list of the main accelerator complex component systems is given in Table 4.1.1.

Table 4.1.1 - ARES Main Components

INJ	Injector	4 MeV
IBAS	Injector Beam Analysis Station	output of INJ
TCI1	Transport line from injector to Linac 1	
L1	SC Linac, Section 1	48 MeV
LBAS	L1: Beam Analysis Station	output of L1
TC12	Transport channel from L1 to L2	
L2	SC Linac, Section 2	48 MeV
TC23	Transport channel from L2 to L3	
L3	SC Linac, Section 3 - Main Sect.	240 MeV
TC2	Recirculation Channel 2	e^- to PC
TC3	Recirculation Channel 3	e^- or e^+
PC	Positron converter	
LW4	'Warm' Linac Sect.4	52 MeV e^+
TC42	Transport channel: L4 to L2	
TCNF	Transport channel : e^- to Phi-Factory	
TCPF	Transport channel : e^+ to Phi-Factory	

4.2. - BEAM DIAGNOSTICS

The full complement of beam instrumentation is summarized in Table 4.2.1.

Wall current monitors with a bandwidth up to ~ 2 GHz are used for the monitoring of tightly bunched beams.

The total beam current is monitored by toroidal current transformers having a bandwidth in the range from a few Hz to ~ 20 MHz. An auxiliary winding, carrying pulses of known charge provides a calibration signal to be injected in between successive beam pulses. Current transformers are placed at the beginning and at the end of each Linac section and of each transport line, to monitor the accelerated beam current. Whenever a significant beam loss is detected, a beam stopper is automatically inserted upstream and the gun current is lowered.

Table 4.2.1 - Summary of Diagnostic Devices

TYPE OF DIAGNOSTICS	INJ	IBAS LBAS	L1	L2	L3	LW4	Transport Channels	Positron Converter
Wall current monitor	1	1+1	2	2	2	2	2/TC=16	
Toroidal current monitor	1	1+1	2	2	2	2	2/TC=16	2
Beam dump/Faraday cup	1	1+1	1	1	1	1		1
Energy defining slit		2+2					8	1
DC Current transformer	1				1			
Beam position monitor		3+3	7	7	11	2	~160	
Emittance monitor		1+1						
SEM grid/rotating wire	1	1+1					21	1
Fluoresc. screen + TV	1	1+1					21	1

Each Linac section is protected by a retractable beam dump incorporating a Faraday cup for precision current measurement. The Faraday cup structure is coaxial so that it can also be used to measure the incoming beam fast time structure. When the upstream Linac section or transport channel are being set-up or optimized, the input beam stopper of the next section is kept inserted until the incoming beam characteristics are acceptable.

Computer controlled moveable slits are used along transport lines to scrape away any beam halo outside the channel acceptance limit and to prevent distributed beam spills.

At the exit of the injector a measurement station (IBAS) is provided to fully characterize the beam in the longitudinal and transverse phase-space. The measurement station includes a spectrometer magnet to measure the beam energy and energy spread and a transverse RF cavity to measure bunch length.The basic arrangement is similar to that implemented on Lisa [1].

The measurement of a low emittance beam is best done at low energy, at the injector output, in two steps. The beam transverse size is first measured, at a given location, by scraping it with a motorized blade, measuring the transmitted current to a Faraday cup as a function of the scraper position and computing the transverse charge distribution by differentiation. The opening angle is then measured by passing the beam through a narrow slit and measuring the transverse dimensions by means of a fluorescent screen and a TV camera, located downstream the slit after a sufficiently long drift space.

An emittance measurement station (LBAS) is provided at the the end of the first superconducting Linac section, L1.

Energy measurements are done in the non-zero dispersion regions of the transport lines and of the recirculation arcs by means of fluorescent screens and TV cameras or secondary emission devices such as rotating wires or retractable wire grids. No beam intercepting devices are foreseen on the SC Linac.

The beam emittance is measured at the output of the Linac sections LW4, L2, L3 in order to dinamically match the optical functions of the following transport channels and to optimize beam steering; this minimises the emittance degradation. The transverse emittance is determined by measuring the beam transverse dimensions with a fluorescent screen as a function of the orientation of the phase-space ellipse corresponding, i.e. of the strength of an upstream quadrupole. Since the transport matrix from quadrupole to screen is known, the beam emittance can be determined by a quadratic fit of the beam size vs. quadrupole strength curve [2].

4.3. - BEAM POSITION MONITORS

Beam position monitors (BPM) are used to measure and steer the beam trajectory in the Linacs, transport channels and arcs.

Longitudinal and transverse wake fields in the RF cavities, that may blow up the beam longitudinal and transverse emittances, have to be reduced to a minimum; the beam must therefore be made to enter the Linac section as exactly as possible on axis and be kept there. Preliminary calculations [3] show that, because of the relatively low Linac frequency, the absolute accuracy required of the beam position monitors is ~ 0.1 mm, comparable to the

standard quadrupole position alignment tolerance. The resolution should be better than the minimum rms beam transverse size, i.e. ~ 50 μm.

One BPM per quadrupole is foreseen. The BPM's are designed to fit inside quadrupoles and are installed on all Linac, transport channel and recirculation arc quadrupoles . The mechanical center of the monitor is precisely referenced to the quadrupole axis. Shielded bellows at both ends mechanically decouple it from the rest of the vacuum chamber (see Fig. 4.3.1).

To fully exploit the potentials of the Superconducting Linac, the BPM and the associated electronic detector are designed to work with any number of bunches and any time structure of the beam. They consist of four 50 Ω strip-line electrodes [4] short circuited at one end, inside the vacuum chamber. The four strips are everywhere arranged in the horizontal and vertical plane for direct X and Y position readout, except in the vicinity of the spectrometer magnets and in high dispersion regions [2] where they are mounted at 45 degrees.

The strips are 0.15 m long, to produce a broadly resonant response at around 500 MHz, the Linac drive frequency.

The strip-line monitor voltage response is a doublet of opposite polarity pulses, separated by a time interval of 1 nsec, in coincidence with each bunch. Since the waveguide cutoff frequency associated with the vacuum chamber radius is ~ 2.2 GHz, no RF feed-through is expected at the monitor location.

A schematic view of the beam position electronics is shown in Fig. 2. The narrow pulses are smoothed by the filtering action of the cables connecting to the detector head and are fed to band-pass filters resonating at 500 MHz. The pass-band shape is such as to let the ringing response decay within approximately 50 nsec (quality factor ~ 20), in order to discriminate between the electron and positron bursts when injecting into the storage rings. The 500 MHz pseudo-sinusoids are down-converted to 71.4 MHz by means of mixers with a local oscillator frequency of 6 • 71.4 MHz, amplified and fed to the detector. The position detector is based on the phase modulation-demodulation technique, whereby the amplitude ratio of two opposing strips, carrying the position information, is converted by means of a quadrature hybrid junction into a phase difference between two pseudo-sinusoidal signals [5]. The advantage of such type of detector is that it is self-normalizing: i.e. the position information is independent of the current intensity. The output of a phase detector gives the position information.

A gate signal provided by the beam timing system allows to select any one beam pulse (electron, positron, first or second passage). The detector operates at any bunch configuration in the range from single bunch to continous beam. Detectors operate in a multiplexing mode to sample the position of groups of 10 BPM's.

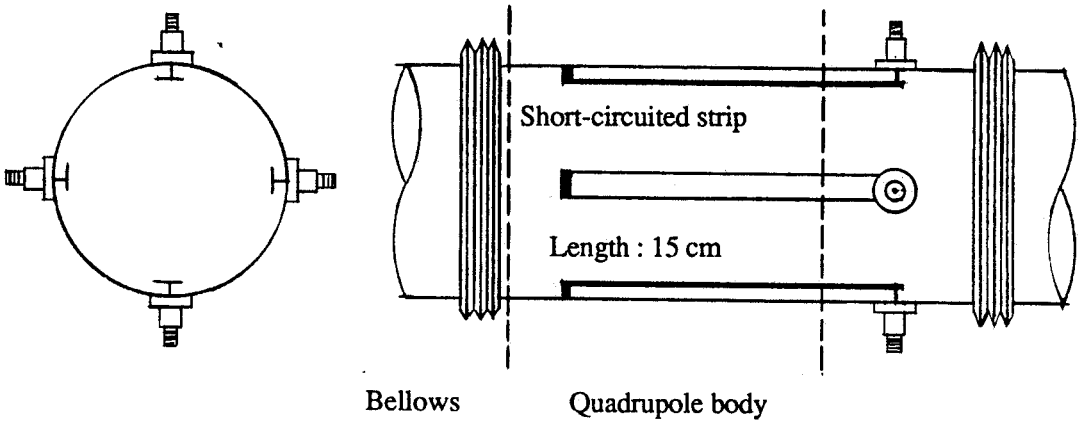

Fig. 4.3.1 - Schematic view of a strip-line Beam Position Monitor of the section L3 quadrupole.

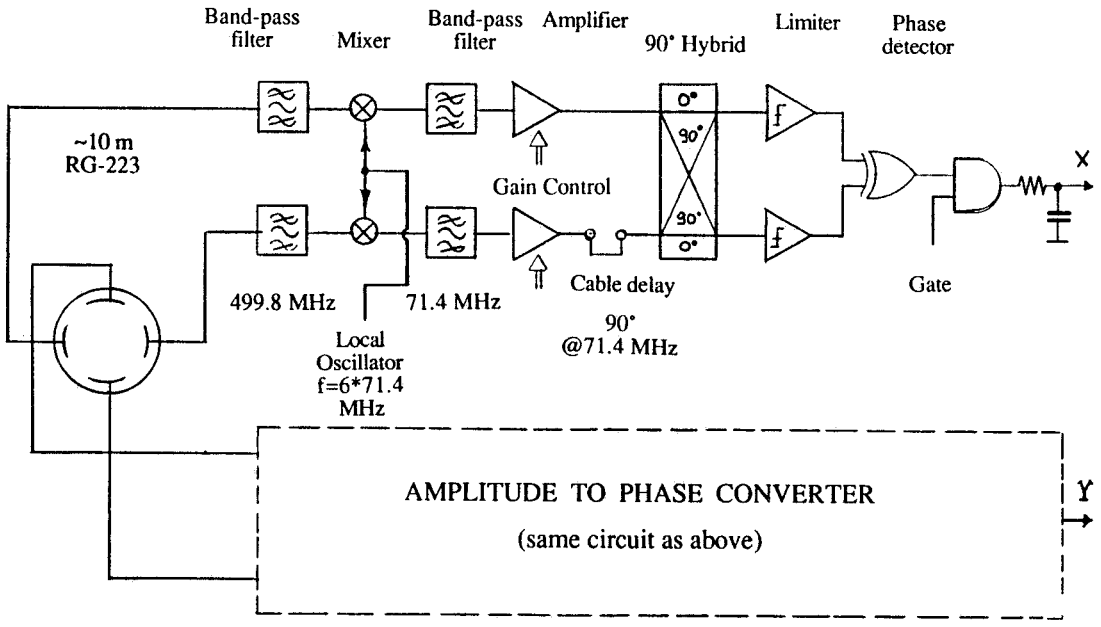

Fig. 4.3.2 - Schematic diagram of the beam position monitor detector.

4.4. - CONTROL SYSTEM

4.4.1 - Introduction

The Control System is a very critical point for an accelerator complex, especially if tight constraints are posed on beam quality and or on the performance of the machines, the last being heavily dependent on the availability of a good and reliable hardware and software environment.

The Control System has therefore to be part of the machine design itself and must develop in parallel with it. It can be thought of as having two main parts:

- the "real machine" part consisting of the control hardware and software used to interface equipment and instrumentation; its design must take into account the accelerator topological and functional distribution and avoid data flow bottle-necks.
- the "virtual machine" part consisting of the control, modeling, simulation and optimization software; its design and commissioning is determined by accelerator physics and is, therefore, closely related to the machine type and the specified overall performance.

The initial design of a new accelerator control system is always complicated by the accelerator components and parameters to be controlled not usually being completely specified at the beginning of a project and also by the fact that performance as well as cost of components and tools that come on the market evolve very fast on the time scale of the average project.

The vertical growth of hardware capabilities in the computer field (computing power and memory capacity keep doubling every 2-3 years, and the growth curve shows no signs of a plateaux) creates an environment where whatever is functioning is definitely old. Moreover, the corresponding development in the software field keeps delivering new tools which are not only powerful, but also easy to learn and to use. The situation is thus definitely unstable but, on the other hand, an ever increasing number of powerful tools, which become reliable very soon because the number of users is also growing fast, are thrown on the market. The involvement of industry in the electronic standards also provides the user with always new and more reliable instruments. A classical example is the amazing speed at which the VME standard has diffused, as compared to CAMAC.

On the other hand the lifetime of an accelerator is comparatively long and during its span the machines are usually partially or even totally reconfigured. Hardware and software products used in the system should therefore be standard, possibly non proprietary, with large diffusion, so that they may be expected to receive strong support from the manufacturer over many years.

We have here tried to lay down some basic scenarios, based on current philosophies about hardware and software architectures[6] so as to be able to derive reasonably reliable cost and manpower estimates. A definite detailed solution has not however being singled out as yet and a

final committment will be made only at the very last moment compatible with the time scale of the project.

It is worth recalling here that, from the point of view of the control system, the general features of the ARES accelerator complex are:

- Linac and Φ-Factory are separate but must be able to operate synchronously and in very strict correlation.
- The physical dimensions of the site are of the order of a few hundred meters.
- The accelerators are also to be used as a test benches for accelerator development. This means that the control system must be particularly flexible and friendly towards both professional operators and machine physicists.

Two different lines of approach to the problem of designing the system are being investigated, based on what has or is being done on similar projects such as LEP[7], ESRF, ELETTRA[8], and our own LISA[9].

One is a 'conventional' distributed system, along the lines of those installed and tested on LEP or being implemented at ESRF and ELETTRA, the other is a less conventional centralized system based on the one being implemented for LISA.

Both have advantages and disadvantages that will be briefly discussed in the following. From the point of view of capital cost there are no substantial differences and a final decision on which to adopt can be taken later.

Both are based on the use of VME as a peripheral interface.It is the most modern, practical and widespreaded modular electronics interface standard and distributed processing system. Because many of multi-vendor products based on the 68K family are available, specific choices are not critical.

4.4.2 - Distributed system

As said above, the accelerator complex consists of two distinct parts: the recirculating linac and the double storage ring. Although the control system is unique the linac and the rings machines are operated separately. From the machine component point of view several sub-systems can be identified such as magnet power supplies, RF, vacuum and refrigeration equipment, beam diagnostics sensors, alarm monitoring and access control. A structure capable of coping separately with all procedures and functionalities along the machine - a flexible, modular and open scheme, implemented using intelligent and hierarchical levels - is the answer to the problem.

It includes a local area network (i. e. ETHERNET), workstations with high processing speed and very powerful graphics to serve as consoles for the human interface, one of the

several software tools able to generate windows, menus, etc., and finally an operating system for the peripheral CPU's which has already been used and debugged.

The whole system is distributed, so to ensure local processing power to set, monitor and diagnose the hardware. Topological and/or functional criteria are taken into account. A modular approach, provides the required flexibility.

Based on the above concepts, the four logical level architecture briefly described in the following is proposed[10]; its block-diagram is shown in Fig. 4.4.1. Note that although not each box in the diagram has been named at this stage, real products have been considered for the various blocks.

First level

A few workstation consoles and one server provide the man interface to operate the accelerator. The powerful graphics capabilities can be used to increase the "bandwidth" of the operator comprehension and the processing power provides adequate support for modeling and/or simulation.

The server provides the general Data-Base, the normal spooling and log file management, other service programs and the link to the external network. Sub-systems and low level instrumentations can be deep-accessed through personal computers, with unsophisticated tools. A special personal computer is completely dedicated to the continuous monitoring of alarm messages incoming from the lower levels.

Second level

It consists of several supervisor processors that manage all procedures needed to operate different machine sub-systems and provide general control functions for all main accelerator parameters. To limit the need for throughput to the first level, they also filter-out insignificant messages and are thus able to manage the sector they supervise without overloading the consoles.

The processors are connected to an appropriate network so that they can be physically placed where they are most useful.

Third level

The third level consists of several additional processors, sharing the VME bus, that manage smaller accelerator parts or sub-systems. They mainly provide setting and readout functions for all linked modules. A continuous monitoring procedure informs the second level supervisor on the status of the hardware. A distributed Data-Base can thus be up-dated.

Fourth level

The lowest level is the interface to the accelerator hardware proper (such as magnet power supplies, RF, vacuum and diagnostics components etc.). Many of the interfaces have only a limited number of channels (typically ADC, DAC and I/O bits) and can be served by a same, simple, general purpose module. General purpose instrumentation interfaces, typically IEEE-488 and the new VXI, are also foreseen.

The physical size and the topology of the accelerator complex and the need to provide distributed power, require a network system that can serve different kind of processors.

In principle each processor (console, server, sub-system supervisor and lower level distributed CPU) could have a different operating environment (a general or special purpose operating system or simply a real-time kernel). Standardization is however a must, in order to reduce the amount of software development and improve the message-exchange performance in a non homogeneous environment.

Careful analysis of the requirements in terms of message size, necessary speed and transmission rate, indicates that three different types of links are required:

- link between consoles, server and supervisor processors. Because of the small number of nodes (<20) an IEEE 802.3 Ethernet CSMA/CD link with TCP/IP protocol is the most suitable. Non deterministic behaviour can be minimised by leaving most of the machine management to the sub-system supervisor so that the number and size of messages are drastically decreased.
- link, connecting each supervisor to the lower level CPU's (both in VME crates). It consists of a fast parallel bus, like VICbus (formerly VMV bus), and of a slower serial multi-drop, such as MIL-1553-B. Depending on the particular demand, both can provide optimal links among several crates, a feature not foreseen by the VME standard.
- link between end-level VME crates and specific equipment. As earlier mentioned, a very simple special module can be implemented to interface to several types of power supplies. A multi-drop highway based on a simple command-response protocol is a very cost-effective solution.

As concerns software, one notes that while hardware costs are falling and high performance products are continuosly coming on the market, overall software charges - including development - are on the rise. As a consequence a multitude of soft/hardware integrated solutions, are offered on the multi-vendor market as turnkey solutions.

In line with the general scheme outlined above, we choose the UNIX operating system,with C and FORTRAN, for the console level. As a data-base we will adopt Oracle, the most diffused and supported. General modeling programs (such as MAD and PARMELA) will be

implemented to serve as tools for the "virtual machine" control system programs. Lower levels will use the OS-9 operating system, C, FORTRAN and Assembler.

To make the system as user-friendly and possible all modern tools such as X Windows, Dataviews, DV-Draw and DV-Tools are being investigated.

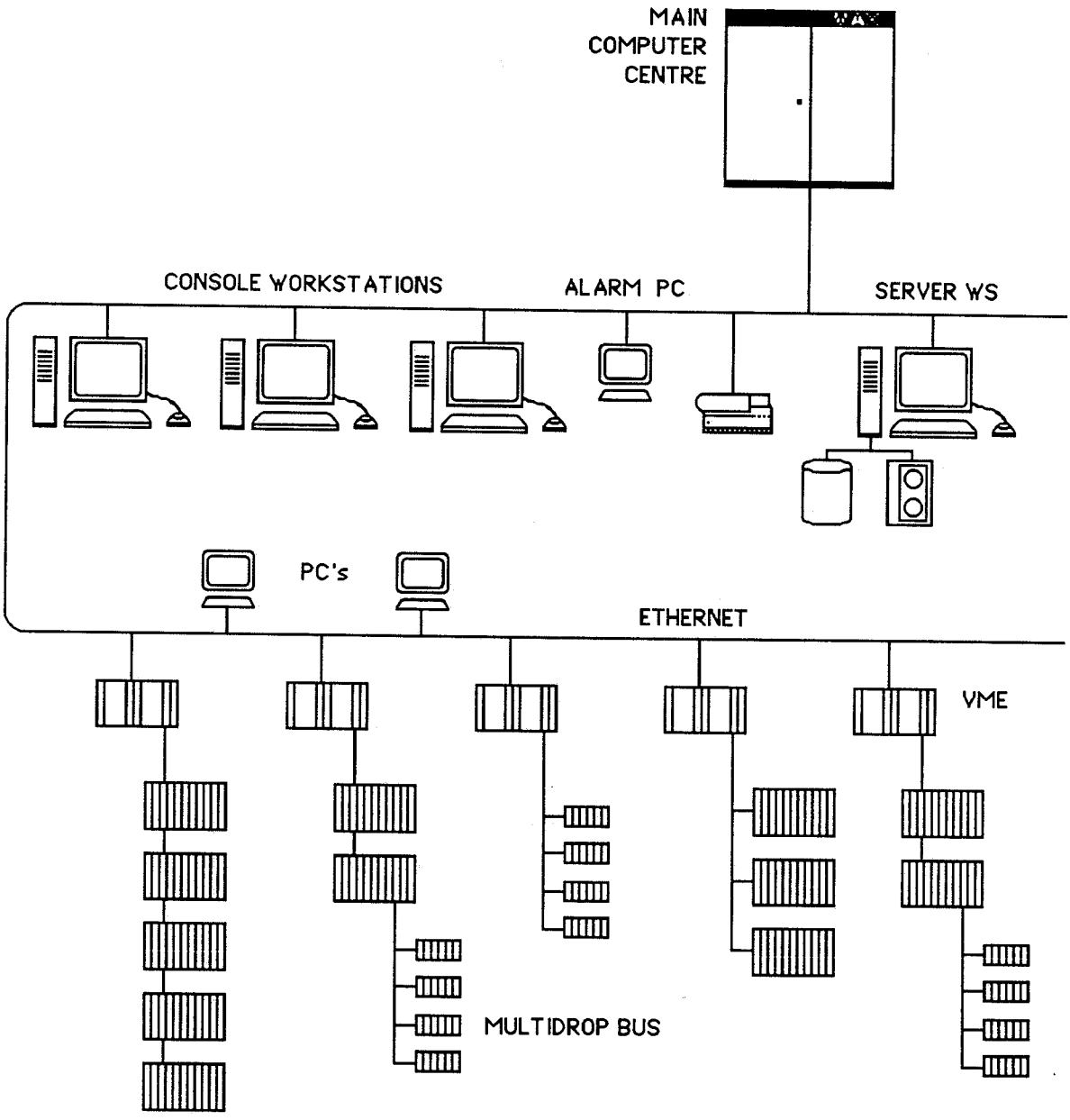

Fig. 4.4.1 - Block diagram of the Distributed System Configuration

The main advantage of the system is mainly that of requiring very little development and of being able of readily making use of the hardware and software tools, developed for instance in the course of the joint program between ESRF, Elettra, CERN, et al. that has resulted in a marked improvement in standardization.

4.4.3 - Centralized system

The controls for LISA [1] were (and are being) developed in an attempt to develop a new approach to an integrated accelerator control system and to use the fact that increasingly powerful tools are continuously being marketed.

As an example it will become possible to use FDDI instead of ETHERNET, with a net increase in speed of a factor of ten. Copper cables will be replaced by fiber-optics cables, allowing larger distances to be covered without repeaters and increasing the connection reliability, at least as long as low radiation environments are considered. OS-9 will be probably replaced by the Motorola VMEexex, which supports not only multitasking but also multiprocessor systems.

During the development of the LISA control system, quite a few new ideas have been implemented and more are being tested.

The basic idea is to concentrate and centralize the communication system because a centralized system is more simple to handle and also more reliable, since attention can be paid to only a small number of easily replaceable units.

This is contrary to what is generally claimed about the reliability of a distributed system, but it has to be noted that there is a conceptual difference between an accelerator control system and a system which has to meet military standards: reliability considerations can change dramatically when a network which has to be able to continue functioning, even partially, in case of intentional damage is considered instead of a control system - limited to a few buildings - for an experimental physics setup.

The implementation of a centralized system is made possible by the availability of very fast parallel buses [2].

The LISA system is built around a central VME processor which coordinates all the communications between different parts of the entire setup and keeps updated a central memory which constitutes the prototype of the system database.

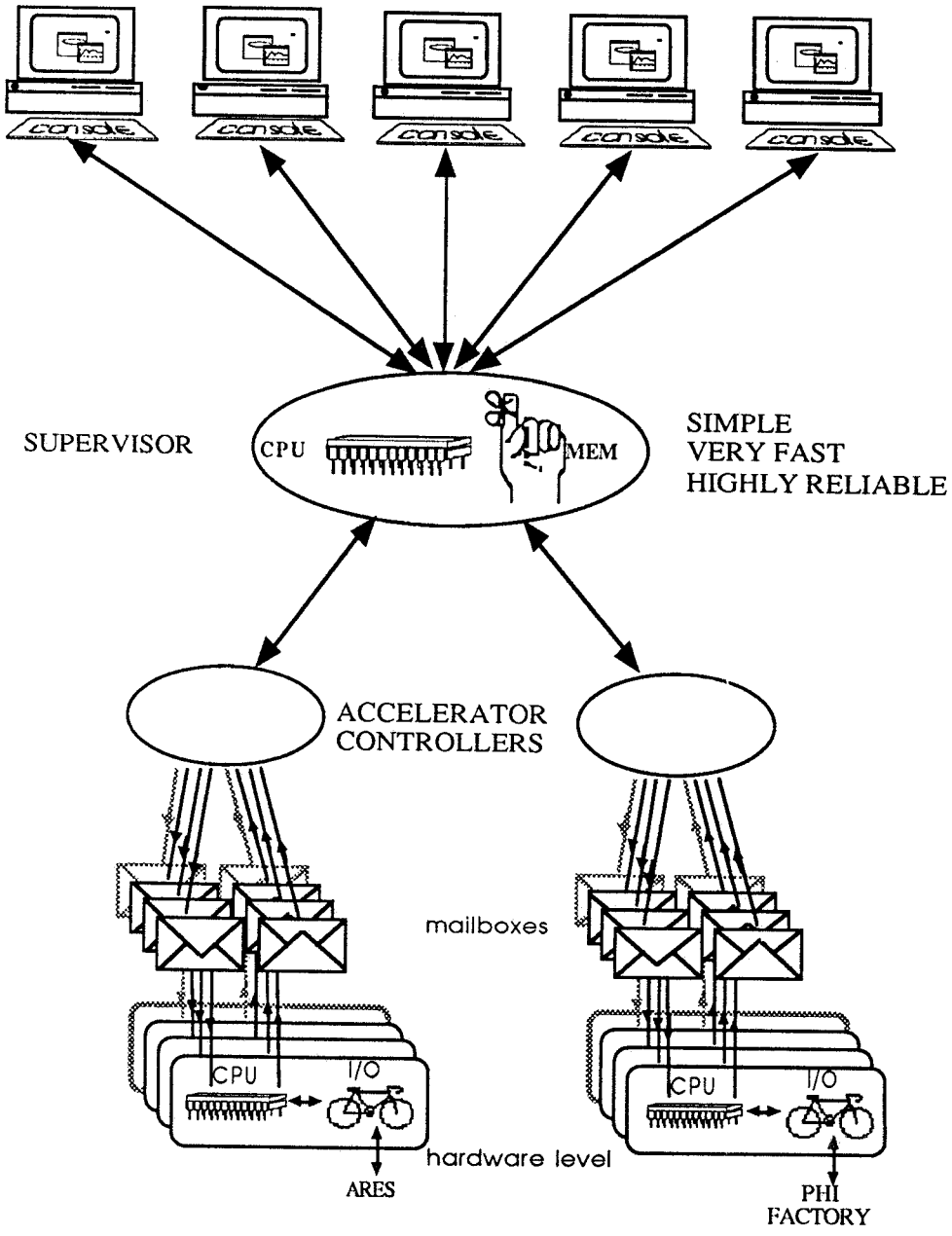

Fig. 4.4.2 - Block diagram of the Centralized System Configuration.

In a multiple accelerator environment it would be very easy to extend this scheme using a tree configuration. You would have more than one central processor, possibly one for each machine, and an additional upper level coordinating the local supervisors. The different roots of the tree would act as filtering bridges, transmitting to the upper levels only the necessary

information and shielding the main supervisor from local traffic. A possible block diagram is shown in Figure 4.4.2.

The high speed local buses used in LISA suffer from distance problems: it is very difficult to operate them at distances over 100 meters. Fortunately, several fiber optic connections are appearing on the market to replace our 60 conductor cables. Although the optical fibers are sensitive to radiation damage, it is easy to implement a mixed system where large distances are covered by fiber optics trunks, while local cables could cover the high radiation level sections.As far as software aspects are concerned, new and powerful tools are being developed for the easy implementation of the human interface, which has been a gigantic problem up to now. Hypercard is a first example of this kind of software.

For the peripheral CPU software the usual solution of a multitasking system is nowadays strongly under objection. A multitasking system for a peripheral CPU which only has to look at a few memory locations every now and then looks very much like trying to kill a fly with a cannon. The opposite point of view is represented by the famous statement "One task, one processor". This is an optimal way to look at things, although, as with every beautiful theoretical construction, it sometimes suffers from implementation problems, like having to buy a new CPU to perform some really trivial task. The intrinsic soundness of the principle however lies in its extreme simplicity.

The main advantages of the centralized system configuration is the large bandwidth afforded by the direct memory access mechanism. For example, the LISA system allows the exchange of 1700 messages per second in between (the three) levels, while comparable systems built around ETHERNET have a capacity of only a few tens of messages per second.

An additional advantage of such a hierarchical system is the centralized database. A single location for all machine status data means no problems of memory consistency and very easy maintenance.

Although some authors find the 'centralized' software a difficulty, the central argument for this kind of solution is that new, powerful tools are becoming available and should be used and that the statement "old is more reliable" does not apply to software.

References

(1) B. Spataro, LNF Internal Memo LIS-30 (1988)
M. Bassetti, B. Spataro, LNF Internal Memo LIS-42 (1989)
M. Castellano, LNF Internal Memo LIS-53 (1989)
R. Boni, A. Gallo, LNF Internal Memo LIS-68 (1990)

(2) J. Rees, L. Rivkin, SLAC-PUB-3305 (1984)
K.T. Mc Donald, D.P. Russel, Lecture Notes in Physics-343, M. Month and S. Turner eds., pp. 122-132. Springer-Verlag 1989.

(3) S. Bartalucci, C. Biscari, L. Palumbo, LNF Internal Memo ARES-20 (1989)

(4) R. E. Shafer, IEEE Transactions on Nuclear Science, Vol NS-32, No 5, p. 1933 (1985).

(5) E. F. Higgings, J. E. Griffin, IEEE Transactions on Nuclear Science, Vol NS-22, No 3, p. 1574 (1975). J. Borer, R. Jung, CERN 84-15, p. 416 (1984).

(6) Int. Conf. on Accelerator and Large Experimental Physics Control Systems, Vancouver, October 1989.

(7) P.G.Innocenti, "The LEP Control System: Architecture, feature and performance", CERN-SPS/89-35 (ACC) (1989).

(8) M.Mignacco, Int. Conf on Accelerator and Large Experimental Physics Control Systems, Vancouver, October 1989.

(9) M.Castellano et al., IEEE Trans, on Nucl. Sci. 36, 1619 (89).

(10) N.Cavallo, LNF Internal Memo ARES-29 (1989)

5. - BUILDINGS AND UTILITIES

5.1. - GENERAL DESCRIPTION

A site independent design study of the civil engineering work for the project has been done to identify the main requirements and estimate the costs (see Chapt. 5).

A flow chart of the approach to project planning is shown in Fig. 5.1.1. All main elements of the plan have been studied to arrive at the proposed choices.

The planimetry shown in Fig. 5.1.2, includes the Linac tunnel and experimental hall, the Φ-Factory hall including the detector assembly space, the power and plant buildings, urbanization and roadwork.

The tunnel, the Φ-Factory hall and the Linac experimental hall structures are underground earth covered concrete structures for reasons of radiation shielding.

The concrete structure thickness and the foundation depth should be optimized to minimize costs. At this stage it has been assumed that five meters of 2.4 t/mc concrete, or an equivalent earth (1.6 t/mc) thickness are required to guarantee good shielding under all operating conditions. Such a preliminary estimate is probably conservative and will be refined by more detailed shielding calculations.

The Linac tunnel is a 162 m long box-like concrete structure having a useful internal width of 10 m; it is equipped with two 3 ton cranes having a minimum hook height of 3.7 m. The first 30 m of tunnel house the linac injector and the last 30 m serve as experimental hall for the Linac itself. A line of central pillars at 6 m intervals divides the tunnel in two longitudinally; unencumbered passage of people and cable runs from one side to the other, flexible space allocation and the possibility of future upgrades are thus guaranteed. At present it is foreseen to lay out the RF structure on one side and the recirculation channels on the other.

The roof is a 1 m thick concrete slab covered by 6 m of earth. The accelerator floor is 12 m below the ground level. To keep a minimum beam height with respect to the floor of 1.2 m , the floor is actually at -13 m over the first 60 m of tunnel and at -12.7 m over the last 35 m; two ramps, with a maximum slope of 8%, connect these terminal areas to the central one.

The tunnel entrance is connected to the surface by a 5 m wide ramp road; in front of the entrance a yard provides manouvering space for incoming lorries. Two more accesses to the tunnel, to serve as personnel accesses and fire escapes, are placed one at the linac end opposite to the entrance and the other at the tunnel midpoint. They are equipped with stairways and with a goods lift. The maximum distance to a fire escape is thus about 40 m, in compliance with existing regulations.

The three 580 MeV beams generated by the Linac lie in the same vertical plane. The center beam continues straight-on towards the linac experimental area, the other two are bent sideways and brought through the side shielding wall to the Φ-Factory Hall, whose floor is at the same level as the tunnel floor, for injection into the storage rings.

A 46 m by 20 m hall, physically separated from the tunnel by the side shielding wall, houses the Φ-Factory and its experimental equipment. A ramp like the one mentioned above allows heavy equipment to be brought to it. The hall is also equipped with a personnel access and fire escape exit similar to the ones giving access to the tunnel.

The Hall houses the storage rings and the Detector. Extra space, separated from the rest of the room by a wall of moveable shielding blocks, is also provided, into which the Detector detector can be retracted, using hydraulic lifting-jacks and rails, for assembly and maintenance while the storage rings are in operation. A 28 m span, 50 ton crane serves the whole area. A 5 m high clearance is provided above the detector for installation and shielding.

The Hall is about 16 m high and its roof, ≈ 2 m above ground, is forseen to serve as the floor for a service building. The solution will have to be cleared by Health Physics; at this stage of the design, it has been foreseen to protect the service building by providing concrete shielding right next to and above the storage rings.

All other service buildings are at ground level.

A general purpose service building, also used as a klystron gallery, runs above and parallel to the Linac tunnel, is connected to it by one of the above described staircases and goods lift, and extends over part of the Φ-Factory hall ; connecting cable ducts are provided for cables and piping (RF wave guides, electrical cables, cryogenic transfer lines, water piping, etc.).

The building is 12 m wide and is serviced by a crane with 6 m hook height.

Besides the RF generators it houses the cold-box, all magnet power supplies and all conventional plants such as heating and air conditioning, compressed air, water cooling, electrical distribution etc. for the Linac and the Φ-Factory, and includes some office space, a few small laboratories and the main control room.

A full description of he urbanization works, such as sewer system, internal roads, water cooling system, electric and telephone installations, landscaping, fences, illumination etc., is at the moment missing, because details will depend almost entirely on the chosen site.

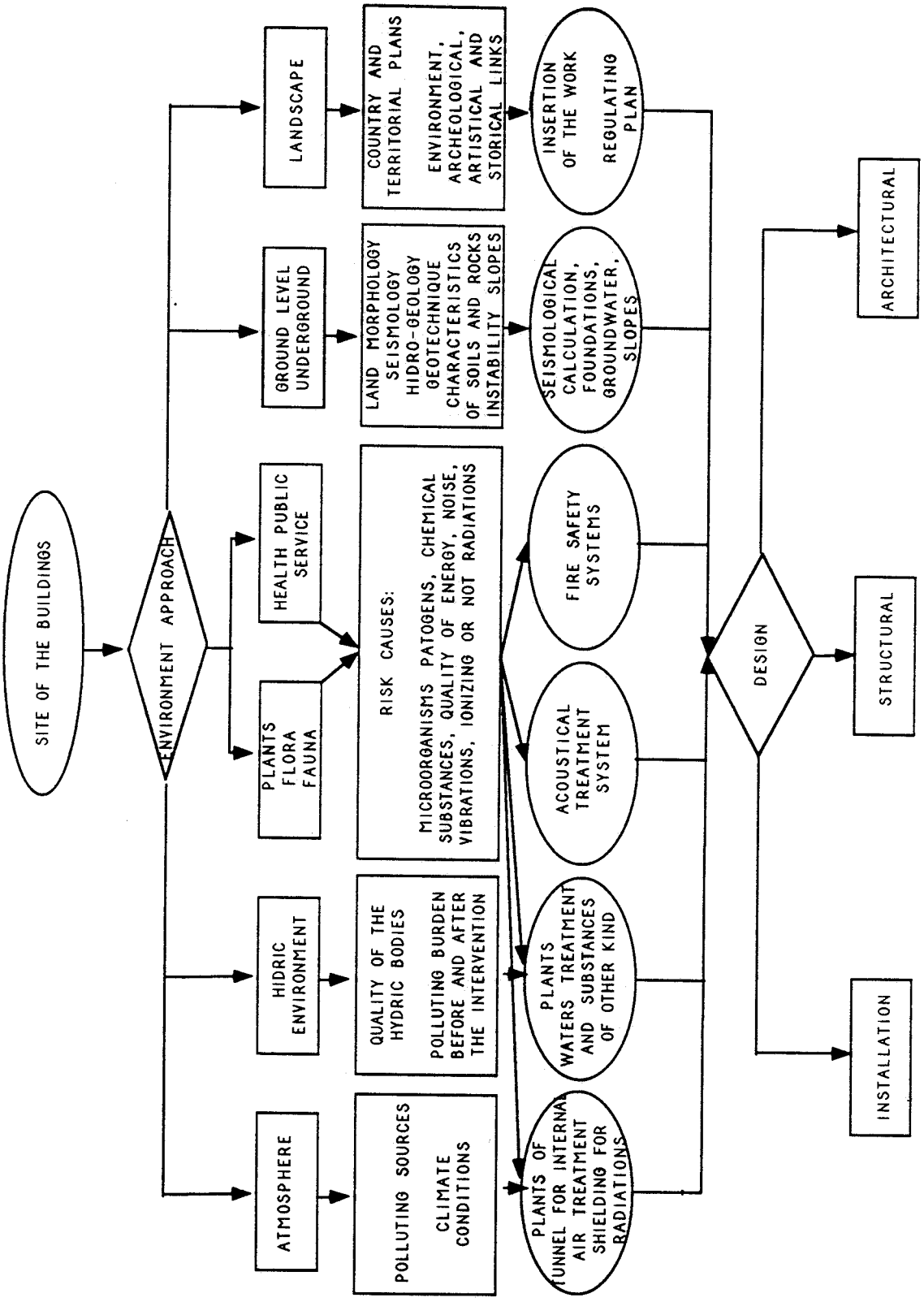

Fig. 5.1.1 - Flow chart of the approach to project planning.

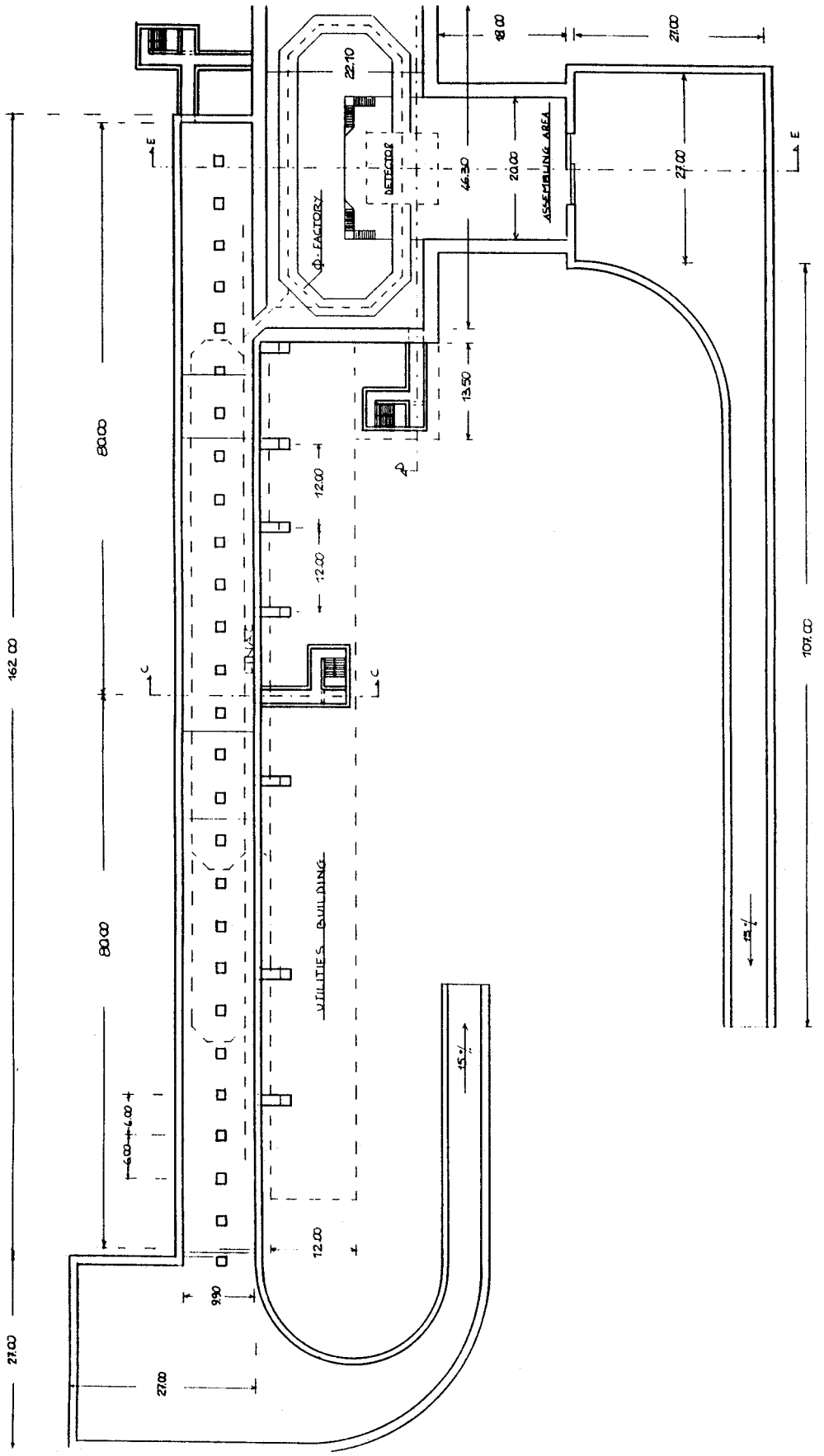

Fig. 5.1.2 - Planimetry including the Linac tunnel and experimental hall, the Φ-Factory hall with the detector assembly space, the power and plant buildings, urbanization and roadwork.

5.2. - PLANTS AND GENERAL SERVICES

5.2.1 - Description

The two main buildings housing technological and conventional industrial plants, laboratories, offices, control rooms, etc., one serving the Linac the other serving the Φ-Factory, are at ground level.

The first runs above and parallel to the Linac tunnel and is equipped with a 5 ton crane covering the full building length. This solution optimizes plant layout and costs.

The cold-box is installed on central area so that a symmetrical feed system for the accelerator cryostats can be implemented with only one liquid helium and gas descent, serving the same numbers of cryostats right and left, is needed. The balanced load makes the plant less expensive.

The Linac service building includes offices and laboratories physically separated from the plants mentioned by means of moveable walls which provide maximum flexibilty in adapting to any future requirement.

The helium compressors to which the cold box is connected are noisy and must therefore be accomodated outside the main building; a 7 m x 20 m industrial type building will house a sound-proof enclosure containing two 1 MW compressors; another separate compartment in the same building is used for the gas purification and oil removal machinery. Three 12 atm, 200 m^3 gas storing tanks are installed in the open.

The central heating system will also occupy a small, separate construction.

The Φ-Factory service building is built over the latter (Fig. 5.2.1.), to which it is connected by an internal stair with an adjacent goods lift (Fig. 5.2.2). Also this one receives at its interior all the plants for the machines and the conventional ones, offices and laboratories included.

Only one control room, for the linear accelerator and the Φ-Factory is located in this building. It is necessary therefore to provide for it an enhanced removable floor which permits the passage of computers cables and others services, as well as an air-conditioning pipe system.

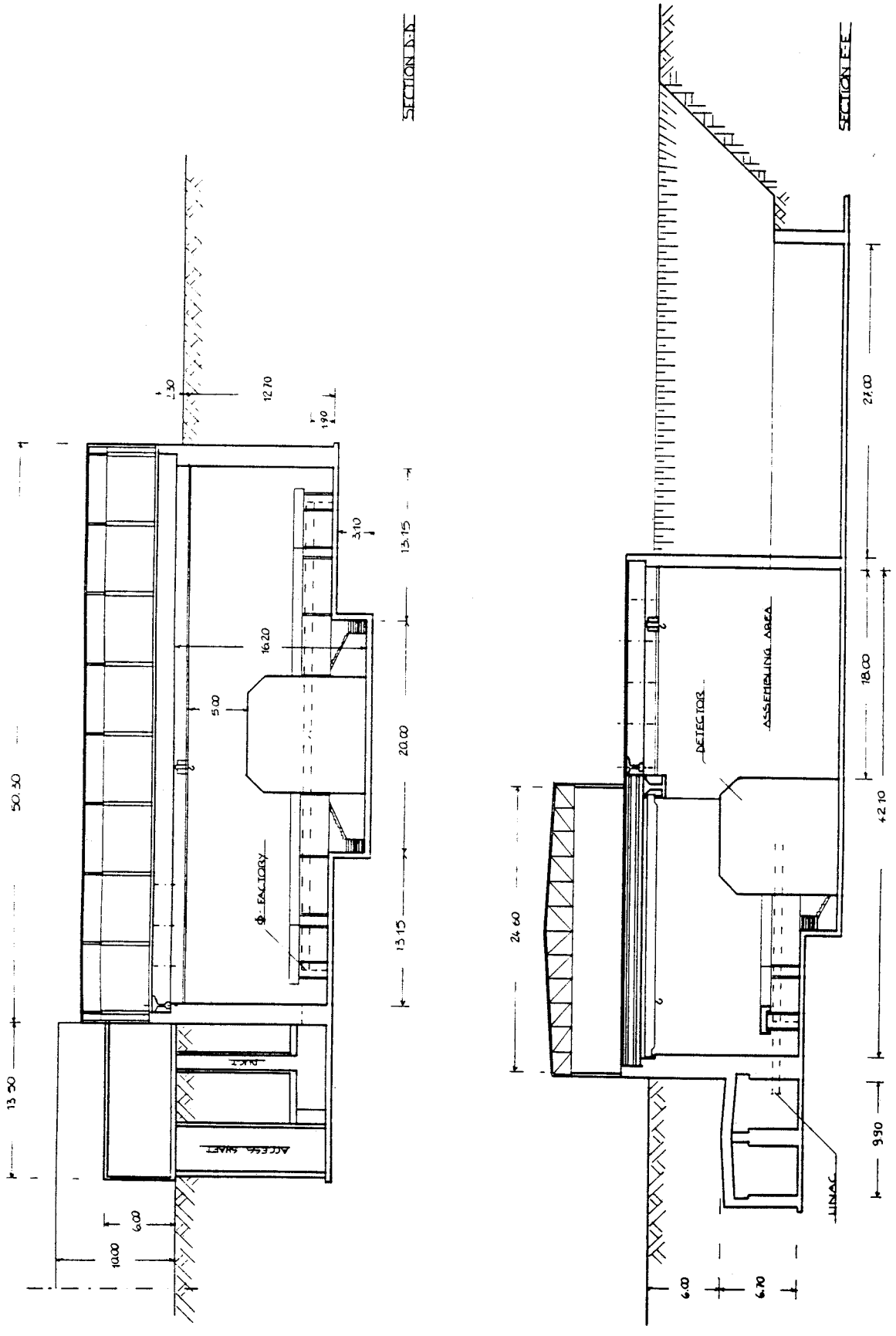

Fig. 5.2.1 - Φ-Factory service building, built over the Φ-Factory one.

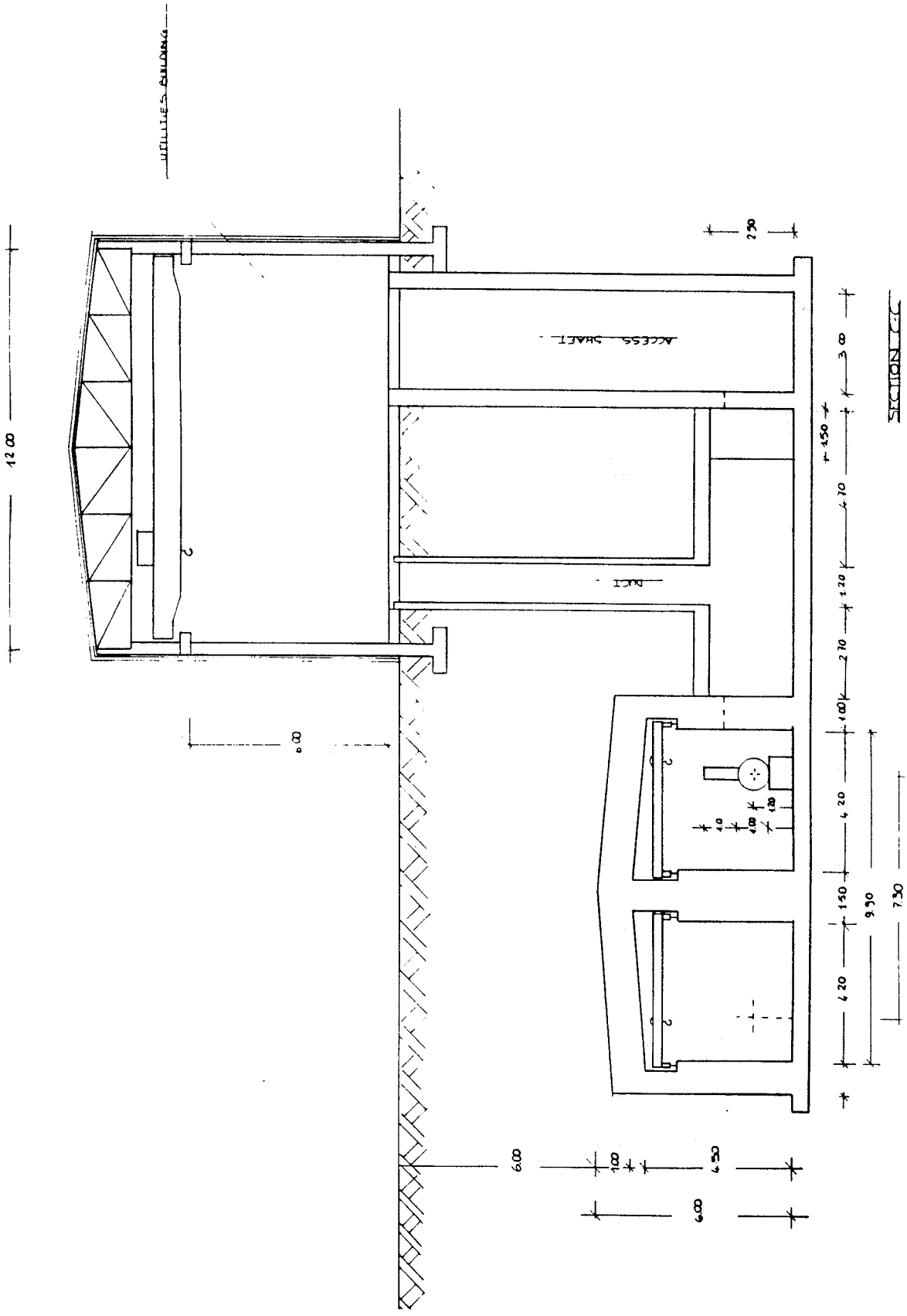

Fig. 5.2.2 - Connection between service and Linac buildings by an internal stair with an adjacent goods lift.

5.2.2 - Power Inventory

Usual the most power demanding systems are the magnets and the radio frequency,but here the use of superconducting components requires a significant part of the whole power to be devoted to cryogenics.The numbers listed in the power inventory are a first order estimate done for the purpose of cost evaluation; for minor details, still missing, concerning mostly conventional electrical services, the forecast is based on estimates derived from similar installations.

In particular, conventional plants include heating, air conditioning, lighting, compressed air plants, alarm & fire protections, etc. The power devoted to helium compressors depends on the liquefaction rate needed by the s.c. cavities and by the main detector solenoid. Another important power demand comes from the conventional 1.9 Tesla wigglers for the Φ-Factory; the numbers are scaled from those of the wiggler installed on Adone. Finally, it must be noted that the listed power - except ,of course, that for the general building services - is intended as maximum requirement, with both machines in operation at maximum energy.

The total power inventory is detailed in the following Table 5.2.1 and adds up to about 7.5 MW.

Table 5.2.1 - Power Inventory [kW]

LINAC	
Injector	300
Conventional & s. c. linac Quadrupoles	10
Recirculation Arcs Dipoles	240
Recirculation Arcs Quadrupoles	250
Special magnets (beam splitting magnets, chicanes, etc.)	250
Helium compressors	1300
Radiofrequency	250
Subtotal	2600
Φ-FACTORY	
Dipoles (two rings)	500
Quadrupoles " "	100
Wigglers 1.9 Tesla	1500
Other special magnets & devices (septum, deflectors, etc.)	200
Detector (integral field compensation)	500
Helium compressors (for detector solenoid)	1000
Radiofrequency	200
Subtotal	4000
GENERAL SERVICES	
Cooling water system	
Primary circuits with forced ventilation cooling towers	200
Secondary circuits for purified water	200
General building services	
7 % of the operating power	500
Subtotal	900
TOTAL	7500

APPENDIX

X-VUV POSSIBLE FEL EXPERIMENTS

L.Serafini, M.Ferrario, C.Pagani, A.Ghigo*, P.Michelato, A.Peretti

INFN and Università di Milano - Via Celoria 16 - 20133 Milano
*INFN Laboratori Nazionali di Frascati - P.O. BOX 13 - 00044 Frascati

1 - Introduction

The availability of intense electron beams of high quality makes the ARES SC LINAC complex a unique facility to perform several experiments in the X-ray VUV FEL mainstream. In this chapter we present a feasibility study of a device able to generate coherent radiation of high brightness in the soft X-ray VUV spectral region (photon energies in the 10-120 eV range), together with a tentative list of the possible FEL experiments.

Detailed, but still preliminary, numerical simulations will be extensively reported: they anticipate the FEL performances and support the enclosed lists of parameters concerning the beam quality requirements and the wiggler characteristics. These simulations have been carried out taking into account a new recently proposed technique: the "ion focussing" of the beam, achieved with a pre-ionized plasma channel added inside the beam pipe in the wiggler[5].

Some new applications of old ideas are also presented here for the first time, in the last two sections: they deal with the subject of coherent spontaneous emission. Inside our range of radiation wavelengths such new schemes will open the possibility to obtain coherent radiation wavelength of $\approx$ 50 Å, in the so called "water window". The new experimental physics field which may be explored with such a radiation source is, in our opinion, as wide as needed to justify the big effort to build such a device.

Indeed, it is well known that the shorter is the radiation wavelength, the higher must be the beam quality needed to operate a single pass high-gain FEL in the SASE (Self Amplified from Spontaneous Emission) mode. As shown elsewhere[1], the choice of a low frequency and a superconducting structure for the beam acceleration plays a crucial role in minimizing the beam quality degradation through the LINAC. In this respect, the injection system turns out to be one of the most important part of the whole complex.

It is worthwhile to mention that the SC LINAC will also constitute an experimental tool to study the beam-beam and the beam-radiation field interactions: such effects are of great relevance in the design of all future e^+ e^- TeV colliders. A better understanding of the beamstrahlung processes will surely allow to improve the feasibility and the performances of such machines.

2 - One Dimensional Model Predictions.

As elsewhere presented in more detail[1], the expected beam characteristics at the LINAC output, for FEL experiments, can be summarized as shown in Table 1. Having available beams with a relativistic factor, γ, in the range 600÷1200, one can easily observe that the resonant radiation wavelength, given by the usual FEL resonance relationship, lies in the range 200-20 nm (for the first harmonic) when wigglers with typical periods of a few centimetres are considered. In fact the FEL resonance equation is:

$$\lambda_r = \frac{\lambda_w (1 + a_w^2)}{2 \gamma^2 n}$$

where: λ_w is the wiggler period, λ_r the n-th harmonic radiation wavelength and a_w is the dimensionless vector potential of the wiggler. In a planar wiggler a_w is related to the peak magnetic field, B_w, by the formula: $a_w \approx .66\, \lambda_w$ [cm] B_w [T].

Table 1 - Expected Beam Characteristics

Beam energy	[MeV]	300 ÷ 580 (820*)	
Peak current	[A]	400	1000
Norm. transv. emitt.	[m rad]	$4 \div 8 \cdot 10^{-6}$	$4 \div 5 \cdot 10^{-5}$
Relative energy spread		$.5 \div 1 \cdot 10^{-3}$	$2 \div 5 \cdot 10^{-3}$

* Eventually obtainable with a second recirculation.

Unfortunately, the scaling law for the exponential growth of the radiation field is quite unfavourable in the very short wavelength domain. The gain length, L_g, i.e. the length over

which the radiation field intensity grows by a factor e, scales indeed like the beam energy divided by the cubic root of the wiggler period, as in the following formula, which holds in the cold-beam limit and before saturation[2]:

$$L_g \approx \frac{\gamma}{\sqrt[3]{J \lambda_w B_w^2}}$$

where J is the beam current density.

To reach the VUV to soft X-ray domain (radiation wavelength between 10 and 100 nm) high γ and short wiggler periods are both needed, B_w being dependent on λ_w as will be shown later. That implies that fine and intense beams must be used in order to overcome by the increase in current density the corresponding increase of the gain length.

It is well known that in an untapered wiggler, because of the exponential growth of the radiation field, once the high gain regime is achieved, intensity reaches saturation after a typical length of the order of $4 \pi L_g$: at that point the radiation power, P_r, is roughly given by the beam power, P_b, times the Pearce parameter, ρ, ($\rho = \lambda_w/4\pi L_g$), that is $P_r = \rho P_b$[2]. Then, the saturated radiation power comes out invariant with respect to the beam energy.

A more important scaling law sets a threshold for the radiated power, which must be high enough to ensure that the quantum fluctuations in the photon beam do not destroy the coherence properties of the radiated field: the condition is given by

$$P_r[\mathrm{MW}] > \frac{5.9\ 10^{-6}}{\lambda_r^2 q_f^2}$$

where q_f is the maximum quantum fluctuation compatible with the radiated field coherence; q_f should actually be of the same order of magnitude as the ratio between the incoherent radiated power and the coherent one, so as to ensure that the incoherent quantum noise does not significantly perturb the coherence of the radiated field. The previous relationship comes from the scaling of the quantum fluctuation with the inverse square root of the number of photons per wavelength[3].

The requirement of a radiated power scaling like the square of the frequency (i.e. the square of the photon energy) actually sets one of the major limits in going towards the X-ray domain.

The transverse size, r_b, of the electron beam in a wiggler with appropriate shaping of the pole face is given by[4]:

$$r_b = \sqrt{\frac{\varepsilon_n \lambda_\beta}{2\pi\gamma}} \qquad \text{being:} \qquad \lambda_\beta = \frac{\sqrt{2}\,\gamma\lambda_w}{a_w} H \tag{1}$$

Where ε_n is the transverse normalized emittance of the beam and the parameter H represents the effect of the ion focussing in decreasing the betatron wavelength λ_β. In absence of ion focussing H = 1; the ion focussing effect makes H < 1 [5].

The relevance of producing low emittance beams and to increase the focussing strength of the wiggler optics is then straightforward. The ion focussing scheme consists essentially in producing, inside the beam pipe along the wiggler, a tenuous ion channel: this is generated by injecting an intense leading low energy (≈ 300 MeV) electron beam into a low pressure helium column. The beam ionizes the helium gas and the space charge field of the beam ejects the detached plasma electrons from the beam vicinity. The charge of the second injected electron beam is partially, or totally (depending on the helium pressure) compensated in passing through the ion channel. The pinch field acting on the beam increases the focussing strength, decreases the beam transverse size and produces a substantial gain length contraction. Finally, it is worthwhile noting that the gain length scales with the cubic root of H.

Two major constraints on the quality of the electron beam injected into the wiggler must be taken into account when the cold beam limit approximation is abandoned. The transverse and the longitudinal phase spaces of the electron and of the photon beams must be matched if the interaction between the two beams has to be ensured all along the wiggler, in order to set up the energy exchange which is the basic condition to achieve an exponential gain in the radiated field power. For the transverse phase space one must match the emittance of the electron beam with the emittance of a diffraction limited radiation beam; this means that[6]:

$$\varepsilon_n = \frac{\lambda_r \gamma}{2\pi} f_1 \tag{2}$$

where f_1 must be kept below 1 (as discussed later).

Since the line-width of the radiated field at saturation is of the order of ρ, the energy spread of the injected beam must be less than this quantity: in practice it has been found from simulations[7] that the proper condition is given by:

$$\frac{\Delta\gamma}{\gamma} < \frac{\rho}{4}$$

A last condition comes from the requirement that diffraction does not remove radiation from the edge of the electron beam over a length shorter than the gain length; this requires the Rayleigh length, Z_r, to be larger than the gain length, L_g[8]:

$$L_g = Z_r f_3 \quad \text{being} \quad f_3 \leq 1 \quad \text{and} \quad Z_r = \frac{\pi r_b^2}{\lambda_r}$$

In some sense this condition sets a limit to the extent to which the ion focussing can be pushed: a reduction of the beam radius causes a decrease of the gain length, scaling like the square of the cubic root of the radius, but unfortunately also the Rayleigh length decreases scaling like the square of the radius. The best compromise on the effectiveness of the ion focussing technique is reached when $f_3 \approx 1$, that is when the diffracted power is not higher then the power increase due to the exponential gain. A further ion focussing increase, making $f_3 > 1$, no longer improves the FEL performance, as will be shown later.

Taking into account what could be a typical step-by-step upgrading of the SC LINAC facility, especially in terms of beam current and output emittance, we listed in Table 2 the corresponding envisageable FEL experiments: the table has been divided into four sections, to list the quantities related to the beam requirements, to the wiggler characteristics, to the FEL radiated power and to the above mentioned parameter f_i, that control the validity of the one-dimensional evaluation. The quantity $f_2 \equiv f_1^2 \cdot f_3$ must be less than 1[5]. The two parameters S and K measure the slippage effect and the superradiance behaviour of the FEL, as defined in ref.(9).

Moving from left to right on Table 2 the difficulty of the FEL experiment grows, both because of the tighter beam quality requirements and of the difficulties in manufacturing the required wiggler.

A few comments on the beam parameters are in order:

- the first anticipated beam will be produced by the LINAC without any recirculation, with a peak current of 200 A and a transverse normalized emittance (rms value of $1 \cdot 10^{-5}$) fully consistent with the preliminary design of the injection system[1].

- the energy spread shown in the Table takes into accounts the effect of the longitudinal wake-field excited inside the RF cavities: here it must be remarked that such low values for the energy spread are made possible only by the low RF frequency selected for the LINAC.

Table 2 - Possible FEL Experiments

Beam energy, T	[MeV]	292	500	580	580	B
Peak current, I_{peak}	[A]	200	400	400	400	E
Bunch length, σ_b	[mm]	.3	.3	.2	.2	A
Norm emittance, ε_n	[m rad]	$1 \cdot 10^{-5}$	$8 \cdot 10^{-6}$	$1.5 \cdot 10^{-6}$	$4 \cdot 10^{-6}$	M
Energy spread, rms	[keV]	±100	±150	±200	±200	
Wiggler period, λ_w	[cm]	3	3	2	2	W
Peak mag. field, B_w	[T]	.75	.75	1.	1.	I
Wiggler parameter, a_w		1.49	1.49	1.32	1.32	G
Wiggler pole gap	[cm]	.9	.9	.45	.45	G
Max. field for SmCo	[T]	.8	.8	1.1	1.1	L
Ion focussing param, H		1	1	1	.38	E
Beam radius, R_b	[μm]	210	190	67	67	R
Rad. Wavelength, λ_r	[nm]	133	50	21	21	
Pierce parameter, ρ		$2.1 \cdot 10^{-3}$	$1.7 \cdot 10^{-3}$	$2.0 \cdot 10^{-3}$	$2.0 \cdot 10^{-3}$	F
Photon energy	[eV]	9	25	58	58	E
Saturation power, P_{sat}	[MW]	190	380(40*)	550(320*)	550	L
Gain length, L_g	[m]	.66	.81(1.36*)	.46(.62*)	8.2	
Intensity at saturation	[W/cm^2]	$4.2 \cdot 10^{10}$	$1.0 \cdot 10^{11}$	$1.2 \cdot 10^{12}$	$1.2 \cdot 10^{12}$	
$(\Delta\gamma/\gamma)/(\rho/4)$		1.06	1.4	1.15	1.15	
Quantum fluctuation param., q_f		$4 \cdot 10^{-6}$	$8 \cdot 10^{-6}$	$1.6 \cdot 10^{-5}$	$1.6 \cdot 10^{-5}$	C
$f_1 \equiv 2\pi\varepsilon_n/(\lambda_r\gamma)$		.79	1.02	.34	1.04	H
$f_2 \equiv f_1^2 f_3$		.59	.65	.11	.97	E
$f_3 \equiv L_g/Z_r$		.95	.62	.99	.9	C
S		.15	.056	.053	.053	K
K		.007	.003	.002	.002	

* FRED-3D calculations.

Therefore the first FEL experiment will be just a standard single pass FEL amplifier at a resonance radiation wavelength of = 133 nm, where an input signal is available by a Nd-YLF laser multiplied in frequency at the eighth harmonic by a passage through a triple BBO crystal[10]. A few MW of peak power can be delivered in 50 ps pulses at a repetition rate of 1 kHz. The wiggler parameters are consistent with the Halbach scaling law for hybrid magnet wigglers[11]: with a gap of 9 mm the maximum allowed peak field is .8 T, versus the selected .75 T.

Integrating numerically the standard Compton-FEL equations for the one-dimensional model, we observe a saturated power of 190 MW after 8 meters of wiggler, when a 1 MW of input power has been injected into the wiggler: the value of ρ is in this case $\approx 2 \cdot 10^{-3}$. As shown in Table 2, the test quantities are all under control, especially the f_1 parameter, while the slippage and the superradiance parameters, being very small, indicate that the steady state regime is adequate to describe the exponential growth of the FEL radiation field.

The other three columns of Table 2 show the parameters required to operate a FEL amplifier starting from spontaneous emission, at radiation wavelengths of 50 and 21 nm, respectively. The beam must be recirculated once in the second stage of the LINAC to raise the energy to roughly .5 GeV ; the peak current increases up to 400 A, as anticipated[1]. The input signal is in this case the incoherent spontaneous synchrotron emission, P_{inc}, which reaches a few tens of kW per meter of wiggler, as estimated by the formula[12]

$$P_{inc}\,[\mathrm{kW/m}] \;=\; 1.9\;\frac{a_w^2\,(\,1 + a_w^2\,)\;I\,[\mathrm{A}]}{\lambda_w\,[\mathrm{cm}]\;\lambda_r\,[\mathrm{nm}]}$$

The fourth column deals with a particular application of the ion focussing technique: since the required emittance, as shown in the third column, is too small, a slight amount of ion focussing (H = .38) allows to increase the maximum emittance by a factor of three, keeping ρ constant. Further comments on this case will be given in the next section, where the 3-D simulation results are presented.

3 - Numerical Simulations of the High Gain FEL

The computer code FRED-3D has been used[20] to simulate the behaviour of the coupling between the electron beam and the radiation field induced by the wiggler field, for a 3-D beams (i.e. taking into account the transverse phase space evolution for both the particles and the field). Slippage effects are in this frequency-domain and, for millimetre long electron bunches, quite negligible; the steady state approximation used by FRED-3D is then completely adequate.

The input electron beam is actually mono-energetic, but it is well known that for energy spreads below the value given by the Pellegrini's rule[6] no serious deterioration of the FEL performance is to be expected. The field power growth is shown on a logarithmic scale, in Fig. 1, for the case of the parameters presented in column 2 of Table 1, i.e. for a radiation wavelength of 50 nm.

After three meters of lethargy, the signal grows exponentially up to 30 MW; the latter value is reached at the end of a 20 m long wiggler. Since the gain is about 3.2 dB/m, as shown in Fig. 2, a further 3.5 meters of wiggler length would be needed to reach the 1-D estimated saturation power at 380 MW.

The observed gain length, L_g, is therefore 1.36 m, which must be compared to the value of .81 m, predicted by the 1-D model. The discrepancy can be understood taking into account that the Rayleigh length, Z_r, for this case is slightly above the gain length. Since the 1-D model is valid in the limit $Z_r >> L_g$ (i.e. $f_3 << 1$), the gain decrease due to diffraction effects cannot be accounted for by the 1-D model. The same holds for the transverse phase space effects: since the emittance is just above threshold, ($f_1 = 1.02$), one must expect the 1-D calculation to predict a higher gain than the 3-D one.

We want to point out that a coherent input signal of 100 W has been used to start the FEL, even though no coherent signal is available at this wavelength (50 nm). In particular, since FRED-3D is not able to simulate the start up from the Schottky noise or from the incoherent spontaneous emission, 100 W has to be taken just as a reference value, to be compared to the incoherent synchrotron radiation power, which is in this case 36 kW/m. Harmonic switching (see below) or other exotic ideas like the SHOK scheme[13] could overcome the input signal problem.

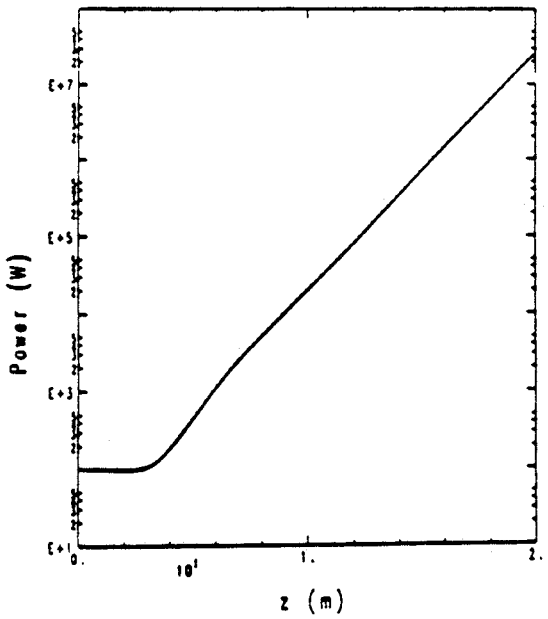

Fig. 1 - Field power growth, on a log scale, with the parameters presented in column 2 of Table 1.

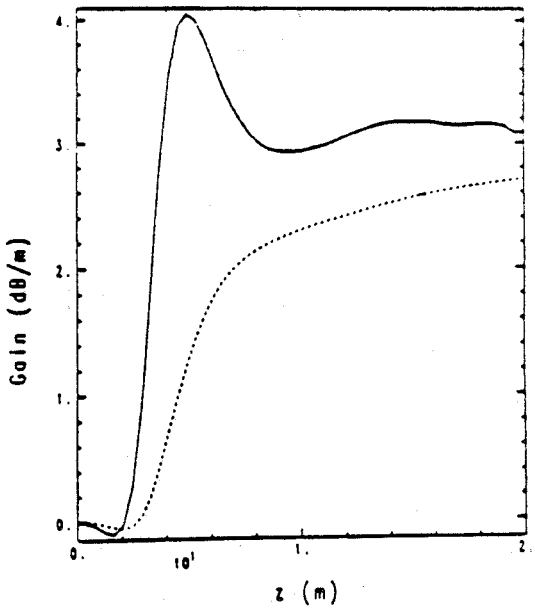

Fig. 2 - Incremental (solid line) and average (dashed line) gain along the wiggler for the case of Fig. 1.

The full exploitation of the ion focussing technique has been carefully studied for the case of the 21 nm radiation wavelength, with a 580 MeV beam at 400 A (third column of Table 2). The field power computed by FRED-3D along the wiggler is shown in Fig. 3 and 4 on logarithmic and linear scales, respectively. The input signal is still a 100 W coherent field. The incoherent synchrotron radiation power is in this case 85 kW per meter of wiggler, or, equivalently, 1.7 kW per wiggler period.

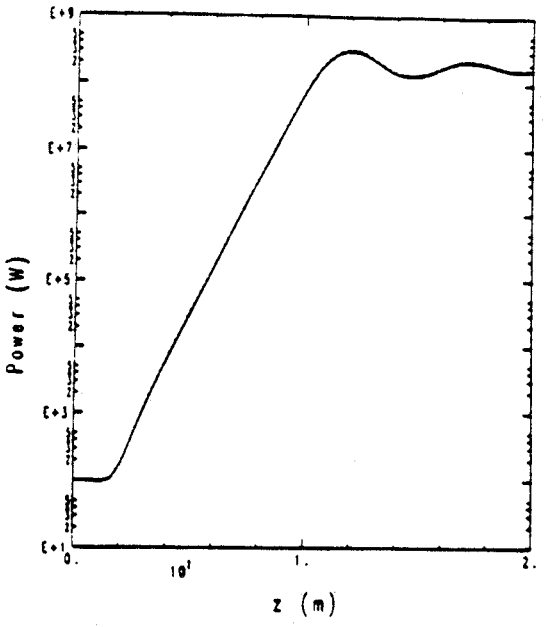

Fig. 3 - Field power growth, on a log scale, with the parameters presented in column 3 of Table 2.

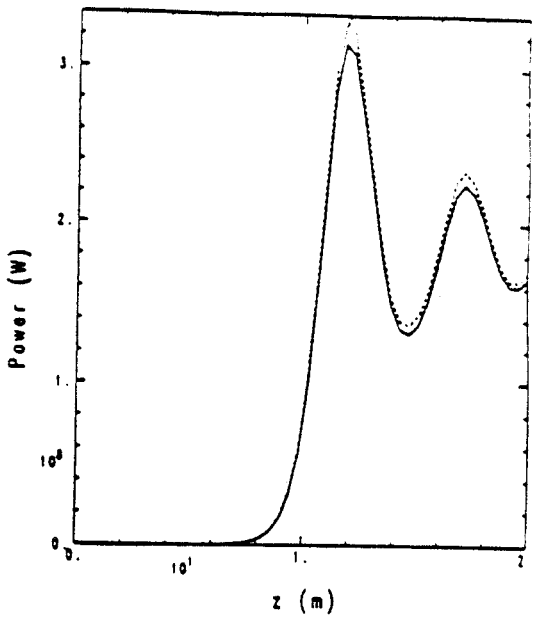

Fig. 4 - Same as Fig. 3, but on a linear scale. The power is in units of 10^8 W.

After 2 meters of lethargy the exponential gain sets in and the radiation field reaches the 320 MW saturation power level at z = 12 m: the corresponding intensity is $1.2 \cdot 10^{12}$ W/cm^2, confined in a narrow cone of about .1 mm rms radius and $1.1 \cdot 10^{-5}$ rad rms angular width. In Figs. 5 and 6 the intensity profiles are plotted as functions of the transverse coordinate x of the wiggler, at the entrance (z = 0) and at the exit of the wiggler (z = 20 m) respectively.

The input field is a gaussian laser beam focussed at z = 0. At the wiggler exit the intensity profile, due to diffraction effect, shows that some radiation escapes from the electron beam: the gaussian fit (dashed curve in Fig. 6) reveals that the optical guiding and the diffraction along the wiggler produce a distortion of the intensity profile, which is no longer gaussian. It should be noted that the peak value of Fig. 6 ($5 \cdot 10^{11}$) is lower than the peak value ($1.2 \cdot 10^{12}$) at saturation (z = 12 m).

Moreover, the phase profile of the radiation field at z = 20 m, shown in Fig. 7, indicates that the radiation beam is de-focussed, since the phase increases off-axis.

The "natural" betatron wavelength, λ_β, for this case is 24.5 m, which gives an rms beam radius in the wiggler of about 53 microns with a normalized rms emittance of 1.5 mm mrad. The incremental gain is shown (solid line) in Fig. 8: with an average value of 7 dB/m during the exponential growth, the gain length is approximately .62 m, slightly above the 1-D predicted one.

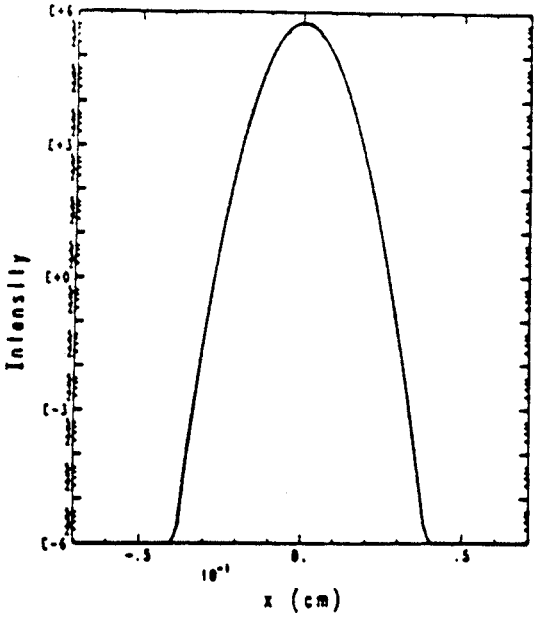

Fig. 5 - Intensity profile as a function of the transverse coordinate x of the wiggler at the start-up (z = 0 m), for the case of the parameters presented in column 3 of Table 2.

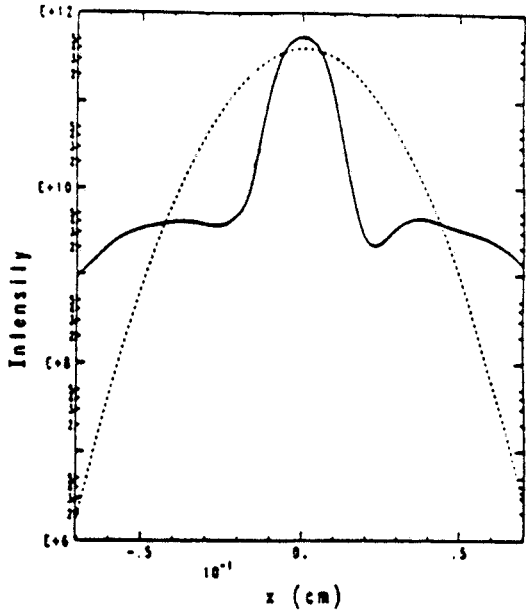

Fig. 6 - As Fig. 5 at the end of the wiggler (z = 20 m). Actual intensity (solid line) and gaussian fit (dashed line).

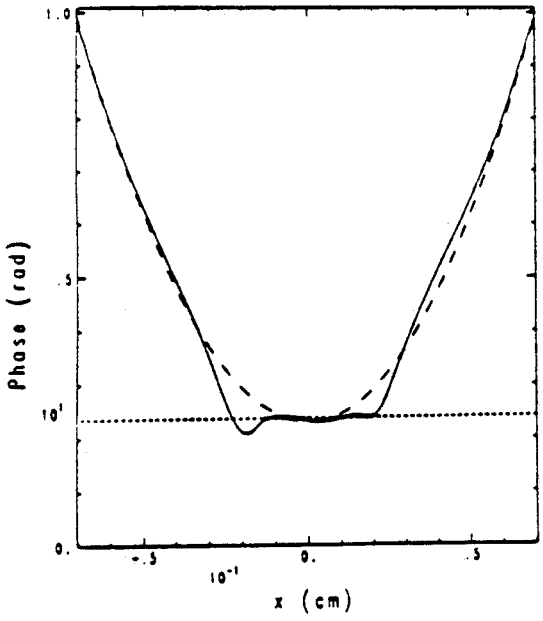

Fig. 7 - Radiation field phase profile (solid line) and its gaussian fit (dashed line) at z = 20 m.

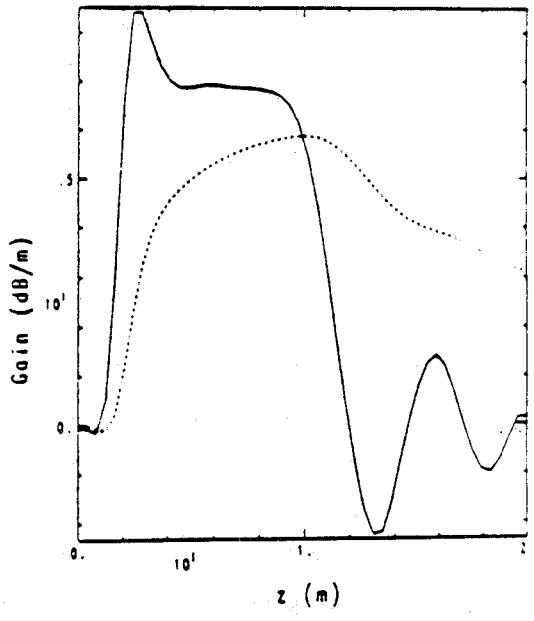

Fig. 8 - Incremental gain (solid line) and average gain (dashed line).

The total gain is about 65 dB after 12 metres of wiggler. Since the Rayleigh length is .41 m, the diffraction effects are probably responsible for such a decrease in the gain.

Introducing some amount of ion focussing one can decrease the betatron wavelength and squeeze the electron beam. In Fig. 9 is presented the radiated field power produced by reducing by a factor ten the betatron wavelength, i.e. by setting H = 0.1. The saturation is reached at z = 8 m, with a wiggler much shorter than the previous one (H = 1, no ion focussing), but the saturation level is slightly lower: 250 MW versus 320 MW of the no-ion focussing case.

The peak field intensity at saturation, I_{sat}, is about $4.4 \cdot 10^{12}$ W/cm^2, with a spot radius of .6 mm and an rms angular divergence of $1 \cdot 10^{-5}$ rad. The incremental gain has now a plateau at 10 dB/m, with a total gain of 64 dB along the 8 meter wiggler.

The intensity profile is plotted in Fig. 10, at the wiggler exit. The exit profile exhibits very clearly the substantial fraction of field escaped from the electron beam, which has a maximum radius of about 50 microns.

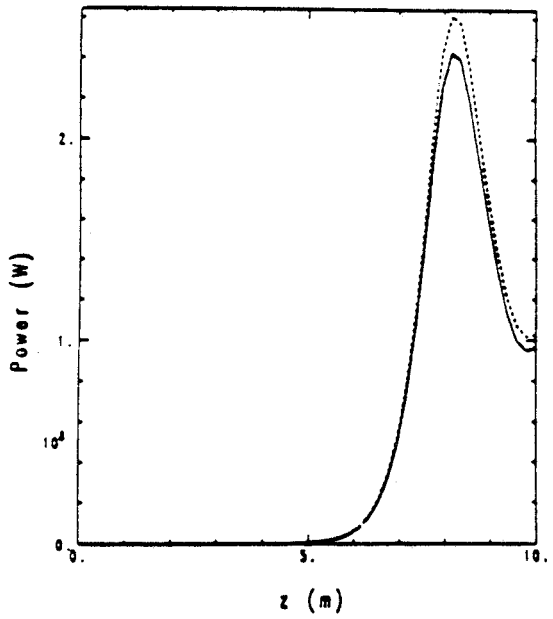

Fig. 9 - Radiated field power produced by reducing the betatron wavelength by a factor ten, i.e. setting H = 0.1.

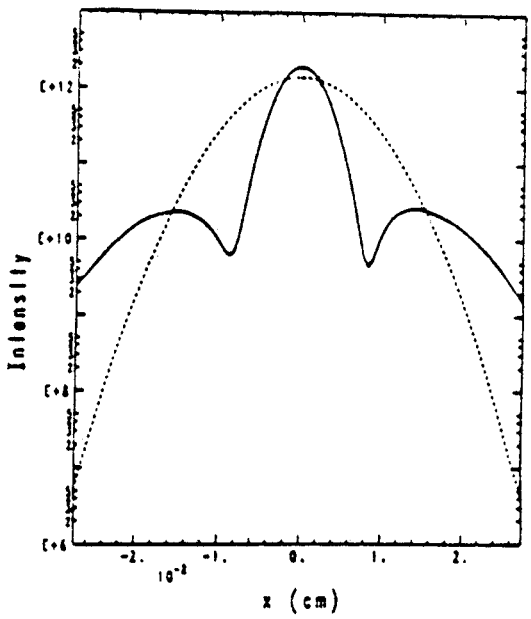

Fig. 10 - Intensity profile at the wiggler exit. The exit profile exhibits very clearly the substantial fraction of field escaped from the electron beam.

The optical guiding applied by the electron beam on the laser field is however better evidenced by the phase profile of the laser field, plotted in Fig. 11 at the wiggler exit: inside the electron beam, i.e. for x < 60 microns, the field phase decreases with the transverse coordinate, then the optical beam is converging. Outside the electron beam the field phase is instead strongly increasing, showing that the optical beam is defocussed in that region. The electron beam acts on the laser field as an optical fiber with a high refractive index. The optical guiding,

already observed elsewhere [21], is stronger during the exponential gain than after saturation. That is clearly shown in Fig. 12, where the iso-intensity curves are plotted in the (x,z) plane for the case without the ion focussing: the laser beam is squeezed and focussed whenever the field is growing, i.e. the gain is positive.

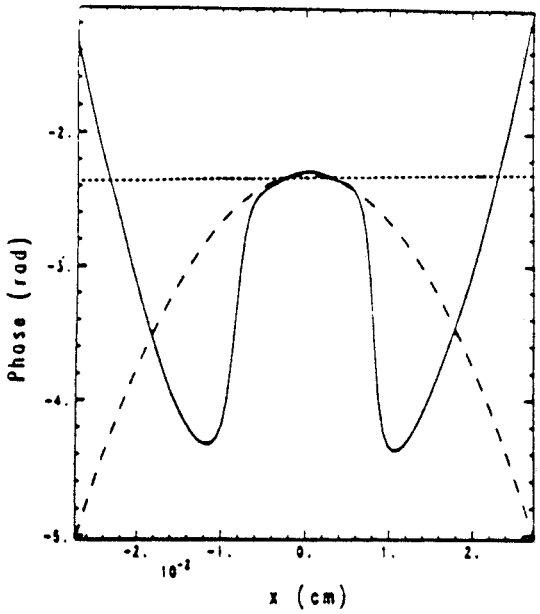

Fig. 11 - Phase profile of the laser field at the wiggler exit (solid line) and its gaussian fit (dashed line).

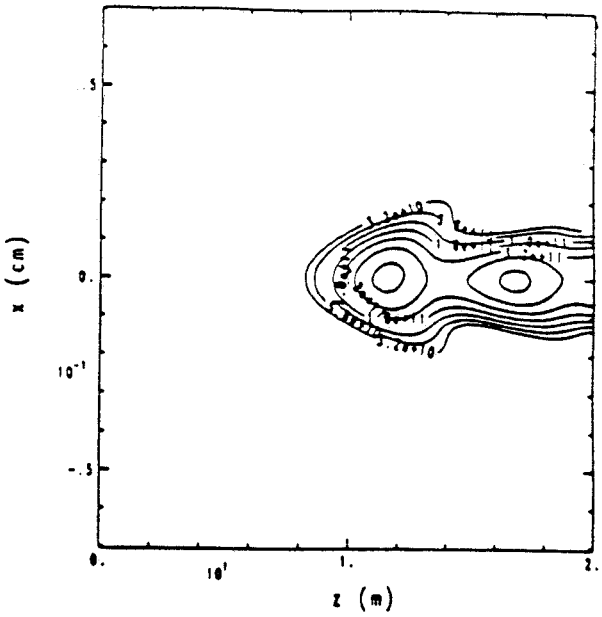

Fig. 12 -Iso-intensity curves, plotted in the (x,z) plane for the case without ion focussing.

The effect of ion focussing in decreasing the gain length has been explored performing FEL simulations with FRED-3D also at H = .75 and at H = .2. The results are summarized in Fig. 13, where the gain length observed in the FRED-3D calculations is plotted (dashed line) versus the betatron wavelength (H = 1 corresponds to λ_β = 24.5 m). The solid line in the same figure represents the gain length scaling as $H^{1/3}$, as predicted by the 1-D model: the gain length observed in the 3-D calculations then indicates that the FEL performance is enhanced by the ion focussing technique, but not as much as one would expect from the 1-D model considerations. That can be explained observing the dashed line plotted in Fig. 13, showing the f_3 coefficient, which gives the ratio between the gain length and the Rayleigh length: this ratio grows quickly above 1, indicating that diffraction effects become more and more relevant for the FEL performance.

It can be therefore concluded that the maximum benefit from the ion focussing technique can be obtained not by increasing the FEL performance, keeping constant the beam parameters, but relaxing the beam quality requirements keeping unaltered the gain length. It can be easily seen

from equation (1) that the emittance can be scaled like the inverse of the amount H of ion focussing applied, keeping constant the beam radius, hence the gain length. One can therefore reduce the tight requirement on the beam emittance shown in the third column of Table 2 and list a new set of parameters in the fourth column, by simply scaling the emittance by a factor 2.7 and taking H = .38. In this way the gain length should stay constant since the Rayleigh length is not changed (the beam radius is not varied) and the FEL performances are unaltered but achieved with a beam which is now consistent with the ones of Table 1. The f_1 parameter is still within the safety range $f_1 \approx 1$, the quantum fluctuations parameter being very low, $q_f = 1 \cdot 10^{-5}$.

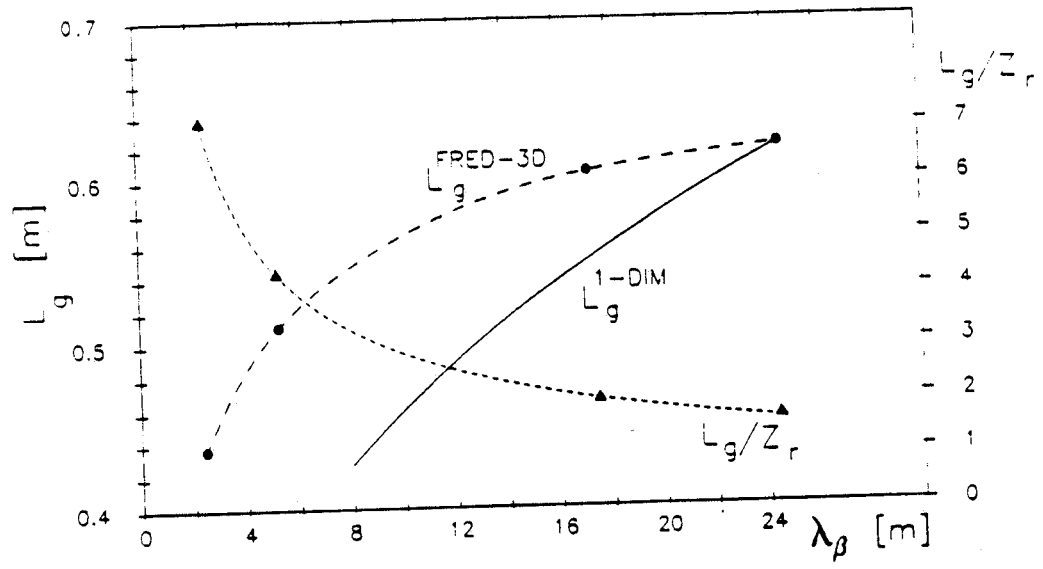

Fig. 13 - Effect of the ion focussing in decreasing the gain length (see text for details).

At 250 MW of peak power the number of photons per bunch is $3 \cdot 10^{13}$. With a bunch length of 1.2 ps the number of wavelengths contained in the laser pulse will be of the order of $2 \cdot 10^4$ with about $1 \cdot 10^5$ electrons per wavelength.

Since the maximum electron beam wiggle amplitude is in the range of 5 microns, very small with respect to the beam size, no serious problems are envisaged for the production of a uniform ion channel over the ±100 microns of the beam transverse size.

4 - High Gain Optical Klystron and the Coherent VUV

The Self Amplified Spontaneous Emission (SASE) regime of an FEL allows to produce coherent VUV and soft-X-ray radiation starting from the incoherent spontaneous emission in the wiggler. In such a regime, the incoherent radiation, having an optical power proportional to the number of the electrons, is amplified by the electron beam in a single pass through the wiggler. The stimulated radiation grows exponentially to a saturation level which is proportional to $N^{4/3}$, N being the number of electrons in the bunch.

Beside the problems arising from the wiggler length needed to achieve saturation starting from the incoherent spontaneous emission (they will be discussed in the next section), one of the major points is that the coherence of the output signal is lower than that obtainable from an FEL amplifier with a coherent input signal.

The coherence length of the output signal produced in the SASE regime is indeed given roughly by the slippage length: since the electrons interact with one another via the common radiation field, the interaction length is equal to the slippage length, hence the photons separated by more than the slippage length are of course decoupled. Therefore, the start up of the field amplification process from photon and electron populations which are both randomly distributed in phase cannot assure a narrow bandwidth and a coherent output signal.

Since the availability of coherent input signals (i.e. of a photon population peaked around a given phase) in the UV region decreases strongly with the wavelength, one could try to start with a "coherent" beam instead of a coherent input signal, i.e. with a bunched beam. The start up from a pre-bunched beam ensures a higher coherence of the radiation since the spontaneous emitted photon population is no longer randomly distributed in phase, but is peaked in phase around the electron beam bunching phase[14].

In Figs. 14 a and b the longitudinal phase-space for the electron beam of the FRED-3D simulation previously discussed is shown at two different positions along the wiggler:

- at z = 4 m, where the field power is still a few orders of magnitude lower than the saturation level, the beam has achieved an energy spread from the input signal but is still distributed fairly uniformly in phase. Since the wiggler field is dispersive, the energy spread will be transformed, along the wiggler, into a phase spread
- at z = 8 m, near saturation, the phase space appears like in Fig. 14 b, where the beam has achieved a substantial bunching, being well known that the bunching in the exponential regime grows exponentially too (the bunching parameter b is defined, as usual, $b=\langle e^{i\theta}\rangle$, where the average <> is performed over the θ electron phase distribution).

Integrating numerically the 1-D FEL equations[9] in the Compton limit ($\rho << 1$) one finds that, starting with a signal six orders of magnitude lower than the saturation level (in the present case 100 W), the field power saturates at 550 MW after 10.5 meters of wiggler length, and the bunching grows up to ≈.7 just before saturation, as shown in Fig. 15, according to the sets of parameters presented in Table 2, column 3.

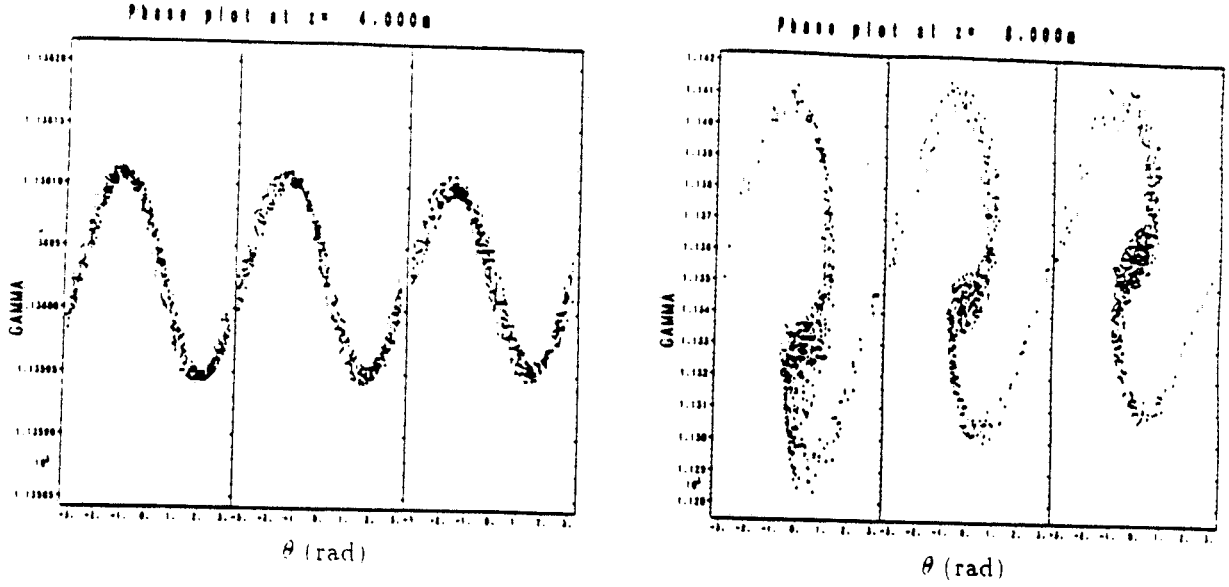

Figs. 14 a & b - Longitudinal phase spaces for the electron beam of the FRED-3D simulation at two different positions along the wiggler:

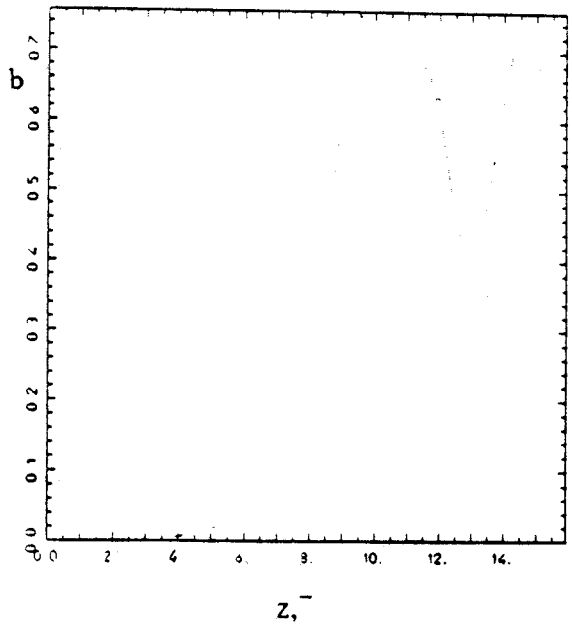

Fig. 15 - Beam bunching along the wiggler for the sets of parameters presented in Table 2, column 3.

Starting from these considerations and following the scheme of the optical klystron[15], we propose to separate the wiggler into two parts: the first one acts as a buncher and the second one as a radiator. If the two parts are decoupled, that is the radiation generated in the buncher is discarded, the radiator works as a generator of coherent spontaneous radiation at its proper resonant wavelength. In other words, truncating the exponential gain at a suitable point close to saturation and discarding the radiated field generated so far (which is scarcely coherent), one can get a bunched beam able to radiate coherent synchrotron radiation, in a transient "superradiant" regime involving the overall beam.

The separation of the electron and the radiation beam can be achieved via a small magnetic deflection at the end of the first wiggler: such a deflection must of course ensure that the debunching effect on the beam is negligible with respect to the radiation wavelength scale. Since to the first order, the path length difference, ΔL, for a beam with energy spread $\Delta\gamma/\gamma$ deflected by a magnet of angle θ (assumed small) and radius of curvature ρ_b is given by:

$$\Delta L \approx \rho_b \frac{\Delta\gamma\,\theta^3}{6\gamma}$$

setting $\rho_b = 2$ m (B = .96 T at 580 MeV) and $\theta = 5$ mrad, ΔL is less than 1 nm for $\Delta\gamma/\gamma$ of the order of 1 %, as typical near the saturation. Over 1 m, which could be the separation of the two wigglers (in order to achieve a shift of a few mm between the beam and the radiation) the path length difference due to the emittance, given by:

$$\Delta L \approx \frac{L\,\Delta\theta^2}{2}$$ where $\Delta\theta$ is the rms beam divergence

is of the order of 1 nm. Therefore the debunching effect at the entrance of the radiator can be kept small with respect to the radiation wavelength (20 nm).

Other possibilities to achieve the beam-field separation such as thin radiation absorbers or wiggler truncations (no half period at the wiggler end) must be investigated, but could in principle be exploited.

In order to evaluate the field power generated in the radiator we apply a cut to the numerical integration of the FEL-Compton equation[9], which corresponds to the first wiggler exit. At the cut (working actually as a variable threshold) we simply reduce the field intensity to zero, we keep the particle phase space unaltered (assuming zero debunching in the transport between the two wigglers) and we insert the new resonance condition (proper of the radiator) by zeroing the

detuning. This is simply achieved by keeping <p> = 0, i.e. by summing the quantity <p> at the threshold to all the particles, where <p> is the normalized detuning, given by:

$$<p> = \frac{<\gamma - \gamma_r>}{\rho \gamma_r}$$

That is equivalent to shift the resonant wavelength to the new value - proper of the radiator - which is determined by the beam energy at the end of the first wiggler.

In the present case the beam energy loss in the first wiggler, $\delta\gamma$, is always small - .04% ÷.15% of its initial energy - hence the wavelength increase, $\delta\lambda_r$, of the radiation emitted in the radiator is very small with respect to the resonant wavelength, λ_r, of the first "bunching" wiggler, according to the equation:

$$\frac{\delta\lambda_r}{\lambda_r} = -2\frac{\delta\gamma}{\gamma} \leq .3\ \%$$

The field power generated in the radiator is plotted in Fig. 16 versus the cumulative length of the system buncher wiggler - radiator, for three different threshold positions. The crosses show the standard steady state behaviour of the field power (i.e. for a buncher wiggler extending without any threshold) with a saturation level of 550 MW at z = 10.5 m: the curve is plotted just for reference. The solid line, the dashed line and the dotted one mark the field growth in the radiator when the length of the buncher wiggler is 8 m, 8.8 m and 9.6 m respectively. When the threshold is located at z = 8.8 m one gets 100 MW of field power from the first wiggler, then with two meters of radiator length (from z = 8.8 m to z = 10.8 m) the coherent spontaneous emission grows to 700 MW and then saturates again. Shifting the threshold towards larger z's causes the radiation to saturate in a shorter length (from z = 9.6 m to z = 10.9 m) lowering at the same time the power level (260 MW).

Since the threshold variation requires a variable length of the buncher wiggler (which can cause serious technological problems), the same effect can be achieved by varying the input signal power and taking a fixed buncher wiggler length, as shown in Fig. 17. Here the buncher wiggler length is assumed to be 8 m and the radiator starts at z = 8 m. The effect on the longitudinal phase of the beam transport from the wiggler to the radiator is neglected. As in Fig. 16, the crossed line shows the standard steady state exponential growth, while the other lines show the field power in the radiator for three different input powers at the entrance of the buncher wiggler: the solid line is referred to 100 W, the dashed to 400 W and the dotted one to 1000 W.

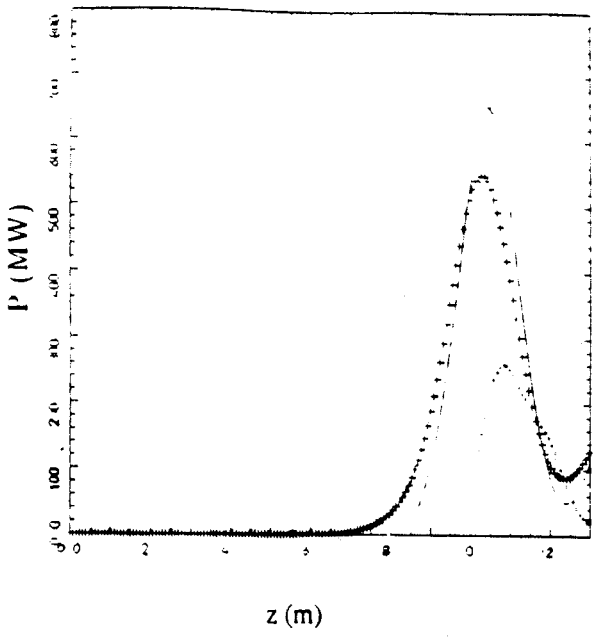

Fig. 16 - Field power generated in the radiator versus the cumulative length of the system buncher wiggler - radiator for three different threshold positions: the crossed line shows the standard steady state behaviour, whereas the solid line, the dashed line and the dotted one mark the field growth in the radiator when the length of the buncher wiggler is 8 m, 8.8 m and 9.6 m respectively.

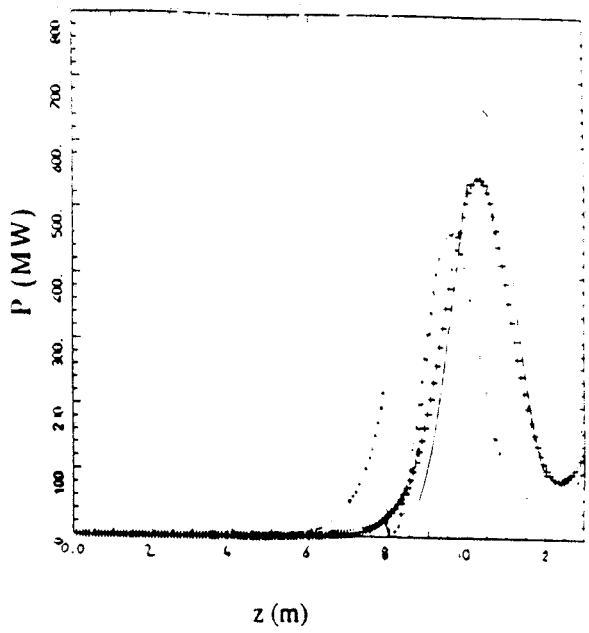

Fig. 17 - As Fig. 16, but varying the input signal power at the buncher wiggler entrance and taking a fixed buncher wiggler length (z = 8 m). The crosses show the standard steady state exponential growth (no threshold on the buncher wiggler, 100 W of input power), while the other lines show the field power in the radiator for three different input power signals: the solid line refers to 100 W, the dashed to 400 W and the dotted one to 1000 W.

In Fig. 18 the bunching factor, b, is plotted for the same cases versus the cumulative length of the buncher wiggler-radiator system. It is clearly visible that the dashed line, corresponding to the 400 W input signal case which has the maximum field power generated in the radiator, has also the higher bunching level, fairly constant between z = 8 m and z = 10 m, where the saturation is reached in the radiator.

Moreover the solid line clearly exhibits a departure from the exponential law, also typical of the bunching in the steady state high gain regime: the field power is not growing exponentially in the radiator, as shown in Fig. 19, where the logarithm of the field power is plotted for the steady state and for the three different threshold positions.

We can interpret the emission in the radiator in the following way: the bunched beam, once injected into the radiator is initially superradiant since it does no longer interact with the radiation field that caused the bunching. The coherent radiation generated has an intensity (before saturation) scaling with $b^2 \cdot N^2$ (N is the electron number) and grows very rapidly, as shown in Fig. 20, where a peak gain of 60-70 dB/m is reached in the first part of the radiator. This value is one order of magnitude higher with respect to the 8 dB/m of the steady state exponential gain.

It is interesting to notice that the radiated field still reaches saturation. This is due again to the potential well produced by the radiation, in which the electrons are trapped: when the electron oscillation period in the potential well is fairly equal to the exponential growth rate the electron beam starts to absorb energy from the radiated field. The OK experiments at Orsay are very similar to this scheme, with the exception that they operate in the low gain domain, where saturation cannot be reached, and the bunching can be assumed constant[16].

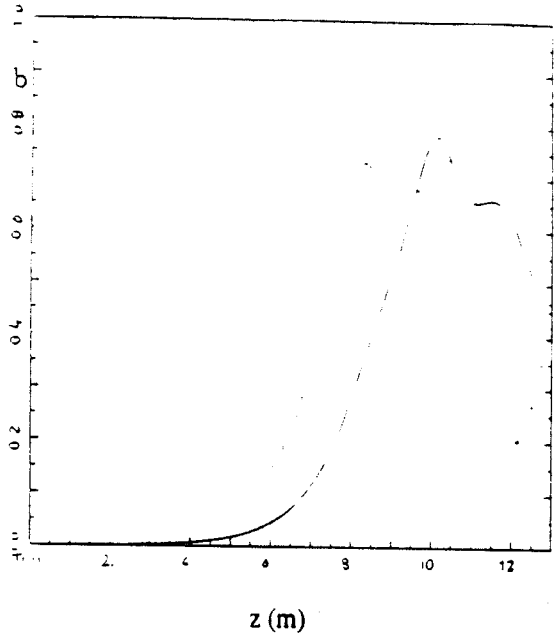

Fig. 18 - The bunching amplitude, b, plotted for the same cases of Fig. 17 versus the cumulative length of the buncher wiggler-radiator system.

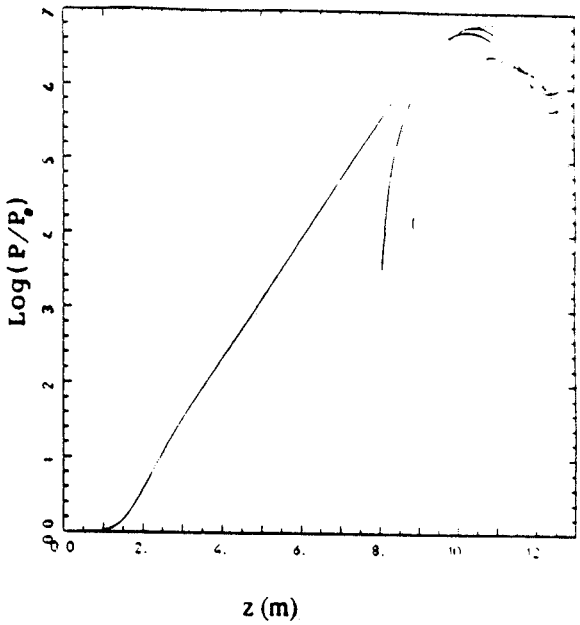

Fig. 19 - The logarithm of the field power in the radiator plotted for the steady state and for the three different threshold positions, specified in Fig. 16.

In some sense the first part of the radiator shows a transient superradiant behaviour, involving all the electrons in the bunch: the observed superradiance is only transient since the slippage effects are, in our case, negligible, hence the field is always "sitting" on the electrons of the beam, interacting with them. The transient superradiance is therefore switched off when the field intensity grows and the bunching is no longer constant. To evaluate the coherence quality of the radiated field we can assume a constant bunching and use the formula[15]:

$$\frac{dP_{coh}/d\Omega}{dP_{inc}/d\Omega} \approx |b|^2 \zeta$$

which gives the ratio between the coherent power radiated per unit solid angle and the incoherent one. ζ is the number of electrons in the coherence length $N_w \lambda_r$ of the radiation, N_w being the number of the radiator periods.

Assuming in our case: $|b|^2 = .35$, $N_w = 100$ and $\zeta = 10^7$, the ratio between the coherent power and the incoherent one is in the order of 10^6.

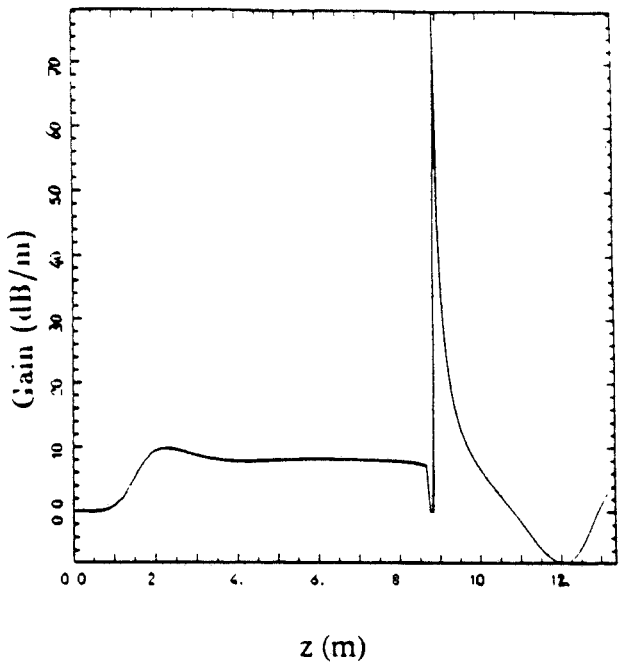

Fig. 20 - Coherent radiation growing in the wiggler-radiator system. A peak gain of 60-70 dB/m is reached in the first part of the radiator. This value is one order of magnitude higher with respect to the 8 dB/m of the steady state exponential gain.

5 - HASW: Harmonic Switching and Far Future Experiments

In the first wiggler, the buncher wiggler, the beam is bunched not only on the fundamental but also on higher harmonics. It is well known that in a planar wiggler only the odd harmonics are present on axis. The dimensionless field intensity $|A|^2$ and the bunching on the fundamental harmonic are plotted in Fig. 21 as a function of the dimensionless wiggler length $z,^- = 4\pi\rho z/\lambda_w$ for a typical case with $a_w = 1.48$, while the bunching on the higher harmonics is plotted in Fig. 22. The third and fifth harmonic bunchings are quite pronounced (.3 and .5 respectively) just before saturation: that clearly indicates the possibility to use a radiator tuned not on the fundamental but on a higher harmonic.

This idea has already been exploited by the OK experiments in Orsay[16,17,18] and has recently been proposed in the high gain domain with a varied scheme[19]. Nevertheless, the novelty of our wiggler+radiator scheme is that we do not take the radiation from the first wiggler into the radiator, but we transfer only the bunched beam. The rational for this, in this

range of wavelengths, is to avoid any phase slips between the beam and the radiation field generated in the passage from the buncher wiggler to the radiator wiggler. In fact, at the entrance of the radiator, a change in the relative phase can cause a shift in the beam-field coupling from an emission regime to an absorption one. It must be stressed that a difference of only 1 nm between the path lengths of the electron beam and of the radiation field produces, with a radiation wavelength of 5 nm, a significant change in the relative phase. In this case the electron beam, at the radiator entrance, is no longer in-phase with the radiation field, fact that causes a dramatic decrease of the radiation field and, eventually, of the beam bunching all along the first part of the radiator wiggler. In this respect, the relevance to cut out the beam-field interaction, avoiding to inject the radiation field into the radiator, is straightforward.

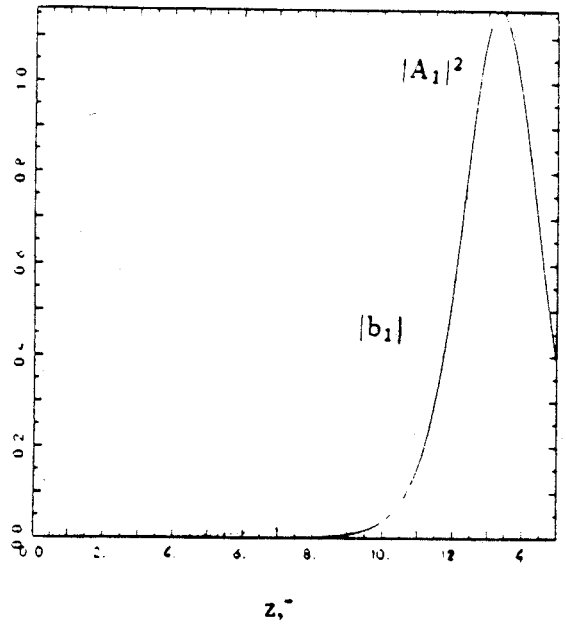

Fig. 21 - Dimensionless field intensity and bunching on the fundamental first harmonic along a wiggler with $a_w = 1.48$ (see text for details)

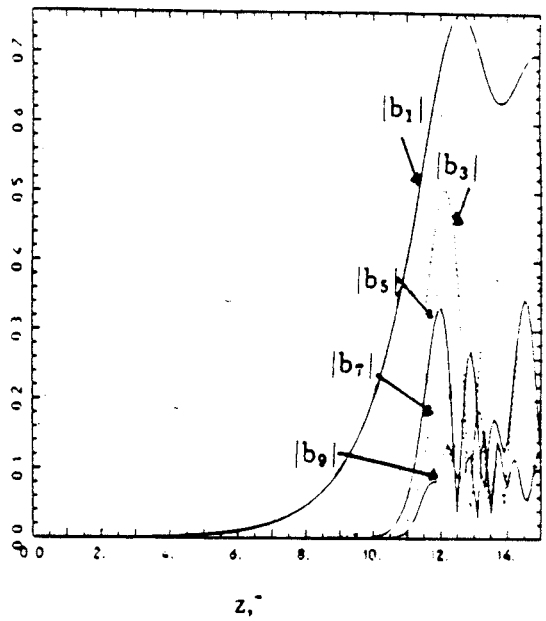

Fig. 22 - Higher harmonic bunching parameters for the same wiggler as in Fig. 21

Since the previously illustrated possible experiments are foreseen with a radiation wavelength in the range of 20÷50 nm, it is a natural choice to consider a jump in frequency of a factor 5 in order to point directly towards ≈ 5 nm, i.e. towards the so called "water window". The experiment described in the following will therefore deal with a fifth harmonic switching, but the scheme is in principle completely general and applicable to other harmonics.

The main parameters of the foreseen experiment are listed in Table 3. Recirculating the beam twice in the L3 section of the ARES Linac, its energy can be boosted to 820 MeV: in the first wiggler the beam radiates at a fundamental wavelength of 25 nm plus the higher odd harmonics.

Table 3 - HASW Experiment Main Parameters

	T [MeV]	I [A]	ε_n [m rad]	$\Delta\gamma/\gamma$ [keV]
Beam Parameters	820	400	$3 \cdot 10^{-6}$	± 250

	λ_w[cm]	λ_r[nm]	B_w[T]	H	R_b[μm]	ρ	f_3	f_1
Buncher wiggler	4	25	.56	.5	92	$2 \cdot 10^{-3}$	.82	
5th Harm. Radiator	2	5	.41	.1	50	$1 \cdot 10^{-3}$		2.35

	P_{sat}[MW]	I_{sat}[W/cm^2]	Photon Num.	q_f
Radiation parameters for λ_r = 5 nm	140	$1.8 \cdot 10^{12}$	$6.5 \cdot 10^{12}$	$4 \cdot 10^{-5}$

Adding a slight ion focussing, one can achieve $\rho = 2 \cdot 10^{-3}$ and reach, after a 14 m wiggler, a fifth harmonic bunching, b_5, of the order of 0.05. The added ion focussing must be kept low in order to avoid too short Rayleigh lengths: at this wavelength the beam is very fine and the diffraction effects can dominate. In our case we choose a safe value for the parameter f_3, i.e. f_3=.82.

Injecting now the beam into the radiator, whose fundamental is tuned at 5 nm (the fifth harmonic of the previous wiggler), we achieve coherent emission at 5 nm with a quasi-exponential growth of the radiation.

The dimensionless field intensity and the bunching on the fundamental in the buncher wiggler, i.e. λ_r = 25 nm, are plotted in Fig. 23 up to the dimensionless $z,^- = 10.5$: thereafter the bunching and the dimensionless field intensity are referred to the fundamental of the radiator wiggler, i.e. λ_r = 5 nm, plotted up to $z,^- = 20$.

The corresponding field power is shown by the dashed line plotted in Fig. 24, where 50 MW at λ_r = 25 nm are generated in the buncher wiggler (14 m long). The saturated power level

in the radiator wiggler (10 m long, from z = 14 m to z = 24 m) is 160 MW at λ_r = 5 nm. The logarithm of the field power, plotted in Fig. 25, clearly shows that the field growth in the radiator has an initial very rapid but non-exponential behaviour, followed by a quasi-exponential one (i.e. quasi linear on a log. scale) up to the saturation.

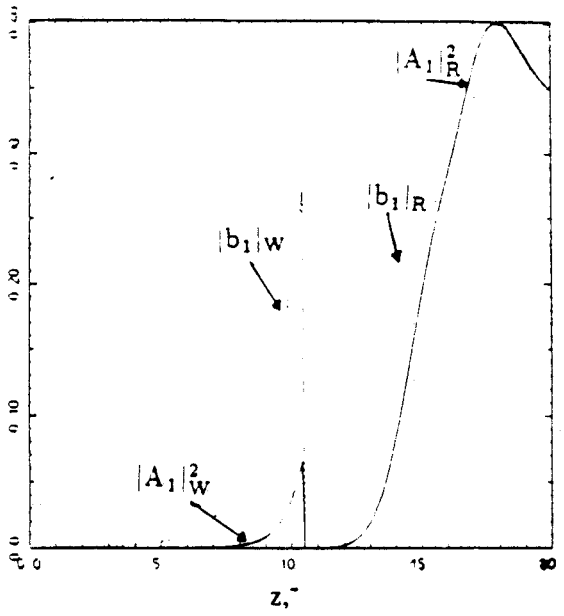

Fig. 23 - Dimensionless field intensity (solid line) and bunching (dashed line) for the λ_r = 25 nm ($z,^{\sim} < 10.5$) in the buncher wiggler and for λ_r = 5 nm ($z,^{\sim} > 10.5$) in the radiator. (see text for details).

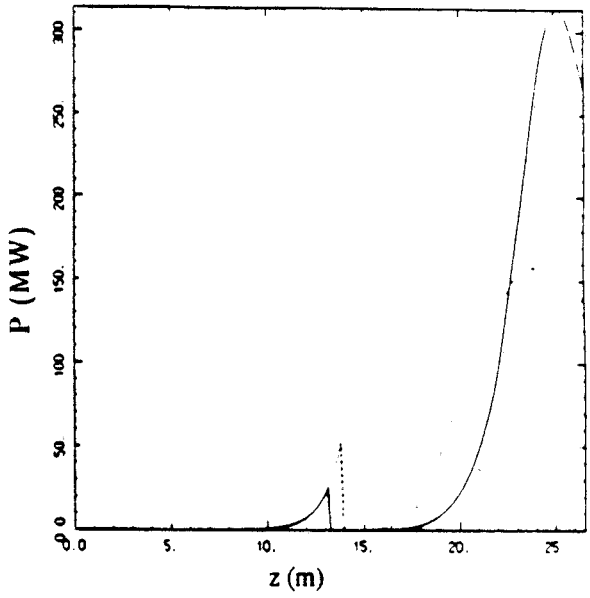

Fig. 24 - Field power growth at λ_r = 5 nm for two different lengths of the buncher wiggler (see text for details).

The bunching on the fundamental harmonic of the radiator (i.e. on the fifth harmonic of the buncher wiggler) is indeed low at the radiator entrance, around 0.05, hence the radiation emission is no longer a pure coherent spontaneous emission as in the case of the previous section, where the bunching was 0.5. In this case the bunching and the field grow together in a way more similar to the standard steady state regime. Cutting the buncher wiggler at z = 13 m the fifth harmonic bunching is now lower: $|b_5|$ = .001 . The evolution of the field power and of the bunching in the radiator, shown by the solid line of Fig. 25 and 26 respectively, are more similar to the exponential gain regime, with a saturated power level at 320 MW. This larger value is due to the lower energy spread achieved by the beam at the end of the buncher wiggler. Such a spread, which is modulated on the scale of the fundamental radiation wavelength λ_r = 25 nm, grows in the buncher wiggler together with the bunching b_1 . At the entrance of the radiator the spread on λ_r = 25 nm acts as an incoherent beam spread since the radiator is tuned at the lower wavelength λ_r = 5 nm . We can conclude that higher is the value of $|b_5|$ at the radiator entrance, more is the incoherent energy spread of the beam and lower is the gain in the

radiator. Since the emittance condition relationship (2) is violated inside the radiator ($f_1 = 2.35$), one would like to have the highest possible $|b_5|$ at the radiator entrance in order to overcome the emittance condition, which is strictly true for an unbunched beam. Hence a trade off between the two opposite requirements must be found: 3-D simulations are needed to evaluate what is the maximum value of f_1 (as a function of the bunching $|b_5|$ at the entrance) which ensures an acceptable gain deterioration.

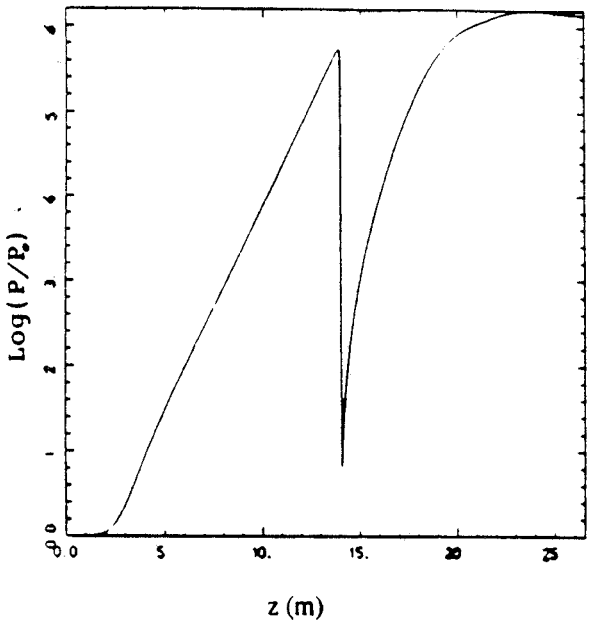

Fig. 25 - Logarithm of the field power on $\lambda_r = 25$ nm (for z<14 m) in the buncher wiggler and on $\lambda_r = 5$ nm (for z>14 m) in the radiator (see text for details).

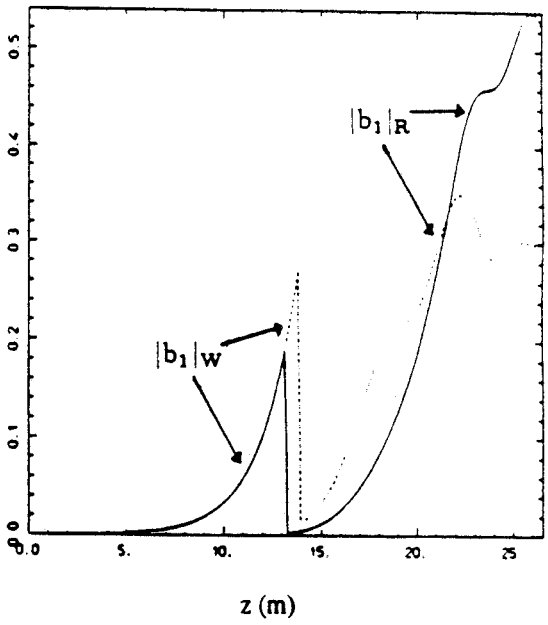

Fig. 26 - Bunching parameter amplitude in the buncher wiggler and in the radiator for two different buncher wiggler length (see text for details).

The electron longitudinal phase spaces along the radiator are shown in Fig. 27a to 27d . The phase space, extending in the buncher wiggler over 2π radians of the radiation $\lambda_r = 25$ nm, is scaled at the radiator entrance over the corresponding 10π radians of the $\lambda_r = 5$ nm. The energy spread on the scale of the wavelength $\lambda_r = 25$ nm is clearly visible (the spread is normalized to the parameter $\rho = 1 \cdot 10^{-3}$). Since the radiation at 25 nm is no more resonant in the radiator, the onset of the radiation at 5 nm stimulates the bunching over the five buckets contained between 0 and 10π of the phase space. At z = 18 m, slightly before saturation, the bunching on the radiation at 5 nm is clearly visible. The initial energy spread has been taken as the expected spread of the beam, $\Delta\gamma/\gamma = \pm 3 \cdot 10^{-4}$

The coherence of the radiated field can be estimated assuming a constant $b_5 \approx 0.1$: the ratio between coherent and incoherent power per unit solid angle comes out to be $1.7 \cdot 10^{-5}$, which is just consistent with the quantum fluctuation parameter, $q_f \approx 4 \cdot 10^{-5}$.

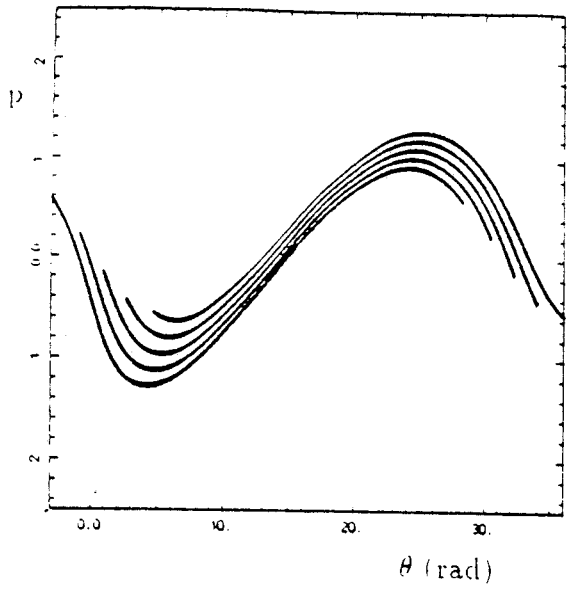

Fig. 27a - Longitudinal phase space at the buncher wiggler exit (z = 14 m).

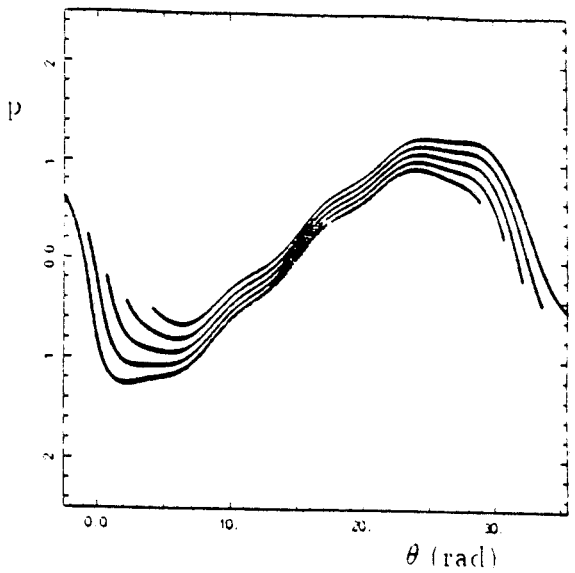

Fig. 27b - Longitudinal phase space at z = 15.3 m (1.3 m far from the radiator entrance)

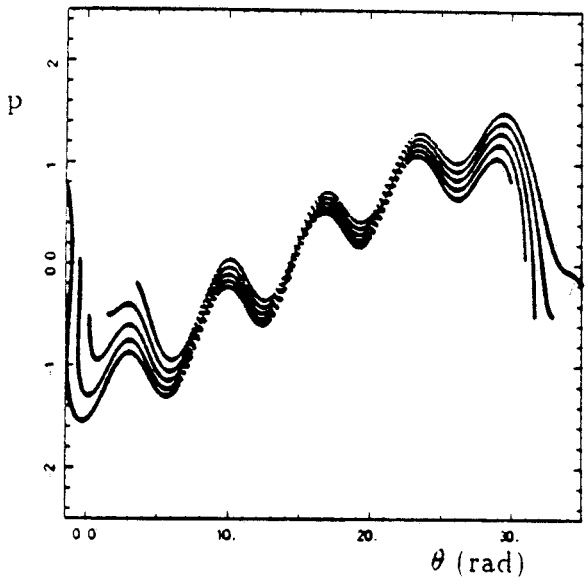

Fig. 27c - Longitudinal phase space at z = 16.7 m (2.7 m far from the radiator entrance)

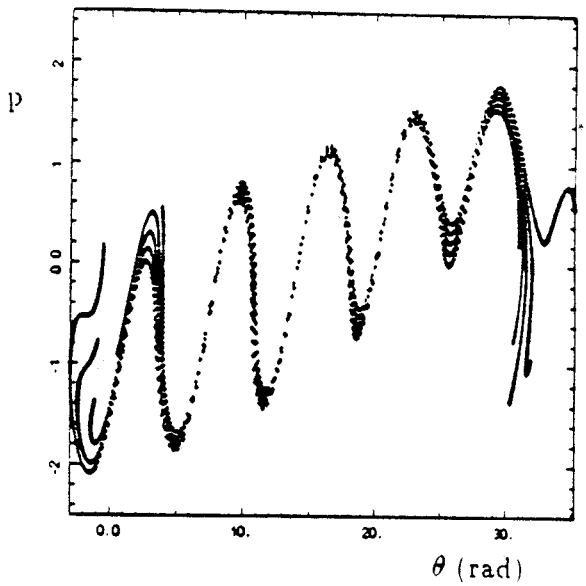

Fig. 27d - Longitudinal phase space at z = 18.8 m (4 m far from the radiator entrance)

6 - Conclusion

The high energy particle accelerator community agrees that one of the most relevant topic, on the way of the TeV electron-positron collider realization, is the capability to generate electron beams with high peak current and very low normalized emittance. The construction of an intermediate energy LINAC able to produce high quality beams seems to be a necessary step towards the TeV collider. In this respect, a soft X-ray FEL must be viewed as a test bench of the beam quality achieved. We have shown that with the ARES SC Linac facility several experiments in this context are envisageable: the link X-ray FEL's - SC LINAC's will hopefully be a marriage of convenience.

Acknowledgments

We are indebted to W.A.Barletta and A.M.Sessler for their support and encouragement in proposing the X-VUV FEL experiments in the ARES project context. We thank especially W.A.Barletta for the numerical simulations made with FRED-3D and we are also grateful to G.Vignola and M.Castellano for helpful and valuable discussions.

References

(1) "Ares Design Study (The Machine)" - Report LNF-90/005(R), January 17th 1990, Frascati.

(2) R.Bonifacio, C.Pellegrini and L.M.Narducci - Optics Comm 50 (1084) 373.

(3) G.Preparata - QFT of the FEL- Phys. Rev. A38, 233 (1988)

(4) E.T.Scharlemann - "Wiggle plane focussing in a linear wiggler" - LLNL Report UCRL-92429.

(5) W.A.Barletta and A.M.Sessler - Proc. of the INFN Int. School on Electromagnetic Radiation and Particle Beams Acceleration - Varenna (Italy), June 1988, p. 211-220.

(6) C.Pellegrini - NIM A227 (1980) 177.

(7) J.B.Murphy, C.Pellegrini and R.Bonifacio - Optics Comm. 53 (1985) 197.

(8) E.T.Scharlemann, A.M.Sessler and J.S.Wurtele - NIM A239 (1985) 29.

(9) R.Bonifacio et al. - Proc. of the INFN Int. School on Electromagnetic Radiation and Particle Beams Acceleration - Varenna (Italy), June 1988, p. 35.

(10) A.Ghigo, Int. Rep. LNF-Ares, 35 (1990)

(11) K.Halbach - Proc. of "Undulator Magnets for SR and FEL" - Trieste (Italy), June 1987.

(12) N. Cavallo - Ph.D. Thesis - University of Salerno, 1985.

(13) L.Serafini et al. - To be published.

(14) D.F.Alferov and E.G.Bessonov - Sov. Phys. Tech. Phys. 24 (4) 1979, 450.

(15) R.Coisson - Part. Accelerators, 11 (1981) 245.

(16) J.M.Ortega et al. - NIM A237 (1985) 268.

(17) R.Prazeres and J.M.Ortega - IEEE Journal of Q. El. 25 (1989) 2316.

(18) M.Billardon, R.Coisson and Y.Lapierre - Appl. Phys. B39 (1986) 9.

(19) R.Bonifacio et al. - Proc. Int. FEL Conference 1989.

(20) W.A.Barletta, private communication.

(21) E.T.Scharlemann, A.M.Sessler and J.S.Wurtele, Proc. of Int. Work. on Coherent and Collective Prop. in the Int. of rel. electr.and e.m.Rad., Como, Italy, Sept. 1984, p.29.